**UNIVERSITY OF SOUTHAMPTON**

FACULTY OF ENGINEERING SCIENCE AND MATHEMATICS

Optoelectronics Research Centre

# Direct UV Written Planar Devices for Sensing and Telecommunication Applications

by

Christopher Holmes

Thesis for the degree of Doctor of Philosophy

September 30, 2009

UNIVERSITY OF SOUTHAMPTON

ABSTRACT

Optoelectronics Research Centre

Doctor of Philosophy

Direct UV Written Planar Devices for
Sensing and Telecommunication Applications

Christopher Holmes

This thesis reports the development and potential applications of several direct UV written devices. The material platform of these devices is a silica-on-silicon composite, fabricated using flame hydrolysis deposition.

The device development within this thesis considers wet etching, micromachining and sputtering processes to enhance the physical and chemical actuation of direct UV written planar Bragg gratings. Physical actuation has been investigated through thermo-optic and strain-optic means, chemical actuation has been achieved through evanescent field exposure. Combining the chemical and physical actuators developed, a monolithic lab-on-a-chip based device has been fabricated. The demonstrated chip has the ability to monitor pressure, flow, temperature and refractive index of a measurand, flowing through a microfluidic channel.

A novel multimode interference (MMI) based device is also presented, which uses an adaptive Bragg period to define the side walls of the device. The reported structure shows a potential reduction in excess loss, compared to alternative raster scanned device geometries for power splitting operations.

# Contents

# List of Figures

# List of Tables

# Declaration of Authorship

I, **Christopher Holmes** declare that the thesis entitled

**Direct UV Written Planar Devices for Sensing and Telecommunication Applications**

and the work presented in the thesis are both my own, and have been generated by me as the result of my own original research. I confirm that

- this work was done wholly or mainly while in candidature for a research degree at this University;
- where any part of this thesis has previously been submitted for a degree or any other qualification at this University or any other institution, this has been clearly stated;
- where I have consulted the published work of others, this is always clearly attributed;
- where I have quoted from the work of others, the source is always given. With the exception of such quotations, this thesis is entirely my own work;
- I have acknowledged all main sources of help;
- where the thesis is based on work done by myself jointly with others, I have made clear exactly what was done by others and what I have contributed myself;
- parts of this work have been published as in Publications, Appendix A.

Signed:.....

Date: September 30, 2009

# Acknowledgements

There are of course many people to whom thanks are due for the help and inspiration they have gave me, over the course of my PhD. I whish to thank:

First and foremost, Prof. Peter Smith who supported and advised me throughout my time at the ORC. He has given me a tremendous amount of freedom to set my own goals and seek my own solutions to problems, but at the same time he has always be approachable and encouraging when I got stuck. I am deeply indebted to Peter.

I am extremely grateful to all the past and present members of the group including Dr. James Gates, Dr. Corin Gawith, Dr. Dmytro Kundys, Dr. Rafiq Adikan, Huw Major, Ben Snow, Richard Parker and Helen Rodgers whose enthusiasm and knowledge has been a perpetual inspiration.

I also thank past and present colleagues at the Optoelectronics Research Centre including: Eve Smith, Simon Butler, Edwin Weatherby, Chris Nash, Tim McIntyre, Mark Lessey, Elliot Peach, Kenton Knight, Dave Saga, Neil Sessions, Dave Oliver, Kevin Sumner, Tim May-Smith, Daniel Friedrich, Hamish Hunt and Andrew Webb. I would also like to thank Brian Mellor and Jack Lambert from the School of Engineering Science for their assistance with mechanical testing. All of whom have shown tremendous patience in assisting and teaching me throughout the course of my PhD.

Thank you to my friends, family and especially my girlfriend Catherine Varcoe-Baylis, for their unwavering support and understanding. Thank you to my parents, George and Jean Holmes for providing me with the best educational opportunities, for supporting all my decisions, and for shaping me into the person I am today.

Finally, thank you to EPSRC and Stratophase for supporting me over the past four years of my PhD and giving me the experience of working at the ORC.

Christopher Holmes

# NOTATION

| | |
|---|---|
| AFM | Atomic Force Microscope |
| AOM | Acousto-Optic Modulator |
| ASE | Amplified Stimulated Emission |
| au | Arbitary Units |
| BG | Bragg Grating |
| BSA | Bovine Serum Albumin |
| cw | Continuous Wave |
| CVD | Chemical Vapour Deposition |
| DGW | Direct Grating Writing |
| DUW | Direct UV Writing |
| EDX | Energy-dispersive X-ray spectroscopy |
| FDM | Frequency Division Multiplexed |
| FHD | Flame Hydrolysis Deposition |
| GLS | Gallium Lanthanum Sulphide |
| GODC | Germanium Oxygen Deficient Centre |
| IO | Integrated Optics |
| LPG | Long Period Grating |
| MEMS | Microelectromechanical Systems |
| MMI | Multimode Inteference |
| NOV | Neutral Oxygen Vacancy |
| OADM | Optical Add Drop Multiplexed |
| OSA | Optical Spectrum Analyser |
| PECVD | Plasma Enhanced Chemical Vapour Deposition |
| RI | Refractive Index |
| RIU | Refractive Index Units |
| SEM | Scanning Electron Microscope |
| SPP | Surface Plasmon Polariton |
| SPR | Surface Plasmon Resonance |
| TE | Transverse Electric |
| TM | Transverse Magnetic |
| TMM | Transfer Matrix Method |
| WDM | Wavelength Division Multiplexing |

*"We have a habit in writing articles published in scientific journals to make the work as finished as possible, to cover up all the tracks, to not worry about the blind alleys or describe how you had the wrong idea first, and soon. So there isn't any place to publish, in a dignified manner, what you actually did in order to get to do the work."*

Richard P. Feynman, Nobel Lecture, *1965*

# Chapter 1

# Introduction

This PhD thesis has been submitted exactly forty years from the publication of a concept introduced by Miller [8], which posed the possibility of optical components being integrated into one single substrate. This concept of integrated optics (IO) is entirely analogous to integrated microelectronics and likewise exhibits similar benefits of miniaturisation, performance enhancement and usability.

Today, there is a rich variety of IO devices, substrates and fabrication techniques, which have a wide variety of applications including physical/chemical sensors and telecommunication components. This PhD thesis examines potential applications of IO devices fabricated using a relatively new direct UV grating writing technique [9] [10].

The purpose of this chapter is to give a brief overview of the integrated optical devices and material platforms that exist today. It is hoped this will give the reader a sufficient background for the context of the work undertaken, which shall be summarised at the end of this chapter.

## 1.1 Integrated Optical Materials

Unlike the microelectronics industry that has one distinctly dominant platform for fabrication (silicon) the photonics industry has several competing platforms. The reason for this is that they all possess to some degree restrictions and advantages over each other, some of which have been highlighted in Table 1.1. An impor-

tant feature of IO components is their possession of active and passive properties. [5], [11]. In general optically inactive components are incapable of light generation, whereas optically active components are capable of light generation. It must be noted that through rare-earth element doping passive platforms can be made active. Therefore, it must be explicitly stated that the listings in Table 1.1 do not consider variants of the platform with rare earth dopants.

Silica-on-silicon is one of the most common materials used for IO devices. The advantages of the silica-on-silicon platform include an associated low propagation loss and coupling loss. In addition, as the platform consits of a silicon part they have a unique potential integration capacity with electronic components. Their disadvantage is that they are not an inherently active material; however silica can be made active through rare earth doping.

The properties an IO device can possess is dependent upon the optical material from which it is fabricated. Device application is thus largely dictated by the material properties of the chip. The two most common applications for commercial IO devices are in telecommunications and sensing, which shall be described in the following section.

## 1.2 Optical Device Applications

The market pull for IO devices has traditionally been associated with the telecommunication industry, where high consumer demand for network bandwidth and flexibility has driven the technological development. Currently, local, metropolitan and wide area telecommunication networks are being enhanced to meet with an ever increasing demand. This is generally achieved by adding more optical fibres, increasing the bit rate per optic fibre or upgrading the switches' size, throughput and functionality. A developing trend for network switch upgrades is converting optical-electronic-optical conversion switches to integrated optical devices. This makes the network all-optical (except at the end nodes) thus providing improved economy, flexibility, robustness and speed to existing networks.

The advancement in integrated optical components has not only been of benefit to the telecommunication industry. It has been realised for many years that components principally developed for telecommunications can also be used/modified

| Material System | Propagation Loss (dB/cm) | Fiber Coupling Loss (dB) | Refractive Index | Optically Passive/Active |
|---|---|---|---|---|
| Silica [$SiO_2$] (e.g. silica-on-silicon, | 0.1 | 0.5 | 1.44-1.47 | y/n |
| Silicon [Si] (e.g. silicon-on-insulator) | 0.1 | 1.0 | 3.48 | y/n |
| Sol-Gels | 0.1 | 0.5 | 1.2-1.47 | y/n |
| Polymers (e.g. acrylate, polyimide) | 0.1 | 0.5 | 1.3-1.7 | y/n |
| Lithium Niobate [$LiNbO_3$] | 0.5 | 2.0 | $n_o$=2.213 $n_e$=2.138 | y/n |
| Indium Phosphide [InP] | 3 | 10 | 3.1 | y/y |
| Gallium Arsenide [GaAs] | 0.5 | 2.0 | 3.374 | y/y |

**Table 1.1:** Properties of some common integrated optical material platforms at 1550 nm wavelength [5], [6]

for physical and chemical sensing applications.

The following subsections shall address some telecommunication and sensing applications for integrated optical circuits.

### 1.2.1 Telecommunications

The optical telecommunication industry is currently in a state of growth, which is driven by several factors including an increase in demand for high-definition multimedia over the internet and a change of global dynamics [12] including the emergence of strong eastern economies. However, the response to meet with consumer demand has been slow partially as a result of optical telecommunication industry living in the shadow of one of the greatest economic collapses in the modern history.

The burst of the telecommunication 'bubble' erupted in a wave of liquidations, reorganisations and bankruptcy filings which engulfed both small start-ups and corporate titans. The burst of the bubble has often been discussed in terms of external factors, such as a macroeconomic slowdown, sliding stock markets and unsavoury investment banking. This has been a convenient way of explaining the crash, without criticising internal issues, including a belief that internet and broadband applications would fuel an unending demand for network capacity to support the increasing flow of data traffic. The current increasing demand for network bandwidth is therefore, not surprisingly, met with caution. However, emerging technologies such as HDTV over the internet and a globally expanding digital economies are market pulls that need to be addressed.

The vast amount of optical telecommunication transmission is achieved through silica based optical fibres, as they can be cheaply fabricated and have an associated low optical loss. To coincide with silica's spectral regions of low loss (and the availability of light sources), specific telecommunication windows exist. The most common window being the so-called 1550 nm window, which spans a spectral range from 1480 nm to 1600 nm and resides between regions of low infrared absorption and Rayleigh scattering. This window also takes into consideration an $OH^-$ resonance, associated with $\sim$1400 nm wavelength, illustrated in Figure 1.1.

Rayleigh scattering occurs because of silica's vitreous state, which results in vari-

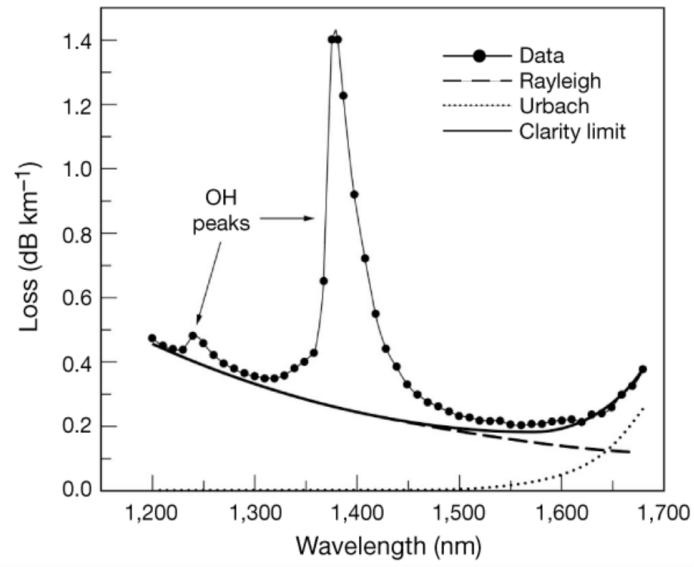


**Figure 1.1:** Spectral attenuation of light in a silica fibre optic, the solid points with a solid line interpolated through them is measured data. The thick solid line is obtained from the sum of the behaviour calculated from Rayleigh scattering (dashed line) and the behaviour from the Urbach tail of the silica atomic vibrational spectrum (dotted line) [1].

ation in density that is small compared to one wavelength. UV and IR absorption, including $OH^-$ absorption, is an inherent property of the silica [13].

It should be noted that the capacity of optical networks can be extended from 1260 nm to 1625 nm, by using so called zero water peak fibre, achieved through fibre drying [1]. Network capacity can also be increased by either laying additional optical fibre or increasing the density of channels that exist within the telecom window. Channels are defined in the wavelength regime using a system known as Wavelength Division Multiplexing (WDM). WDM is conceptually identical to Frequency Division Multiplexing (FDM) used in microwave radio and satellite system communication. Just as in FDM the channels are correctly spaced to avoid inter-channel interference. WDM channel spacings are principally decided by taking into consideration the guard band for the laser sources and modulation bandwidth used for each wavelength. The bandwidth is assigned to take into account temperature effects and aging. Typical bandwidths of 0.4 nm to 1.6 nm are employed, corresponding to 50 GHz and 200 GHz respectively, at 1550 nm wavelengths. The key feature of WDM is that the discrete wavelengths form an independent set of carriers which can be separated, routed, and switched without interfering with one another.

Optical networks require the routing of signals between WDM channels. This can be achieved using various optical filtering techniques including arrayed waveguide gratings, diffraction gratings, thin film filters, Bragg gratings, micro-resonators, photonic crystals or liquid crystals and further description of these methods can be sought in a recent review by Eldada [11]. For control over network routing these filters require tuning, which can be achieved through thermo-optical, electro-optical or mechanical-optical means, achieved using optical fibre components or integrated optical circuits. The elegance of using IO is that many components can be compactly fitted onto a single chip.

Bragg grating structures [14] are an effective filtering method utilised in today's optical network, which have the advantages of potential narrow bandwidth, low crosstalk, and a flat-top passband. Bragg gratings consist of a grating structure, which selectively filters specific WDM wavelengths. An example of a routing procedure that Bragg gratings can be implemented for, is Optical Add/Drop Multiplexing (OADM), illustrated in Figure 1.2. This example depicts two optical circulators and a Bragg grating that is designed to reflect 'red' light. At the Bragg grating the red light is reflected and re-enters the circulator from which it came, which can either added or droped from a signal.

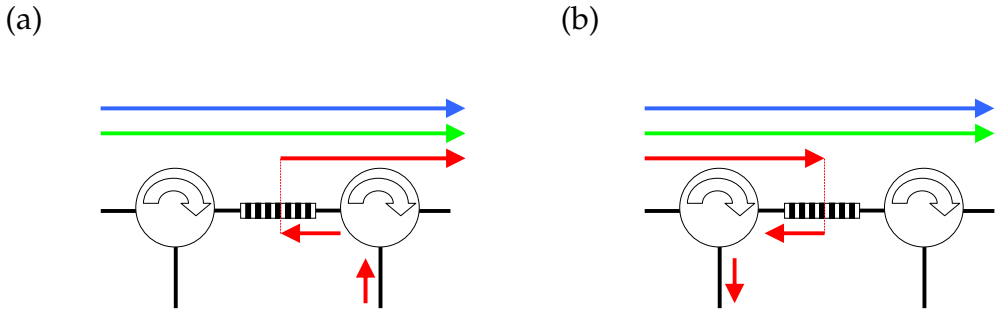


**Figure 1.2:** An optical add/drop multiplexer realised using a Bragg grating and two circulators, depicting (a) adding (b) dropping functions

It must be noted that control over the spectral response of an OADM is essential as small amounts of spectral degradation can drastically degrade their filtering performance; this is especially true for filter misalignments and cascaded operations [15].

Over the past several decades there has been a considerable amount of investment made in advancing optical telecommunications. The technology brought about

through this investment brings an opportunity to disrupt other markets, such as those involved with chemical and physical sensing. Optical based sensors are of particular interest as they possess advantages which include immunity to electromagnetic interference, high sensitivity, and potential for mass production.

### 1.2.2 Sensing

A wide range of sensors exist today. The purpose of any sensor can generally be categorised as monitoring either chemical or physical changes. The operation of chemical sensors differs significantly from physical sensors in that the number of potential chemical parameters to monitor is almost infinite. In addition, whilst physical sensors can be hermetically encapsulated the chemical sensor cannot and therefore becomes easily affected by interfering substances and environmental effects.

The chemical sensor market contains a variety of competing technologies that can be classified into four main categories [16]: chromatography, mass, electrochemical, and optical. Chromatography sensors involve the separation of complex mixtures and include standard techniques found in analytical chemistry, such as High Performance Liquid Chromatography (HPLC). Mass sensors involve the detection of mass (or mechanical modulus) changes upon a surface [17], generally the detection is characterised by a shift in resonance frequency, e.g. resonance of a cantilever [18]. Electrochemical sensors involve the detection of an electrical signal [19] and monitor electrical changes e.g. resistance [20]. Finally, optical devices detect changes in the electromagnetic waves as they interact with a chemical. The general advantages and disadvantages associated with these devices are given in Table 1.2. It must be noted that this is a generalisation of all the devices in a class and that some specific examples may deviate from the criteria.

The majority of commercial optical chemical sensors are either bulk optic based (e.g. spectrophotometer, refractometer) or exploit optical fibre [21] and/or IO [22] based structures for detection.

As a result of their inherent nature IO based chemical sensors have the unique potential to form part of so termed lab-on-a-chip devices [23] [24]. The lab-on-a-chip concept aims to bring together multiple chemical process, which may traditionally

| Technique | Advantages | Disadvantages |
|---|---|---|
| Chromatography | excellent precision<br>sensitive<br>repeatability | not portable<br>requires training<br>expensive<br>not in situ |
| Mass | portable<br>wide chemical range | expensive<br>not in situ |
| Electrochemical | small<br>low power<br>cheap<br>good sensitivity<br>in situ | questionable discrimination |
| Optical | low power<br>very sensitive<br>detect variety of chemicals<br>durability<br>in situ | can be expensive |

**Table 1.2:** A comparison of different sensing techniques

require a (bio)chemical lab and integrate them on a single compact chip. Such devices inherently use small volumes and thus reduce the time taken to synthesize and analyse a product, effectively reducing reagent costs and the amount of chemical waste. Compact devices also allow samples to be analysed at the point of need rather than in a centralized laboratory [24].

Physical sensors monitor physical changes about their environment and have a huge expanse of applications, which can range from large scale structural health monitoring of bridges, oil rigs, skyscrapers etc to the small scale monitoring of temperature of an integrated optical or electrical chip. Physical sensors do not have the complexity of measurand distinction associated with chemical sensors, which have a near infinite chemical set to distinguish. In addition they can be hermetically encapsulated to reduce environmental effects.

Optical physical sensors are currently gaining large footholds in the physical sensor market, which has up-till-recently been dominated by electrical devices. A notable example being the increasing use of optical fibre based sensors in civil engineering, which are used as a tool for monitoring stresses in both new and old constructions [25]. Physical optical sensors are not always the best choice for every application but can perform the function of virtually any conventional sensor and have the associated advantages of optical devices.

Optical sensors often exhibit greater sensitivity and faster readings than conventional sensing methods [26]. They also have the advantage of immunity to electromagnetic and radio frequency interference and an inability to create sparks meaning they can be implemented in explosive environments. Generally, the materials from which they are made can function under adverse temperature, pressure toxicity or corrosive atmospheres that would otherwise rapidly erode metals. However, as the technology matures in the market place device cost is expected to reduce, in addition to increased consumer familiarity.

## 1.3 Aim of Research

This PhD thesis investigates direct UV grating written IO structures, for potential telecom and sensing applications. The direct UV writing system consists of a dual UV laser beam set-up, beneath which a photosensitive silica-on-silicon composite

sample is translated, as illustrated in Figure 1.3. Using this technique both waveguide and Bragg gratings can be defined in a one-step process.

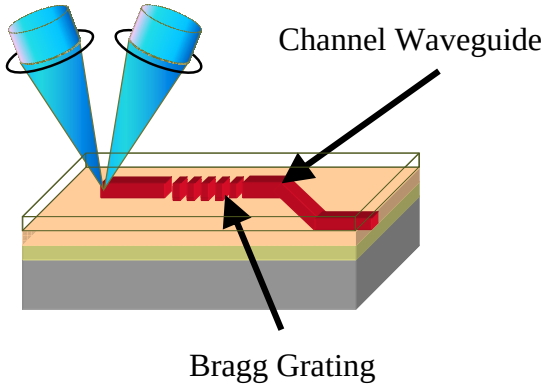


**Figure 1.3:** A conceptual schematic of the direct UV Bragg grating writing system

The original aims of this PhD thesis were to develop Direct UV Written devices for:

- Chemical Actuation
- Physical Actuation
- Lab-on-a-Chip

Before establishing how the aforementioned aims have been fulfilled, it must be noted that this PhD has been undertaken as part of a CASE sponsored award, with the photonics company Stratophase Ltd. As a result, some of the work undertaken in this PhD thesis has been a collaborative pursuit, it is therefore necessary to distinguish the author's original contributions to the field when discussing how the aims have been achieved.

The aims of this PhD thesis have been met through the development of several novel direct UV written components/devices. It has been demonstrated that several of these components can be multiplexed to form novel devices in their own right that have potential application as physical/chemical sensors or for telecommunication OADM operations.

Chemical actuation has been investigated through evanescent field exposure. The developments of these devices were principally made in collaboration with the

University of Southampton, Stratophase, Davin Optics and Smart Fibres. The author's unique contribution in this collaboration was to computationally investigate device design through observing: geometries of evanescent field exposure; fabrication parameters (including writing fluence, cladding/core refractive indices); dielectric and metal enhancement layers; surface functionalisation and dispersive properties of measurands. All computational investigations made in this thesis are the author's original work. In addition to computational investigations the author has fabricated these devices through wet etching and using novel micromachined groove geometries. Fabricated devices, with subsequently deposited enhancement layers have been achieved with the assistance of Kenton Knight (GLS deposition) and Stratophase (Titania deposition). Investigation into surface quality using surface profilers (Atomic Force Microscope and alpha-stepper), spectral analysis of measurands and repeatability of device operation after cleaning procedures are specific original contributions made by the author.

Physical actuation has been understood both theoretically and experimentally, using mechanisms of external stress and localised thermal heating. This work is a specific original contribution made by the author to the field, as prior to this thesis no external physical actuation had been made on direct UV written silica-on-silicon devices. To this extent this reported work is a specific original contribution made to the field by the author. The theoretical derivation of silica-on-silicon composites and fabrication of chips for bending and lateral compression measurements was solely made by the author. The bending experiments were undertaken by the author and the lateral compression measurements were jointly made by the author and Jack Lambert from the School of Engineering Science. All theoretical interpretation of the physical actuation was the author's original work and had not been established before this PhD thesis. Fabrication of thermal elements for localised heating was jointly achieved by the author and Dmytro Kundys. All physical actuation devices were designed and tested by the author.

The concept, development and fabrication of thin silica membranes with inherently defined planar Brag gratings is an original contribution made to the field by the author. This work includes the integration of Bragg gating based evanescent sensor with silica membranes. The resulting fabricated chip can monitor pressure, flow, temperature and refractive index of a test fluid. This work is a specific original contribution made by the author. Chip design, development and fabrication

was made solely by the author.

A novel Multimode Interference (MMI) device was developed by author during his PhD. The novel device exploits an adaptive period antiresonant side-wall condition to reduce excess loss associated with low index contrast devices. To optimise device performance the author co-wrote a beam propagation method algorithm, with Huw Major. The author's unique contribution to the algorithm was to refine a 2-dimensional model through the use of an effective index method. The author also developed the algorithm so that the refractive index structure could be manipulated as a function of propagation length and such that the boundary conditions of the algorithm were absorbing. The fabricated realisation of this novel device was made by the author.

It must be noted that as a result of the fire in the Mountbatten building on October 30th 2005, the author's office, in-house flame hydrolysis deposition system, and the characterisation set-ups in lab 1083 were destroyed. This meant that the flame hydrolysis deposition and wafer dicing fabrication steps were outsourced for the aforementioned work. In addition all cleanroom facilities including etching and sputtering were removed for several months during the authors PhD. However, the direct UV writing system survived during this time as it was not housed in the Mountbatten building. The wet etching and direct UV writing fabrication steps mentioned in this thesis were done by the author. All characterisation stated was made by the author. The Labview data interpretation program was written by James Gates.

The remainder of this chapter shall set-out how this work has been organised in the thesis, through the use of a synopsis.

## 1.4 Thesis Synopsis

This PhD thesis is structured as follows:

A theoretical understanding of optical waveguide and Bragg grating operation is tackled in **Chapter 2**. Developed from Maxwell's equations the chapter examines both analytical and numerical methods of mode solving, for slab and channel waveguides. For channel waveguides the finite difference, finite element and film

mode matching (FMM) methods are presented, as numerical examples of mode solving algorithms. This sets the scene for **Chapter 4**, where a commercial FMM algorithm (FIMMWAVE) has been used by the author. **Chapter 2** also describes a fast Fourier transform beam propagation method (FFT-BPM) as an example of a beam propagation algorithm. This sets the scene for **Chapter 8** where an FFT-BPM algorithm has been written (presented in **Appendix B**) and implemented by the author. **Chapter 2** concludes by exploring the spectral response of a Bragg grating.

The method of device fabrication is addressed in **Chapter 3**. This chapter covers the theory and history of direct UV writing, comparing it to other competing methods of fabrication including photolithography and direct femtosecond writing. The chapter begins by describing the chemical vapour deposition techniques, which can be used to form a silica-on-silicon platform. This includes the considerations of composition required for direct UV writing, including the introduction of a UV photosensitive dopant such as germanium to the silica. The phenomenon of photosensitivity is discussed and means by which it can be enhanced are explained, this includes the efforts undertaken by the author to extend the longevity of the writing process. The dual beam direct UV writing technique is described including methods of grating design to achieve uniform, chirped and apodised Bragg grating structures. This chapter concludes by discussing how the Bragg gratings are characterised and the associated standard error associated with their measurement.

Following the two foundation chapters, which report on the underlying theory of device operation and fabrication the subsequent chapters report upon device optimisation for physical and chemical actuation.

The chemical actuation of a Bragg grating is investigated in **Chapter 4**. This is achieved through evanescent field exposure gained through wet etching and micromachining techniques. The chapter discusses the theory of evanescent field exposure and how sensitivity can be increased using enhancement layers for surface and bulk detection. Combining empirical measurements and computer simulation the effectiveness of metal and dielectric enhancement layers as well as the manipulation of basic design parameters is investigated. The chapter also examines the potential exploitation of an analyte's dispersion to gain enhanced discrimination. To understand the dispersive properties, absorption data was collected and converted into dispersive data using the Kramers Kronig relation. **Chapter 4** also

address fabrication considerations including surface quality and topology. The chapter concludes by discussing the effect surface wetting has on a device's repeatability of measurements and how this can be negated.

The physical actuation of a Bragg grating is investigated in **Chapters 5, 6** and **7**. **Chapter 5** develops the strain relationship for the composite silica-on-silicon platform. The theory is then used to explain the spectral response of a strain tuned Bragg grating under three-point and four-point bending and lateral compression.

**Chapter 6** considers actuation of a thin silica membrane with a Bragg grating inherently defined within it. The chapter begins by considering buckling theory of a membrane, which is exploited in device operation. The membrane device is demonstrated to quantify effectively differential pressures across the membrane structure and to monitor flow in a microfluidic channel. **Chapter 6** concludes by combining the membrane based pressure and flow sensors with chemical and thermal sensors upon a single monolithic chip.

As well as physical actuation through mechanical force, physical actuation can also be achieved through thermal means. Localised thermo-optic tuning of a direct UV planar Bragg grating is demonstrated in **Chapter 7**.

A novel multimode interference based device is introduced in **Chapter 8**. The chapter tackles the theory and through an optimisation algorithm simulates an optimised design. This structure is compared to raster scanned device and fabrication considerations made.

**Chapters 9** and **10** summarise the work and future developments are highlighted in respectively.

# Chapter 2

# Theory and Analysis

## 2.1 Introduction

This chapter summarises the theoretical bedrock and analysis techniques that can be applied to integrated optical circuits. There are many good texts which do this [5] [27] [28] and so the purpose of this chapter is to complement the literature and does not act to replace it. This chapter summarizes Maxwell's equations and develops the (scalar) eigenmode equations for electromagnetic fields in a weakly guiding waveguide. Using this theory, analytical and numerical techniques for analysing waveguide structures and Bragg gratings are described.

## 2.2 Waveguides

One of the most fundamental structures of an optical circuit is a waveguide. Just as electronic circuits manipulate current with conducting strips, waveguides are used in an analogous way to manipulate the path of light in integrated optical circuits. A waveguide is defined as a structure capable of guiding the flow of electromagnetic energy in a direction parallel to its axis. Loosely speaking, a dielectric waveguide is formed when a core region of high refractive index is surrounded by regions of low refractive index. This can be achieved through a slab waveguide structure, as illustrated in Figure 2.1. Light can be confined in the high index core of a slab waveguide if the incident angle upon the index boundary satisfies the condition for total internal reflection (TIR) [29].

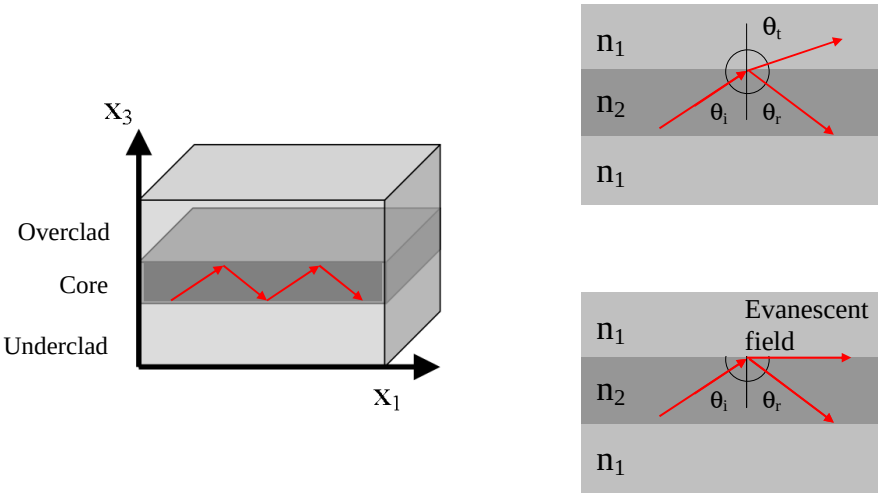


**Figure 2.1:** Schematic of a slab waveguide, where the darker shaded regions represent an area of higher refractive index

It may first appear that any lightwave with an angle of incidence greater than a critical angle, for TIR conditions [30], will be confined. However, for the majority of waveguides there is a discrete set of angles greater than the critical angle that corresponds to successive boundary reflections having phase fronts which coincide. For a given waveguide these discrete set of angles can be thought of as a discrete set of characteristic waves, called modes. Modes are the fields that maintain the same traverse distribution and polarisation at all distances along the waveguide axis. The following section shall further develop the concept of mode solutions by applying boundary conditions to Maxwell's and the Helmholtz equations.

### 2.2.1 Maxwell's Equations

Maxwell's equations irrefutably hold the solution to all problems in electrodynamics. Indeed the foundation of this entire thesis is bound together by four equations published by Maxwell in 1873. To understand the equations we must know differential calculus. However, as stressed by Feynman [31] to interpret a problem we need to understand the nature of the equations. We shall be doing this in the following sections by visualising guided light in terms of characteristic waves (modes).

The evolution with time, t, of the electric field **E**(t) and magnetic field **H**(t), in a medium of magnetisation density **M**(t) and polarisation density **P**(t) can be described by the following Maxwell's equations:

$$\nabla_{\wedge}\mathbf{E}(t) = -\mu_0\frac{\partial \mathbf{H}(t)}{\partial t} - \frac{\partial \mathbf{M}(t)}{\partial t} \quad (2.1)$$

$$\nabla_{\wedge}\mathbf{H}(t) = \mathbf{J}_f(t) + \epsilon_0\frac{\partial \mathbf{E}(t)}{\partial t} + \frac{\partial \mathbf{P}(t)}{\partial t} \quad (2.2)$$

$$\nabla.\epsilon_o\mathbf{E}(t) = \rho_0(t) - \nabla.\mathbf{P}(t) \quad (2.3)$$

$$\nabla.\mathbf{H}(t) = -\nabla.\mathbf{M}(t) \quad (2.4)$$

$\mu_0$ is the permeability of free space, $\rho(t)$ is the charge density and $\mathbf{J}_f$(t) is the free current density, which relates to all charges not associated with the polarisation density **P**(t).

Maxwell's equations are sometimes expressed in terms of the electric displacement field **D** and magnetic flux density **B**, which relate to **E**, **P** and **M**, **H** as

$$\mathbf{D} = \epsilon\mathbf{E} = \epsilon_o\mathbf{E} + \mathbf{P} \quad (2.5)$$

$$\mathbf{B} = \mu\mathbf{H} = \mu_o\mathbf{H} + \mathbf{M} \quad (2.6)$$

were $\mu$ and $\epsilon$ is the permeability and permittivity of a media in which the field exists.

The waveguides treated in this PhD thesis shall be assumed to be nonmagnetic (**M**(t)=0), have no resultant charge ($\rho_0$ = 0), no free current (**J**(t) = 0) and a time-dependence of $e^{i\omega t}$ (where $\omega$ is angular frequency), thus Maxwell's equations can be restated as

$$\nabla_{\wedge}\mathbf{E} = -i\mu_0\omega\mathbf{H} \quad (2.7)$$

$$\nabla_{\wedge}\mathbf{H} = i\omega\epsilon\mathbf{E} \quad (2.8)$$

$$\nabla.\epsilon\mathbf{E} = 0 \quad (2.9)$$

$$\nabla.\mathbf{H} = 0 \quad (2.10)$$

Through separating variables **E** and **H**, this set of partial differential equations

can be represented as two Helmholtz equations. The Helmholtz equation for the dielectric field can be derived by taking the curl of Equation 2.7 to give

$$\nabla_\wedge(\nabla_\wedge \mathbf{E}) = -i\mu_0\omega\nabla_\wedge \mathbf{H} \tag{2.11}$$

which can be simplified using a vector identity[1] and Equation 2.8, to give

$$\nabla(\nabla.\mathbf{E}) - \nabla^2\mathbf{E} = \epsilon\mu_0\omega^2\mathbf{E} \tag{2.12}$$

rewriting Equation 2.9 gives

$$\begin{aligned} \nabla(\epsilon\mathbf{E}) = \mathbf{E}.(\nabla\epsilon) + \epsilon\nabla.\mathbf{E} = 0 \\ \Rightarrow \nabla.\mathbf{E} = -\frac{1}{\epsilon}\mathbf{E}.(\nabla\epsilon) \end{aligned} \tag{2.13}$$

and combining this with Equation 2.12 gives the electric full vectorial Helmholtz equation

$$\nabla^2\mathbf{E} + \nabla\left(\frac{1}{\epsilon}\nabla(\epsilon).\mathbf{E}\right) + \epsilon\mu_0\omega^2\mathbf{E} = 0 \tag{2.14}$$

In a similar manner, we can consider the magnetic field and obtain

$$\nabla^2\mathbf{H} + \frac{1}{\epsilon}\nabla\epsilon_\wedge(\nabla_\wedge\mathbf{H}) + \epsilon\mu_0\omega^2\frac{\partial^2\mathbf{H}}{\partial t^2} = 0 \tag{2.15}$$

The full vector Helmholtz equations are used in the numerical mode solving techniques discussed in Subsection 2.2.5 and so have been described here for completeness. It must be noted however that many waveguides display so called weakly guiding characteristics and result in the simplification of this full vectorial equation into a scalar equation. Before weakly-guiding waveguides are discussed further it is important to establish the boundary conditions at the index interfaces, which hold true for all waveguide types.

[1] $\nabla_\wedge(\nabla_\wedge\mathbf{A}) = \nabla(\nabla.\mathbf{A}) - \nabla^2\mathbf{A}$

### 2.2.2 Boundary Conditions

Waveguides have index interfaces between the core and cladding layers. Using Maxwell's equations, boundary conditions can be defined for an electromagnetic wave existing at an interface between media $i$ and media $j$, given as

$$(\mathbf{E}_i - \mathbf{E}_j)_\wedge \hat{\mathbf{n}} = 0 \tag{2.16}$$

$$(\mathbf{H}_i - \mathbf{H}_j)_\wedge \hat{\mathbf{n}} = 0 \tag{2.17}$$

$$(\epsilon_i \mathbf{E}_i - \epsilon_j \mathbf{E}_j).\hat{\mathbf{n}} = 0 \tag{2.18}$$

$$(\mathbf{H}_i - \mathbf{H}_j).\hat{\mathbf{n}} = 0 \tag{2.19}$$

where $\hat{\mathbf{n}}$ is a unit vector. These boundaries dictate a magnetic field that is tangentially and normally continuous (Equations 2.17 and 2.19 respectively) and an electric field that is tangentially continuous (Equation 2.16) but can be normally discontinuous (Equation 2.19). The normal components of the electric fields can be discontinuous as the normal field of $\epsilon\mathbf{E}$ is continuous. These boundary conditions are a result of Maxwell's equations and so must hold true for any considered mode. The following sections shall now use these boundary conditions to address two modes encountered in this PhD thesis, guided and leaky.

### 2.2.3 Weakly-Guiding Waveguides

Guided modes are solutions that fulfil the TIR condition and thus require the waveguide to have a greater refractive index than the surrounding cladding. For many waveguides the refractive index contrast varies by only a small amount. That is, the refractive index of the central core layer varies only by $\sim$0.3 $\%$ relative to the cladding layers. These types of waveguides are referred to as weakly guiding waveguides. By saying this we do not mean that the light leaks out! On the contrary one of the many reasons that optical fibre (an example of a weakly-guiding waveguide) is replacing copper wire in telecom infrastructure is precisely because the light doesn't leak out and can effectively transport information continental distances. Weakly guiding merely means that the refractive index contrast is small. The waveguides considered in this PhD thesis are assumed to be weakly

guiding, thus we assume $\nabla\epsilon \approx 0$. Under such conditions Equations 2.14 and 2.15 reduce to:

$$\nabla^2\mathbf{E} + n^2k^2\mathbf{E} = 0 \tag{2.20}$$

$$\nabla^2\mathbf{H} + n^2k^2\mathbf{H} = 0 \tag{2.21}$$

where k is the wavevector and n is refractive index.

What happens to the electromagnetic field at the boundary can be understood through considering Maxwell's equations, from Equations 2.7 and 2.8 it can be stated that

$$i\beta E_2 = -i\omega\mu_0 H_3 \tag{2.22}$$

$$\frac{\partial E_2}{\partial x_3} = i\omega\mu_0 H_1 \tag{2.23}$$

$$-i\beta H_3 - \frac{\partial H_1}{\partial x_3} = i\omega\epsilon_0\epsilon E_2 \tag{2.24}$$

$$i\beta H_2 = i\omega\epsilon_0\epsilon E_3 \tag{2.25}$$

$$\frac{\partial H_2}{\partial x_3} = i\omega\epsilon_0\epsilon E_1 \tag{2.26}$$

$$-i\beta E_3 - \frac{\partial E_1}{\partial x_3} = -i\omega\mu_0 H_2 \tag{2.27}$$

where the numbered subscripts refer to the vector field components along the $x_1$, $x_2$ and $x_3$ dimension respectively, which are indicated in Figure 2.1 relative to the slab waveguide. It must be noted that $x_1$ is the direction of propagation.

Equations 2.22-2.24 involve only $E_2$, $H_3$ and $H_1$ and Equations 2.25 - 2.27 involve only $E_3$, $E_1$ and $H_2$, meaning there are two independent sets of solutions to Maxwell's equations. One of these sets will correspond to non-vanishing values of $E_2$, $H_3$ and $H_1$ and vanishing values of $E_3$, $E_1$ and $H_2$. The mode solutions in this instance are known as Transverse Electric (TE). For the alternative set of solutions the vanishing and non-vanishing terms are swapped and produce a set of modes known as Transverse Magnetic (TM). These two polarisation sets of modes can be interpreted in terms of ray optics, as illustrated in Figures 2.2

Firstly considering the TE modes by substituting $H_3$ and $H_1$ from Equations 2.22 and 2.23 in Equation 2.24 to obtain

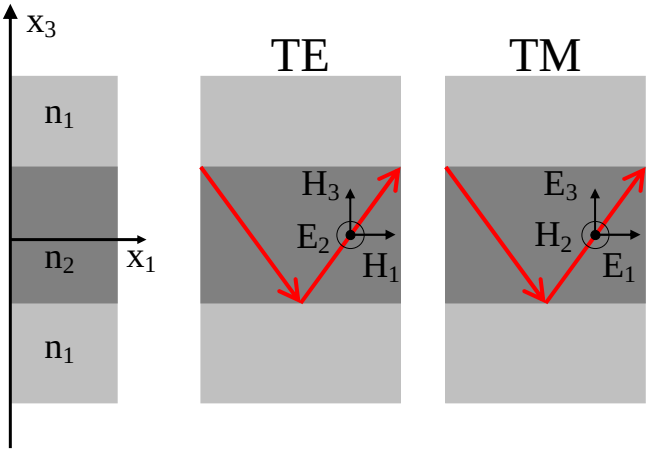


**Figure 2.2:** The field components for TE and TM polarisations

$$\frac{d^2E_2}{dx_3^2} + [k_0^2 n^2(x) - \beta^2]E_2 = 0 \tag{2.28}$$

where $\beta$ is the propagation constant of the supported mode and $k_0$ is the wavevector in free space. Considering a symmetric slab waveguide of core dimension d, cladding index of $n_1$ and core index $n_2$ , as illustrated in Figure 2.2, Equation 2.28 can be expressed as

$$\frac{d^2E_2}{dx_3^2} + [k_0^2 n_2^2(x_3) - \beta^2]E_2 = 0 \qquad |x_3| < d/2 \tag{2.29}$$

$$\frac{d^2E_2}{dx_3^2} + [k_0^2 n_1^2(x_3) - \beta^2]E_2 = 0 \qquad |x_3| > d/2 \tag{2.30}$$

For a guiding mode the field existing within the cladding must be exponential decaying in the transverse direction of the cladding layer, such that at $+\infty$ and $-\infty$ the field is 0. Therefore, in order for guided modes to exist

$$n_2^2 < \frac{\beta^2}{k_0^2} < n_1^2 \tag{2.31}$$

Equations 2.29 and 2.30 has symmetric TE solutions

$$E_2(x_3) = \begin{cases} Acos(\kappa x_3) & |x_3| < d/2 \\ Be^{-\gamma|x_3|} & |x_3| > d/2 \end{cases} \tag{2.32}$$

and antisymmetric TE solutions

$$E_2(x_3) = \begin{cases} Csin(\kappa x_3) & |x_3| < d/2 \\ \frac{x_3}{|x_3|} De^{-\gamma|x_3|} & |x_3| > d/2 \end{cases} \tag{2.33}$$

where A, B, C and D are constants and the substitutions $\kappa^2 = k_0^2 n_2^2 - \beta^2$ and $\gamma^2 = \beta^2 - k_0^2 n_1^2$ have been made. Continuity requirements of $E_2(x_3)$ and $dE_2/dx_3$, leads to solutions of the form

$$\xi tan(\xi) = \frac{\gamma d}{2} \tag{2.34}$$

$$\xi cot(\xi) = \frac{\gamma d}{2} \tag{2.35}$$

where $\xi = \kappa$ d /2. These equations can be represented more conveniently by introducing a dimensionless parameter, V. The V-parameter is a normalisation of the waveguide's structure and the wavelength of the launched light. The parameter is generally used to infer the number of modes supported in a waveguide [32] and is expressed as

$$V = k_0 d(n_1^2 - n_2^2)^{1/2} \tag{2.36}$$

meaning the symmetric and antisymmetric solutions (Equations 2.34 and 2.35) can be expressed as

$$\xi tan(\xi) = \left(\frac{V^2}{4} - \xi^2\right)^{1/2} \tag{2.37}$$

$$\xi cot(\xi) = \left(\frac{V^2}{4} - \xi^2\right)^{1/2} \tag{2.38}$$

Solutions for $\xi$ can be visualised by evaluating the LHS and RHS (labelled $\eta$), shown in Figure 2.3. A similar treatment can also be shown for TM modes [29] and a similar graphical representation plotted, the difference being due to boundary conditions the form of the symmetric and antisymmetric solutions are

$$\xi tan(\xi) = \left(\frac{n_1}{n_2}\right)^2 \left(\frac{V^2}{4} - \xi^2\right)^{1/2} \tag{2.39}$$

$$\xi cot(\xi) = \left(\frac{n_1}{n_2}\right)^2 \left(\frac{V^2}{4} - \xi^2\right)^{1/2} \tag{2.40}$$

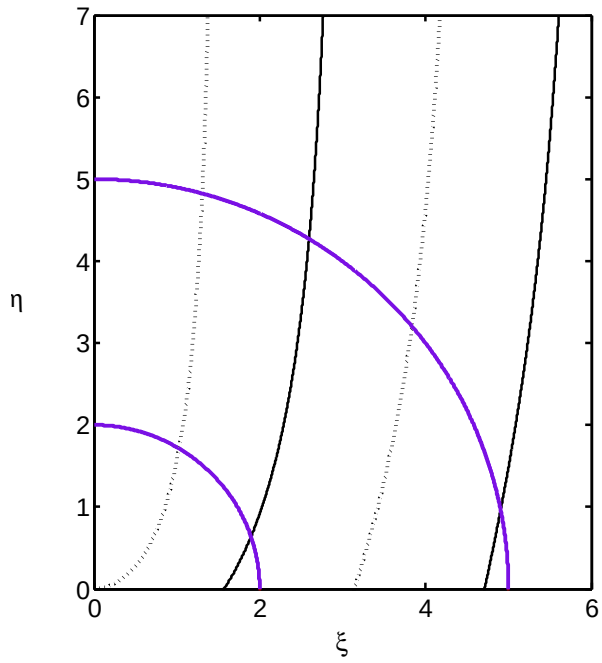


**Figure 2.3:** Illustrating the graphical solution of TE guided modes, dashed black lines symmetric, solid black line antisymmetric

The RHS of Equations 2.39 and 2.40 now represent an ellipse not a circle, due to the $(n_1/n_2)^2$ term.

Introducing a normalised propagation constant, b, defined as

$$b = \frac{(\beta/k_0)^2 - n_2^2}{n_1^2 - n_2^2} = 1 - \frac{4\eta^2}{V^2} \tag{2.41}$$

It must be noted that $\xi$ and $\eta$ are convenient parameters for obtaining equation solutions and have no specific physical interpretation. The solutions for Equations 2.37, 2.38, 2.39 and 2.40 can be graphically represented for different normalised frequencies, shown in Figure 2.4 for the first three orders of TE and TM mode. The intermodal dispersion of the supported modes is referred to as the effective refractive index $n_{eff}$. It must be noted that cut-off occurs at b=0.

The work in this thesis is primarily concerned with guided modes. However, other classifications of modes exist. Evanescent and radiation modes are a continuous spectrum of modes whose effective index is less or equal to the index of the cladding [5]. Another useful mode set are leaky modes which guide light beyond the TIR regime. Leaky modes are so called as they cannot keep the optical

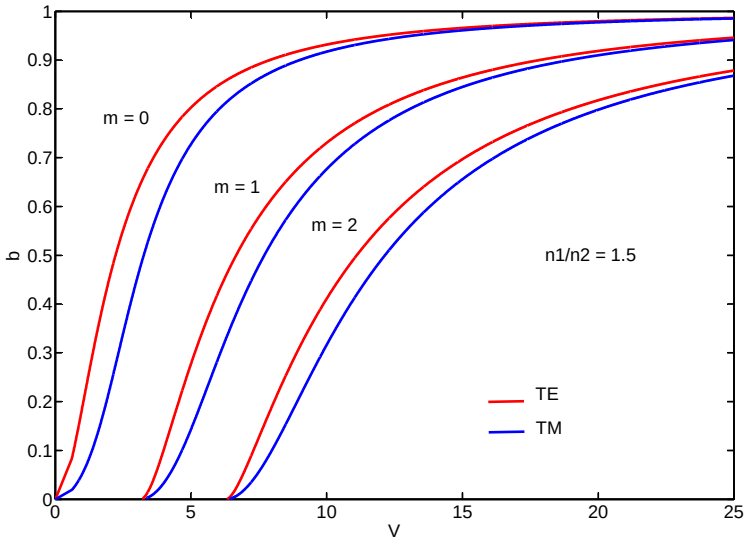


**Figure 2.4:** Normalised solutions for TE and TM modes

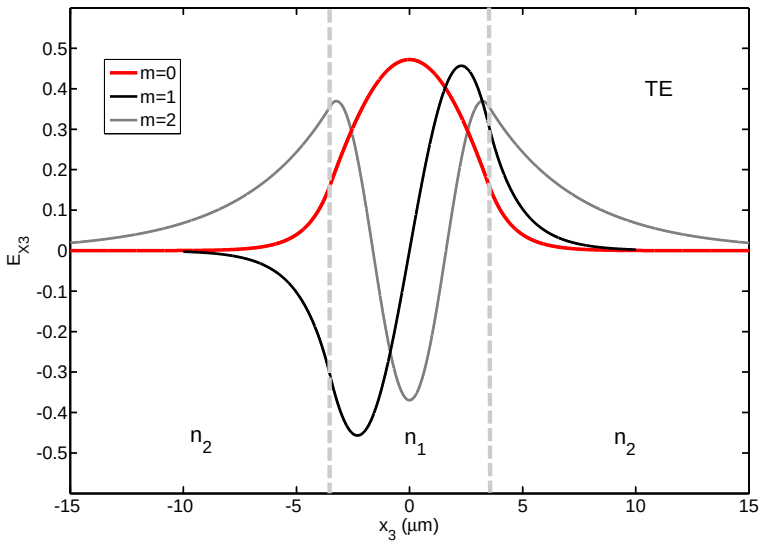


**Figure 2.5:** TE mode solutions for a symmtric slab waveguide, $n_1$=1.45,$n_2$=1.44, thickness for supporting 1500 nm wavelength light

power within the core and are supported when the index of the core is less than the cladding [33]. Strictly speaking leaky modes are not modes at all, but marked resonances in a continuous spectrum. A recent review by Hu and Menyuk gives a quantitative discussion about the nature of leaky modes [34]. Whereas guided modes have discrete exponential attenuation solutions within the cladding regions, leaky modes have exponentially increasing solutions [35]. Now, clearly this behaviour is unphysical in the limit $x_3 \rightarrow \pm\infty$ and for this reason the optical power carried by these waves can never be computed.

The waveguide solutions so far have only considered slab waveguide structures, which are not the most practical waveguide designs as they only control the path of light along one dimension. Several more practical waveguide geometries exist which confine the light in two dimensions as shown in Figure 2.6. These can be categorised as diffused, rib and buried. The waveguide geometry used is generally dependent upon the material and method of fabrication used [5].

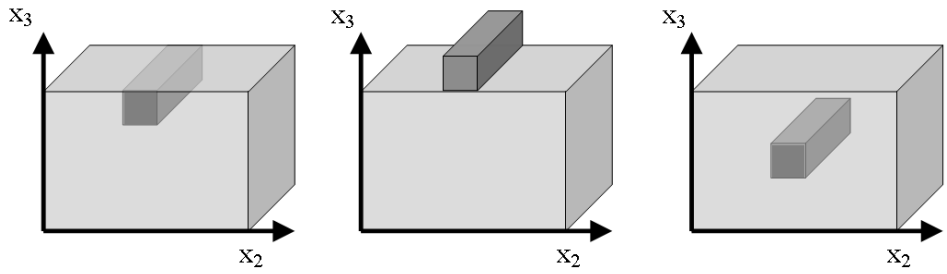


**Figure 2.6:** The three basic geometries that support channel waveguides, diffused, rib and buried structures

The index profile of these waveguides can be stated mathematically as.

$$\epsilon(x_2, x_3) = \epsilon_0 n^2(x_2, x_3) \tag{2.42}$$

where n is the refractive index, $\epsilon_0$ is the permittivity of a vacuum and $\epsilon$ is permittivity in a given medium. In general, refractive index is a complex value; the imaginary part can represent loss or gain depending on the sign of the value.

The mode solutions for the waveguides illustrated in Figure 2.6 can be achieved efficiently and accurately using a variety of approximations [5]. One of the primary workhorses for mode solution approximation is the effective index method.

### 2.2.4 Effective Index Method

The effective index method is one of several techniques for analysing weakly guiding two-dimensional optical waveguide structures [5] [29]. The method assumes that the refractive index can be split into separate $x_2$ and $x_3$ dependencies. Under these assumptions it operates by simply repeating the slab optical waveguide analyses.

The effective index method splits the problem into a series of 1D slab waveguide structures. The first step of the method calculates the effective indices along the $x_3$ dimensions, as if they constituted to individual slab waveguides. This is illustrated in Figure 2.7 for a buried waveguide structure.

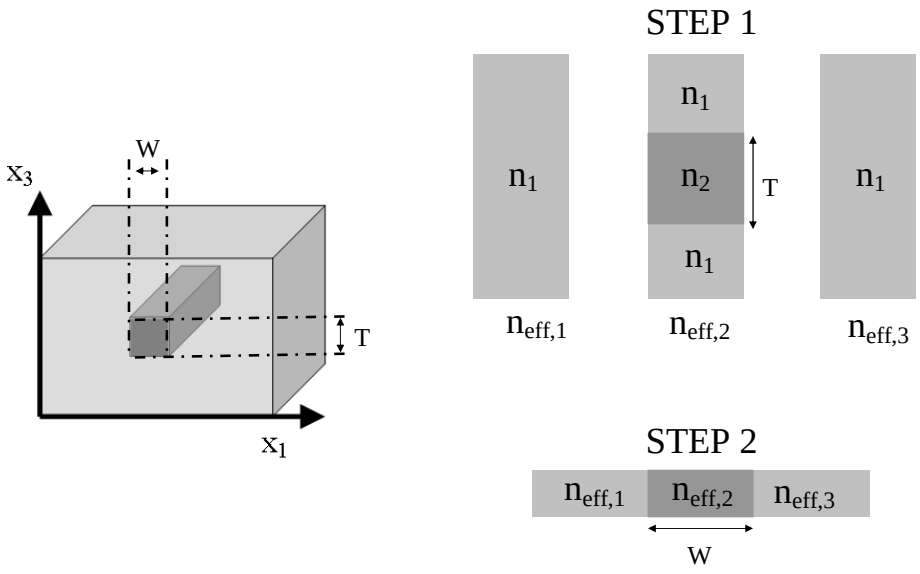


**Figure 2.7:** Calculation steps to find the effective index of a buried waveguide, using the Effective Index Method

Once the $n_{eff}$ are calculated for the $x_3$ dimension, they are used to build another 1D structure in the $x_1$ dimension. From these an overall effective index approximation can be made.

The treatment of photonic waveguide modes has so far considered analytic solutions. Numerical solutions to a waveguide's mode, are required in situations were there is no simple analytical solution. With the rapid increase in inexpensive computing power numerical tools have become common place in industry and academia, where they are used to optimise and test design parameters. The

solution accuracy gained by a numerical technique relative to the required computational processing (speed) and memory has traditionally been an important factor for consideration. However, with exponentially increasing sophistication of modern computers the processing and memory requirements are becoming less important. Today, most mode solving algorithms can be executed on desktop computers. This is a contributing factor to why the popularity of certain mode solving techniques has increased at the expense of others.

Numerical methods are encountered in three main areas of photonic waveguide modelling, these include mode solving, beam propagation and network simulation. The following subsections tackle the operation of mode solving and beam propagation methods, which shall be explicitly used in this PhD thesis.

### 2.2.5 Numerical Mode Solving

The effective index method and other such approximations are idealised solutions for weakly guiding modes and remain accurate for only very simple waveguide geometries. The geometries of real world waveguides are in fact generally much more complicated and may require a full vectorial treatment. A numerical mode solving technique is primarily required for the work outlined in Chapter 4 of this thesis, which reports on how the design of a waveguide is optimised for chemical sensing. One route of investigation for sensitivity enhancement tackles the use of surface enhancement layers, labelled schematically in Figure 2.8 as layer B.

In Chapter 4 the enhancement layer is considered to be of much greater index than the surrounding media. Hence a full vectorial numerical mode solving method has been employed to ensure mode solution accuracy. This chapter details the technique of the numerical mode solver used and compares it to the effectiveness and efficiency of alternative numerical methods.

Most numerical mode solving techniques operate by adapting the mathematical computational philosophy of subdivide and conquer. This general technique subdivides the space into sections which can be more readily solved than the whole problem head on. The list of mode solving techniques that can solve the full vectorial Helmholtz Equation in this manner is an extensive one [36] [37]. The numerical methods that can find the eigenmodes of an arbitrary waveguide include

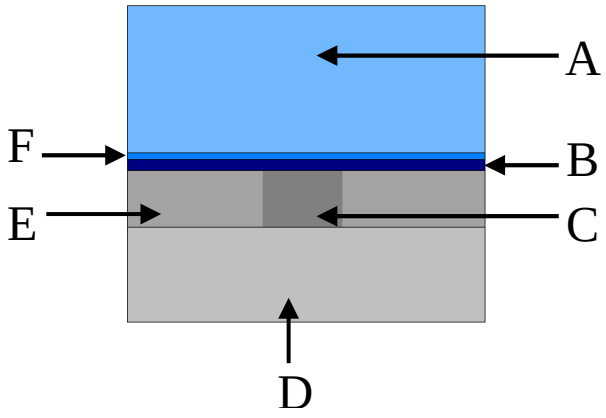


**Figure 2.8:** The cross sectional area of our waveguide design that needs to be solved includes an analyte A, two possible surface layers of arbitary thickness B,F a core layer E with slightly higher index than the underclad D and a UV written waveguide approximated as a square C.

Finite Difference Method (FDM), Finite Element Method (FEM), Beam Propagation Method (BPM) based mode solvers and Film Mode Matching (FMM). A full description of all these methods would be beyond the scope of this thesis. The purpose of this subsection is to outline the operation of the two most common numerical mode solvers FDM and FEM and compare their operation with the FMM method implemented in this thesis.

The Finite Difference Method has been a very successful numerical technique for mode solving [37] [36]. The technique's success is largely to do with the simplicity of its formulation. The basic operation of the method is to replace the partial derivatives of Helmholtz equation with finite difference equations. The method operates by firstly setting up a grid of nodes onto the cross section of the waveguide, illustrated in Figure 2.9. Approximations of the partial differential equations at a node can be made by considering the finite differences between it and its nearest neighbours. The simplest way of doing this is considering the four nearest neighbours from which either full vectorial [38], semi-vectorial [39] [40] or scalar formalisms can be made. FDM is relatively straight-forward to program compared to other numerical techniques and so can have an associated lower development cost. Its disadvantage is that it has difficulty discriminating certain structures, due to the technique regularly subdividing space, rather than having an adaptive subdivision of space, such as that used in FEM and FMM.

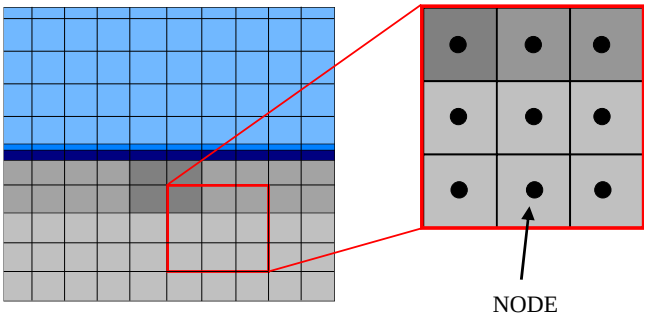


**Figure 2.9:** The Finite Difference Method of subdividing a structure into nodes.

The Finite Element Method was first reported by Yeh in 1975 [41] and is now considered to overshadow the FDM of numerical mode solving [37] [36], due to its versatility. It overcomes the discrimination issue associated with FDM as its elements can take the forms of various shapes. This is a computationally taxing technique however, with the evolution of desktop computational power FEM has found increased popularity in industry and academia. The elements in FEM are non-overlapping and usually take the form of triangles [27], illustrated in Figure 2.10. The field over each element is then expressed in terms of a low degree interpolating polynomial weighted by the field values at the nodes of each element. The field is then evaluated from the linear summation of the fields over each element. The limitation of the technique arises when modes are close to cut-off. For these modes the field extends beyond the core and many more elements/computational resources are required to maintain accuracy.

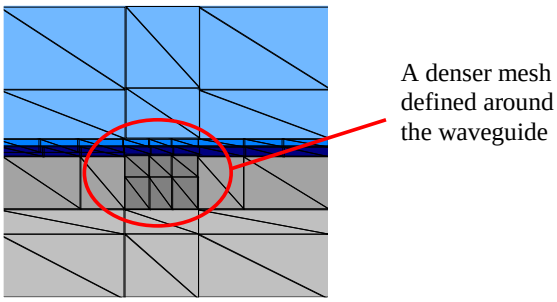


**Figure 2.10:** The Finite Element Method of subdividing a structure into triangular subdivisions.

The modes in this thesis are solved using a commercial mode solving package called FIMMWAVE, which is based upon a Film Mode Matching (FMM) method

reported by Subdo [42], [43]. This full vector mode solver can be faster and more accurate than alternative methods of mode solving based upon FDM and FEM. The program has an advantage when large sections of uniform refractive index make up the waveguide, this is because the algorithm inherently subdivides the geometry up into areas of refractive index chunks, illustrated in Figure 2.11. The larger the uniform refractive index areas the fewer subdivisions exist, meaning fewer calculations are required. The subdivision occurs by splitting up the geometry into a sandwich of slices m=1,2,...,M, each considered to be cut from a film waveguide, with layer n=1,2,...N. The definition of film and slice is better understood from Figure 2.11. It must be noted that just as with some FEM and FDM algorithms, the FMM algorithm procured can take advantage of symmetries in device geometry making these symmetry identities reducers the required number of calculations.

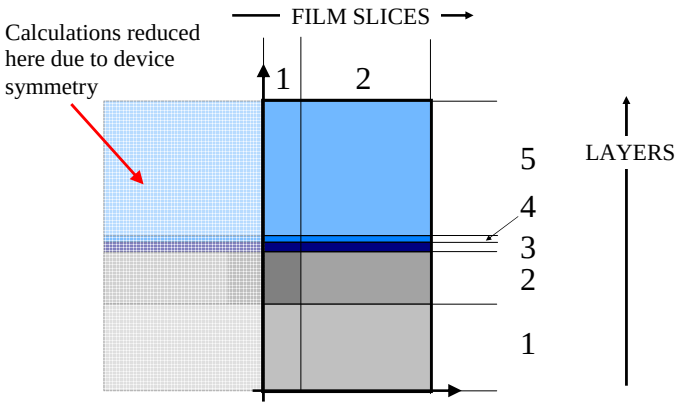


**Figure 2.11:** The FMM method of solving the supported modes of a waveguide structure, through splitting it up into a series of film guide slices and layers. This example also reduces the total number of required calculations by making a symmetry identity

Subsequent to FMM subdivision of space, the supported modes of the defined structure are obtained by the algorithm collecting the modes that have the same wavevector along the propagation dimension and matching the field distributions at the slice interfaces by adjusting the modal amplitudes in each film. The power of the FMM compares fairly well against alternative FEM and FDM for the application in this thesis.

Another useful numerical method in waveguide design is the beam propagation algorithm. This can be used to simulate the evolution of a guided mode and is

particularly useful in structures whose index profile is dependent upon the length propagated. Examples of such structures include tapered waveguide, x-couplers, y-splitters and MMI devices all of which can be fabricated using direct UV writing.

### 2.2.6 Beam Propagation Method

Waveguides are indispensable components in constructing integrated optical circuits. The Beam Propagation Method (BPM) is the most powerful technique to investigate lightwave phenomena in axial varying waveguides. Several methods for BPM simulation exist [27], this thesis shall be concerned with a Fast Fourier Transform (FFT) based BPM algorithm that assumes the structure is weakly guiding. BPM algorithms implement a stepwise routine to transport the optical field within one propagation step. BPM works under a slowly varying envelope approximation, which assumes that the envelope of the forward-travelling wave pulse varies slowly in time and space compared to its associated wavelength. It is also assumed that the refractive index structure of the modelled device changes negligibly during each iterative step. To allow for faster computation, the FFT-BPM algorithm implemented reduces a structure's three dimensional refractive index profile to two dimensions. This is achievable through using an effective index method [27]. The BPM algorithm described in this section is implemented in Chapter 8 to model the operation of a novel multimode interference device.

BPM algorithms numerically solve the Helmholtz equation under conditions of a time-harmonic wave. The electric field in such an instance can be separated into two parts, an axial slowly varying envelope, $\phi(x_1, x_2)$ and a rapidly varying term $exp(-ikn_0x_1)$ such that

$$E(x_1, x_2) = \phi(x_1, x_2)exp(-ikn_0x_1) \tag{2.43}$$

Substituting Equation 2.43 into Equation 2.28 we obtain

$$\frac{\partial^2\phi}{\partial x_2^2} - 2ikn_0\frac{\partial\phi}{\partial x_1} + k^2(n^2 - n_0^2)\phi = 0 \tag{2.44}$$

we now assume a low index contrast, such that we can make the weakly guiding approximation $n^2 - n_0^2 \approx 2n_0(n - n_0)$, thus giving

$$\frac{\partial \phi}{\partial x_1} = -\frac{i}{2kn_0}\frac{\partial^2 \phi}{\partial x_2^2} - ik(n - n_0)\phi \tag{2.45}$$

If $n = n_0$ then only the first term of Equation 2.45 remains, hence this term represents free space light propagating in a medium of refractive index $n_0$. It follows, therefore, that the second term is the 'waveguide bit' and represents influence of the waveguide structure. Although both of these terms affect the light propagation simultaneously the BPM analysis shall assume the two terms can be considered separately. Hence, these two terms shall be split into operators **A** and **B** respectively, giving:

$$\begin{aligned} \frac{\partial \phi}{\partial x_1} &= (\mathbf{A} + \mathbf{B})\phi \\ \mathbf{A} &= \frac{-i}{2k_0 n}\frac{\partial^2}{\partial x_2^2} \\ \mathbf{B} &= -ik[n(x_1, x_2) - n_0] \end{aligned} \tag{2.46}$$

The solution for which is

$$\phi(x_2, x_1 + h) = exp(h(\mathbf{A} + \mathbf{B}))\phi \tag{2.47}$$

From the Barker-Hausdorff theorem we can reinterpret this as [27]:

$$\phi(x_2, x_1 + h) = exp(\frac{h\mathbf{A}}{2})exp(h\mathbf{B})exp(\frac{h\mathbf{A}}{2})\phi(x_2, x_1) \tag{2.48}$$

This can be considered as three different operations as the mode propagates along distance h, illustrated in Figure 2.12 for a tapered waveguide. Firstly there is the free space bit which propagates the mode to a distance of $^h/_2$. Secondly there is the waveguide bit which is the phase retardation occurring at $^h/_2$. Finally, there is another free space bit, which propagates the mode to distance h.

This PhD thesis iterates these three steps using a Fast Fourier Transform (FFT) BPM algorithm, written in MATLAB (presented in Appendix B). The three computational steps are:

**STEP 1:** $\phi_{STEP1}(x_2, x_1 + \frac{h}{2}) = IFFT(exp(i\delta\beta\frac{h}{2})FFT(\phi(x_1)))$
**STEP 2:** $\phi_{STEP2}(x_2, x_1 + \frac{h}{2}) = exp(hB(x_1))\phi_{STEP1}(x_2, x_1 + \frac{h}{2})$

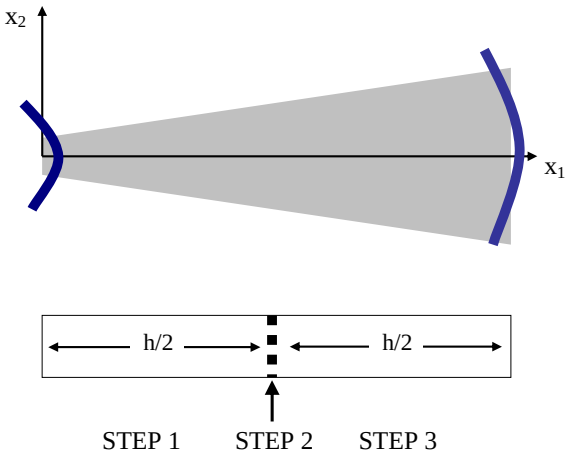


**Figure 2.12:** The three steps involved to propagate a mode along a distance h for a tapered waveguide

**STEP 3:** $\phi_{STEP3}(x_2, x_1 + h) = IFFT(exp(i\delta\beta\frac{h}{2})FFT(\phi_{STEP2}(x_2, x_1 + \frac{h}{2})))$

where

$$\delta\beta = \beta - kn_0 \tag{2.49}$$

This chapter so far, has considered the confinement of light via waveguide structures. The final part of this chapter shall introduce the concept of waveguide gratings, which have been fabricated in this thesis and analysed in terms of their spectral response upon actuation. In general, waveguide grating structures serve as a useful filtering tool in modern telecommunication networks and are utilised in many sensing applications, both physical and chemical.

## 2.3 Bragg Gratings

Wave propagation in a periodic medium is a well studied phenomenon. The diffraction of X-rays by a crystal lattice being a classic example [44]. Gratings in waveguides are only different in the sense that light is confined in the transverse direction so the interactions are one dimensional.

Waveguide gratings are achieved through a periodicity, $\Lambda$, in refractive index.

Gratings can be classed in two categories, long period gratings [45] (also known as transmission gratings) and short period gratings (also known as reflection gratings or Bragg gratings) [46] [14]. Long period gratings are typically submillimeter period and couple specific wavelengths of light from forward propagating guided modes into forward-propagating cladding modes. Cladding modes typically loose energy through absorption and scattering, resulting in a transmission dip at wavelengths corresponding to the coupled light condition. In contrast, short period gratings have a submicrometer period and reflect the light into counter-propagating modes, as illustrated in Figure 2.13. This results in a reflected peak as well as a transmission dip for the coupled wavelength. This remainder of this chapter shall quantify the spectral response of such a structure.

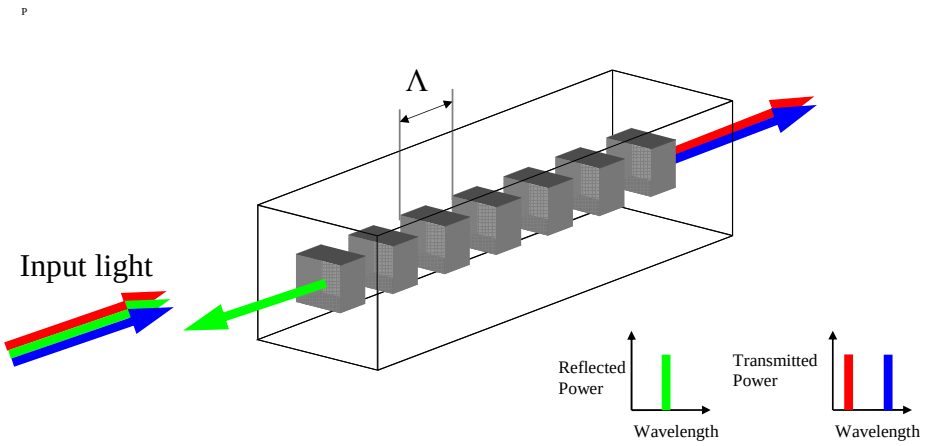


**Figure 2.13:** A conceptual operation of a Bragg grating structure

The periodic structure of a Bragg grating can be interpreted to have a wavevector component, $\mathbf{k}_G$. If this wavevector component matches the wavevectors of forward-propagating, $\mathbf{k}_I$, and counter-propagating modes, $\mathbf{k}_R$, the Bragg condition shall be satisfied. This can be defined mathematically as:

$$\begin{aligned} \mathbf{k}_R &= \mathbf{k}_I + \mathbf{k}_G \\ \Rightarrow nsin(\theta_C) &= nsin(\theta_F) + m\frac{\lambda}{\Lambda} \end{aligned} \tag{2.50}$$

where m is the diffraction order of the grating, as depicted schematically in Figure 2.14.

Considering first order diffraction (m=-1) coupling a forward-propagating mode

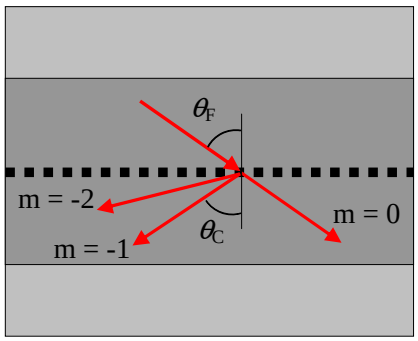


**Figure 2.14:** The diffraction of light by a Bragg grating

($n_{eff}$=n sin($\theta_F$) ) into an equal but counter-propagating mode (-$n_{eff}$=-n sin($\theta_C$) ), Equation 2.50 can be rewritten as

$$\begin{aligned} -n_{eff} &= n_{eff} - \frac{\lambda}{\Lambda} \\ \Rightarrow \lambda &= 2n_{eff}\Lambda \end{aligned} \tag{2.51}$$

Equation 2.51 defines the Bragg condition and the wavelength which satisfies it is the Bragg wavelength. It must be noted that the Bragg wavelength can be changed through either variations in effective index of the mode and/or the period of the grating.

### 2.3.1 Bragg Grating Structures

So far, it has been considered that a Bragg grating is a uniformly periodic structure, as illustrated in Figure 2.15 (a), which has a sharply-defined beginning and endpoint. Often, either through design, fabrication, or actuation the Bragg grating will deviate somewhat from a uniformly periodic structure. The most general refractive index perturbation profile, $\delta$n, of a grating can be defined mathematically as

$$\delta n(x_1) = \delta\bar{n}(x_1)\left(1 + v(x_1)cos\left[\frac{2\pi}{\Lambda}x_1 + \phi(x_1)\right]\right) \tag{2.52}$$

where $\delta\bar{n}(x_1)$ is a constant offset component of the index variation, v is the fringe visibility and $\phi(x_1)$ is a phase term that gives the deviation from the expected part

of the cosine due to chirp. If a grating's pitch (or refractive index) varies slowly over its length, it is defined as being chirped. Figure 2.15 (b) illustrates an example of a linearly chirped grating structure. If a grating's fringe visibility changes with position, the grating is defined as being apodised. Figure 2.15 (c) illustrates a Gaussian variation in fringe visability as an example of grating apodisation.

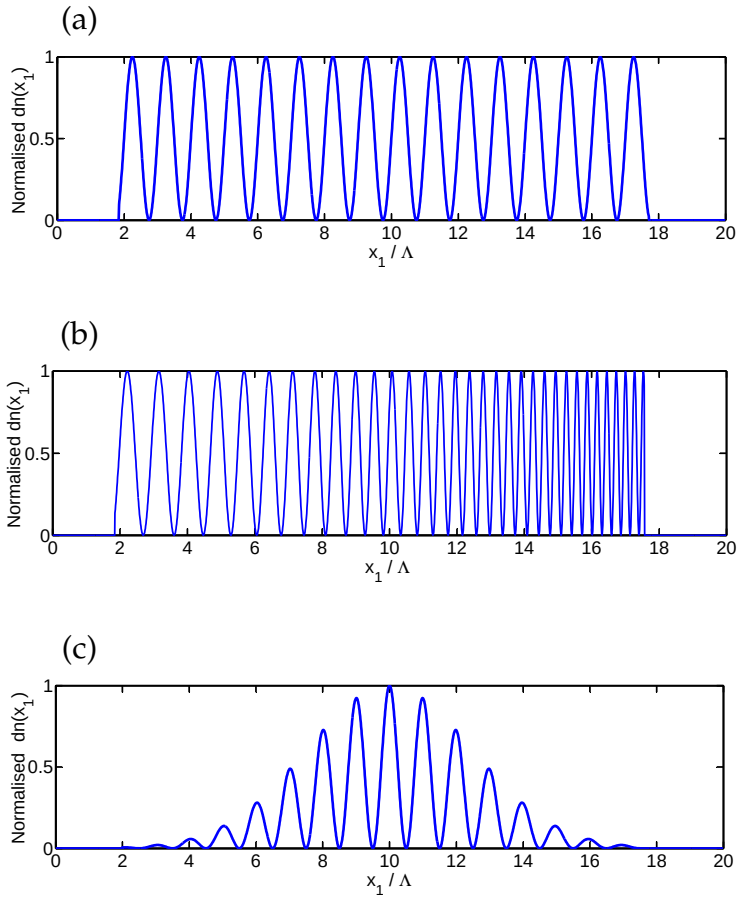


**Figure 2.15:** The index profiles of (a) uniform (b) linear chirped and (c) Gaussian apodised Bragg gratings

A good approximation to the spectral response of a grating can be achieved through taking the Fourier Transform of the spatial structure, e.g. a uniform grating has a top hat form and so transforms into a sinc function. For a more detailed analysis of a grating's spectral form, including temporal components, codirectional coupled mode theory is usually applied [29] [5].

### 2.3.2 Coupled-Mode Theory

The theoretical spectral response of a Bragg grating can be achieved using coupled mode equations [47]. In this approach the grating is modelled as small perturbations, which produce a coupling between the forward and backward propagating modes. The coupled mode equations, can be expressed in matrix form as

$$\frac{d}{dx_1}\begin{bmatrix} a_+(x_1) \\ a_-(x_1) \end{bmatrix} = \begin{bmatrix} -i\delta & \kappa \\ \kappa^* & i\delta \end{bmatrix}\begin{bmatrix} a_+(x_1) \\ a_-(x_1) \end{bmatrix} \tag{2.53}$$

where: a represents an amplitude, the subscript of which refer to forward (+) and backward (-) propagating; $\kappa$ is the complex coupling constant and describes the rate at which power transfers between the forward and backward modes and is usually referred to as the reflectivity per unit length of the grating; $\delta$ is a measure of the deviation from the Bragg condition, known as the detuning coefficient it is given by

$$\delta = \beta - \frac{\pi}{\Lambda} \tag{2.54}$$

### 2.3.3 Spectral Response of a Bragg Grating

The Transfer Matrix Method (TMM) is a succinct form of the coupled mode equations, which can be used to understand theoretically the spectral response of a Bragg grating spectra. The TMM becomes especially elegant when considering more complicated physical grating structures [48]. However, considering the most simple Bragg grating structure, a uniform Bragg grating, $\delta\bar{n}$ and $\kappa$ are constant and $\phi$=0. The TMM can thus be stated as [49]:

$$\begin{bmatrix} a_+(x_1) \\ a_-(x_1) \end{bmatrix} = \begin{bmatrix} cosh(\gamma x_1) - i\frac{\delta}{\gamma}sinh(\gamma x_1) & \frac{\kappa}{\gamma}sinh(\gamma x_1) \\ \frac{\kappa^*}{\gamma}sinh(\gamma x_1) & cosh(\gamma x_1) + i\frac{\delta}{\gamma}sinh(\gamma x_1) \end{bmatrix}\begin{bmatrix} a_+(0) \\ a_-(0) \end{bmatrix} \tag{2.55}$$

The solution of Equation 2.55 for a grating of length L has a closed solution, which can be achieved by applying appropriate boundary conditions. The boundary conditions assumed, are that light is injected into the left hand side of the grating

($a_+(0)=1$) and there is none injected from the right ($a_-(L)=0$).

$$R(\delta) = \frac{k^* tanh(\gamma L)}{\gamma + i\delta tanh(\gamma L)} \tag{2.56}$$

where

$$\gamma = \sqrt{|\kappa|^2 - \delta^2} \tag{2.57}$$

Figure 2.16 plots the calculated reflection spectra for five different Bragg gratings, of normalised coupling strength and length, $\kappa$L.

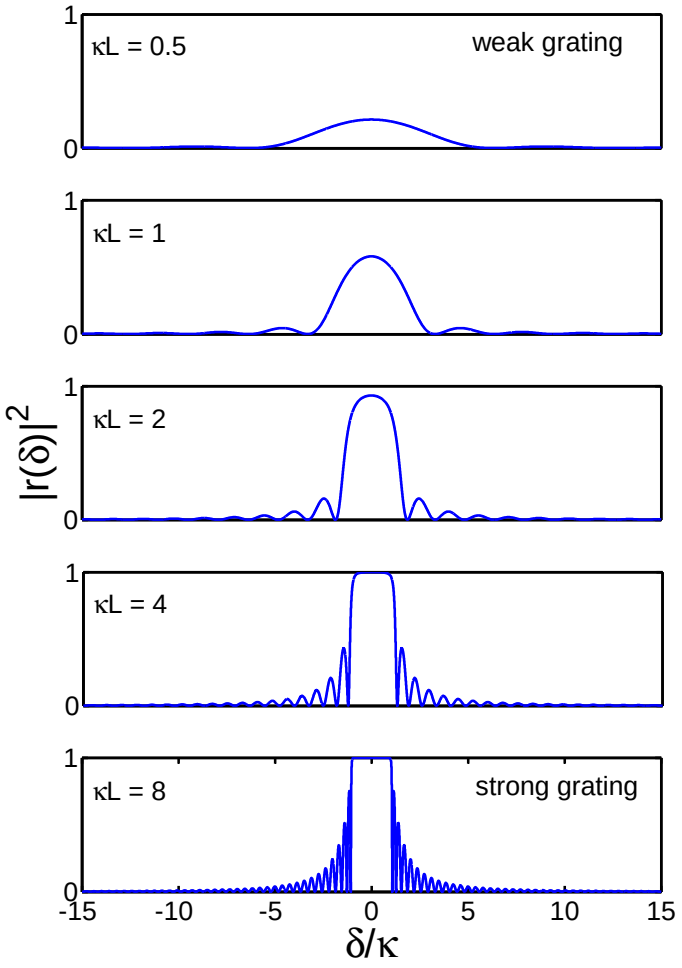


**Figure 2.16:** Normalised reflection spectra's of a uniform Bragg grating, for corresponding grating strengths

It has been discussed in Chapter 1 that Bragg gratings can be used for OADM operations in telecommunication networks. A weak Bragg grating does not make

a suitable add/drop filter, because it only partially reflects the input light. For gratings with $\kappa$L>1, the spectral shape plateaus, as illustrated in Figure 2.16. This regime has strongly reflected input light, at certain frequencies called the stop-band. The bandwidth of the spectral response can be defined from the spacing of the first minima either side of the central peak response, defined as

$$\frac{\Delta\lambda}{\lambda} = \frac{\Delta n_{eff}}{n_{eff}} \sqrt{1 + \left(\frac{\lambda_B}{\Delta n_{eff} l}\right)^2} \tag{2.58}$$

Beyond the bandwidth the spectral features have associated sidelobes, which quickly decay away from the Bragg condition. It must be noted that this is one definition of bandwidth, a more common definition is the spectral width at the peak's full width half maximum (FWHM). This later definition shall be used throughout this thesis. In real gratings it is also necessary to consider cladding modes, notably observed in transmission.

## 2.4 Summary

This chapter has introduced the concept of waveguides and Bragg gratings, both of which have been fabricated as part of this PhD thesis. The theory behind these devices has been developed from Maxwell's equations and the conditions for light to be supported discussed. Guided mode solutions, for TE and TM polarisations, have been considered using an analytical technique. However, for more complicated waveguide geometries analytical techniques are generally not sufficient and so numerical mode solving techniques have been explored for this means. The commercial mode solver FIMMWAVE, which uses a full vectorial FFM algorithm, shall be utilised in the following investigations for mode analysis. The analysis of light propagation has also been discussed and shall be implemented to analyse MMI structures, using a FFT-BPM algorithm, as detailed in Appendix B.

The following chapter shall now outline how waveguides and Bragg gratings can be simultaneously fabricated using the direct UV writing technique.

# Chapter 3

# Fabrication

## 3.1 Introduction

In the pursuit to drive down fabrication costs of IO devices many high-tech companies are developing existing and relatively inexpensive microelectronics processes, for IO device fabrication. These devices are either defined in silicon wafers [50] or silica deposited upon a silicon wafer [51] [52] [53]. One unique advantage of using silicon and silica-on-silicon platforms is that they have the potential to integrate both photonic and microelectronic operations onto the same chip.

The definition of optical circuits in a silica-on-silicon platform is commonly achieved through silica deposition, photolithography and etching. This PhD thesis investigates devices that have been fabricated by a technique that does not require photolithography and etching. The relatively new method of circuit definition uses a versatile direct UV grating writing technique to define IO components in a germanium doped silica-on-silicon wafer.

The purpose of this chapter is to familiarise the reader with the direct UV grating writing technique, implemented in this PhD thesis. The advantages and disadvantages of the technique shall be discussed alongside comparisons with alternative fabrication methods. The chapter shall also address the author's contributions to increase the longevity of photosensitivity and describe device characterisation and packaging including a treatment of the standard errors generally associated with data collection from written devices from the interrogation equipment used.

## 3.2 Silica-on-Silicon Platform

The direct UV writing process described in this thesis takes place upon a silica-on-silicon platform, illustrated in Figure 3.1. The first stage of fabrication involves the growth of a thin thermal oxide layer upon a standard silicon wafer. The reason for growing this layer is to aid the adhesion of subsequently deposited silica layers.

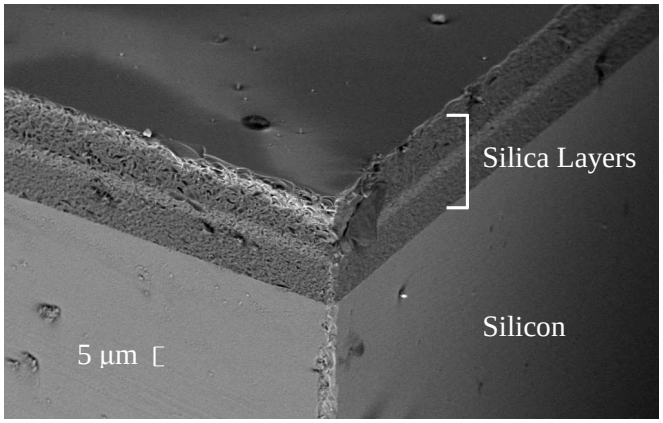


**Figure 3.1:** An SEM image of a typical silica-on-silicon wafer, consisting of thin multiple silica layers upon a thick silicon substrate

Thermal oxide growth is achieved using a similar technique to that used in the microelectronics industry, were the silicon wafers are placed in a furnace containing water vapour and set at $\sim$1100$^o$C. However,the oxide thicknesses required are generally up to a hundred times thicker than those encountered in the microelectronics industry and so typically take several weeks to grow the desired thickness, of up to 14 $\mu$m. Upon the thermal oxide, doped silica is deposited using a derivative of the Chemical Vapour Deposition (CVD) technique. Derivatives of this technique include Flame Hydrolysis Deposition (FHD) and Plasma Enhanced Chemical Vapour Deposition (PECVD), both of which have been studied by previous members of the research group [54], [9], [10].

The wafers used in this PhD thesis were fabricated using an FHD process, by a company known at the time of thesis publication as Centre of Integrated Photonics (CIP). For completeness both PECVD and FHD process, with their relative advantages and disadvantages shall be described in the following subsections.

### 3.2.1 Flame Hydrolysis Deposition

Flame Hydrolysis Deposition (FHD) is a common technique used to deposit doped silica glass upon a silicon wafer. In the process a soot layer is formed by oxidising halides in an oxy-hydrogen flame, as illustrated in Figure 3.2. After soot deposition a heat treatment step is implemented to consolidate the soot layer [55] [56].

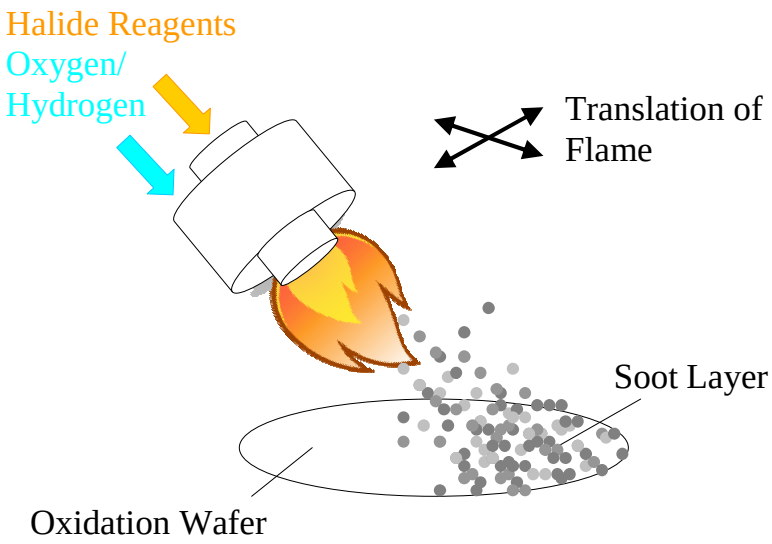


**Figure 3.2:** Flame Hydrolysis Deposition

The chemical reactions occuring in the oxy-hydrogen flame include

$$\begin{aligned} O + H_2 &\rightleftharpoons OH + H \\ H + O_2 &\rightleftharpoons OH + O \\ OH + H_2 &\rightleftharpoons H_2O + H \end{aligned}$$

The precursors for FHD are required to be halide based. For silica deposition this halide precursor is silicon tetrachloride ($SiCl_4$). Silica soot is formed principally through the direct oxidation of $SiCl_4$. This reaction occurs at the centre of the flame, where temperatures reach approximately 2000 $^oC$. For temperatures below 1200 $^oC$ the principle reaction is hydrolysis. The direct oxidation and hydrolysis reactions for $SiCl_4$ are:

$$\begin{aligned} &\textbf{Direct Oxidation:} && SiCl_4 + O_2 \rightarrow SiO_2 + 2Cl_2 && (> 1200^oC) \\ &\textbf{Hydrolysis:} && SiCl_4 + 2H_2O \rightarrow SiO_2 + 4HCl && (< 1200^oC) \end{aligned}$$

The resulting products are solid silica (soot) and hydrochloric acid (vapour). The hydrolysis is achieved thermally, by directly mixing the halide with an oxy-hydrogen flame.

Phosphorus boron and germanium dopants can also be added to the silica by introducing the halides $POCl_3$, $BCl_3$ and $GeCl_3$ respectively, the reactions in each instance are

$$\begin{aligned} &\textbf{Germanium:} && GeCl_4 + O_2 \rightarrow GeO_2 + 2Cl_2 \\ &\textbf{Phosphorus:} && 2POCl_3 + 3H_2O \rightarrow P_2O_5 + 6HCl \\ &\textbf{Boron:} && 4BCl_3 + 6H_2O \rightarrow 2B_2O_3 + 12HCl \end{aligned}$$

Successive silica layers are deposited onto the wafer, with different concentrations of the relevant dopants. Most importantly the addition of germanium dopant increases the photosensitivity of the glass to UV light, a phenomenon exploited in the fabrication of waveguide circuits in this thesis. At 1550 nm wavelengths, silica that is doped with germanium or phosphorus has an increased refractive index, whilst silica doped with boron has a decreased refractive index. These properties can be used to manipulate the indices of the respective layers.

The typical FHD layer structure fabricated for direct UV writing contains either three or four layers. Figure 3.3 illustrates a four-layer wafer containing a thermal oxide (buffer) layer, underclad, core and overclad. The thickness of the core is typically 5-7 $\mu$m, which ensures lateral single mode operation when UV written. The cladding layers are typically over 14 $\mu$m in thickness as this is the maximum penetration depth of the first order guided mode's evanescent tail for the indices used. The construction of the three-layer wafers is similar, but lacks an underclad. As there is no underclad the thermal oxide is grown to a thickness of over 14 $\mu$m, this thesis uses wafers of both three-layer and four-layer composition.

The phosphorus concentration in the overclad is made much greater than that in the underclad. This can be observed quantitatively in Figure 3.3 (b). The reason

(a) (b)

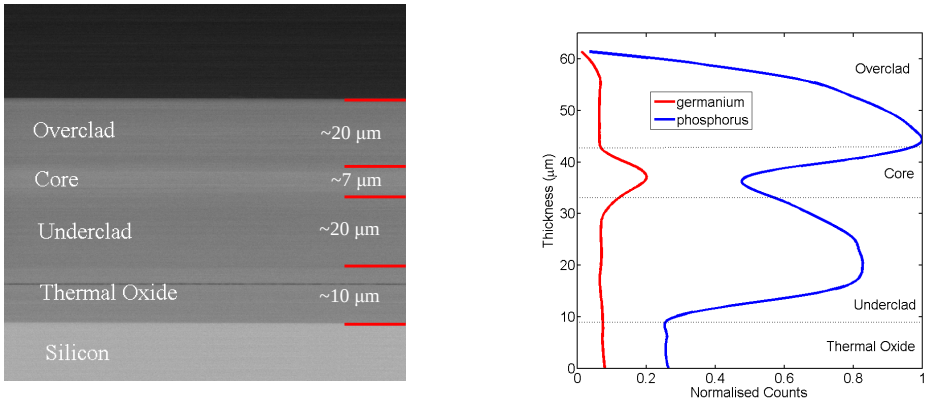


**Figure 3.3:** The typical structure and composition of a silica-on-silicon observed via (a) an SEM and (b) SEM-EDX of an end face polished silica-on-silicon wafer

for this distribution is not accidental. Phosphorus reduces the melting point of the silica and so keeps the integrity of the layers after consolidation.

Two variations on the basic three/four-layer wafer construction are investigated in this PhD thesis, which result from the desire to optimise specific device performances. Chapters 4 and 7 detail wafers that do not have an overclad layer and Chapter 8 preferentially makes the refractive index of the core layer greater than the clad layers.

An alternative approach to FHD is to use a plasma to assist in chemical deposition, using the so called Plasma Enhanced Chemical Vapour Deposition (PECVD) technique.

### 3.2.2 Plasma Enhanced CVD

The first demonstration of direct UV writing into planar silica-on-silicon utilised Plasma Enhanced Chemical Vapour Deposition (PECVD) for silica deposition [57]. In this work an RF field was used to generate plasma, from chemical precursors, illustrated in Figure 3.4. The precursor used to deposit silica are commonly silane and nitrous oxide. This method of PECVD is an established process for layer deposition in many industries including microelectronics and photonics [58].

The gas precursor introduced into the PECVD chamber forms part of a plasma as a result of collisions with charged particles, accelerated by an RF electric field. Some

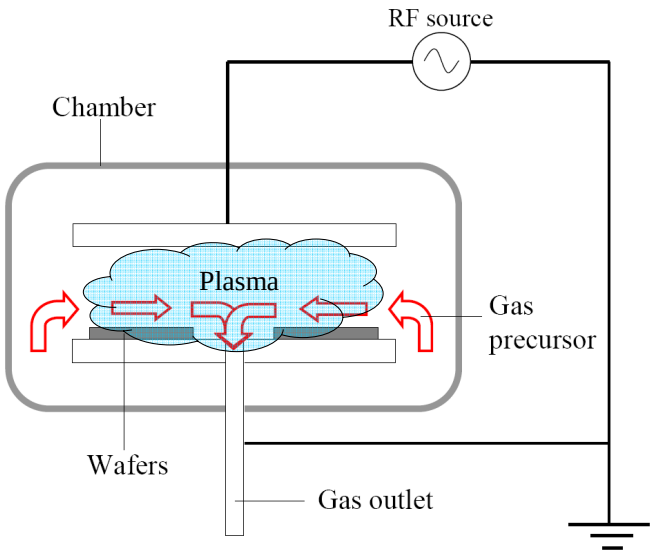


**Figure 3.4:** Typical parallel plate PECVD deposition chamber

of the reactive plasma comes into contact with the confinements of the chamber and the silicon wafers. As the particles hit the surface of the chamber wall or silicon wafer their energy is dissipated and absorption may occur. It must be noted that, despite reaching the surface of the silicon wafer the charged particle does not become bonded to it until reactions with other absorbed species on the surface form chemical bonds [10].

The deposition of PECVD silica typically results in the inclusion of free or bonded hydrogen and nitrogen. The inclusion of these atoms can result in the formation of OH, SiH and NH bonds in the silica, which can produce high losses (3-10 dB/cm), in the 1550 nm telecommunication band [59] [60]. The high losses can be reduced using an annealing process (1100 $^{o}$C for several hours). However, this negates to some extent the benefits of low temperature deposition that PECVD achieves. It has been shown that careful process control and exclusion of nitrogen from the deposition can reduce losses to $\sim$0.2 dBcm$^{-1}$, without the need for a high temperature annealing stage [61].

PECVD has an advantage over FHD in that it has a greater selection of dopants, which it can be deposited. This wider variety of dopants is brought about by the fact that the precursor is not required to be halide based. However, the disadvantage of PECVD is that it is restricted in the thickness it can deposit per run. Due to volatiles in the deposited layers, deposition steps of germanosilica in excess of

5 $\mu$m can result in the sample blistering [10]. Considering the thicknesses of layers required in this PhD thesis, multiple deposition runs would be required to overcome blistering. This makes the technique more labour intensive and expensive compared to that of FHD.

Generally, chemical vapour deposition is the foundation for silica-on-silicon based platforms. Built upon this technique direct UV writing can be used to define IO circuits. However, direct UV writing is a relatively new technique for defining IO circuits and competes directly against established technologies such as photolithography and etching. For completeness the following section shall discuss the photolithography and etching technique as a comparison to direct UV writing.

## 3.3 Photolithography and Etching

Photolithography, also referred to as optical lithography is a technique that has been used for many years, principally in the microelectronics industry. However, it has recently crossed over into the photonics industry for integrated optical circuit fabrication. The following section shall give a brief account of the photolithography process, which shall be explained in further detail in Chapter 7.

To fabricate IO circuits using photolithography requires a silicon wafer with thermal oxide layer and deposited higher index silica layer, usually achieved using germanium doping. The photolithography procedure begins by spin coating a photoresist upon the surface of the device and the subsequent selective exposure of it to UV light, as illustrated in Figure 3.5.

The developed photolithographic design is then etched using a wet/dry etch technique to define the circuit structure. The process usually applies an additional CVD run to add a lower refractive index (relative to core) capping layer.

The advantage of photolithography is that it is a cost efficient means for mass production. However, when considering small device numbers (i.e. for device prototyping) the technique becomes expensive, primarily due to the cost of the UV exposure mask. In addition, the fabrication of small device numbers is time consuming as unique masks need to be designed and fabricated.

The primary reason for doping the core layer with germanium in this technique

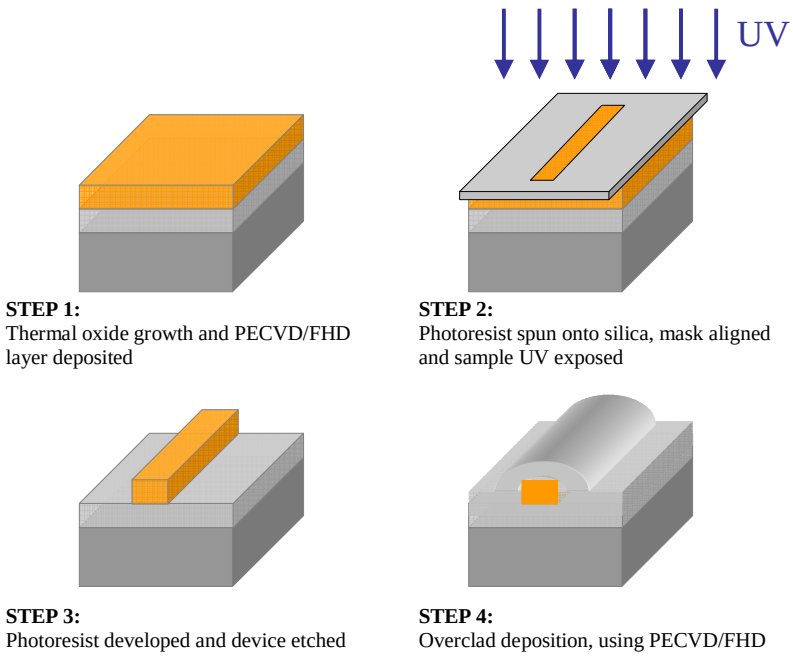


**Figure 3.5:** The photolithography and etching technique for optical circuit fabrication

is to ensure it has a greater refractive index than the surrounding cladding layers. For direct UV written devices germanium doping is important as it introducers photosensitivity.

## 3.4 Photosensitivity

The photosensitive material detailed in this work is germanium doped silica (germanosilica). Under sufficient exposure to UV light germanosilica undergoes physical changes resulting in an increase in the refractive index. The devices fabricated as part of this PhD thesis utilise this index change to literally write integrated optical structures, such as waveguides, within the germanium doped glass.

### 3.4.1 Photosensitivity of Germanosilica

The first observations of refractive index change in germanosilica was reported by Hill and co-workers in 1978 [62] [63]. They launched 488 nm light from an argon ion laser into specially designed optical fibres, which were heavily doped with

germanium and had a small guiding core thickness. In these experiments it was observed that for a 1 m length of fibre, the launched laser light would gradually become 100 % reflected over minute timescales. This phenomenon was the result of a standing wave intensity pattern being established in the fibre. The high intensity points of the standing wave produced a periodic $10^{-6}$ index change, thus along the length of the fibre a grating structure resulted. The structure was self enhancing, hence the gradual growth of the 100 % Bragg reflection achieved.

Today Bragg gratings are very useful structures for telecommunication and sensing applications. However, as the Bragg wavelength of Hill's device reflected limited wavelengths outside the telecoms window, hence its potential telecommunication applications were also limited. Also, as the strength of the index modulation was relatively weak, long grating lengths were required for sufficient reflected power, making them impractical for localised sensing.

Investigations into the photosensitivity of germanosilica by Lam and Garside [64] discovered that the magnitude of the photoinduced refractive index change depended upon the square of the power of the source. From this it can be deduced that a two photon process is occurring, meaning that 244 nm wavelength light can be used to induce a refractive index change. It must be noted that changes in the absorption spectra at 244 nm wavelengths can affect the refractive index spectra at 1550 nm wavelengths. This phenomenon can be understood as a result of the dispersion relation, which links the absorption and dispersion of a material. The mechanisms of dispersion relation shall be discussed further in Chapter 4. Photosensitivity is described as being quasi-permanent as although the lifetime is long, annealing at temperatures below that required to re-flow glass, can remove the induced index change. Typical annealing conditions to achieve erasure is $\sim 800^{o}C$ for 30 minutes.

It is understood that the exposure of germanosilica to UV light results in the bleaching of absorption defects [65]. It was later found that absorption bands located between 240-250 nm wavelengths [66] [67], directly result in index changes. Directly stimulating germanosilica with such wavelengths can improve the induced refractive index change by three orders of magnitude ($\sim 10^{-3}$). The following subsection shall describe the absorption defects which exist in germanosilica and their suspected mechanisms of bleaching.

### 3.4.2 Defects in Germanosilica

Defects are present in both pure amorphous silica and germanosilica. The idealised structure of pure silica is tetrahedral, illustrated in Figure 3.6 (a). However, defects will occur, if for example, there is a lack of oxygen during fabrication. Defects that result from this oxygen deficiency are labelled Oxygen Deficient Centres (ODC). A specific ODC is the Neutral Oxygen Vacancy (NOV), which is the 'wrong-bonding' of two silicon atoms, as illustrated in Figure 3.6 (b).

(a) (b)

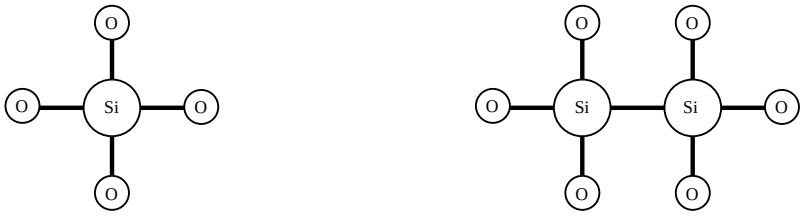


**Figure 3.6:** The structure of (a) pure silica and (b) neutral oxygen vacancy 'wrong-bond' silica defect

As germanium has the same valency as silicon, germanosilica must have a further two combinations of NOV defects, corresponding to Si-Ge 'wrong-bonding' (as in Figure 3.7 (a)) and Ge-Ge 'wrong-bonding'.

(a) (b)

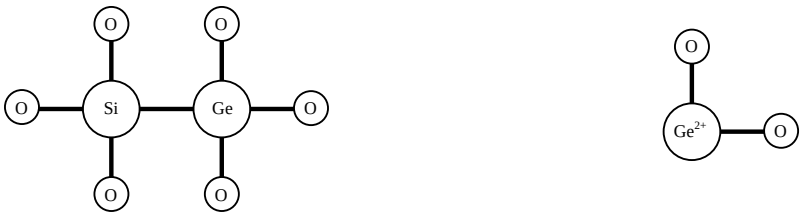


**Figure 3.7:** The structure of germanosilicate (a) neutral oxygen vacancy defect and (b) $Ge^{2+}$ defect

In addition to NOV defects, another important defect in germanosilica is the $Ge^{2+}$ defect, illustrated in Figure 3.7 (b). Both NOV and $Ge^{2+}$ defects have absorptions between 240-245 nm wavelengths [66] and are understood to contribute to germanosilica's photosensitivity.

Photosensitivity theories suggest that the exposure of germanosilica to UV light changes the concentration of ODC's. UV exposure achieves this through exciting and releasing electrons, as illustrated in Figure 3.8 (a). For the case of the NOV defect this breaks the 'wrong bond' creating a GeE' centre. The released electron then may either recombine immediately with the GeE' centre, to give recombination luminance, or it may diffuse through the matrix. The electron may eventually become trapped at a Ge(1) or Ge(2) centre to form $Ge(1)^{-}$ (Figure 3.8 (b)) and $Ge(2)^{-}$ defects respectively. It must be noted that a Ge(1) centre corresponds to a germanium atom being the centre of four O-Si bonds, whereas Ge(2) centres corresponds to a germanium atom being the centre of three O-Si bonds and one O-Ge bond.

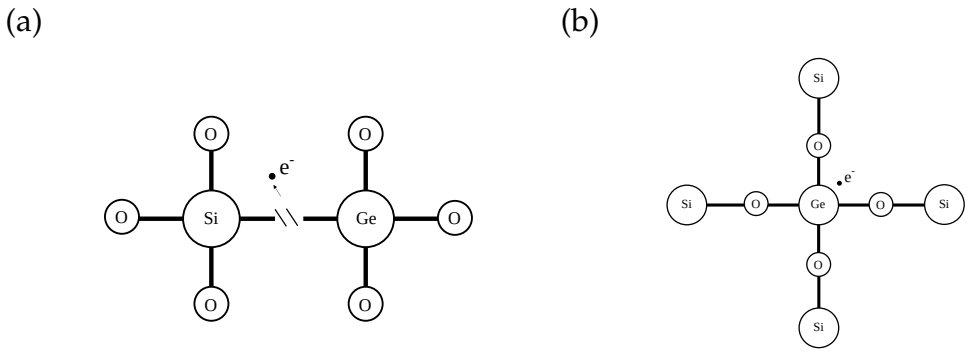


**Figure 3.8:** A schematic showing (a) the direct affect of UV light on NOV defect and (b) the indirect effect of a trapped electron producing a $Ge(1)^{-}$ defect

The picture of photosensitivity presented so far is not entirely complete as calculations suggest additional mechanisms must occur [68] [69] [70]. Possible explanations include thermal effects and stress modification [71] [72] [73]. Densification is a thermally driven process, not a photo-induced one which results in a refractive index change. The phenomenon arises as a result of absorptions in the silica matrix being converted into thermal energy. As a result of high power densities this results in local heating to such a degree as to sinter, melt or even ablate the germanosilica.

The photosensitivity of germanosilica can be further enhanced through loading the sample with hydrogen. The theory and process of hydrogenation shall be discussed in the following subsection.

### 3.4.3 Hydrogenation

In 1993 Lemaire et al reported that the refractive index change of germanosilica glass can be enhanced by an order of magnitude ($10^{-2}$) through hydrogen loading the samples at high pressures ($\sim$120 bar), prior to UV exposure [74]. It must be noted, however, that at room temperature and pressure the in-diffused hydrogen/deuterium will out-diffuse and thus the level of photosensitivity will reduce as a function of time.

Enhancement through hydrogenation is believed to occur as a result of two mechanisms. The first is believed to be a result of the hydrogen's interaction with $GeO_2$ sites. The proposed reaction occurs through thermal or photovoltaic triggering resulting in the breaking of a germanium and oxygen bond resulting in SiOH and an ODC. The second mechanism for enhancement is believed to be a result of the hydrogen acting as a photobleaching catalyst.

An associated problem with hydrogenation is that it increases absorption in the telecoms window, due the formation of extra OH bonds in the glass [75] [76]. This can be overcome by loading the sample with deuterium, instead of hydrogen. Like hydrogen, deuterium has the effect of enhancing the induced index change of the germanosilica glass. However, OD bonds are formed instead of OH bonds. As the mass of deuterium is greater than hydrogen the resonant frequency of the OD bonds are lower than OH bonds, thus absorption occurs at higher wavelengths, such that between 1.3 $\mu$m and 1.6 $\mu$m there are no absorption peaks [75].

Prior to direct UV writing the germanium doped silica wafers in this work were hydrogenated. Hydrogen was selected over deuterium as the reduction in absorption did not justify the increase in cost. Photosensitivity in the hydrogenated FHD wafers used in this work was observed to induce an index change of $5\times10^{-3}$ to $2\times10^{-2}$. This give the ability to direct UV write weak guiding waveguides and gratings. The theory and methodology of direct UV writing shall be described in the following section.

## 3.5 Direct UV Writing Process

Direct UV writing (DUW) takes full advantage of germanosilica's UV photosensitivity, to fabricate IO circuits. The technique was predominantly developed by Svalgaard in the late 1990's [77] and is an established methodology for fabricating integrated optical circuits in silica-on-silicon wafers.

The technique itself uses a UV laser and a set of high precision translation stages. In Svalgaard's early experiments 514.5 nm wavelength radiation from an Argon-ion ($Ar^+$) laser was frequency doubled to produce 257.25 nm radiation. The work detailed in this thesis frequency doubles the 488.0? nm line from an $Ar^+$ laser to produce 244.0 nm radiation. Whilst 514.5 nm line has the highest output power from the $Ar^+$ laser, the 488.0 nm line can be frequency doubled to a frequency that within the germanosilica absorption bands that correspond to refractive index change, discussed in the previous section.

The typical silica-on-silicon wafer construction used in DUW consists of three consecutively deposited silica layers, the central 'core' layer being doped with germanium. If the UV laser is focused into the photosensitive core layer it results in a local refractive index change. Using the translation stages to move the wafer relative to the focused beam two-dimensional refractive index structures can be defined, as illustrated in Figure 3.9.

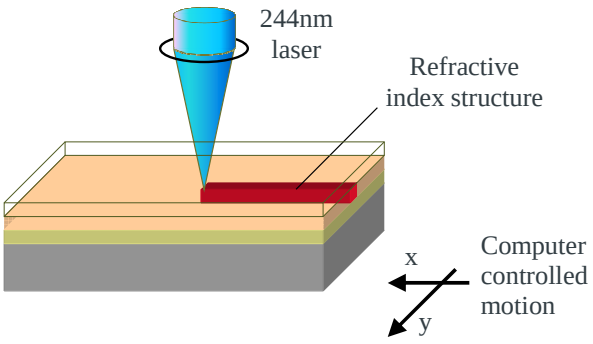


**Figure 3.9:** UV writing into the core layer of a silica-on-silicon wafer

The refractive index contrast of the UV written structures has been demonstrated to be as high as $2 \times 10^{-2}$, but is more commonly in the order of $5 \times 10^{-3}$ or lower. The resultant refractive index change induced depends upon the total number of

UV photons incident upon a point during the writing process. To quantify this exposure the concept of fluence is introduced, formulated in Equation 3.1.

$$F = \frac{I_{UV} d}{v} \tag{3.1}$$

Fluence, $F$ is a measure of the energy delivered to the sample and is dependent on the UV power and the translation speed, $v$. UV power is represented by the multiplication of average power intensity $I_{UV}$ and the spot diameter, $d$ with a typical 1/e width of $\sim 7\mu$m.

Direct UV writing is not the only direct writing technique. In recent years there has been an increased interest in femtosecond (fs) lasers to directly write both waveguides and gratings in bulk transparent materials, including fused silica glass.

## 3.6 Direct Femtosecond Writing

The first demonstration of direct fs-writing was made by Davis et al in 1996 [78]. Fs-writing operates by focusing a near-infrared fs-laser into a glass substrate, the high energy density at the focus causes localized densification leading to a positive change in the refractive index as large as 0.035. Waveguides can be fabricated by translating the sample relative to the laser beam. Bragg gratings can be fabricated by actively modulating the exposure [79].

The fs-writing technique is similar in principle to that used in direct UV writing, in terms of focusing a laser into a material to induce a refractive index change. However, it must be noted that the physical writing process does not rely on photosensitivity, but rather nonlinear effects within the material.

The advantage fs-writing has over UV writing is that it can write three dimensional circuits, in many different bulk materials [80], whilst UV writing is generally confined to only two dimensions. The disadvantage of fs-writing in relation to UV writing is that the laser system required for fabrication is much more expensive and temperamental in terms of stability. In addition, as the field is still relatively new there are several issues that are still to be addressed, including the propagation loss of the resulting waveguide.

The Direct UV Grating Writing (DGW) technique is a derivative of the DUW process, developed at the Optoelectronics Research Centre. The method has the added flexibility of waveguide and simultaneous Bragg grating definition.

### 3.6.1 Direct Grating Writing

Direct UV Grating Writing (DGW) is an established technique for defining both channel waveguides and Bragg gratings [81]. The technique uses two overlapping UV laser beams to give an inherent interference pattern, illustrated in Figure 3.10.

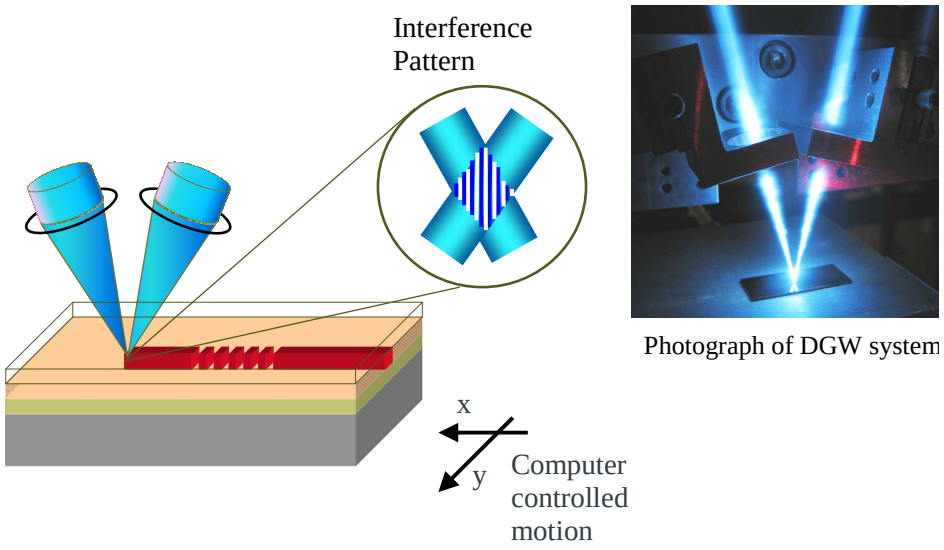


**Figure 3.10:** Direct grating writing setup (cross beam), showing schematic of operation and photograph of operation

Using precision air-bearing stages to traverse the wafer under the focused beams, results in the fabrication of channel waveguides. By modulating the writing beam during sample translation such that the inherent interference pattern stamps periodically upon itself results in the fabrication of Bragg gratings. To write Bragg gratings in the telecommunication 'C-band' (wavelength window 1530 nm to 1565 nm), the angle of the two beams must be pre-set to match the periodicity required. Considering the effective index of the guided mode in a UV written waveguide to be ~1.445, an intrinsic period of ~540 nm is required (as dictated by Equation 2.51). The crossing angle, $\theta$, required to achieve this period, $\Lambda$, can be calculated using the formulism [9]

$$\theta = 2arcsin\left(\frac{2\Lambda}{\lambda_{UV}}\right) \tag{3.2}$$

Where $\lambda_{UV}$ is the wavelength of the UV laser. For an intersecting angle of $26^o$, an intrinsic period of 542 nm is established, corresponding to a Bragg reflected wavelength of 1566 nm. The system focuses the dual beams to a spot of $\sim$4 $\mu$m diameter, using a pair of identical lenses of NA 0.18 and focal length 40 mm. The focused beam contains approximately 7 periods.

The concept is similar to the side exposure with dual UV beam technique, used in fibre Bragg grating fabrication [66]. However, instead of the beams overlapping to give a $\sim$100 $\mu$m diameter spot, they are focused to produce a 4-10 $\mu$m diameter spot, which allows for greater control when engineering a Bragg grating structure.

The optical set-up for the DGW system is illustrated in Figure 3.11, it consists of an argon-ion laser, with a frequency doubled crystal, which emits approximately 80 mW of continuous wave 244 nm light. After leaving the laser head, the output beam is directed into an Acousto-Optic Modulator (AOM) and then 'cleaned' by an iris, which removes beam structure caused by the frequency doubling crystal to give an approximately 'Gaussian' output beam. After this arrangement the power of the laser has reduced to approximately 50 mW. An arrangement of optics then leads the beam into the DGW setup.

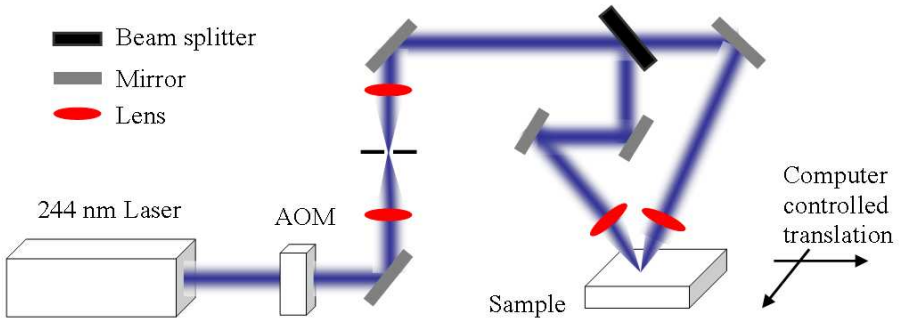


**Figure 3.11:** A schematic of the cross beam UV writing setup

As previously described, the Bragg gratings are written by exposing the interference structure into the photosensitive core. To achieve the level of positional accuracy required for this, computer controlled air-bearing translation stages are used, with $\sim$10 nm of positional accuracy. The positional translation is controlled by G-code, which is a standard CNC (computer numerically controlled) software tool.

Typical writing fluences of 20 kJcm$^{-2}$ have been used in this thesis, which relates to a translation speed of 0.2 mm/min. To imprint the grating the translation needs to be coupled with intensity modulation of the laser beam, this is attained through the AOM.

It has been described so far that imprinting a Bragg grating, of a particular period, can be achieved through using a specific crossing angle. What is not immediately obvious is that this system can access a variety of periods around the intrinsic period without altering the angle of the cross beams. This is realised through detuning the imprinted interference pattern. Detuning operates by having an additional displacement $\Delta$ added to or subtracted from the inherent period of the interference pattern $\Lambda$. Thus this technique gives a Bragg grating period of $\Lambda \pm \Delta$, illustrated in Figure 3.12. This effect is inherently limited, as the greater the intrinsic interference pattern is detuned, the weaker the reflectivity of the grating becomes. However, using this detuning technique the telecommunication E, S, C, L, and U bands have been accessed [82]. This corresponds to a spectral window spanning 1400 nm to 1700 nm wavelengths.

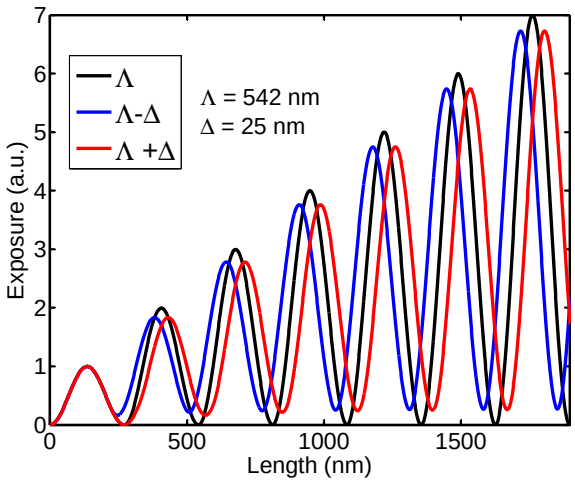


**Figure 3.12:** Mathematical simulation of 7 exposure detuning

Through manipulating the modulation and translation of an interference spot it has been described how uniform Bragg gratings can be fabricated. Modulation and translation can also be manipulated to fabricate other Bragg grating structures. Before understanding methods of Bragg grating engineering concepts of impedance matching and duty cycle should first be tackled. The following subsection shall define the importance of these parameters.

### 3.6.2 Impedance Matching and Duty Cycle

Impedance (index) matching a Bragg grating, to the waveguide leading up to it, significantly improves the Bragg reflection spectrum. The average refractive index of the Bragg grating and the channel can be thought of as two interfaces. The greater the index contrast between two interfaces, the greater the percentage of unwanted Fresnel reflections. To reduce this effect between the waveguide and the grating the index of the waveguide is matched to the average index of the grating. This is achieved by adapting the fluence such that the duty cycle is taken into consideration.

In terms of Bragg grating fabrication, the duty cycle is the fraction of the periods distance for which the laser is on, illustrated in Figure 3.6.2.

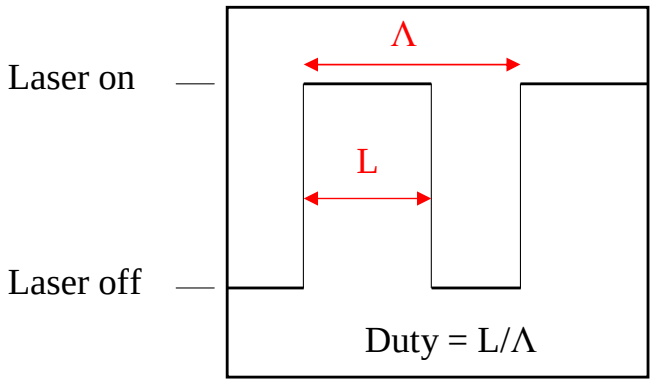


**Figure 3.13:** Duty cycle concept

A duty cycle of 1 corresponds to the laser being constantly on and results in the fabrication of a channel waveguide. DGW with a duty of 0 results in the fabrication of no index structure. One would presume that the lower the duty cycle the higher the index contrast, which is theoretically correct [9]. However, as the duty cycle of the written grating reduces the index contrast of the grating must increase, to impedance match. This higher index contrast requires a higher fluence and so the structure takes longer to write, which has the associated issue of the hydrogen out-diffusing that shall be discussed further in the following section. It is also understood that due to a maximum achievable index change an optimum duty cycle exists for the highest reflected power. Previous investigations into this suggest optimum duty cycles of 0.35 [9]. However, it is understood that this value is very much dependent upon the wafer used and the fluence at which the waveguides are written. The duty cycle for uniform gratings in this work was set at 0.5 for 20

kJcm$^{-2}$.

The variables that can be manipulated across the length of a grating include duty cycle, pitch and refractive index. The variation of these variables across a grating's length affects its spectral response, as discussed in Chapter 2. Variable variation may also result from an external response, i.e. chemical or physical transduction or engineered into the grating.

### 3.6.3 Grating Engineering

Uniform, apodised and chirped Bragg gratings have been fabricated as part of this PhD thesis. As discussed in Chapter 2 the spectral response of a Bragg grating can be approximated by the Fourier Transform of its physical shape. Uniform Bragg gratings have a physical shape that can be approximated by a 'top-hat' function, thus have an expected spectral response approximating a 'sinc' function. The spectral side lobes associated with uniform Bragg gratings can become problematic, especially for gratings that are spectrally in close proximity, as illustrated in Figure 3.14. In such an instance the side lobes of each grating maybe superimposed upon its neighbour, thus complicating the extraction of a grating's individual spectral information.

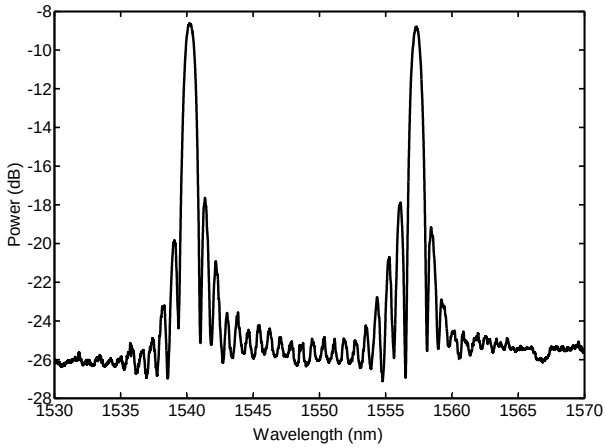


**Figure 3.14:** Reflection spectra from two DGW uniform Bragg gratings, each 2 mm in length, written with a duty cycle 0.5 and fluence 16 kJcm−2

Apodisation literally means "removing the foot"; here it is used to describe gratings which suppress the spectral side lobes previously discussed. There are different types of apodisation [14], the type used in this thesis is Gaussian. As previously mentioned the spectral response of a Bragg grating can be approximated by

the Fourier Transform of its physical form. Therefore, a grating with the physical structure of a Gaussian function is expected to have an approximately Gaussian spectral response, which is indeed observed as illustrated in Figure 3.15.

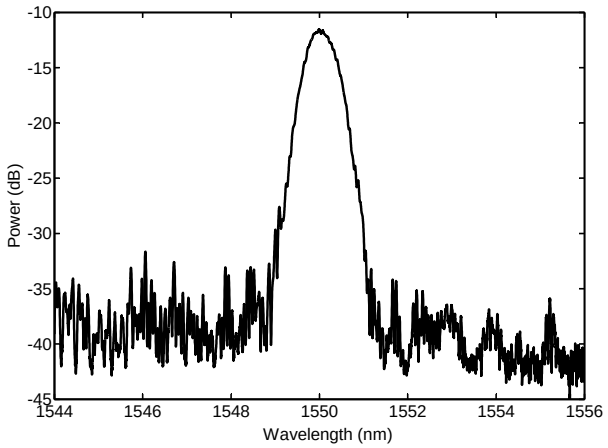


**Figure 3.15:** Reflection spectra of a DGW Gaussian apodised Bragg grating, 2 mm in length, written with a duty cycle 0.5 and fluence 16 kJcm$-2$

It is understood that a Gaussian apodised grating must have a constant averaged refractive index for each consecutive period, otherwise unwanted spectral features can arise as a result of Fabry-Perot resonances occurring between peripheral sections [83]. To achieve period averaged refractive index for the Gaussian apodised Bragg grating's fabricated both the duty cycle and the induced index change are given a Gaussian profile, illustrated in Figure 3.16.

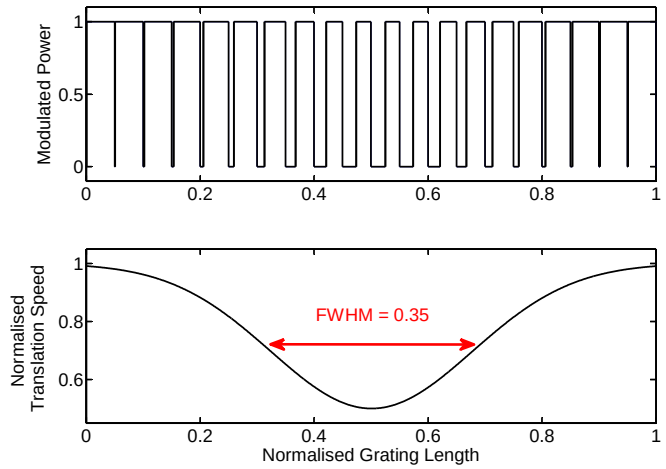


**Figure 3.16:** An illustration of the pitch and fluence variation used to achieve a period averaged refractive index that is constant

It must be noted that as the grating length is finite, wrapping its physical structure

to a Gaussian function will result in the ends of the function being cropped. As this cropping becomes more significant the spectral response will deviate from an idealised Gaussian. It was observed experimentally that a Gaussian apodised grating with a FWHM set to 35 % of the grating's length gave significant side lobe suppression, for the grating lengths written, without compromising grating strength or introducing spectral ringing [83].

In addition to apodised Bragg gratings the author has also engineered linearly chirped Bragg gratings. Chirped gratings are useful structures which are predominantly used in the telecommunication industry for dispersion compensation of signals traversing kilometre lengths of optical fibre. Figure 3.17 (b), demonstrates a 9 mm long grating that has 3.5 nm of spectral linear chirp, this can be compared to a uniform Bragg grating, illustrated in Figure 3.17 (a), which has been fabricated under similar writing conditions. Chirped Bragg gratings shall be encountered in Chapter 5, where they are actuated to have a chirped nature.

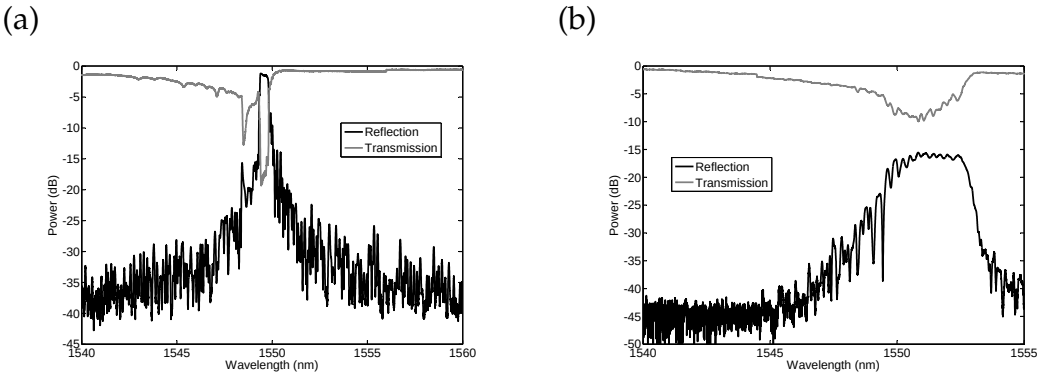


**Figure 3.17:** Reflection and transmission spectra of a DGW (a) uniform and (b) linearly chirped (3.5 nm) Bragg grating, 9 mm in length, written with a duty cycle 0.5 and fluence 30 kJcm$^{-2}$

The grating structures considered so far have been relatively simple. They have considered written waveguides and gratings that have a combined length of less than ∼10 mm. Such structures have associated writing times of less than 10 minutes. When considering devices with a much greater writing time ($>$ 30 minutes) a consideration for hydrogen out diffusion must be made. The following section describes work undertaken by the author to reduce the effect of hydrogen out-diffusion during DGW. It is assumed that similar process will hold true for deuterium loaded samples.

## 3.7 Reducing Hydrogen Out-Diffusion

For typical FHD planar samples detailed in this PhD thesis, hydrogen out-diffusion is understood to affect notably photosensitivity for timescales >30 minutes, which is comparable to the writing time of more complicated DGW circuits. The motivation of the following work is to maximise the writing time window, by enhancing photosensitivity. This will alter circuit designs which have long writing times, access to the higher index contrasts associated with hydrogenated enhanced photosensitivity.

This section describes the theory behind out-diffusion and methods of reducing it, including the use of a cold chuck during writing and thermally locking the samples prior to writing.

### 3.7.1 Diffusivity

Diffusivity, also referred to as the diffusion coefficient, is defined as the rate at which diffusing substances traverse between opposite faces of a unit cube with unit concentration difference between them, expressed as [2]

$$D = D_0 e^{\left(-\frac{E}{RT}\right)} \tag{3.3}$$

where $D_0$ is a pre-exponential factor, E is the diffusion activation energy (~40 kJmol$^{-1}$ [76]), values for which can be obtained experimentally. $\alpha$ is the concentration of deuterium/hydrogen, R is the gas constant (8.3 JK$^{-1}$mol$^{-1}$) and T is the absolute temperature. From the literature it is known that the 1/e decay time, $\tau_{UV}$ can be expressed as [2]

$$\tau_{UV} = -ln(\alpha)\tau_0 e^{\frac{E}{R}\left[\frac{1}{T}-\frac{1}{T_0}\right]} \tag{3.4}$$

where $\tau_0$ is the decay time at temperature $T_0$. This can be interpreted graphically through extrapolating accepted values for silica-on-silicon wafers [2], as illustrated in Figure 3.18.

It was observed experimentally by the author that both liquid nitrogen and dry

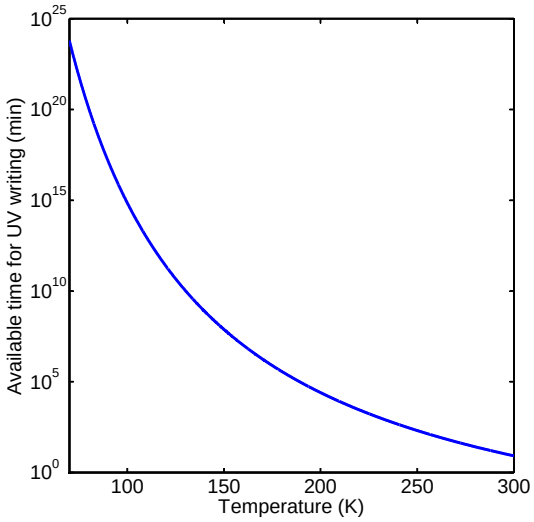


**Figure 3.18:** The temperature dependency of available time for UV writing (1/e decay time) for a temperature range spanning from the temperature of liquid nitrogen to room temperature (Extrapolated from data obtained by Svalgaard [2])

ice can be used to transport and store hydrogenated wafers over timescales of several hours, without a significant level of out-diffusion resulting. This can be inferred from Figure 3.18, as a sample stored at liquid nitrogen temperatures (77 K) is expected to maintain a sufficient concentration of hydrogen for a considerably long period. At dry ice temperatures (194 K) the UV writing time increase from ∼15 minutes at room temperature to ∼3.5 days.

Temperature reduction has also been achieved during UV writing, by using a cold chuck. This concept was developed by the author and leads from work undertaken by Svalgaard for single beam DUW [2]. Out-diffusion can also be stopped by locking the hydrogen/deuterium in the germanosilica structure using high temperature [84] [85] or a UV light catalyst [86].

High temperatures act to lock hydrogen in the germanosilica. There are two ways of achieving this, either through thermal hypersensitisation or high temperature flashing. Thermal hypersensitisation, occurs for temperatures of the order of 400$^{o}$C [84], high temperature flashing also known as OH-flooding [87] [85] occurs for temperatures of the order $\sim$ 1100 $^{o}$C. It must be noted that high temperature flashing can result in a significant increase in optical loss at 1.4 $\mu$m. The increase in associated loss is a result of the formation of additional hydroxyl species in the germanosilica, which have an optical absorption peak near 1.4 $\mu$m [87]

Hypersensitization can also be achieved through UV (355 nm) exposure, achievable through the use of a laser or standard UV sterilization lamps [86] [88].

The following subsections shall examine reducing out-diffusion during UV writing by using a cold chuck and locking photosensitivity within a wafer using OH-flooding.

### 3.7.2 Cold Chuck

The rate of hydrogen out-diffusion can be reduced by lowering the thermal energy of the system. However, achieving a significant level of cooling during the DGW process has many associated complications. Previous efforts by Svalgaard significantly increased the UV writing time, by using a cold chuck system incorporated into the DUW set-up [2]. This system kept the samples at -33 $^{o}$C during writing and overcame issues of ice formation and condensation, whilst increasing writing time from $\sim$ 15 minutes to $>$ 10 hours. The work undertaken by the author applied this technique to DGW, which has additional complications principally due to the system being an interferometric technique. Complications arise as factors such as air currents and/or vibrations compromise the quality of the written Bragg grating.

A cold temperature can be maintained actively or passively, meaning heat can be actively pumped out from the wafer during writing, or the sample can be cooled prior to writing and insulated sufficiently that it maintains its temperature throughout the writing process. As the interferometric system is vibration sensitive, passive cooling was adopted as it lacked the requirement of cooling fans or water circulation systems which are inherently associated with active cooling and can induce unnecessary vibration to the system.

The cold chuck consisted of a central puck, which acted as a thermal reservoir and an outer shell which was separated from the puck by a vacuum, as illustrated in Figure 3.19.

The central puck was made from invar which has a large thermal capacity, making it an ideal thermal reservoir. To reduce thermal conductivity to the cold chuck's outer shell, the puck was placed upon three supporting ceramic legs. To further reduce conductivity the space between the outer shell and the puck was vacuumed

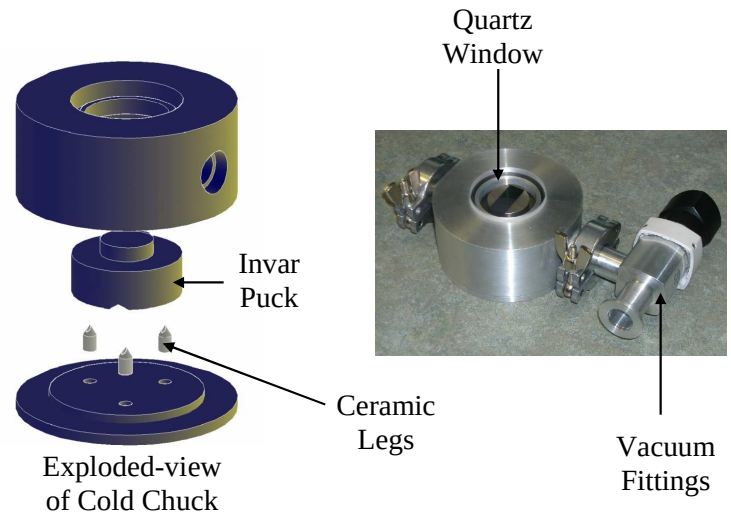


**Figure 3.19:** The Cold Chuck design

and sealed prior to writing, again to prevent detrimental vibrations that would occur if it remained on.

A pure quartz window allowed UV light to be transmitted into the chuck. To reduce aberrations resulting from the presence of the window compensation quartz windows were placed before the main window of the chuck. Prior to writing the chuck was reduced to -78.5 $^{o}$C (temperature of dry ice) and successfully demonstrated the ability write Bragg gratings, as shown in Figure 3.20. However, it was found that the complicated alignment associated with DGW was made significantly more difficult using the cumbersome cold chuck system.

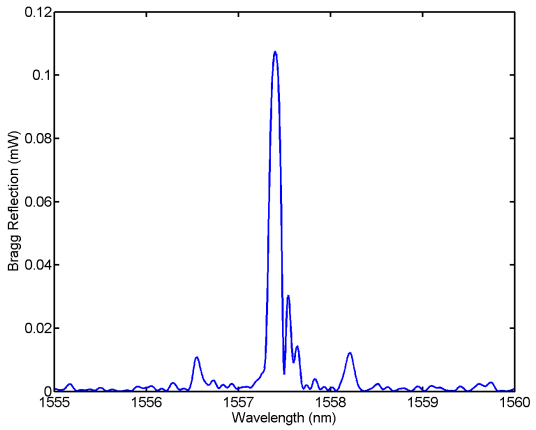


**Figure 3.20:** Bragg grating reflection spectra written with cold chuck

To overcome the cumbersome cold chuck alignment an alternative method of photosensitivity prolonging was sought. OH-flooding is one such method, which acts

to lock the hydrogen within the germanosilica, using rapid thermal treatment.

### 3.7.3 Rapid Thermal Annealing

OH-flooding, also referred to as thermal locking, is a thermal sensitization process in which hydrogenated germanosilica is elevated to temperatures of $\sim 1100\ ^{o}$C for short time periods (several seconds). Previous work by Riziotis has considered OH flooding of silica-on-silicon wafers using an electric resistance furnace [89]. The following work gives a comprehensive study of OH flooding using a rapid thermal annealer (RTA), which is a more repeatable process than the electrical furnace as the thermal cycle is computer controlled and undergoes feedback from a pyrometer and thermocouple readings.

The commercial RTA JetFirst manufactured by Jipelec was used to OH-flood three-layer FHD samples that had been hydrogenated at 150 bar atmosphere for 22 days. Subsequent to RTA the samples were kept at 70 $^{o}$C for 24 hours to ensure the remaining hydrogen out-diffused prior to UV writing.

An elevation temperature range of 390 $^{o}$C to 1300 $^{o}$C was investigated. The temperature profile of each test consisted of three parts the ramp-up, maintaining and cooling. The ramp-up stage increased the wafer to the desired elevation temperature within 5 seconds, a further 5 seconds was observed at which the elevation temperature was maintained. The cooling stage removed the source of heat and purged the chamber with nitrogen.

After thermal treatment Bragg gratings were written into the wafers as a means to quantify the enhancement made in photosensitivity. Figure 3.21 illustrates the measured effective index of the written Bragg gratings, in relation to the ramp temperatures. The graph highlights three temperatures labelled A, B and C corresponding to 397 $^{o}$C, 592 $^{o}$C and 1253 $^{o}$C respectively. For temperatures below 397 $^{o}$C no OH-flooding takes place. The samples weakly fluoresce pink under 50 mW of UV light and after writing with the given intensities neither waveguide channels nor Bragg gratings are sufficiently strong enough to be characterised. At temperatures above 397 $^{o}$C but below 592 $^{o}$C OH-flooding has taken place. The samples brightly fluoresce purple and under the writing intensities waveguides are characterised, however, Bragg gratings are not observed. At temperatures above 592 $^{o}$C,

but below 1253 $^{o}$C the samples fluoresced bright purple when illuminated with 50 mW of UV light, for the three intensities both waveguide and Bragg grating could be characterised.

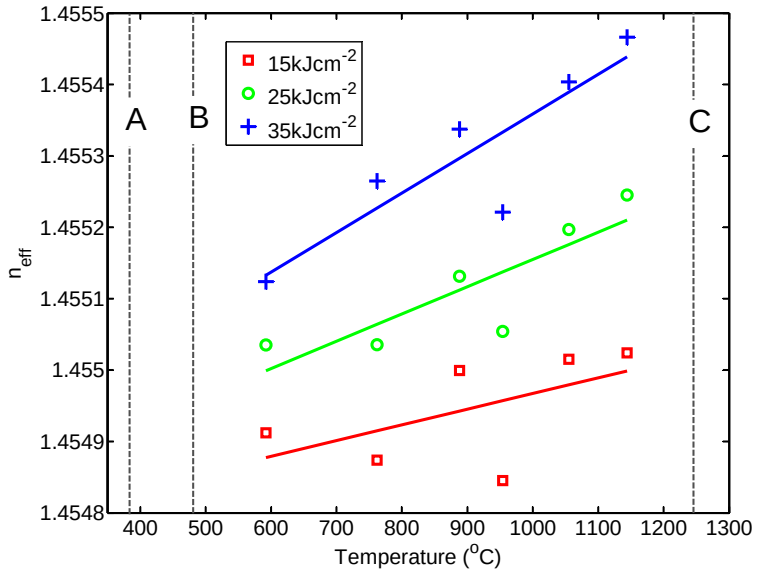


**Figure 3.21:** The dependence of effective modal index upon exposure temperature, for a 5 second maintained temperature period

It can be inferred that that the greater the photosensitivity, the greater the index change hence the greater the effective index will be for similar writing conditions. However, it must be noted that this is not strictly correct as the thermal treatment may enhance the average index of the silica in addition to increasing the photosensitivity.

Birefringence is an additional indicator that can be used to quantify photosensitivity. Through assuming the index profile of the cladding layers remains constant it can be inferred that increasing the index of the core will reduce the difference between TE and TM modes, as asymmetry between the horizontal and vertical mode will become relatively less pronounced.

Figure 3.22 depicts the variation of birefringence as a function of RTA temperature, for maintained temperatures of 5 seconds. It can be observed that as the temperature of the RTA increase the birefringence decreases and drops below 0 at larger temperatures. Negative birefringence maybe a result of thermal stress inherent in the silica, which is a result of the thermal expansion difference between silica and silicon and the high consolidation temperature used in the FHD process. This is approximated in Chapter 4 to be a birefringence offset as large as -2x10$^{-3}$.

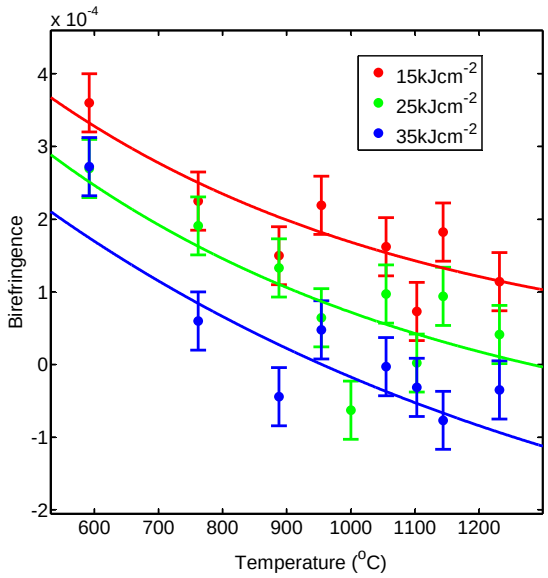


**Figure 3.22:** The dependence of birefingence upon exposure temperature for a 5 second naintained period

From Figures 3.21 and 3.22 it can be inferred that the higher the temperature used for the RTA cycle, the greater the increase in photosensitivity. However, this is limited to wafer temperatures under 1253 $^{o}$C, which is close to the consolidation temperature of the silica layers. Above 1253 $^{o}$C the wafers become permanently deformed. This deformation takes the form of a speckling effect with induced defects that can be classified as a square dip, a mound or a combination of dip and mound, shown in Figure 3.23 (a).

(a) (b)

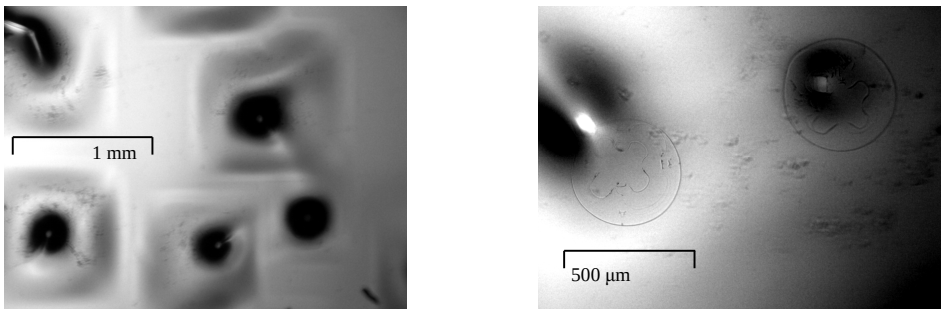


**Figure 3.23:** Microscope images of the FHD deposit layer post 1250$^{o}$C rapid thermal annealing, showing (a) square patterns (b) clover patterns

Focusing the microscope to the top of the mound a four-leafed-clover pattern was seen within a circle, with one of the 'leaves' located upon the top of a mound, shown in Figure 3.23 (b). The exact reasoning for the features is not fully under-

stood. It is postulated that as the wafer heats up the surface expands, however the cooler interior of the wafer restricts the expansion causing a compressive stress at the surface and a tensile stress in the interior. For higher temperature ramp rates this is known to build up high temperature gradient which may exceed the yield stress and cause the wafer to shatter. It is believed that as the silicon cools rapidly shards of silica blister off, this trend was observed on the reverse side of the wafer.

It has been identified that an elevation temperature range between 592 $^{o}$C and 1253 $^{o}$C can be used to thermally lock hydrogen within FHD silica-on-silicon samples. For an RTA elevation temperature of 1150 $^{o}$C a set of experiments were undertaken to observe the influence of time a sample is kept at a particular elevation temperature, shown in Figure 3.24.

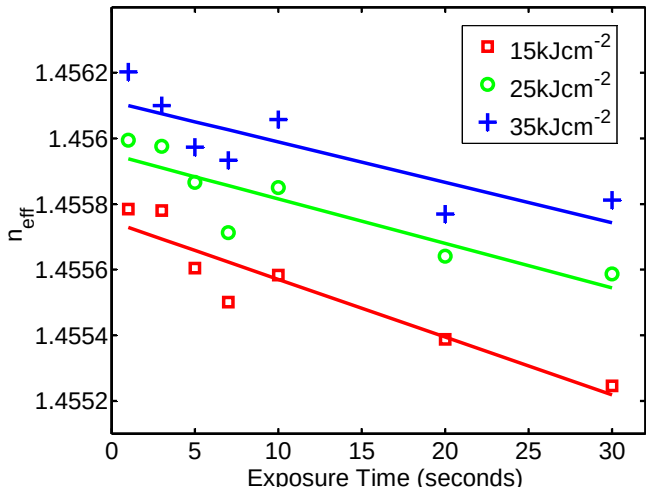


**Figure 3.24:** The dependence of effective modal index upon exposure time, for a set elevation temperature of 1150 $^{o}$C

The longer hydrogen loaded FHD samples are held a particular elevation temperature the lower the effective index. From this it is inferred that to the greatest photosensitivity locking can be achieved by exposing a hydrogen loaded sample to temperatures of the order 1150 $^{0}$C (but below 1253 $^{o}$C) for $\sim$ 1 second. Figure 3.25 compares the spectral response of a hydrogenated sample written at different times to an OH-flooded sample which has undergone 1150 $^{0}$C exposure temperatures for 1 second, both gratings are written with the same writing conditions and from the same batch of wafer. The effective index of the OH-flooded device appears 5 $\times 10^{-4}$ greater than the hydrogenated device. This may be a result of the germanosilica having a larger OH absorption and hence through Kramers-Kronig

relationship having a greater associated refractive index.

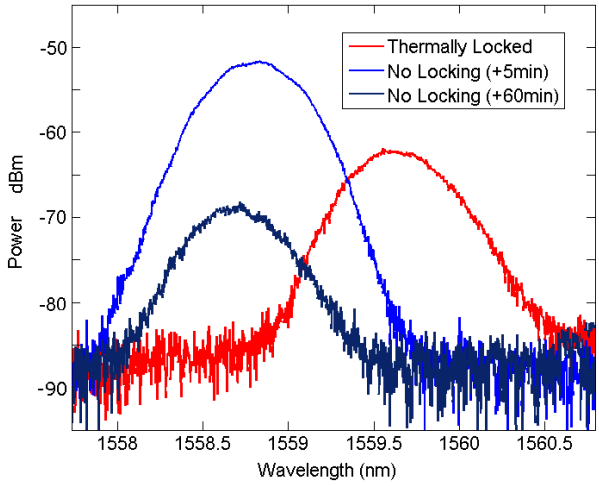


**Figure 3.25:** A comparison between the spectral response of a $H_2$ loaded sample for two different time intervals and an optimised OH-flooded sample

OH-flooding the wafers using RTA is a more quantified approach than using a resistance furnace, as conditions in the resistance furnace are difficult to reproduce. However, it must be noted that Figures 3.21 and 3.24 still display poor correlation, which maybe a result of variation existing between the samples. It is indeed likely that physical variations exist over the 6-inch silica-on-silicon wafer fabricated. Such that even if each sample is fabricated from the same wafer, there is expected to be variation in deposited dopants and stress variation across the wafer.

While it is difficult to account for errors in wafer composition, other errors can be quantified. The following section shall examine the quantifiable errors, including fluctuations in lab temperature and averaging.

### 3.7.4 Error Analysis

When analysing the spectral response of a Bragg grating the largest influence of spectral variation is the fluctuations in laboratory temperature. The thermal fluctuations in a laboratory, over a 20 minute time frame, are typically 3-4 $^{o}$C. As can be observed in Figure 3.26, the thermal response of a Bragg grating is of the order 10 pm$^{o}$C$^{-1}$, meaning a typical experiment lasting 20 minutes may have associated errors of $\sim$ 30 pm.

Throughout this PhD thesis these temperature variations have been accounted for

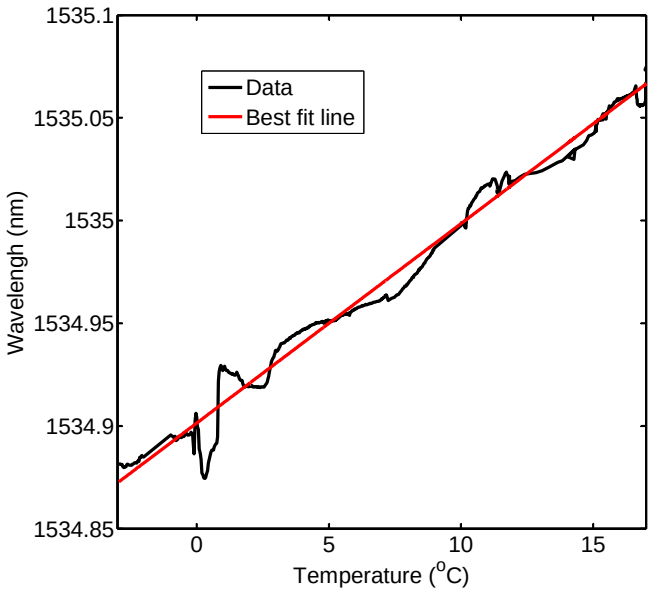


**Figure 3.26:** The spectral response of a typical DGW planar Bragg grating to temperature

during testing. This has mainly been achieved by introducing a reference Bragg grating that is isolated from the method of actuation. When it was not possible to isolate a Bragg grating, for example during mechanical testing, the Bragg grating was either self referenced prior to each actuation or referenced to a thermocouple located onto the device.

The spectral data collected in this thesis was obtained from an Optical Spectrum Analyser (OSA), which had a minimum resolution of 0.01 nm. The characteristics of the reflected Bragg grating spectra were inferred by approximating it to a Gaussian least square fit function. From this fit the centre wavelength, amplitude, background and bandwidth of the reflected spectral response could be measured. The following part of this subsection shall consider the standard error associated with the Gaussian fitting of OSA data. The experiment obtains standard errors by collecting multiple sets of five consecutive measurements over a 20 minute time frame.

The following quantification of standard error considers the largest (9 mm long) and smallest (1 mm long) Bragg grating lengths fabricated in this PhD thesis. The 9 mm long Bragg grating has a spectral bandwidth of 130 pm and the 1 mm Bragg grating has a spectral bandwidth of 800 pm. Both gratings have been written with a duty cycle of 0.5 and a fluence of 20 kJcm$^{-2}$. To allow for a sufficient number of data points for a least square fit, OSA resolutions of 10 pm and 50 pm were

considered. The variations of standard error for 5 averaged data sets over a 20 minute period are represented as boxplots in Figure 3.27.

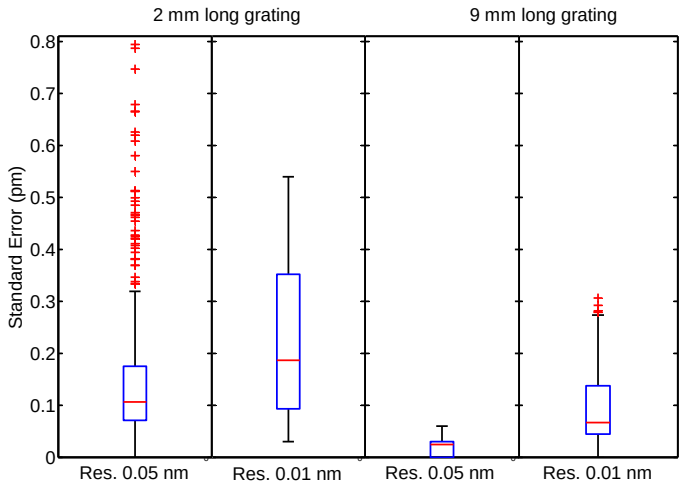


**Figure 3.27:** Boxplots depicting the variation in standard error for a collection of 5 successively collated data points, quantified for 2 mm and 9 mm long gratings at 0.05 nm and 0.01 nm Optical Spectrum Analyser resolutions

It can be observed in Figure 3.27 boxplots that the standard error associated with 5 averaged data points is typically less than 1 pm. In addition, lower standard deviations typically occur for lower resolution scans. This is partially a result of the delay time between successive data scans for each respective resolution.

The time taken to achieve a least square fit is dependent upon the number of points and the quality of the grating considered. Fitting times of 3-6 seconds for 50 pm OSA resolutions and 10-15 seconds for 10 pm resolutions were typical. Longer scan times were more influenced by thermal drift, thus lower resolution scans were preferred. It must be noted that although thermal drift can be normalised against a reference grating the lag time between data collection of the reference and sensor grating(s) is still an influence. It shall be considered throughout this thesis that the associated error for temperature normalised gratings is under 1 pm.

The following section stipulates how the devices were characterised and packaged for testing.

## 3.8 Device Characterisation and Packaging

Subsequent to UV writing the spectral response of the written Bragg gratings are characterised. This process tests if the device has been successfully written and can be used to measure grating properties such as reflectivity, birefringence and effective index.

As the overclad thicknesses in the FHD wafers, used in this work, are ~15 $\mu$m the in-diffused hydrogen is to best approximation depleted by the time the sample is characterised. This period which starts from the time the sample is removed from the hydrogen loading chamber is typically over 3 hours. Negligible difference has been observed for samples characterised 3 hours after writing and several days after writing. Therefore, no annealing stage has been applied to the fabricated samples post UV writing.

Characterisation is achieved by firstly launching broadband light into the written waveguide via a single mode optical fibre. Depending upon the Bragg condition of the grating, the light is either coupled back into the launch fibre through reflection or transmitted and can be butt-coupled out through an additional optical fibre. If further experimentation is required the optical fibre can be replaced by an optical fibre pigtail and secured using a UV curing epoxy. The resulting packaged device is sufficiently robust to withstand even the mechanical testing detailed in this PhD thesis.

In order to launch broadband light into a planar waveguide via an optical fibre waveguide, a HeNe laser source (light of ~633 nm wavelength) is firstly used to align the respective waveguides. This alignment is further refined through focusing the transmitted broadband light (~1400 nm to ~1600 nm wavelengths) upon a CCD camera. To butt-couple the transmitted light out the device a similar process is used on the output side of the planar waveguide.

After alignment the reflection and transmission spectra can be measured using an optical set-up similar to that depicted in Figure 3.28. Spectra analysis is achievable using an Optical Spectrum Analyser (OSA), to deliver the reflected light to the OSA either a coupler or circulator is used as depicted in Figure 3.28.

The reflection and transmission spectra of a multimode Bragg grating is illustrated in Figure 3.29. Such higher order modes can be achieved if the waveguide dimen-

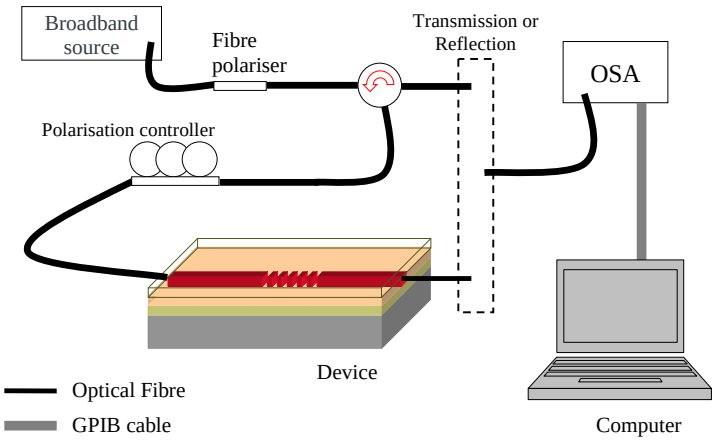


**Figure 3.28:** Characterization setup to measure the transmitted and reflected broadband spectrum after being placed through an optical sensor.

sions and/or the refractive index are sufficiently large. However, the majority of gratings investigated as part of this PhD thesis are single mode and so lack the higher order features labelled A in Figure 3.29.

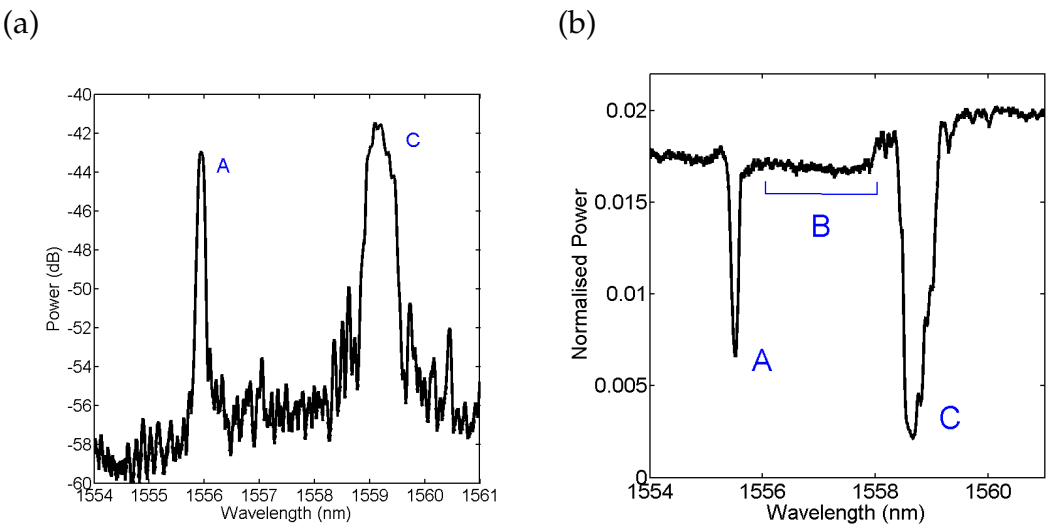


**Figure 3.29:** The (a) reflection and (b) transmission images of a fabricated direct UV written device

The grating illustrated in Figure 3.29 is multimode as the wafer which it is written into has a higher germanium concentration. The grating is 9 mm in length and written with a 0.5 duty cycle and fluence of 20 kJcm$^{-2}$. Typical single mode spectra contain a fundamental mode feature C in both reflection and transmission and a cladding modes B, observed in the transmission spectra only.

When characterising a grating spectra it is important to distinguish between TE

and TM modes as both individual modes can have a different responses when the grating is transduced. TE and TM modes have been selected in this thesis using one of two methodologies. One methodology does not require polarisation maintaining (PM) components the other does.

The polarisation state launched into the device can be controlled through using a standard (not polarisation maintaining) single mode fibre (SMF) and a polarisation controller, illustrated in Figure 3.28. To selectively choose a particular polarisation, the input light itself must firstly be polarised (For an unpolarised source this can be achieved through the use of a fibre polariser). The polarisation within the device can be monitored by focusing the transmitted light from the devices' end face trough a free space polariser and upon a CCD camera. Using the polarisation controller to selectively maximise/minimise the imaged light particular polarisations can be thus selected.

PM components can select distinctive polarisations launched into a planar waveguide. The optical set-up is used to achieve this in this work is similar to that depicted in Figure 3.29, except the polariser and polarisation controller are not present. A PM-polariser is present after the circulator and before the sample. Using a PM-pigtail from the PM-polariser to the planar waveguide ensures the light launched into the waveguide is of one polarisation. Polarisation can then be rotated by using a fibre connector which orientates the faces of the connectors by $90^o$. This latter method, in general, is a much simpler technique to implement and has specifically been implemented in the mechanical testing of planar waveguides, where the use of an objective and CCD camera is cumbersome.

The birefringence of the planar waveguides written is dependent upon their construction and writing conditions. Figure 3.30 shows a typical single mode waveguide with a 9 mm long Bragg grating, written with a duty cycle of 0.5 and a fluence of 20 kJcm$^{-2}$. The birefringence of the device is $1.9\times10^{-4}$, which is the typical order for device fabricated in this PhD thesis. It is understood that through manipulating fluence zero birefringence can be achieved, as demonstrated by Svalgaard [90].

After device characterisation the chip was packaged as pictured in Figure 3.31. A standard V-groove polarisation maintaining fibre pig-tail chip was used to launch light into the device. This was attached using a UV epoxy, which was robust enough to withstand the mechanical testing outlined in Chapter 5.

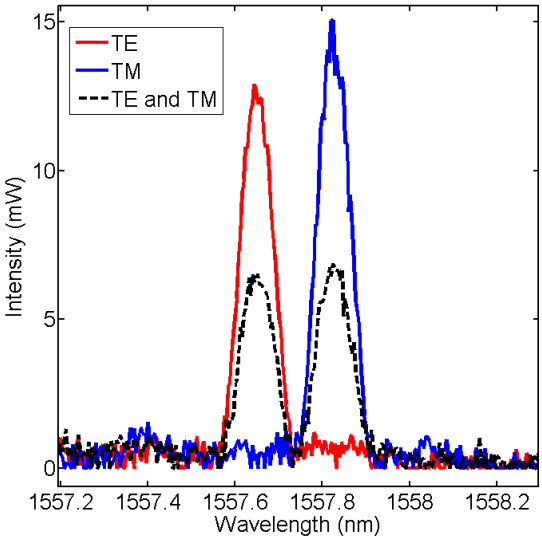


**Figure 3.30:** The Bragg reflection spectra for a 9 mm long uniform grating, giving both TE and TM polarisations

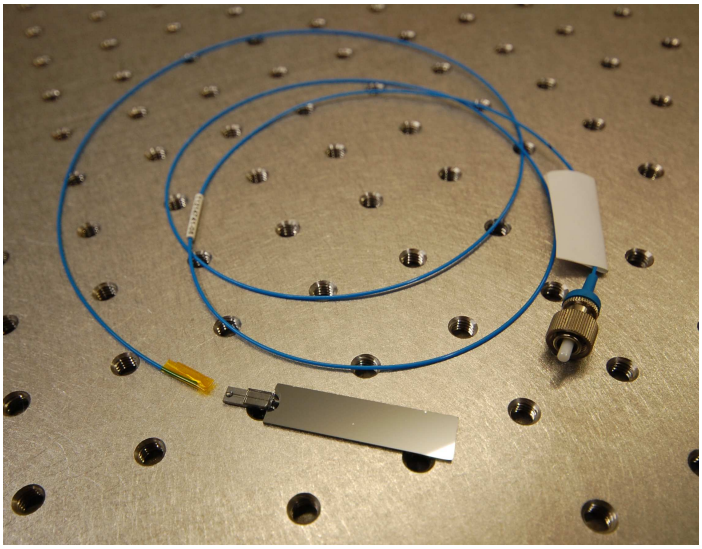

**Figure 3.31:** Basic device

To monitor the reflection spectra of the devices during testing a similar optical set-up to that used during characterisation was implemented. Spectral data was collected from the OSA and transferred to a PC running Labview software via a GPIB (General Purpose Interface Bus) connection. The Labview algorithm fitted a Gaussian profile to the spectra using a least squares method. Understanding the form of the Bragg grating the central Bragg wavelength, bandwidth, amplitude and background intensity could be inferred.

## 3.9 Conclusions

The material platform used in this PhD thesis is silica-on-silicon fabricated using an FHD process. The core layer of silica is doped with germanium which makes it photosensitive to UV light. Photosensitivity is further enhanced by hydrogenating the sample at a pressure of 120 bar for approximately one week.

A combination of waveguide and Bragg gratings are defined into the substrate using a DGW process. This process relies on a photoinduced index change of $\sim$5x10$^{-3}$ in the germanosilica core layer of the waveguide. This has an advantage over photolithographic techniques and etching as it allows for rapid prototyping and is less expensive when small device numbers are made. Bragg gratings can be written from 1400 nm to 1700 nm by detuning and modulating the inherent interference pattern produced by the overlap of two focused coherent UV laser beams.

For device structures that have a long associated writing time hydrogen out diffusion becomes a problem. Two ways of overcoming this have been investigated, including reducing the temperature of the sample during writing and OH flooding the sample. To reduce the temperature of the sample it was placed in a cold chuck during UV writing. Although the system successfully demonstrated UV writing, the alignment was complicated. A simpler method of reducing the effect of out-diffusion is to RTA the sample, at 1150 $^oC$ held for 2 seconds.

The following Chapters shall detail the fabrication of different devices, detailing deviations from the core fabrication process when they occur.

# Chapter 4

# Evanescent Field Sensing

## 4.1 Introduction

Integrated optical devices are being increasingly used for chemical and biochemical sensing applications. These devices have principally been developed in the slip-stream of optical telecommunication technology and the success of optical fibre sensors. This chapter highlights the investigations undertaken by the author to optimise the sensitivity of DGW planar chemical sensors. Just as for the majority of optical fibre based sensors these devices have the principal attraction of high sensitivity, real-time and on-site measurement.

IO chemical sensors typically operate through monitoring a perturbation of an evanescent field as a result of the presence of a chemical or biological [91]. Perturbations in the evanescent field can be monitored through a change in effective index, absorption (imaginary part of effective index) or luminescence. These techniques cover a huge range of different devices that have been reviewed in many books and journal articles [91], [92]. The following work focusses upon effective index based evanescent field sensors, which generally operate in an interference based regime. Examples of such device structures include Mach-Zehnder interferometers, ring resonators and Fabry-Perot resonators [93]. Typically the refractive index resolutions of these devices are of the order $10^{-8}$ RIU [92] [94]. The most well known representatives of this class are grating couplers (e.g. Bragg reflectors) and Surface Plasmon Resonance (SPR) based devices, both of whose interference mechanisms are not immediately obvious. It must be noted that SPR devices and

grating coupler based devices typically have lower sensitivities compared to other interference based devices. However, their advantage lies in the fact that they have a large dynamic range and are less sensitive to variations in supplied optical power.

Grating couplers can be classified as long period gratings (LPG) or short period gratings (Bragg gratings). As with Bragg gratings, LPGs have proven to be effective refractive index sensors [45], [95], [96]. However, it must be noted that the physical length of a BG is typically 1 mm long, which is 10-100 times smaller than an LPG meaning BG's have an associated advantage of near point sensing applications.

Surface Plasmon based sensors represent a large section of the biosensor market and typically demonstrate sensitivities of the order 1700 nm $RIU^{-1}$ (nanometer spectral shift per unit change in refractive index) [97]. In particular they have become an essential tool for the study of biomolecular and chemical interactions on surfaces [98] as a high fraction of their power can be supported in this region [99]. In addition, the surface of the sensor is usually composed of gold, which is a well documented substrate for surface functionalisation and sensitivity enhancement.

SPR and BG based sensors are amongst the most common commercial IO chemical sensors. The author's work formed part of a TSB[1] collaborative project between the University of Southampton, Stratophase, Davin Optics and Smart Fibres, which resulted in the commercialisation of a DGW planar Bragg grating based chemical sensor. The chapter details the work undertaken by the author to optimise the design of the commercialised device. In this investigation, the manipulation of a device's basic structure and operation is considered alongside the introduction of enhancement layers. Device sensitivity is computer modelled to investigate bulk and surface changes, representing surface functionalised and non-surface functionalised based sensors. In addition the dispersion of typical analytes are measured and quantified to relate their spectral dependence on sensitivity. Collectively, this work was used to give a competitive edge against commercially available devices such as those based upon SPR technology.

[1]Technology Strategy Board (TSB) is a UK government body engaged in promoting emerging technologies.

## 4.2 Theory

This section outlines the theory of operation for the developed evanescent field sensors and methods of sensitivity optimisation. The use of enhancement layers to manipulate the evanescent field is discussed, in addition to the exploitation of an analyte's dispersion to improve sensitivity and discrimination.

Evanescent field sensors operate by exposing the evanescent tail of a supported mode to an analyte. Variations in the refractive index of the analyte alter the effective index of the supported mode, which can be monitored. The presented devices monitor effective index through the use of Bragg gratings. As discussed in Chapter 2, the Bragg condition is understood to be dependent upon the grating pitch and the effective index of the guided mode, formulated as

$$\Delta\lambda_B = 2\Lambda\Delta n_{eff} \tag{4.1}$$

The sensors detailed in this PhD thesis have traditionally achieved evanescent field exposure through wet etching the FHD overclad layer with Hydrofluoric (HF) acid [9]. However, as a result of the Mountbatten fire at the University of Southampton in 2005 the facilities required for this acid processing became temporarily unavailable[2], resulting in the author seeking alternative methods of evanescent field exposure.

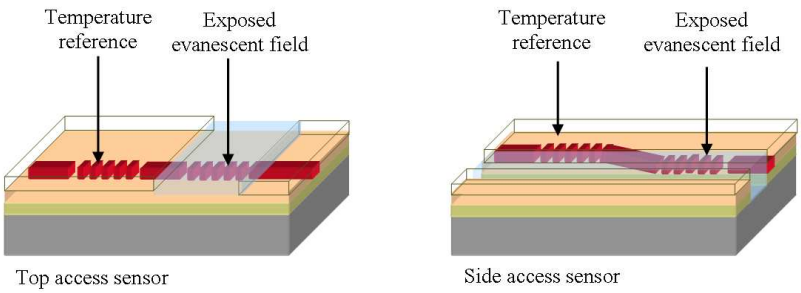


**Figure 4.1:** The top access and side access regimes for exposing the evanescent field in one grating whilst masking another for temperature referencing

Evanescent field access can be gained from the 'top' or the 'side' of the waveguide

[2]Etching facilities were brought back online in July 2007

as illustrated in Figure 4.1. Top access can be realised through wet etching. Side access can be realised through sawing a groove into the silica substrate and post UV writing an S-bend and Bragg grating up to the groove's edge. This was the technique adapted by the author to principally overcome the temporary absence of wet etch facilities. The evanescent field for top access and side access geometries are illustrated Figure 4.2.

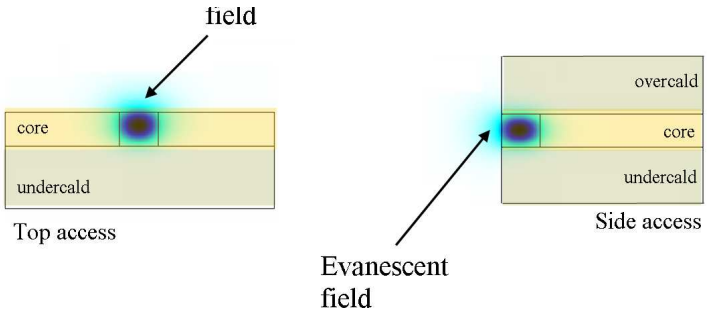


**Figure 4.2:** Cross-section illustration of the supported modes for the two methods of evanescent field access

It must be noted that assuming the FHD layers are perfectly index matched and the written waveguide has a $90^o$ rotational symmetry then the sensitivities of both geometries should be equal. Effectively both geometries under these conditions would be structurally equal, but have a $90^o$ rotational symmetry with respect to each other. This would mean that one geometry's TE polarisation would be the others geometry's TM polarisation (purely as a result of definition) and vice-versa. This would translate to the sensitivity curves, meaning the TE sensitivity curve in one orientation would be essentially the sensitivity curve for the TM polarisation in the other orientation. Major sensitivity differences between top access and side access geometry are only expected to exist if the core layer has different indices to the cladding layers. Typically, the index of the core in the fabricated devices is 1.45 and the index of the cladding layers is 1.444, a feature observed in the simulation and experimental results.

Side access is a novel technique of achieving evanescent field sensing which does not require a HF etching step. In addition it must be noted that the channel formed can be utilised for microfluidic manipulation.

The sensitivity of the devices detailed so far can be enhanced through manipulating the evanescent field, which penetrates into the analyte. One way of manipulating the evanescent field is through the deposition of an enhancement layer.

### 4.2.1 Enhancement Layers

The purpose of enhancement layers is to manipulate the evanescent field in a manner that optimises device sensitivity. As metal and dielectric enhancement layers manipulate the evanescent field in different ways this PhD thesis shall distinctly separate these two forms of enhancements. A question that this chapter shall answer is 'which form of enhancement layer (metal or dielectric) gives the greatest sensitivity enhancement?'

Enhancement layers can be used to manipulate the distribution of a guided mode's power. As illustrated in Figure 4.3 a thin high index dielectric layer between the native device and the analyte can be used to pull more of a mode's power into the analyte, thus enhance device sensitivity.

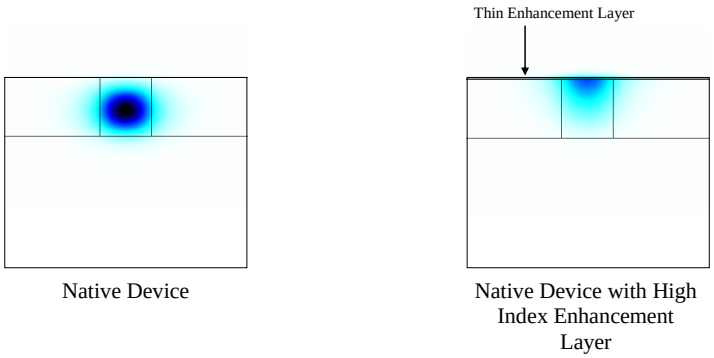


**Figure 4.3:** The simulated modal power distribution plot for a silica waveguide with and without a thin layer (50 nm) of high index (2.1) dielectric overlay

The alteration of a modes distribution as a result of a metals presence is different than that of a dielectric as a so termed plasmon-hybrid mode can result from a metal overlayer, which concentrates a mode's power at the surface of the device. These modes are of interest as they display characteristics of 'pure' plasmons, which are supported in SPR sensor devices.

### 4.2.2 Plasmon-Hybrid Mode

Surface detection is becoming an increasingly important operative in (bio)chemical sensing as the use of functionalised surface chemistry is maturing. Functionalised surfaces can increase device sensitivity and specificity, especially in instances where

there is a low concentration of the detection substance. This is beneficial especially in systems which require early detection of dangerous pathogens in an environment. SPR sensors are especially effective in detecting surface changes as the pure plasmon mode they support is able to concentrate a high fraction of power at the sensing surface, making the device particularly sensitive to surface changes. In addition, typical plasmon supporting materials like gold have a high affinity to surface functionalistion, which can be readily implemented to further enhance the sensitivity of a device.

By placing a metal enhancement layer upon a waveguide a plasmon-hybrid mode can be supported, which is different to a pure plasmon mode. The modes investigated in this chapter are not the 'pure' plsamon modes that are the typical modes in plasmon based sensors, rather 'plasmon-hybrid' modes.

A pure surface plasmon mode, sometimes labelled as a plasmon-polariton (SPP) is an electromagnetic excitation at a metal-dielectric interface that consists of a surface charge density oscillation that is coupled to the electromagnetic fields. If the permittivity of a material (metal) is negative[3], at a particular wavelength, then it can support a plasmon mode. The distinction between a 'pure' SPP and a 'hybrid' SPP is that the 'pure' SPP is localized in the vicinity of the metal layer, exponentially decaying in all other layers including the waveguide. In contrast the 'hybrid' SPP consists of the guided mode of the multilayer dielectric structure coupled with the SPP supported by the metal layer. Recent work by Nemova and Kashyap has theoretically investigated Bragg grating coupling from a 'hybrid' SPP to a 'pure' SPP [100] for sensing applications. The following work considers sensing with a 'hybrid' SPP mode only.

The supported TE and TM modes, as modelled in FIMMWAVE, for a generic DGW device, with a removed overclad and a 40 nm thick deposit layer of Nickel are shown in Figure 4.4.

It can be clearly observed that the TE and TM modes are distinctly different. As expected from theory the TM polarisation displays a 'hybrid' SPP nature. The reason that the TE mode does not display a similar nature can be understood from the boundary conditions. As discussed in Chapter 2 the TM mode has a $H_3$ con-

[3]This is equivalent to the condition the extinction coefficient is greater than the real part of the index.

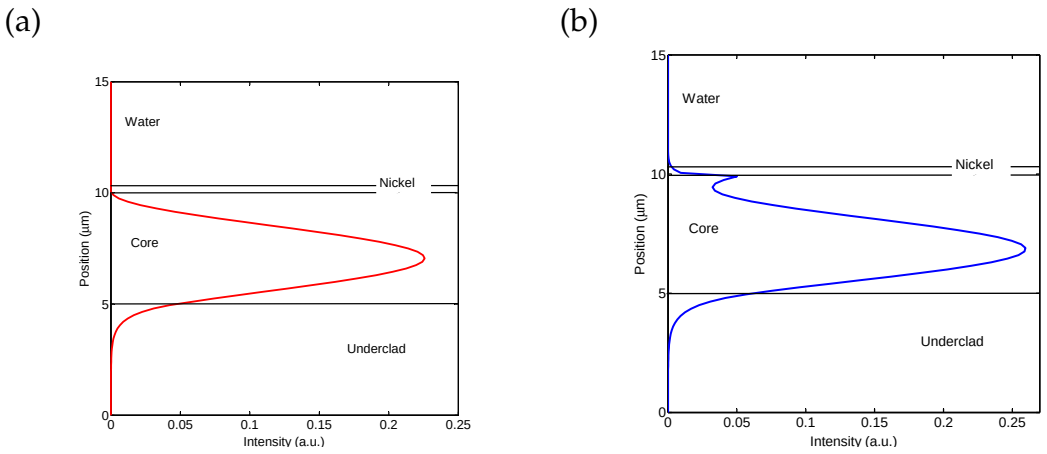


**Figure 4.4:** The mode profile of (a) TE and (b) a TM mode with 40 nm Nickel

tinuity and the TE has a $E_3$ continuity. Considering the boundary condition given in Equations 2.18 and 2.19, it is noted that the continuity condition for TE has a dependency on the permittivity, meaning that it is not possible for the TE field to exist either side of the metal as it has a complex refractive index. Considering the $H_3$ field the boundary condition is irrespective of permittivity.

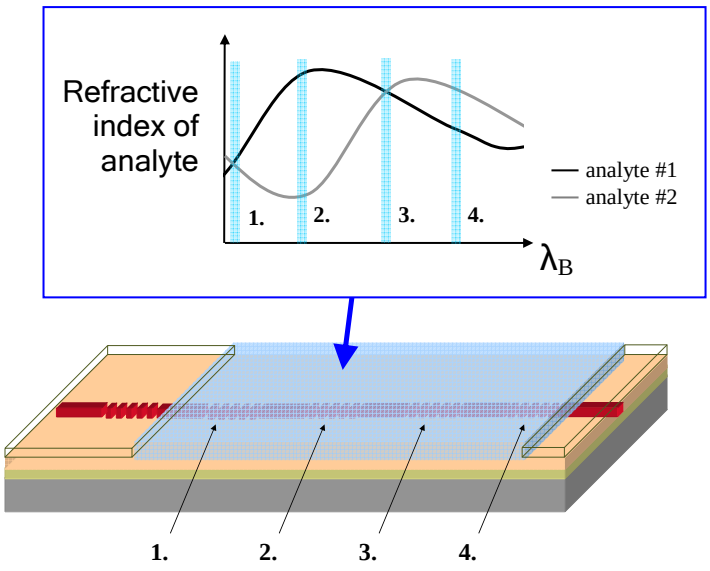


**Figure 4.5:** Illustration of a measurands dispersion characteristic and the placement of Bragg gratings relative to that signature

.

Manipulating the geometry of the sensor platform including the introduction of metal/dielectric layers is one method of enhancing sensitivity; another is to understand the dispersion of the measurand. From dispersion information the spectral locations of the written Bragg gratings can be optimally placed. This concept is

illustrated in Figure 4.5. In this illustration there are four evanescent field sensors (Bragg gratings), spaced at different spectral positions. Considering the dispersion of analyte #1 and analyte #2, it is clear that grating 1 and 3 would observe the same refractive index for both analytes, whereas gratings 2 and 4 observe different refractive indices. Therefore, it is important to understand the dispersion relationships of the measureands to be measured before the spectral locations for the Bragg gratings are set. It must be noted that the dispersion of an analyte can be calculated from its respective absorption spectra, using the Kramers Kronig relation. The theory of this relationship is developed in the following subsection and has been utilised in this work to effectively spectrally position the written Bragg gratings. This is an important exercise as through effectively placing the Bragg gratings spectrally the total number of Bragg gratings required to distinguish different chemicals can be reduced. This increases the bandwidth available for other sensing elements in a multiplexed system as well as, more importantly, reducing the likelihood of a false reading.

### 4.2.3 Kramers-Kronig Methods

To understand the formulism of the Kramers-Kronig relationship the complex nature of refractive index ought to be first understood. The refractive index of a medium $\widehat{n}(\lambda)$ can be split into a real dispersive part n($\lambda$) and an imaginary absorption (or gain) part $\kappa$($\lambda$), formulated as

$$\widehat{n}(\lambda) = n(\lambda) - i\kappa(\lambda) \tag{4.2}$$

were, n is dispersion and $\kappa$ is the extinction coefficient, which indicates the amount of absorption loss (or gain) when the electromagnetic wave propagates through the material. Absorption can also be expressed as the Lambert absorption coefficient $\alpha$, which is related to the extinction coefficient by

$$\alpha\left(\lambda\right) = 4\pi\kappa\left(\lambda\right)/\lambda \tag{4.3}$$

The spectral form of absorption can be mathematically interpreted by considering an electron bound to the nucleus, to be analogous to a small mass bound to a

bigger mass by a spring. If the system is driven by a (light)wave $E_0 e^{-i\omega t}$, the resulting oscillations can be approximated as a damped forced oscillator. Therfore, considering an electron of mass $m_e$ and charge $e$, there is a resonance at $\omega_0$, with a particular viscous drag, $\gamma$, formulated as

$$m_e \frac{d^2\mathbf{x}_e}{dt^2} + m_e\gamma\frac{d\mathbf{x}_e}{dt} + m_e\omega_0^2 x_e = e\mathbf{E}_0 e^{-i\omega t} \tag{4.4}$$

From Equation 4.4 and applying EM identities for an electron density $N$, gives absorption, $\alpha$, in the form of a complex Lorentzian (Equation 4.5).

$$\alpha = \frac{Ne^2}{4\epsilon_o c m_e}\left[\frac{\gamma/2}{(\omega_0-\omega)^2 + (\gamma/2)^2}\right] \tag{4.5}$$

This description of imaginary refractive index is inherently linked to the real part through the Kramers-Kronig (KK) relationship. The interrelationship between n and $\kappa$ can be understood by considering an excited atom that vibrates at the frequency of the light that excited it and re-emits the energy as light of that frequency. The delay in re-emission retards the time taken for light to travel through a material, thus increasing $n$. Absorption is affected by the relative phase of the light that is re-emitted with respect to the incident light. This relative phase shift will produce interference with the original light; destructive interference will result in absorption. In general, collisions dephase the vibrations, causing cancellation of the total medium vibration.

The KK relation is formulated through Fourier analysis, the concept of causality and Cauchy's theorem of complex integration [101]. The relationship is expressed as

$$n(\omega) = 1 - \frac{2c}{\pi} P\int_0^\infty \frac{\alpha(\Omega)d\Omega}{(\omega^2-\Omega^2)} \tag{4.6}$$

In the derivation of this equation, Cauchy's theorem was used thus P stands for the principle value [101] [102]. The Principle value is a method for assigning values to certain improper integrals which would otherwise be undefined. The principle considers the Argand (complex) plane to solve the integral. Thus, it must be understood that P is not a parameter but a definition of the type of integral to be performed. Equation 4.6 can be evaluated by considering absorption in the

complex frequency plane. If $\omega_r$ (real angular frequency) is on the ordinate and $\omega_i$ (imaginary angular frequency) on the abscissa, there will be two infinity points otherwise known as poles, at locations illustrated in Figure 4.6. The poles have a negative complex coordinate, as a result of causality. The principle of causality states that a physical system can have memory of a past event but can't anticipate a future event (information does not travel faster than the speed of light!). The situation at a pole is that due to resonance it hits infinity, as a result of a finite driving force. The arrival of the driving force can not be anticipated therefore infinite amplitude is a result of memory of a force. Since physical processes show natural decay the form of the lightwave must be accounted for, which results in $\omega_i$ being negative [103].

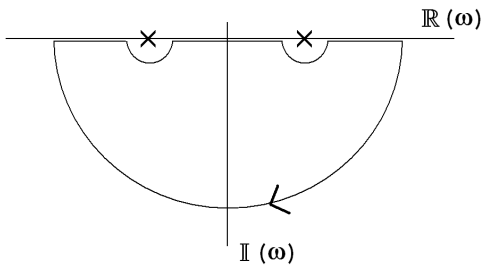


**Figure 4.6:** Complex integration contour avoiding poles

Equation 4.6 can be evaluated by considering the contour integral shown in Figure 4.6. The semicircular integration path is made very large and indentations are made along $\omega_R$ axis to avoid poles or zeros.

The KK relation was computed with an algorithm written by the author. The algorithm was devised using Maple software and is presented in Appendix C. The algorithm requires a Lorentzian peak extinction coefficient input and converts it into dispersion. Comparing the algorithm to accepted absorption and dispersion data of water [3], showed good correlation, illustrated in Figure 4.7. Deviation from accept dispersion values only occurs when the Lorentzian fit for absorption deviates from accepted data.

Through understanding the theory behind evanescent field manipulation and dispersion characteristics of the measured analytes, optimised device designs can be fabricated. The following section shall outline the actual steps involved in device fabrication.

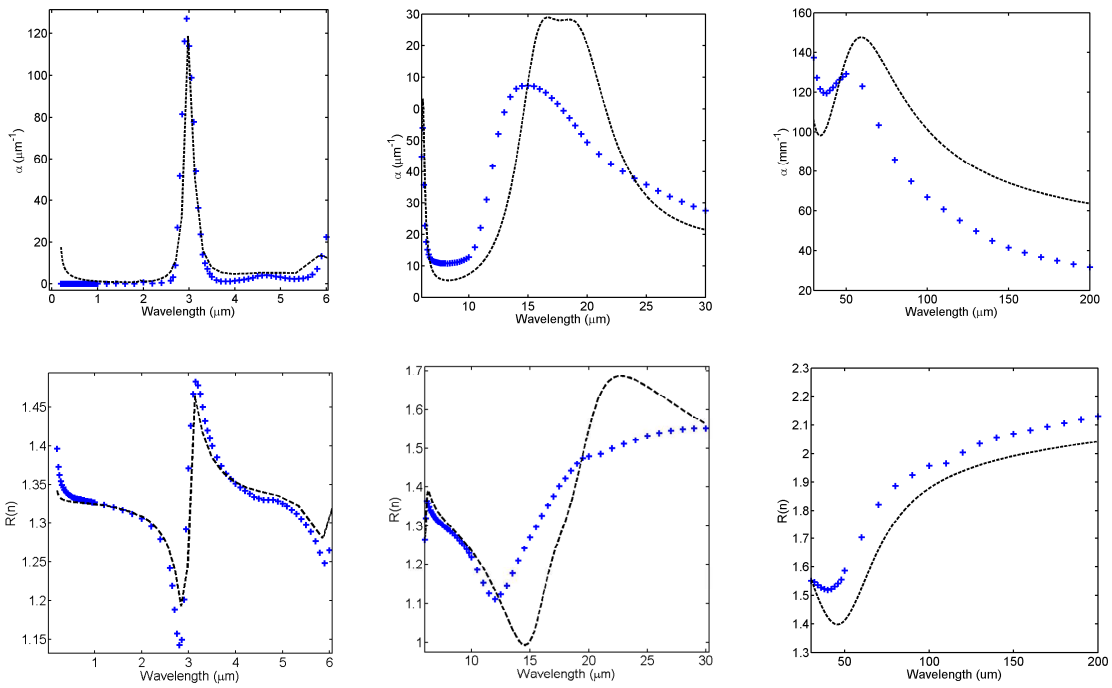


**Figure 4.7:** Comparing accepted refractive index data for water (blue crosses) [3] with simulated data using Kramers Kronig relation (dashed line)

## 4.3 Fabrication

The following section details the processes involved to fabricated top and side access devices, pictured in Figures 4.8 (a) and (b) respectively.

(a) (b)

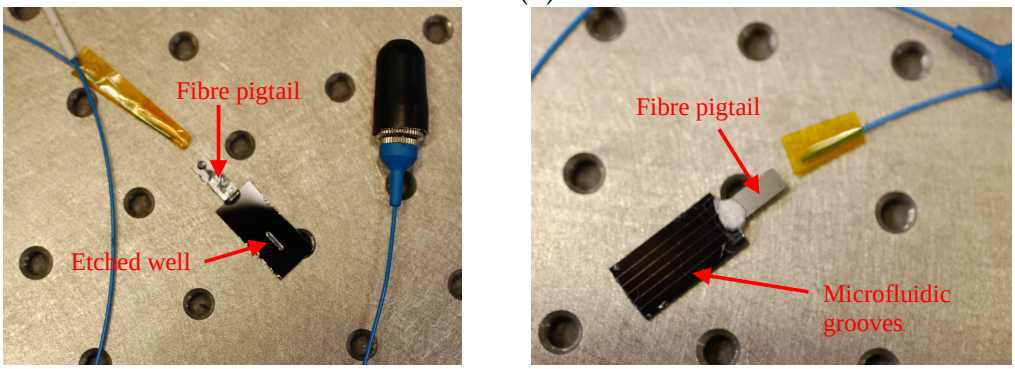


**Figure 4.8:** Photographs of (a) top access and (b) side access evanescent field geometries

### 4.3.1 Top Access

Top access of the evanescent field was primarily achieved through wet etching an FHD overclad, with 48 % concentrated Hydrofluoric (HF) acid. The etching process was monitored in real-time by fibre pigtailing the sample and interrogating the spectral response with respect to exposure time, illustrated in Figure 4.9 for the etching of a 20 $\mu$m thick overclad layer.

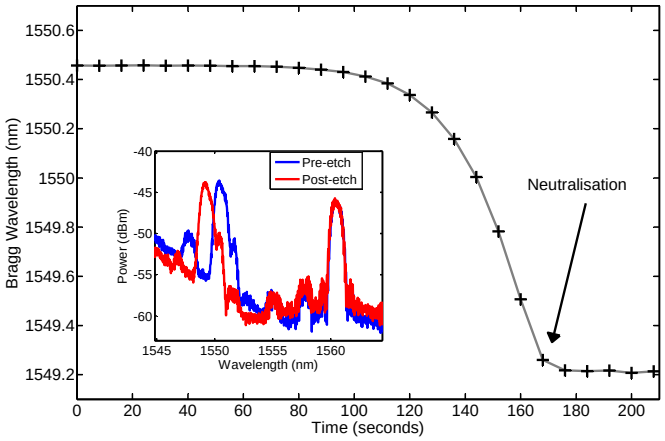


**Figure 4.9:** The etching response of a reflected Bragg wavelength that has a 20 $\mu$m overclad layer, upon exposure to HF acid

The etched device illustrated supported two single mode gratings written at a fluence of 20 kJcm$^{-2}$ and duty cycle of 0.5. The monitored etch depicts an exposed Bragg grating (at ~1550 nm wavelength) and a masked Bragg grating (at ~1560 nm wavelength). Masking of the second grating was achieved using high temperature polyimide tape with silicone adhesive. The tape was resistant to HF and allowed the fabrication of an etched well which exposed the evanescent field of one grating whilst keeping buried a temperature reference grating, pictured in Figure 4.8 (a). Etching was observed until a ~1.2 nm spectral shift was measured, at which point the etching was neutralised. The shift indicates the approximate spectral shift between the presence of all the overclad (refractive index ~1.444) being replaced by HF (refractive index of ~1.35). Etch depth was confirmed using measurements from an SEM to obtain the layer thickness and a surface profiler to obtain the etch depth.

An issue with HF etching is that it results in surface roughening, as illustrated with an Atomic Force Microscope (AFM) image in Figure 4.10 (a). Surface roughness

induces scattering, which becomes more significant the greater the index contrast between the analyte and silica. Surface roughness can be quantified in several ways including measuring the average roughness between the surface and the mean line (referred to as Ra roughness). For a concentrated HF etch this is typically 28 $\pm$2 nm compared to 3.1$\pm$0.4 nm for FHD deposited layers, illustrated in Figure 4.10 (b). In addition, it must also be noted that the density summits for the HF etched device was 190 Å$^{-2}$. This data was obtained through measuring the roughness of five different samples pre and post etching, with an AFM.

(a) (b)

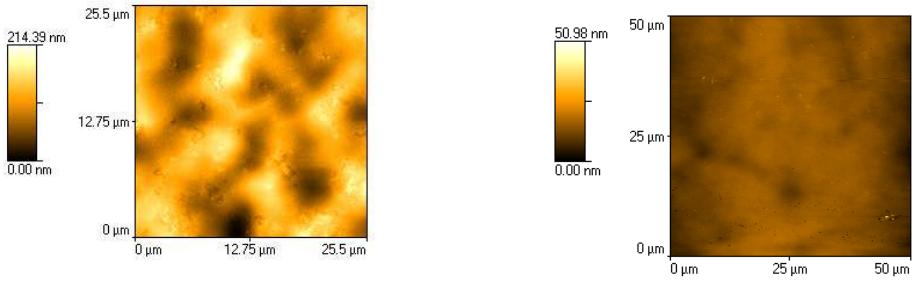


**Figure 4.10:** AFM images of (a) FHD surface post HF etching (b) FHD surface prior to HF etch

An alternative method for achieving the top access geometry is to omit the top clad deposition, during wafer fabrication. This technique has been used to fabricate sensors in this thesis and has most notably been used in Chapter 7. As the sensing surface has a roughness comparable to that of an unetched FHD layer scattering losses are reduced. To require a temperature reference grating in this geometry a capping layer of lower index than the core is required.

### 4.3.2 Side Access

To attain side access of the evanescent field a groove geometry was used, illustrated Figure 4.11. The fabricated grooves were achieved through using a dicing saw, with a 100 $\mu$m thick saw blade. All dicing structures examined during this PhD were fabricated by CIP. As the accuracy in the direct UV writing system's translation stage was of the nanometer order compared with the accuracy of the saw blade's translation stage which was micrometer order, the devices were fabricated by firstly cutting grooves into the substrate and then subsequently direct

UV writing.

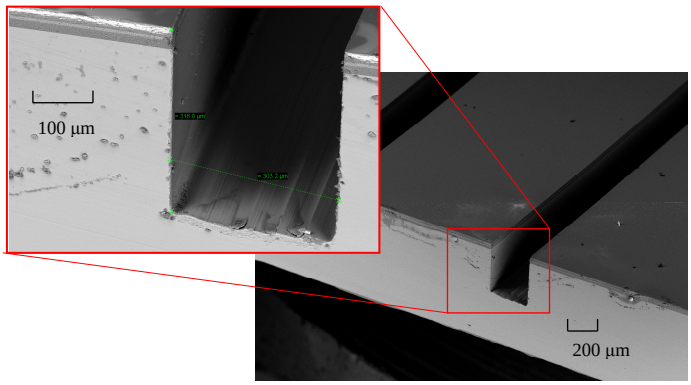


**Figure 4.11:** SEM images of the side access groove geometry

When cutting grooves into silica-on-silicon wafers the quality of the surface roughness is an important parameter to quantify, just as with wet etched devices. It is understood that surface quality of the side walls is dependent upon the cutting conditions including feed-rate, depth of cut, coolant used and coolant flow rate. Whilst the optimisation of surface quality as a result of cutting parameters is still subject to further investigation it was recorded that typical grooves, illustrated in Figure 4.11 have an Ra value of 141.3 nm and a summit density of 13 $Å^{-2}$. Interestingly, it has been observed that post-cut processing can significantly reduce surface roughness. It has been observed by the author the rapid thermally annealing the samples prior to DGW at 1100 $^{o}$C for 10 seconds reduces the Ra value to 9.2 nm, whilst the Ra reduces, the summit density remained at a comparable level.

An advantage of the groove geometry is that it is an inherent platform for microfluidic operations. This proof of principle device had considered channels 300 $\mu$m thick, however, it must be noted that single cuts from 10 $\mu$m thick blades are also possible, to achieve microfluidic grooves of smaller dimensions. The side access geometry also has the benefit of utilising a combination of S-bends and gratings, such that gratings can be placed at different distances from the edge of the groove. If the different gratings are different distances from the edge, their modes will have different penetration depths into the analyte. This information could be used to interrogate refractive index gradients on the surface of the groove walls.

The sensitivity of a typical groove based sensor is illustrated in Figure 4.12 (a),

which compares the empirical data to simulated data using FIMMWAVE software. For these sensitivity calibration measurements different silicone aliphatic and alicyclic based hydrocarbon refractive index oils were used. The device was written with a fluence of 16 kJcm$^{-2}$ and has a duty cycle of 0.5. Device fabrication was achieved through writing a series of gratings successively closer to the leading edge of the groove, using S-bend waveguides, as schematically illustrated in Figure 4.1 for two gratings. The written device consisted of seven gratings, each one spaced 2 $\mu$m closer to the groove edge. The maximum spectral response (analyte refractive index change from 1 to 1.44) at respective distances, $\delta$ is illustrated in Figure 4.12 (b). It must be noted that the seventh grating is not present as it was written off the edge of the groove. In addition, the relative positioning of all the gratings has been approximated by best fitting simulation to empirical data. This approximated the distance, $\delta$ of the most sensitive grating to be 1.5 $\mu$m from the groove edge.

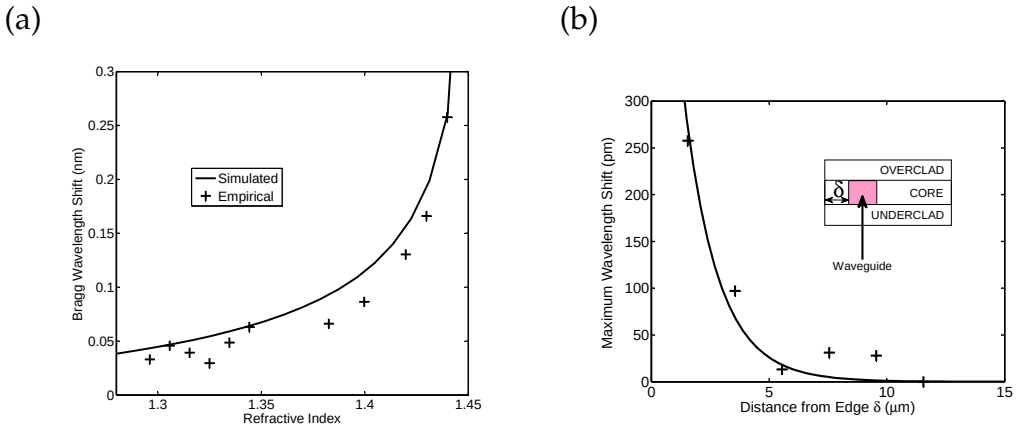


**Figure 4.12:** A side access device depicting the typical sensitivity of an exposed Bragg grating

The sensitivity of the fabricated devices detailed in this section can be enhanced through manipulating parameters during fabrication, which shall be termed 'basic' parameters, or through the use of enhancement layers. To efficiently understand these parameters the following work investigates their effect using computer simulation.

## 4.4 Modelling

Before effectively optimising the developed sensors, through modelling, it is necessary to appreciate the commercial application for these devices. The (bio) chemical sensor market is composed of emerging market pushes such as homeland security and environmental monitoring, in addition to traditional sectors such as food and beverage, medical diagnostic and pharmaceutical. Homeland security is one market push, which follows recent concerns over bioterrorist attacks. In addition, water engineering is receiving heightened interest by government bodies, including those in the UK. This is mainly due to the recent global sense of responsibility towards climate change. As water is likely to be a common denominator for many of these sensors, device sensitivity has been optimised to operate with aqueous targets (targets with a refractive index around 1.33 - i6x$10^{-4}$ [7]).

In general, two types of evanescent field sensors commercially exist, ones that are optimised for distinguishing bulk changes and ones that can distinguish surface changes. Bulk sensing, also called homogenous sensing takes into account the whole evanescent tail, whereas surface sensing does not. Surface sensing is encountered when a chemo-optical transduction layer, also known as chemical interface, is used to enhance sensitivity by binding molecules of interest to the surface. Sometimes such layers are comparable to the penetration depth of evanescent field. However, in other instances the surface sensing receptor molecules are lower than tens of a nanometer. Both surface sensing and bulk sensing have been modelled by the author. The quantification of bulk sensitivity shall be defined as an analyte's bulk refractive index change from 1.3 - i6x$10^{-4}$ to 1.35 - i6x$10^{-4}$. For surface sensitivity only a 10 nm layer shall be considered as having this refractive index change.

The following simulations utilise the commercial mode solver FIMMWAVE to consider a 5 $\mu$m square waveguide of index contrast $5\times10^{-3}$, defined in a core layer of thickness 5 $\mu$m. The refractive index of the cladding layers are taken to be 1.444 and the core layer 1.445.

It must be noted that due to silica-on-silicon samples being consolidated at high temperatures they have an inherent compressive stress in the silica layer, which results in an anisotropy in index due to the stress optic effects. The compressive stress, which is a result of the wafer fabrication, can be approximated to be $\sim$180

MPa (calculated in Chapter 6). Using Hooke's Law [104] [105] this relates to compressive strains of $2.9\times10^{-3}$ for the axes parallel to the silica-silicon interface and a tensile strain of $8.2\times10^{-4}$ for the axis perpendicular to it. Considering the stress-optic effect [106] [107] for silica, this corresponds to a refractive index increase of $2.8\ \times10^{-3}$ and $4.8\ \times10^{-3}$, for TE and TM polarisations respectively. It must be noted that the following simulations will have an associated offset for this property, whose magnitude will vary depending upon fabrication conditions.

## 4.5 Bulk Sensing

The bulk sensitivities of the two basic geometries are represented in Figure 4.13. The sensitivity of the top access geometry is seen to be greater than that for side access, which is a result of the refractive indices of the core and clad not being matched. For the top access geometry the material opposite to the analyte relative to the waveguide (underclad) is lower in refractive index than that in the side access geometry (core layer). It is understood that this acts to pull the mode power into the silica to a greater extent, thus decreasing sensitivity.

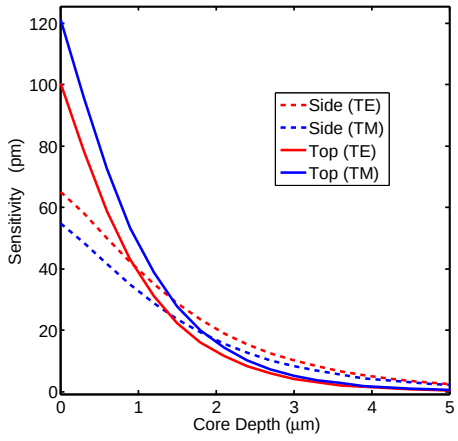


**Figure 4.13:** Simulated comparison of side access and top access sensitivities.

Another feature of Figure 4.13 is that for the top access geometry the TM polarisation has a greater sensitivity than TE and this trend is switched for side access geometry. This feature can be understood by considering the dimensionless slab waveguide analysis made in Chapter 2. Considering Figure 2.4 it is observed that for the fundamental modes the TE polarisation demonstrates a higher normalised propagation constant than the TM mode. If the TM mode has a lower normalised

propagation constant it must have a larger proportion of its power in the analyte, thus be more sensitive to it changing. The reason why this trend flips i.e. TE being most sensitive polarisation for the side access case is that relative to the analyte there has been a $90^o$ rotation in the geometry.

The following subsections consider how bulk sensitivity can be optimised for both side access and top access geometries.

### 4.5.1 Manipulating Basic Parameters

The following work examines variations in 'basic' parameters to optimise the sensitivity of the native device. What are meant by basic parameters are variables that are relatively simple to manipulate during the established fabrication techniques, previously discussed. These parameters include Bragg wavelength, fluence used to write the waveguide and the refractive index of the FHD layers. The term basic parameter is used to distinguish later optimisation regimes, which use enhancement layers and consider the dispersion characteristics of a measurand.

One of the most fundamental questions when considering basic parameter manipulation is 'what is the optimal wavelength to use?' Although this shall be tackled in a later section in terms of dispersion the following analysis examines sensitivity versus wavelength for a constant refractive index variation. The device sensitivity is expected to increase with the wavelength of guided mode because the guided mode is expected, from theory, to be less confined to the core. This is indeed observed in Figure 4.14, which simulates the sensitivity of a top access device between 600 nm to 2000 nm wavelengths.

For longer wavelengths the guided mode is understood to have a greater penetration depth into the measureand and thus the sensitivity is greater. Although Figure 4.14 indicates that to achieve greater sensitivity longer wavelengths should be used, the following modelling sets the wavelength at the 1550 nm, as DGW fabrication has been optimised around this wavelength.

Aside from wavelength, the refractive index contrast of the waveguide is perhaps one of the most straight-forward parameters that can be varied. As discussed in Chapter 3, the induced refractive index variation is dependent upon fluence. The index change is usually of the order $5x10^{-3}$, but can reach up to $2x10^{-2}$. Device

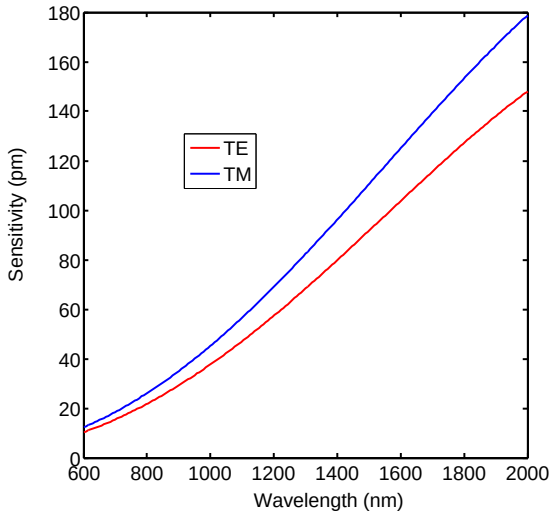


**Figure 4.14:** Dependence of sensitivity on wavelength for the top access geometry device

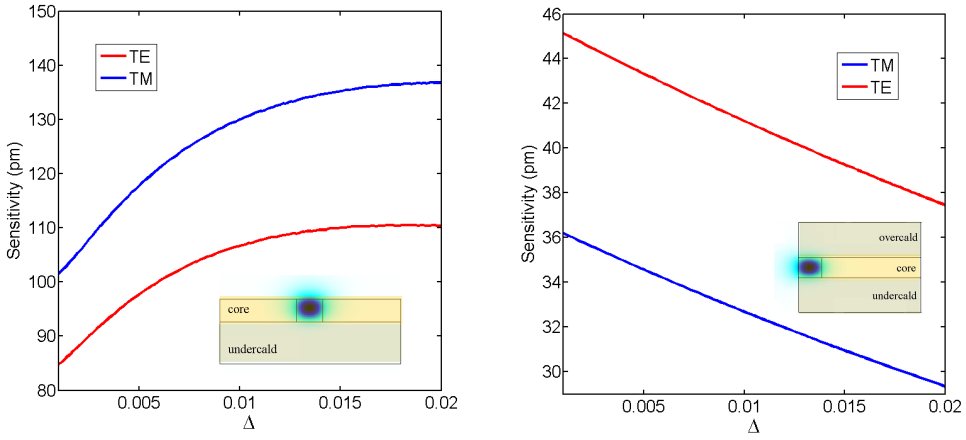


**Figure 4.15:** Sensitivity dependence on waveguide index, $\Delta$, for the top access and side access geometries (bulk analyte refractive index change from 1.3 to 1.35)

sensitivity with respect to the refractive index change in the channel waveguide for both top and side geometries was simulated, presented in Figure 4.15. The results of which are somewhat counterintuitive, as it may be expected that increasing the index of the core means that the mode is more tightly confined within it thus reducing the sensing evanescent tail. Indeed this is the trend observed for the side access geometry. However, for the top access geometry the opposite is true! The reason for this phenomenon can be understood by comparing Figures 4.16 and 4.17.

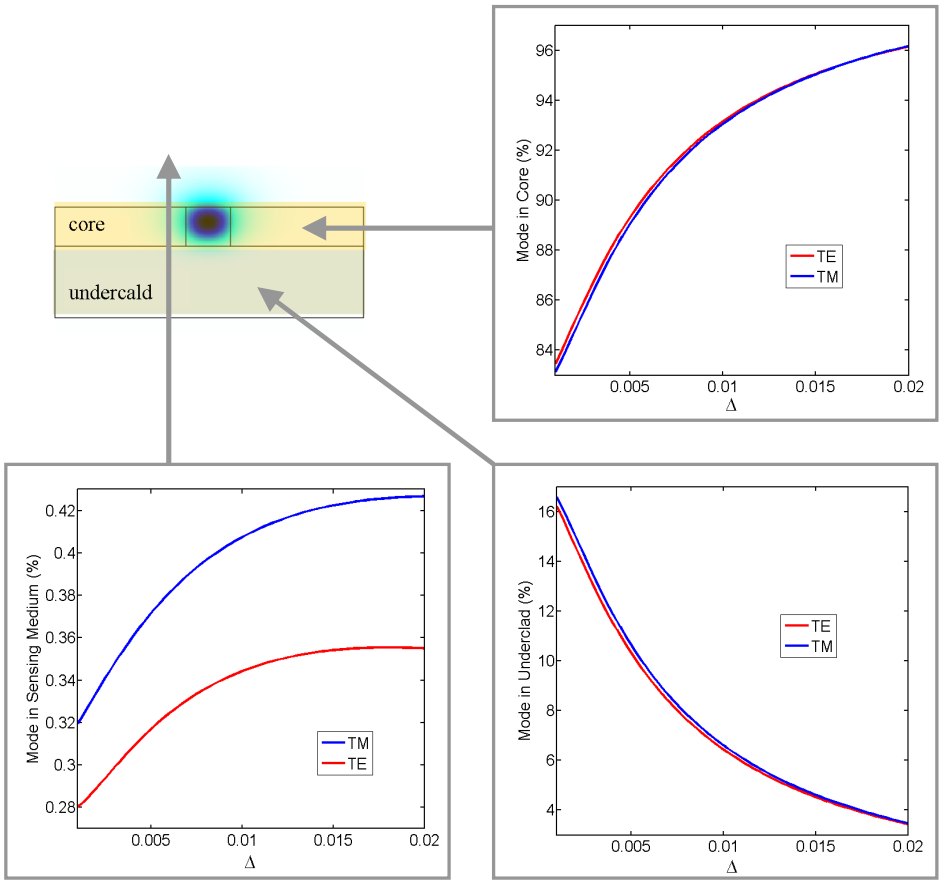


**Figure 4.16:** The distribution of a mode's power with increased values of waveguide index for the top access geometry

For the top access geometry, shown in Figure 4.16, it can be observed that increasing the index of the written waveguide pulls the power of the mode up from the underclad and more towards the sensing region. This results in the higher index changes for the top access waveguides displaying a greater sensitivity. For the side access geometry, shown in Figure 4.17, the core layer is retreating into the bulk of

the device, which pulls the mode into the sensor. For waveguides of larger index changes this effect is accentuated and hence a lower sensitivity trend is observed.

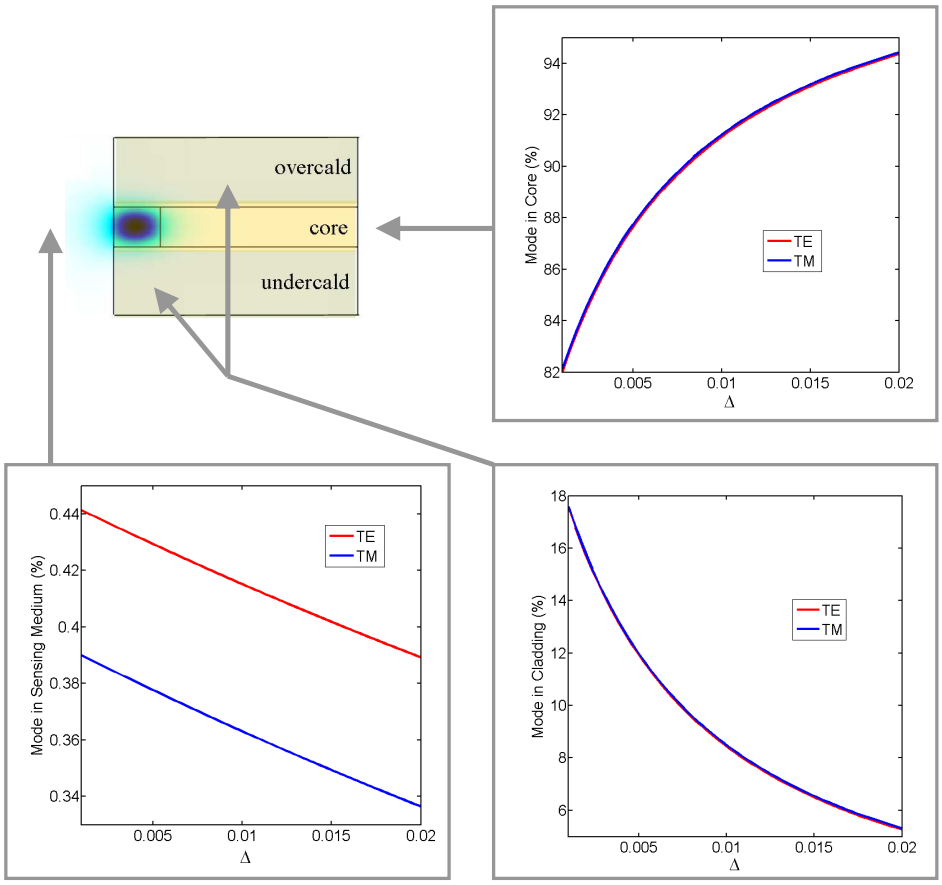


**Figure 4.17:** The distribution of a mode's power with increased values of waveguide index for the side access geometry

The relative refractive indices of the FHD layers are the final 'basic' parameters that shall be considered. The general silica-on-silicon platform fabricated attempts to match the refractive index of the deposited silica layers. This is primarily achieved to efficiently couple light from a single mode fibre into the UV written structures. However, device operation will still occur for non index matched layers. Figure 4.18 shows the variation of device sensitivity as a function of the refractive index of the core layer, for top access and side access geometries respectively.

From Figure 4.18 it can be observed that the sensitivity of both the side and top access geometries increase, as the refractive index of the core increases relative to the cladding layers. It is also noted that the top access geometry can achieve a higher sensitivity than the side access regime, for the refractive index range considered. In addition whilst the top access geometry has an optimum sensitivity

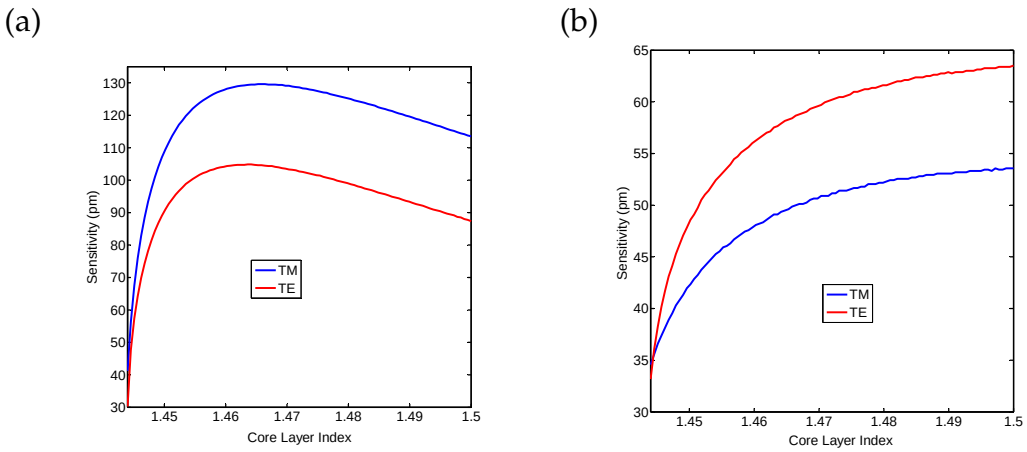


**Figure 4.18:** The simulated sensitivity of a device as a function the refractive index of the core layer, for (a) top access and (b) side access geometry.

for the considered range the side access geometry prefers increasingly large core refractive indexes.

Figure 4.19 simulates the sensitivity of the device with respect to the refractive index of the underclad, in the top access geometry. As expected lowering the refractive index of the underclad increases the sensitivity of the device. However, it must be noted that practically very few materials, which are solid at room temperature exist with a refractive index lower than silica glass.

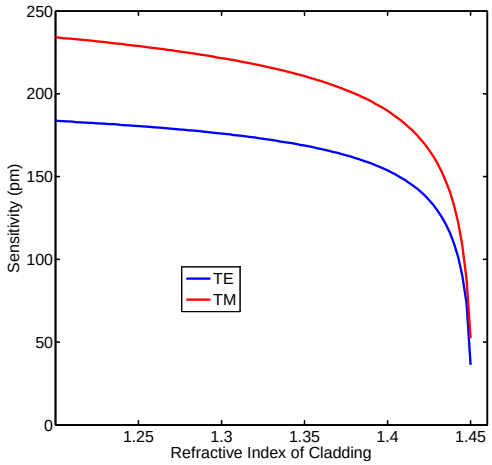


**Figure 4.19:** Manipulation of underclad refractive index to increase device sensitivity

In summary of the basic variable simulations considered, the fabrication requirements for the top access geometry should adopt FHD layers with low refractive index underclad and a high refractive index core layer. During UV writing the top access devices should be written with high fluence, to maximise the refractive

index change of the written waveguide. It must be noted that for the top access geometry the high index core layer has an optimum refractive index, dependent upon the underclad refractive index and the index and dimensions of the written waveguide. For the side access geometry the FHD layers again must have low refractive index cladding layers and a high refractive index core layer. It must be noted that unlike the top access geometry, the index of the core has no optimum value over the viable range considered for device fabrication. During UV writing the side access devices a low fluence should be used, to gain minimum index change in the written waveguide. This is counter to what is required for optimising the top access geometry. The following subsections shall consider the addition of dielectric and metal enhancement layers to further increase device sensitivity.

### 4.5.2 Dielectric Enhancement Layers

Enhancement layers can be used to increase the sensitivity of the native device by manipulating the power distribution of the guided mode. The concept behind dielectric enhancement layers is that a thin layer (~50 nm) with a higher refractive index than the core is deposited upon the sensing surface and acts to pull the power of the mode up into the analyte. As the deposited layer is thin it does not pull out all the power from the waveguide [108].

(a) (b)

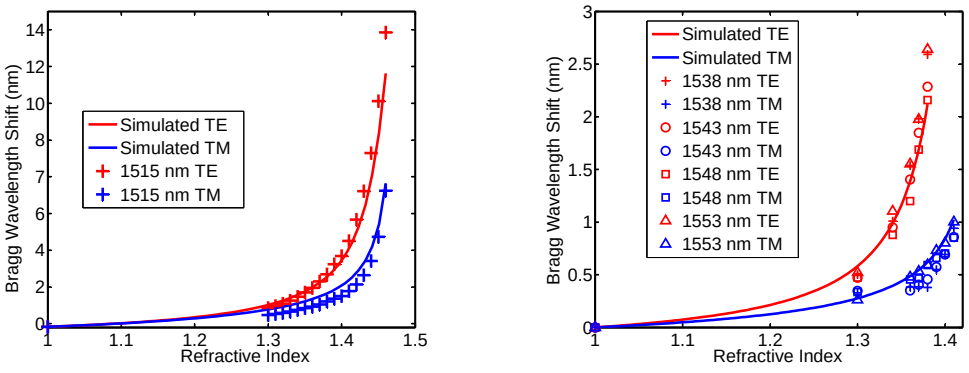


**Figure 4.20:** A comparison between simulated and empirical data for (a) 30 nm titania enhancement layer on an over-etched device (b) 55 nm layer of GLS enhancement layer on a regularly etched device

Figure 4.20 (a) and (b) indicate the sensitivity enhancements made from the deposition of titania and gallium lanthanum sulphide (GLS) respectively, upon top

access devices. It must be noted that the titania enhancement layer is deposited on an over-etched sample, meaning the wet etch has removed the overclad layer and part of the core layer. This is opposed to a regularly etched device which removes the overclad only. Figure 4.21 simulates the over-etching of a native device in the presence and absence of a 30 nm titania enhancement layer.

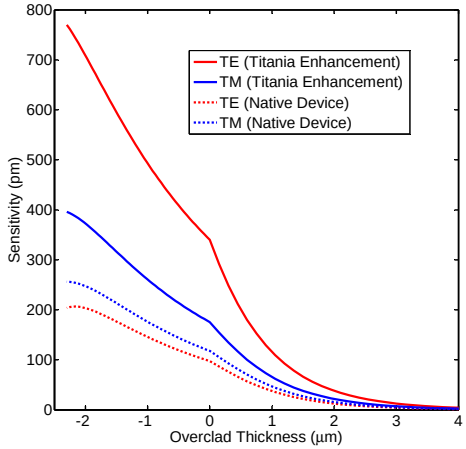


**Figure 4.21:** Simulation of the sensitivity of a native device and one with 30 nm of titania deposition as a function of device etch depth

The fabricated device, presented in Figure 4.20 (a), has been over-etched, such to allow a $\sim$3 $\mu$m thick core layer to remain. As over-etching enhances sensitivity, a thinner deposition layer can be used to achieve the same enhancement compared to a device that has not been over-etched. This can be appreciated by comparing Figure 4.20 (a) and (b). Both GLS and titania have comparable refractive indices after sputtering. However, to achieve a comparable sensitivity, a larger deposition is required in the device that has not been over-etched. It will also be noticed from Figure 4.20 (a) and (b) that this results in the mode being sustained in the core for a higher refractive index of analyte.

The following simulations shall consider titania enhancements for top access devices that have not been over-etched. It is expected that similar trends will exist for GLS and other potential dielectric enhancement layers of comparable refractive index.

Titania exist in a number of crystalline forms [109], in its amorphous form the refractive index of titania tends to be lower due the presence of oxygen-deficient sites [110]. It is known that sputtered titania can have a refractive index ranging from 1.90 to 2.56, depending upon the associated annealing temperatures [111].

For the purpose of the following work it is assumed that the refractive index of titania is 2.15.

Re-examining Figure 4.20 (a) and Figure 4.21 it can be observed that sensitivity is larger for TE than for TM polarisations, which is conversely true in the native device. The sensitivity of TE polarisation at index overlays of 1.46 is 3.70 $\times 10^5$ pmRIU$^{-1}$ and for 1.3 overlays the resolution is 1.13 $\times 10^5$ pmRIU$^{-1}$.

(a) (b)

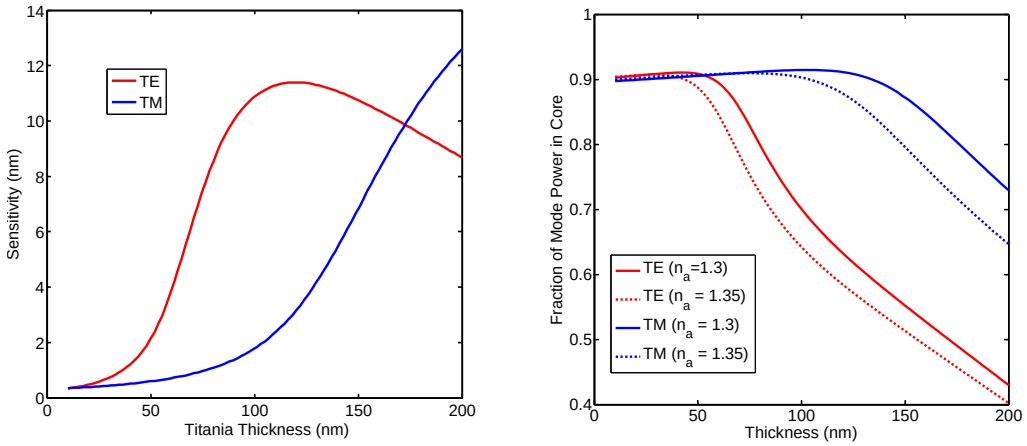


**Figure 4.22:** The variation in (a) sensitivity and (b) fraction of mode in the core with varying thicknesses of titania enhancement layer.

Varying titania thickness showed sensitivity to reach an optimum at ~100 nm for TE and greater at TM, Figure 4.22. However, care must be taken when considering this. If sufficient amount of mode is pulled from the guiding channel the sensor will no longer operate. From Figure 4.22 it can be seen that at thicknesses greater than 50 nm the power of the mode is significantly displaced out of the guiding core, which conforms to the TE mode being lost for analyte refractive indicies higher than 1.38 in Figure 4.20 (b).

As previously mentioned titania can have a refractive index ranging from 1.90 to 2.56 depending upon the annealing temperature used during fabrication. Figure 4.23 examines device sensitivity as a function of this range for a 30 nm thick titania enhancement layer.

So far only dielectric enhancement layers have been investigated. However, metallic enhancement layers also offer the potential to increase device sensitivity. Hence, the following subsection examines the potential of metallic enhancement layers.

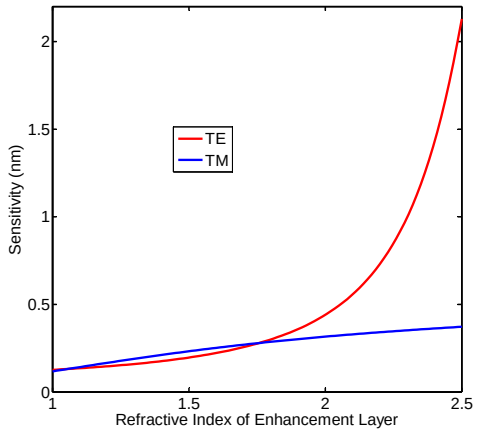


**Figure 4.23:** Increasing sensitivity with a dielectric superstrate of thickness 30nm

| Metal | n | $\alpha$ ($\mu$m$^{-1}$) |
|---|---|---|
| Gold | 0.5283 | 79.53 |
| Silver | 0.4528 | 76.25 |
| Aluminum | 1.3754 | 129.27 |
| Nickel | 3.3211 | 55.76 |

**Table 4.1:** The refractive index assumed for the four metal used for enhancement layer simulations, indicating there real part of refractive index n, and the Lambert absorption coefficient $\alpha$, at 1550 nm wavelengths of light [7]

### 4.5.3 Metal Enhancement Layers

The simulations undertaken to anlyse the sensitivity enhancement made by metallic enhancement layers considered four metals: gold, silver, aluminium and nickel, with refractive indices as given in Table 4.5.3. As expected from theory the TE mode shows no sensitivity to an analyte, as the evanescent field does not exist on both sides of the layer for the refractive indices considered. Hence, the following data only displays the sensitivity for TM modes.

Figure 4.24 shows (a) the surface sensitivity and (b) the associated absorption with the four investigated metal enhancement layers. The enhancement effects appear to be equal for all metals, $\sim 3.6 \times 10^3$ pmRIU$^{-1}$. However, nickel does show the greatest sensitivity but this is at the expense of a large absorption coefficient. Just as with dielectric enhancement layers, the large real refractive index part of the nickel acts to attain a larger sensitivity. What can be concluded from the analysis is that the largest sensitivity enhancement was achieved by the metal with the

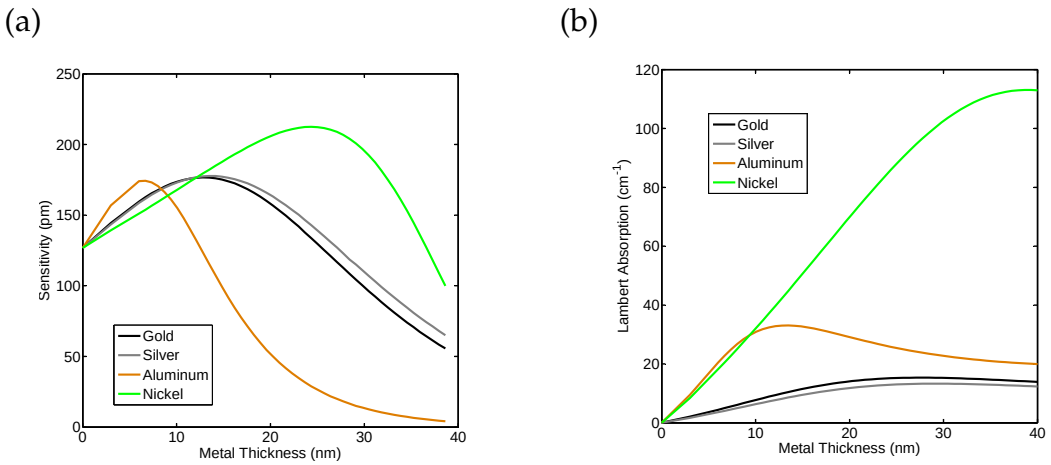


**Figure 4.24:** The effect of enhancement metallic layers, of TM mode for varying thicknesses, on (a) sensitivity and (b) absorption.

greatest real refractive index part, in this instance nickel. However, it must be noted that the most prevalent material used for plasmon based sensing is gold, mainly due to its resilience, stability and known surface chemistry in the context of functionalisation [97].

In comparison to the dielectric enhancement layers, metal enhancement layers increase bulk sensitivity by a much small fraction. However, due to the nature of the plasmon-hybrid mode concentrating a significant amount of its power at its surface its potential for surface sensing needs to still be considered.

## 4.6 Surface Sensing

Surface detection is becoming increasingly important in chemical sensing due to enhancement that is achievable using surface functionalisation. This section involves the modelling of surface functionalisation by considering a 10 nm layer on the surface of the device, which is the typical order of magnitude of a layer of virus adhering to an antibody selective surface. Device sensitivity will again be optimised to operate with aqueous targets. Sensitivity being defined as the index change from 1.3 to 1.35 at the 10 nm surface layer only, i.e. the remaining bulk remains at a real part refractive index of 1.3.

### 4.6.1 Enhancement Layers

Metal and dielectric enhancement layers have already been considered for the case of bulk sensitivity. Figure 4.25 compares the surface sensitivity of a titania enhancement layer to a gold enhancement layer. It must be noted that the sensitivity of TE polarisation with a gold enhancement layer is 0. The reason for which has been explained in the previous chapter. As a result the author has omitted the TE plot from the simulated Figure 4.25. It is observed that the sensitivity of TE mode for the titania enhancement can achieve higher sensitivities than the TM supported mode for both gold and titania enhancement layers. The TE supported mode with a gold enhancement layer displays no sensitivity. Interestingly, this polarisation could be used to locally temperature reference the device.

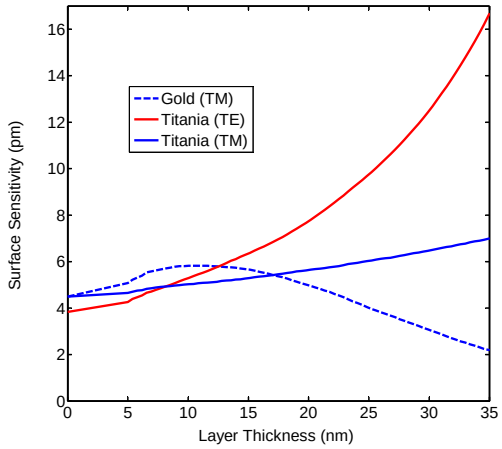


**Figure 4.25:** A comparison between surface sensitivity enhancements of gold and titania

For effective surface functionalisation the surface topology of the sensing surface needs to be understood. This has already been achieved to some extent in the fabrication section of this chapter. However, in addition to general surface roughness resulting from HF etching a more structured topology exists over the Bragg grating.

### 4.6.2 Surface Topology

Mapping the topology of a HF etched device, with an AFM and SEM an unusual rippling effect was observed, illustrated in Figure 4.10.

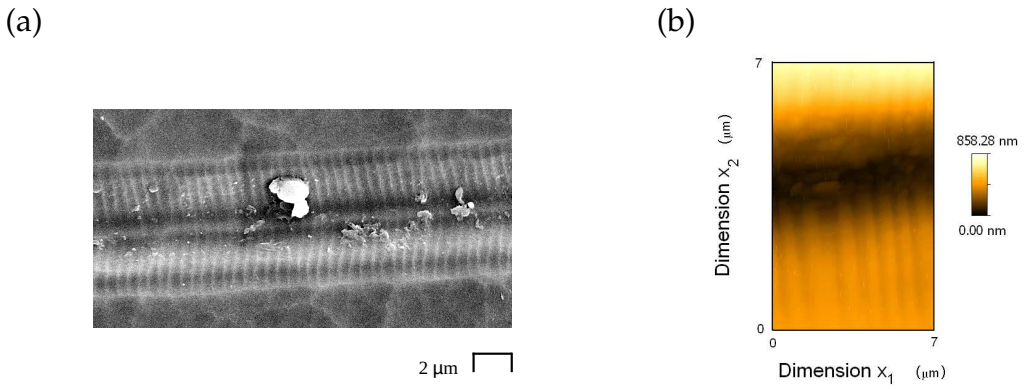


**Figure 4.26:** The 'rib effect' of the accelerated grating written area using (a) SEM and (b) AFM techniques

The ripple consists of a central dip of ~800 nm depth and periodic ripples comparable to the period of the written grating.

Another consideration for transducer platform optimisation is engineering the Bragg gratings such that they give optimum sensitivity. In general Bragg gratings of longer period (longer Bragg wavelengths) will give greater sensitivity, as seen in Figure 4.14. However, in addition dispersion of the analyte ought to also be considered.

## 4.7 Spectral Regions of Interest

Dispersion can inferred from absorption data of an analyte. The following experiments were carried out to acquire absorption data for methanol, ethanol, distilled water and Bovine Serum Albumin (BSA), from 500 nm to 2500 nm wavelengths. The substances chosen are commonly encountered during device cleaning/sensing.

The absorption data was obtained from transmission spectra captured by a UV/IR/Vis double beam spectrophotometer, for two different transmission lengths through the measurand. The chemical under investigation was placed in a crucible cell, illustrated in Figure 4.27. As the cell in the spectrophotometer has four interfaces, four reflections result that diminish the transmitted signal.

Using two different transmission spectra $T_{L1}$ and $T_{L2}$, corresponding to two different path lengths, $L_1$ and $L_2$, the extinction coefficient $\kappa$ was obtained, using

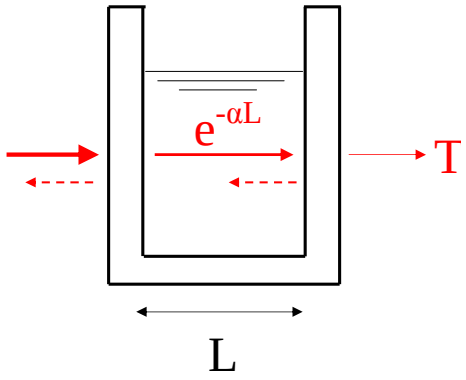


**Figure 4.27:** A schematic indicating the absorption and reflections involved for an arbitary size crucible, of size L

Equation 4.7.

$$\kappa = \frac{\lambda}{4\pi(L_2 - L_1)} \ln\left(\frac{T_{L1}}{T_{L2}}\right) \tag{4.7}$$

Due to high absorptions encountered at IR wavelengths for the measurands the two thicknesses were required to be less than 1 mm.

(a) (b)

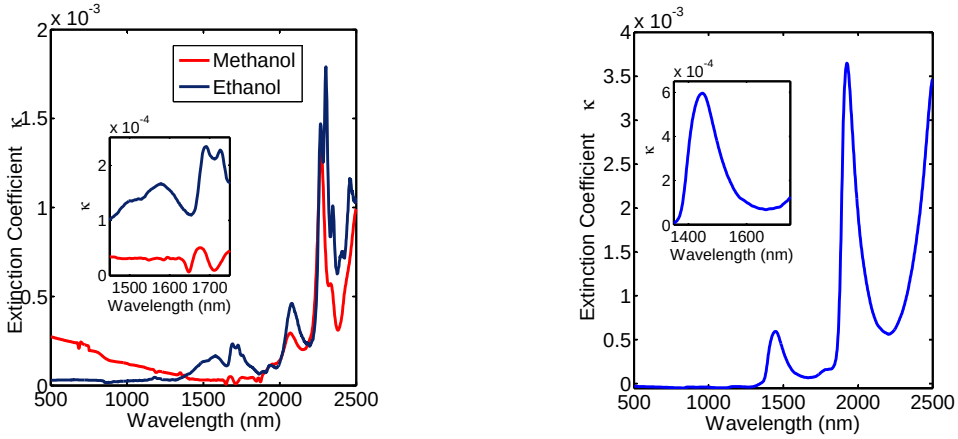


**Figure 4.28:** Extinction coefficient spectra for (a) methanol and ethanol and (b) BSA and water

Methanol, ethanol and water all have distinguishable absorption peaks, the absorption spectra for solvents represented in Figure 4.28 (a) and BSA and water spectra Figure 4.28 (b). Interestingly, BSA and water have the same absorption spectra and are dominated by the large OH absorption band at 1400 nm. Identifying spectral region of interest can also be applied to a plethora of other chemicals,

depending upon the specific demands of the system.

Currently the smallest resolvable refractive index change with our developed sensors is around $10^{-6}$. From Equation 4.6 it can be inferred that such a refractive index change would result from an absorption peak of 100 $m^{-1}$, or extinction coefficient of the order of $10^{-7}$. Hence, absorption peaks of this magnitude should be spectrally resolvable.

A challenge all chemical sensors face is the ability to differentiate the infinite number of potential analytes which exist. So far cleaning based fluids have been considered, which would be required to flush the sensing system between sample runs.

The most likely operation of the developed sensors will be in an environment where nearly all the potential measurands are understood, e.g. components of human blood. Depending upon application this repertoire will vary, hence the following work gives an implementation example of the Kramers-Kronig algorithm, given in Appendix C. To which end for a given operational system this would be implemented upon all the expected measurands.

The following work shall simulate the dispersion of the standard refractive index oils composed of Silicone Aliphatic and Alicyclic, Hydrocarbons, which have been used to characterise the sensitivity of the sample. It may have been noticed in Figure 4.20 (b) that different Bragg wavelengths show different sensitivity responses to the applied refractive index oil. The absorption spectra of a 1.4 refractive index oil is given in Figure 4.29 (a) for spectral range spanning from 1300 nm to 1800 nm. Fitting a Lorentzian curve to this data the dispersion can be inferred using the KK algorithm, illustrated in Figure 4.29 (b).

Figure 4.30 overlays the Bragg wavelength shift, obtained from the data in Figure 4.20 (b), to the dispersion characteristics of 1.4 refractive index oil. As can be observed, the sensitivity of the Bragg wavelengths coincide with the dispersion characteristics of the analyte sensed, indicating the potential usefulness of the developed algorithm.

The work considered so far has been rightfully aimed towards attaining high device sensitivity. High sensitivity is one aspect that the DGW chemical sensors must posses in order for them to achieve an economic impact. Another aspect they must

(a) (b)

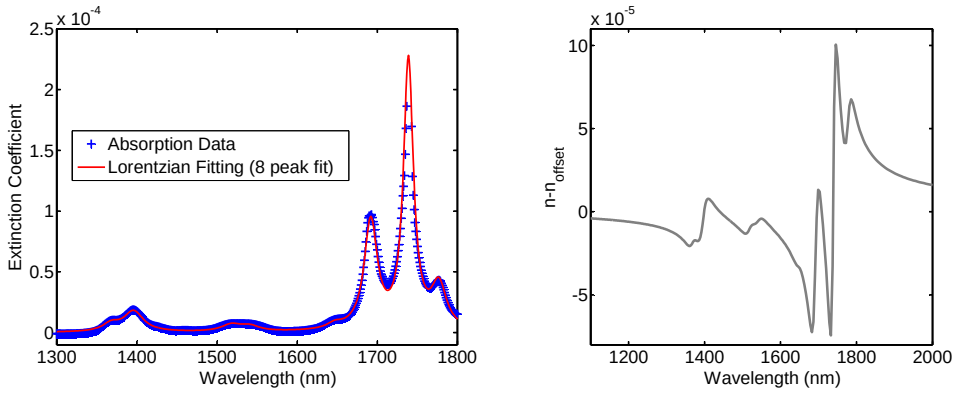


**Figure 4.29:** The spectral absorption (a) and relative dispersion (b) of a 1.4 (silicone aliphatic and alicyclic, hydrocarbon) refractive index oil

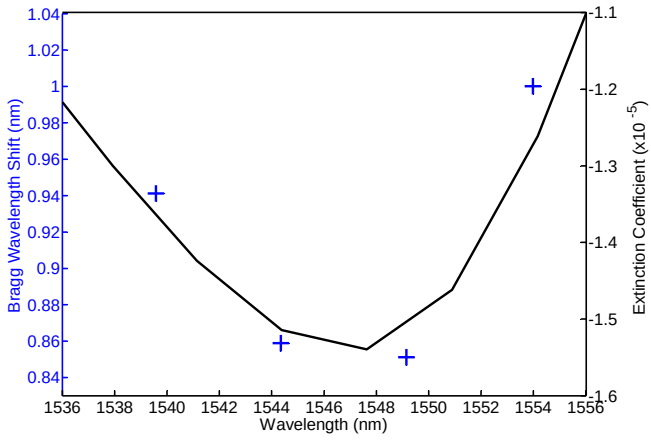


**Figure 4.30:** The Bragg wavelength shifts of a top access sensor, with 55 nm of deposited GLS enhancement cross referenced against the relative dispersion of the analyte that induces the Bragg shift

possess is repeatability. The previous sections have attained the high sensitivity required to make the devices competitive, the following work considers ensuring device repeatability.

## 4.8 Wetting Effect

The ability of a planar Bragg grating sensor to produce repeatedly consistent results is of great importance to its commercial success. However, it was observed that the cleaning process affects the repeatability of measurements of the sensor. Through alternating the cleaning process between successive tests device repeatability can be enhanced.

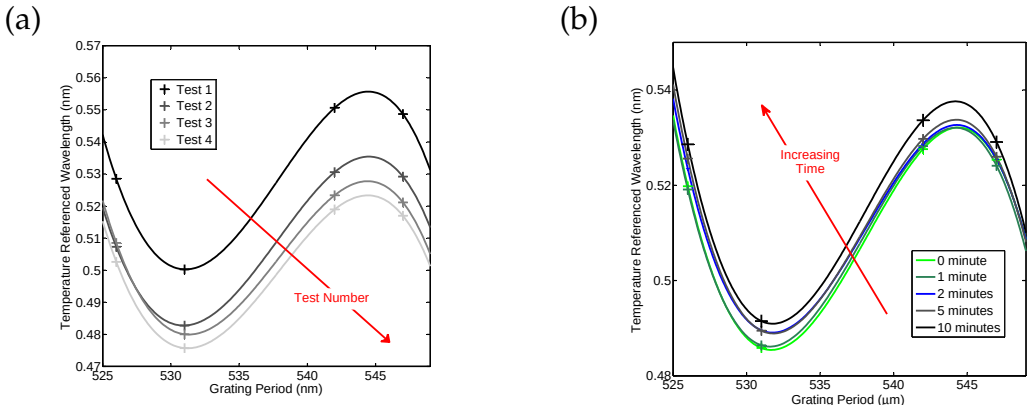


**Figure 4.31:** The cleaning drift as a response of (a) the sequential order of test cleaning and (b) the time between subsequent tests

The following set of experiments considers a HF etched device with four exposed sensor gratings and a buried temperature reference grating. The exposed gratings have no enhancement substrate deposited upon them. The cleaning method followed in the following experiments involves removing the measurand with, IPA and acetone between each successive test. A negative drift in the dispersion fingerprint with successive test number was observed, illustrated in Figure 4.31 (a). Each signature can be observed to shift by several standard deviations.

The time between the sensor being cleaned and the next test beginning was varied in a random fashion, such that the trend observed in test number (Figure 4.31 (a)) would not distort a trend with respect to this variable. Figure 4.31 (b) indicates that increasing the time between successive cleans, results in a positive drift in Bragg wavelength shift, for the whole dispersion fingerprint.

It is believed that the acetone and IPA, used to clean the sensor, contain traces of water. The IPA and acetone may deposit a layer of water on the sensor, each time it is cleaned. The longer the drying time, the more water will evaporate. Likewise, if the timing between repeated results is small, in the order of several minutes, then the deposited water may not be getting sufficient time to evaporate.

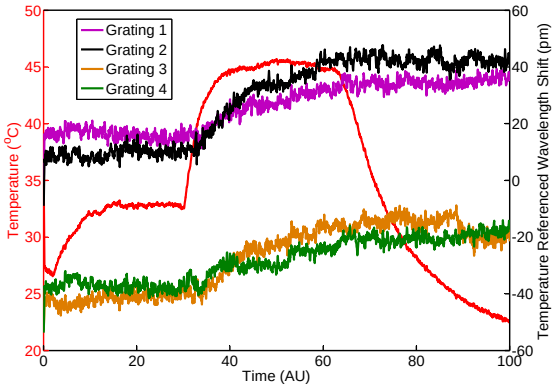


**Figure 4.32:** The effect of heating the sensor after cleaning for the four sensor gratings

Heating the sensor corroborated this theory, as illustrated in Figure 4.32. For this experiment a sensor cell was cleaned using Acetone, IPA and distilled $H_2O$ as in the previous experiments. The sensor was heated up to 43 $^oC$ stabilised for 30 minutes and then cooled down to 23 $^oC$, Figure 4.32. The cleaning drift was removed and subsequent heating cycles did not alter the drift in such a manner.

## 4.9 Conclusion

The sensitivity of a DGW evanescent field based refractive index sensor has been enhanced through computer simulation and experimentation. Exposure of the evanescent field has been investigated using top access and a novel side access geometry. If the index of the core and cladding layers are perfectly matched at the device's operational wavelength and the waveguide structure has a $90^o$ translation symmetry then the sensitivities of both geometry are expect to be equal. The sensitivity of this index matched geometry can be enhanced through manipulating the basic fabrication parameters. Top access devices display optimum sensitivity for low index underclad and high index core layers in addition to high index contrast waveguides. Side access devices show high sensitivity for high index core layers

and low index cladding layers in addition to low index contrast waveguides. It must be noted that the high index core layer for the side access device has no optimum index for realistic depositions (refractive indices less than 1.5). However, the top access geometry does and is dependent upon the other parameters considered.

Higher operational wavelengths have a greater penetration depth associated with them and as such display a greater sensitivity. In addition when considering the spectral positioning of Bragg gratings, not only is it important to place them at higher wavelengths but also to take into consideration the dispersion of the measurand. Using absorption data of a measurand the optimum spectral placement of Bragg gratings can be achieved for effective measurand discrimination.

Enhancement layers can be used to increase the sensitivity of a native sensor. Both metal and dielectric enhancement layers were investigated, for both bulk and surface sensing. Dielectric enhancements typically display greater sensitivities than that of metals. It must be noted that when considering metal enhancement layers TE polarisations lose all sensitivity to the analyte. This is a result of the boundary conditions dictating that the field can not exist on both sides of the metal film [100].

The greatest bulk sensitivity around a refractive index of water can be achieved for a TE polarisation. Considering a 50 nm titania overlay the corresponding sensitivity is $1 \times 10^5$pmRIU$^{-1}$. The surface sensitivity of a 10 nm surface change is an order of magnitude less than this value. The level of sensitivity attainable through dielectric enhancement is comparable to that observed in SPR sensors. Future devices could further ensure this by considering chemical sensors operating through a pure-plasmon coupled waveguide, as proposed theoretically by Nemova and Kashyap [100].

# Chapter 5

# Strain Effects

## 5.1 Introduction

The strain-optic effect is commercially exploited in both optical physical sensors and telecommunication components. In particular, silica based platforms are widely extolled for such applications as silica demonstrates mechanical strength and a low thermal sensitivity, compared with other optical platforms such as polymers [112].

The applications of optical physical sensors are extensive [113], [21], [114], ranging from large scale structural health monitoring of bridges, oil rigs, skyscrapers etc, to small scale monitoring of micro electromechanical devices [115] [116]. A recent trend for large scale structural health monitoring is the fabrication of smart structures from composite materials, such as glass fibre [117] and carbon fibre [118]. These composites integrate fibre Bragg grating waveguides into a planar structure. The work reported in this chapter examines, for the first time, the strain response of UV written Bragg gratings in a composite silica-on-silicon platform. As with smart structures, the developed devices have the potential to map stress profiles in a plane, whilst exhibiting the benefits of a silica based platform. The theoretical understanding developed in this chapter shall be further extended in Chapter 6 where thin silica membranes are investigated for 'small scale' physical sensor applications.

Strain actuation of Bragg gratings is also commercially implemented in the telecommunication industry. Bragg grating filters combine the advantages of a narrow bandwidth, low crosstalk, and the option of a flat-top passband. They are both ef-

fective filters and can display significant levels of mechanical actuation [119] [120] [121]. The silica-on-silicon platform used in this work are an appropriate platform for Bragg grating actuation as it is an established composite platform for optical telecommunication components.

This chapter is structured such to firstly give an overview of continuum mechanics, examining strain in an arbitrary body. From this understanding the theoretical response of a Bragg grating subject to strain shall be formulated. The grating response of two bending geometries and a lateral compression geometry shall be examined and their potential application for physical and telecomm devices investigated.

## 5.2 Continuum Mechanics

This section is intended to refresh the reader with the theory and notation of continuum mechanics, which relates to the physical properties of the bulk material. In continuum mechanics we have infinite material boundary conditions meaning we do not concern ourselves with the complications of edge effects.

Stress and strain are the prerequisite to analyse structurally the silica-on-silicon chip. So firstly the stress tensor will be introduced, followed by the strain tensor. Finally the relationship between stress and strain will be developed.

### 5.2.1 The Stress Tensor

Stress is defined as a distributed force on an internal or external area of a body. The forces involved to induce stress are either externally applied and/or a result of temperature change.

To illustrate the concept of stress consider a point P within a general solid body, as in Figure 5.1. The body has a set of external forces **F** which act upon it. To expose point P an arbitrary slice through the body would need to be made which intersects P. The orientation of the slice is arbitrary but for convenience we shall consider it to be the slice that is normal to the $\mathbf{x}_1$ axis. Now, the forces on P can be resolved into three axial components, illustrated in Figure 5.2. Stress is a point

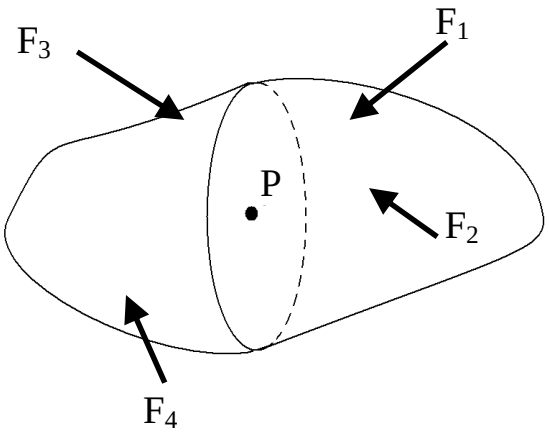


**Figure 5.1:** Continuous body with external forces applied

function, so we shall reduce the area considered to be infinitesimally small.

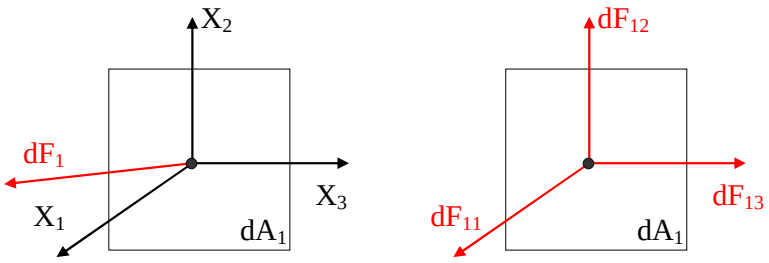


**Figure 5.2:** Considering stress on a point

The stress in the $\mathbf{x}_1$ direction can be formulated as [122]

$$\sigma_{11} = \frac{dF_{11}}{dA_1} \tag{5.1}$$

As this stress is normal to the area it is labelled as the normal stress. Stresses also arise from the tangential forces. As these forces are parallel to the area considered they are a rubbing (sliding) force, which is labelled as shear and formulated as [122]

$$\tau_{ij} = \frac{dF_{ij}}{dA_i} \tag{5.2}$$

It is apparent that an infinite variety of conditions, corresponding to an infinite number of slice areas exist for any given finite point in a body. Fortunately, we

do not need to formulate them all! As a coordinate transform action can be undertaken only three principle coordinates are required. For simplicity the surfaces chosen shall be perpendicular to each other, meaning the stress can be written in a matrix form. To illustrate the tensor nature of stress present at point P in the continuous body, a cubic element will be considered, as illustrated in Figure 5.3

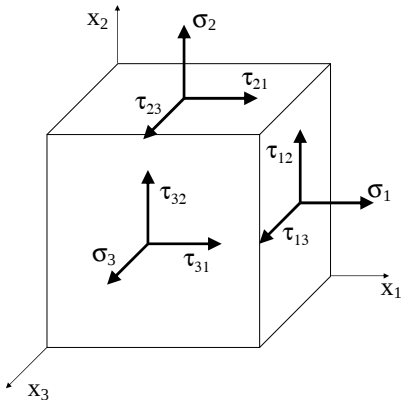


**Figure 5.3:** An infinitesimal cubic element located within a continuous body undergoing nine components of stress

Now, a stress vector $\mathbf{T}_1$ can be considered acting on the plane normal to the $\mathbf{x}_1$ direction. For simplification we shall use the contracted notation $\sigma_{ii} = \sigma_i$

$$\mathbf{T}_i = \sigma_1.\mathbf{x}_1 + \tau_{12}.\mathbf{x}_2 + \tau_{13}.\mathbf{x}_3 \tag{5.3}$$

The stress vector $\mathbf{T}_1$ is the ratio of force acting on a surface. Expanding this idea for a volume wrapped around a point illustrated in Figure 5.3 the stress tensor of that volume is defined by nine stress components acting on the three surfaces of the cube, making up three stress vectors.

$$\sigma_{ij} = \begin{bmatrix} \sigma_1 & \tau_{12} & \tau_{13} \\ \tau_{21} & \sigma_2 & \tau_{23} \\ \tau_{31} & \tau_{32} & \sigma_3 \end{bmatrix} \tag{5.4}$$

### 5.2.2 The Strain Tensor

The application of stress to a body in equilibrium causes it to undergo deformation and/or motion. The measure of deformation is labelled strain, $\epsilon$. As with stress two types of strain exist, normal and shear. Normal strain is the ratio of length change, $\delta$u, of the stressed element in a direction parallel to the normal stress, formulated as [122]

$$\epsilon_i = \frac{\partial \mathbf{u}_i}{\partial \mathbf{x}_i} \tag{5.5}$$

Shear strain is a measure of the distortion of the stressed element, formulated as [122]

$$\epsilon_{ij} = \epsilon_{ji} = \frac{1}{2}\left(\frac{\partial \mathbf{u}_i}{\partial \mathbf{x}_j} + \frac{\partial \mathbf{u}_j}{\partial \mathbf{x}_i}\right) \tag{5.6}$$

A three-dimensional body undergoing normal and shear strain as a result of external force is illustrated in Figures 5.4 (a) and (b) respectively.

(a) (b)

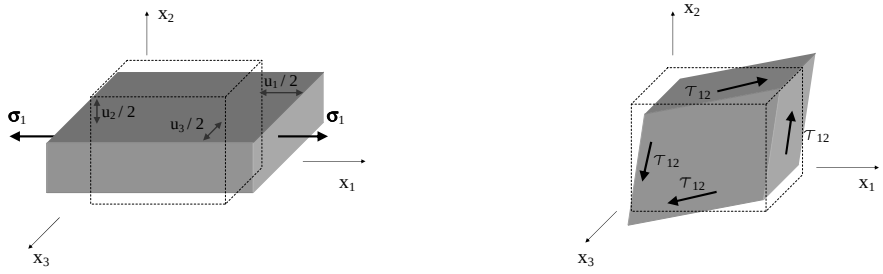


**Figure 5.4:** (a) Normal strain as a result of normal stress and (b) Shear strain as a result of shear stress

Figure 5.4 (a) depicts that a tensile stress in the $\mathbf{x}_1$ direction results in a tensile strain in the $\mathbf{x}_1$ direction. In addition to this there is a compressive strain in the $\mathbf{x}_2$ and $\mathbf{x}_3$ directions respectively. The ratio of strains normal $\mathbf{x}_i$ and perpendicular $\mathbf{x}_j$ to the applied force is labelled the Poisson ratio, $\nu_{ij}$, expressed as

$$\nu_{ij} = -\frac{\epsilon_j}{\epsilon_i} \tag{5.7}$$

There exists an interrelation between stress and strain that is dependent upon the type of material examined.

### 5.2.3 Stress and Strain Relationships

Bodies of different material but of the same dimensions and under the same forces usually deform differently. For treatment in this thesis we shall consider the stress to strain relationship in the elastic region, which can be thought of as 'memory' during deformation, such that when the stress is removed the body returns to its original shape prior to the applied stress. Considering this on a microscopic scale the bonds are stretching but do not break or make new bonds. In this elastic regime stress and strain can be related, by Hooke's law, which states the stress tensor is linearly proportional to the strain tensor, formulated as[1]

$$\epsilon_{ij} = -s_{ijkl}\sigma_{kl} \tag{5.8}$$

$s_{ijkl}$ is known as the elastic compliance tensor [106] and is required to be a fourth rank tensor of $3^4$=81 elements. However, as a result of the shear stress and shear strain definitions (namely $\sigma_{ij}$=$\sigma_{ji}$ and $\epsilon_{ij}$=$\epsilon_{ji}$) this reduces to a tensor of only 36 elements [106]. With this symmetry it is custom to contract the notation, such that $\sigma_{11}$=$\sigma_1$, $\sigma_{22}$ =$\sigma_2$, $\sigma_{33}$ =$\sigma_3$, $\sigma_{12}$ =$\sigma_4$, $\sigma_{13}$ =$\sigma_5$, $\sigma_{23}$ =$\sigma_6$ and similarly for $\epsilon$. The corresponding compliance tensor is thus contracted to $s_{mn}$, containing $6^2$=36 elements.

The devices considered in this thesis form a silica-on-silicon composite, with silica and silicon individually having different compliance tensors, which need to be married together to gain an understanding of the mechanical properties of the whole device.

## 5.3 Mechanical Properties of Silica-on-Silicon

Silica-on-silicon is an example of a composite, as it forms a single bulk composing of two separate materials that are not blended. As the silica and silicon form

[1]Note that the sign convention in Equation 5.8 arise due to the way Pockels defines stress and strain. Compressive stress is considered positive and compressive strain is considered negative.

layered sheets it is categorised as a laminate composite [123]. To understand the mechanical behaviour of the laminate we must firstly define the mechanical properties of its composing parts.

### 5.3.1 Mechanical Properties of Silicon

The structure and mechanical properties of silicon is well documented due to its importance in the semiconductor industry and widespread use in Microelectromechanical systems (MEMS). As a result of its crystal properties, silicon is mechanically anisotropic and silicon wafers are classified in terms of their crystallographic orientation [124]. The silicon wafers used in this work are p-type (111) wafers[2], the crystallographic orientation of which is illustrated in Figure 5.5. The (111) silicon wafer is considered the most useful for mechanical devices, especially for MEMS applications, as the mechanical properties of the wafer in the transverse plane are equal. This means that these devices will be least sensitive to their orientation allowing greater fabrication tolerance.

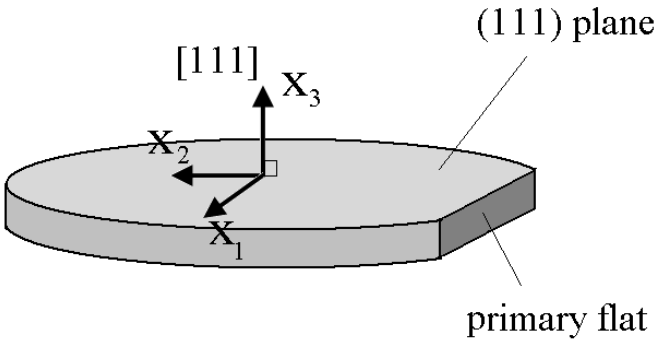


**Figure 5.5:** Schematic of silicon crystal planes with respect to the wafer geometry

The mechanical properties of silicon vary as a result of its inherent anisotropy. The compliance tensor of silicon is [126].

[2](111) is Miller index notation [125] for a plane perpendicular to the [111] crystallographic vector

$$s_{i,j} = \begin{pmatrix} s_{11} & s_{12} & s_{12} & 0 & 0 & 0 \\ s_{12} & s_{11} & s_{12} & 0 & 0 & 0 \\ s_{12} & s_{12} & s_{11} & 0 & 0 & 0 \\ 0 & 0 & 0 & s_{44} & 0 & 0 \\ 0 & 0 & 0 & 0 & s_{44} & 0 \\ 0 & 0 & 0 & 0 & 0 & s_{44} \end{pmatrix} \tag{5.9}$$

where $s_{11}$, $s_{12}$ and $s_{44}$ are 7.68x10$^{-12}$, -2.14x10$^{-12}$ and 12.6x10$^{-12}$ Pa$^{-1}$ respectively [127].

Although silicon is an anisotropic medium it is sometimes convenient to think of it as an isotropic one. For linear, homogenous, isotropic materials, Hooke's law (Equation 5.8) is simply that the normal strain is directly proportional to the normal stress, given by.

$$\epsilon_i = \frac{1}{E}[\sigma_i - \nu(\sigma_j + \sigma_k)] \tag{5.10}$$

where the material constants E and $\nu$ are named the Young's modulus and Poisson ratio. These constants are elements of the compliance tensor that give useful information. The Young's modulus quantifies how much a material will strain along the axis of a given stress, formulated as

$$E_i = \frac{\sigma_i}{\epsilon_i} = \frac{1}{s_{ii}} \tag{5.11}$$

The Poisson's ratio gives information of a materials strain perpendicular to the applied stress (along $x_i$ dimension), formulated as

$$\nu_{ij} = -\frac{\epsilon_j}{\epsilon_i} = -\frac{s_{ij}}{s_{ii}} \tag{5.12}$$

For silicon, Young's modulus can vary from 130.2 GPa to 187.5 GPa and Poisson's ratio can vary from 0.064 to 0.361. For silicon (111), Young's modulus is transversely isotropic at 168.9 GPa and 117.3 GPa perpendicular to the (111) plane. Poisson's ratio has a constant value of 0.262 for directions parallel to the (111) plane and 0.182 for directions perpendicular to it. It must be noted that these moduli need to be interpreted into effective moduli when considering a laminate silica-on-silicon

structure. Such a laminate is conventionally described in the literature as forming a composite beam.

### 5.3.2 Effective Moduli

The silica-on-silicon laminate has silica and silicon constituent parts, as illustrated in Figure 5.6. It shall be assumed that the deposited silica layers and thermally grown silicon oxide have the same mechanical properties i.e., $E_A$=$E_C$. It can be seen that the laminate has directionality due to its layered nature and that transversely the composite beam is isotropic, i.e. the Young's modulus is $E_1 = E_2 \neq E_3$ and the Poisson ratio is $\nu_{12}$=$\nu_{21}$, $\nu_{13}$=$\nu_{23}$ and $\nu_{31}$=$\nu_{32}$.

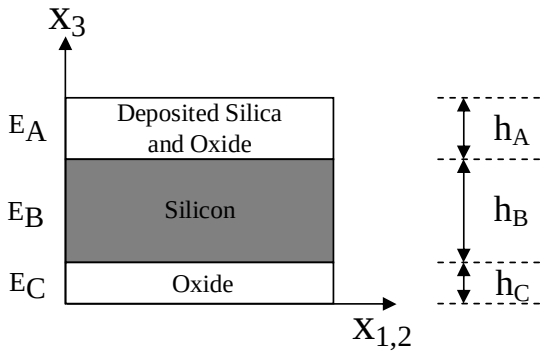


**Figure 5.6:** The constituent parts in a silica-on-silicon wafer

The effective moduli can be calculated by assuming good adhesion between the silica and silicon layers. Making this assumption for strains parallel to the layers (along the $x_1$ and $x_2$ dimensions) must be equal for both silica and silicon, as illustrated in Figure 5.7 (a).

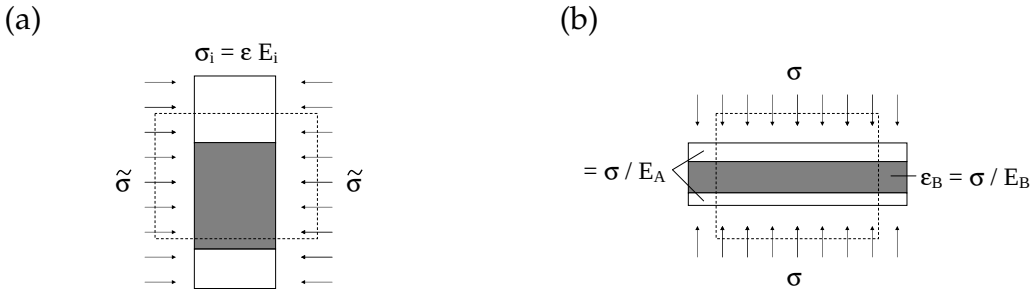


**Figure 5.7:** A conceptual scematic of the composite laminate under (a) parallel and (b) series deformation

As the silicon and silica have different Young's moduli, each material in this parallel deformation will have a different associated stress. Considering an effective (average) parallel stress $\tilde{\sigma}_{1,2}$, on the device and constant strain, one can infer an effective Young's modulus $E_{1,2}$, formulated as [128]

$$\begin{aligned} \tilde{\sigma}_{1,2} &= E_{1,2}\epsilon_{1,2} \\ \Rightarrow E_{1,2}h\epsilon_{1,2} &= \Big(\frac{h_A + h_C}{E_A} + \frac{h_B}{E_B}\Big)\epsilon_{1,2} \\ \Rightarrow E_{1,2} &= \frac{1}{h}\Big(\frac{h_A + h_C}{E_A} + \frac{h_B}{E_B}\Big) \end{aligned} \tag{5.13}$$

where the values of h correspond to the thickness along the $x_3$ dimension, as previously illustrated in Figure 5.6. This is generally referred to as the rule of mixtures [123].

For lateral compression (strains along the $x_3$ dimension) the layers are in series, not parallel. Instead of assuming the strains are equal in the different materials we assume they are all different and experience the same stress, the laminate as a whole now experiences an effective strain, $\tilde{\epsilon_3}$, formulated as [123]

$$\begin{aligned} \sigma_3 &= E_3\tilde{\epsilon_3} = E_3\frac{1}{h}\Big(\frac{h_A + h_C}{E_A} + \frac{h_B}{E_B}\Big) \\ \Rightarrow E_3 &= \frac{E_A E_B h}{E_A(h_A + h_C) + E_B h_B} \end{aligned} \tag{5.14}$$

Applying rules of mixtures and symmetry arguments the Poisson ratios $\nu_{ij}$ for the considered laminate can be analytically determined [123]. Now the mechanical properties of the silica-on-silicon has been outlined we need to understand the effect stress/strain has on a Bragg grating.

## 5.4 A Bragg Grating's Response to Strain

A Bragg grating's response to strain arises due to both a change in the effective refractive index and pitch of the grating [21] [114], this can be written mathematically as

$$\Delta\lambda_i = 2\Big(\Lambda_i \Delta n_i + n_i \Delta\Lambda_i\Big) \tag{5.15}$$

The first term in Equation 5.15 relates the effective index change with strain, $\epsilon$, and is dominated by the photoelastic effect. Physical change in core height and width will also change the effective index. However, the contribution of this, in our devices, has been calculated to be negligible. The second term in Equation 5.15 relates to the physical length change of the grating, corresponding to a fractional change in pitch. This section shall address effects in both photoelasticity and fractional change in pitch.

### 5.4.1 Photoelastic Effects

Photoelasticity deals with the artificial birefringence in a solid under the application of a mechanical stress/strain, quantitatively studied by Neumann in 1841 [106]. To conceptualise the effect we shall consider an ellipsoid whose shape represents the relative refractive indices observed when a ray of light traverses the respective axes of the medium, illustrated in Figure 5.8.

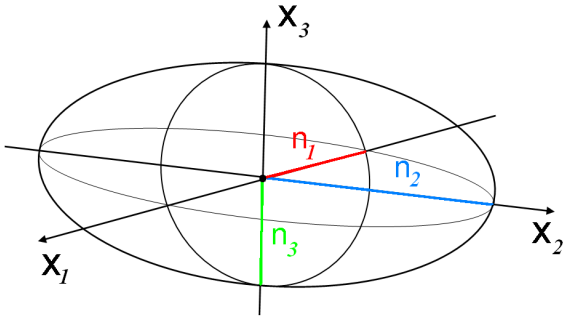


**Figure 5.8:** A schematic of an indicatrix

The fancy name of this construct is an indicatrix and is represented analytically by the ellipsoidal expression

$$\left(\frac{x_1}{n_1}\right)^2 + \left(\frac{x_2}{n_2}\right)^2 + \left(\frac{x_3}{n_3}\right)^2 = 1 \tag{5.16}$$

Simplifying the notation this can be written in terms of a tensor $B_{ij}$ to give Equation 5.17, which can be stated more generally as Equation 5.18

$$B_{11}x_1^2 + B_{22}x_2^2 + B_{33}x_3^2 = 1 \tag{5.17}$$

$$\sum_{i,j=1}^{3} B_{ij}x_i x_j = 1 \tag{5.18}$$

If a solid is stressed it is expected that the respective refractive indices $n_1$, $n_2$ and $n_3$ shall change, meaning that the original indicatrix has also changed giving, another indicatrix tensor, $B'_{ij}$. The difference between these indicatrix tensors is

$$\Delta B_{ij} = B'_{ij} - B_{ij} \tag{5.19}$$

Introducing a theory of photoelasticity proposed by Pockels [106] this change in index as a result of stress/strain can be quantified. Pockels' theory is based on the following two postulates.

I. Homogenous deformations will change the indicatrix.

II. Within the elastic limit stress induces an optical change that can be represented as a linear function of nine stress components.

Considering Pockels' two postulates the change in indicatrix tensors can be stated as

$$\Delta B_{ij} = -q_{ijkl}\sigma_{kl} \tag{5.20}$$

The tensor $q_{ijkl}$ has 81 elements called the stress-optical or piezo-optical coefficients. As previously introduced with stress and strain, contracted notation can be used for an anisotropic crystal due to symmetry arguments. Thus B reduces to single suffix notation and q reduces to a tensor of only 36 elements [106].

$$\Delta B_i = \sum_{i,j=1}^{6} -q_{ij}\sigma_j \tag{5.21}$$

From the stress and strain relationship, Pockels assumes that the changes in $B_{ij}$ are also linear functions of all nine components of the strain tensor. This gives the strain version of Equation 5.21 to be Equation 5.22

$$\Delta B_i = \sum_{i,j=1}^{6} p_{ij}\epsilon_j \tag{5.22}$$

The change in indicatrix tensor can be approximated as

$$\begin{aligned} \Delta B_i = B_i' - B_i &= \frac{n_i^2 - n_i'^2}{n_i^2 n_i'^2} \\ &\cong \frac{(n_i - n_i')(n_i + n_i')}{n_i^4} \\ &\cong \frac{-\Delta n_i . 2n_i}{n_i^4} = \frac{-2\Delta n_i}{n_i^3} \end{aligned} \tag{5.23}$$

Combining Equation 5.23 and Equation 5.22 and considering the thermal induced strain as a result of temperature variation, $\Delta T$ the change in index, as a result of strain, can be deduced to be

$$\begin{aligned} \Delta n_i &= \sum_{i,j=1}^{6} \frac{\partial n_i}{\partial \epsilon_j}\epsilon_j + \frac{\partial n_i}{\partial T}\Delta T \\ &= -\frac{n_i^3}{2}\sum_{i,j=1}^{6} p_{ij}\epsilon_j + \frac{\partial n_i}{\partial T}\Delta T \end{aligned} \tag{5.24}$$

The second factor that affects a grating's response to stress is fractional change in pitch as a result of mechanical effects, which shall now be formulated.

### 5.4.2 Mechanical Effects

Physical change in length as a result of strain will affect the grating's pitch and so affect the grating's Bragg condition. The following treatment shall consider the dependence pitch has on stress.

The definition of strain is the fractional change in an arbitrary length. Hence, the change in pitch $\Delta\Lambda$ can be expressed as

$$\Delta\Lambda_i = \Lambda_o\epsilon_i \tag{5.25}$$

Substituting Equation 5.24 into Equation 5.15 it can be stated that light polarised along the $\mathbf{x}_2$ (TE) and $\mathbf{x}_3$ (TM) directions is

$$\begin{aligned} \Delta\lambda_i &= 2\Lambda_i\Big( -\frac{n_i^3}{2}\sum_{i,j=1}^{6} p_{ij}\epsilon_j + \frac{\partial n_i}{\partial T}\Delta T + n_i\epsilon_i\Big) \\ \frac{\Delta\lambda_i}{\lambda_i} &= -\frac{n_i^2}{2}\sum_{i,j=1}^{6} p_{ij}\epsilon_j + \eta\Delta T + \epsilon_i \end{aligned} \tag{5.26}$$

where $\eta$ is a thermal coefficient, brought about through the thermal strain (thermal expansion). This has been quantified in Chapter 3 to be typically 10 nm$^o$C. This is the most general formulation for the spectral response with respect to strain. The following subsection shall pin down this formulation for the specific case of silica based waveguides.

### 5.4.3 Optical Properties of Silica

Silica is an isotropic solid, and such the photoelastic tensors only consist of 2 elements. Considering fused quartz the photoelastic tensor $p_{ij}$ is

$$p_{i,j} = \begin{pmatrix} p_{11} & p_{12} & p_{12} & 0 & 0 & 0 \\ p_{12} & p_{11} & p_{12} & 0 & 0 & 0 \\ p_{12} & p_{12} & p_{11} & 0 & 0 & 0 \\ 0 & 0 & 0 & p_{44} & 0 & 0 \\ 0 & 0 & 0 & 0 & p_{44} & 0 \\ 0 & 0 & 0 & 0 & 0 & p_{44} \end{pmatrix} \tag{5.27}$$

Considering 589.3 nm wavelength light traversing through fused quartz the stress-optic coefficients for $p_{11}$ and $p_{12}$ are 0.100 and 0.285 respectively, where $p_{44}$ = 1/2( $p_{11}$ - $p_{12}$ ) [107], as the refractive index of silica is similiar for 589.3 nm and 1550 nm wavelengths only small deviation from these values are expected.

Introducing these specific values into Equation 5.27 gives

$$\frac{\Delta\lambda_2}{\lambda_2} = \epsilon_1 - \frac{n_2^2}{2}[p_{11}\epsilon_2 + p_{12}(\epsilon_1+\epsilon_3)] + \eta\Delta T \tag{5.28}$$

$$\frac{\Delta\lambda_3}{\lambda_3} = \epsilon_1 - \frac{n_3^2}{2}[p_{11}\epsilon_3 + p_{12}(\epsilon_1 + \epsilon_2)] + \eta\Delta T \tag{5.29}$$

The following section shall compare theoretical wavelength shifts for bending and compression geometries to real mechanical stress tests. For consistency the same device has been used for all of the following mechanical tests. The device consists of a single mode uniform Bragg grating of 535.2 nm period and a length of 9 mm. The total thickness of the chip is 1.06 mm, it has a transverse width of 10 mm and a length of 40 mm. The thermal oxide was 14 $\mu$m thick and the thickness of deposited silica was 46 $\mu$m. Light was launched into the device via a polarisation-maintaining fibre V-groove. The single mode Bragg grating was measured using a broadband source and an optical spectrum analyser with a resolution of 0.01 nm. The full width at half maximum bandwidth of the grating is 16 GHz. The centre wavelength of the reflection spectra was obtained by a numerical Gaussian fitting algorithm. In the absence of an externally applied force the TE and TM Bragg reflected wavelengths were 1550.43 nm and 1550.61 nm respectively.

## 5.5 Bending

An effective way of inducing strain on the Bragg grating within our devices is through bending. Depending upon the geometry of the bending, tensile or compressive strain can be achieved at the grating as illustrated in Figure 5.9.

Previous work has considered three-point and four-point bending techniques primarily in fibre based devices [129] [130]. Three-point bending utilises three points of leverage to induce bending and four-point bending uses four points of leverage. This section investigates the effectiveness of these two techniques as mechanisms of strain tuning our fabricated device.

### 5.5.1 Normal Strains in Bending Beams

The silica-on-silicon devices is an example of a beam, with rectangular cross section of height h and width b. When subject to a bending moment, M, a beam deforms to an assumed circular arc, illustrated in Figure 5.10 (a). Such bending

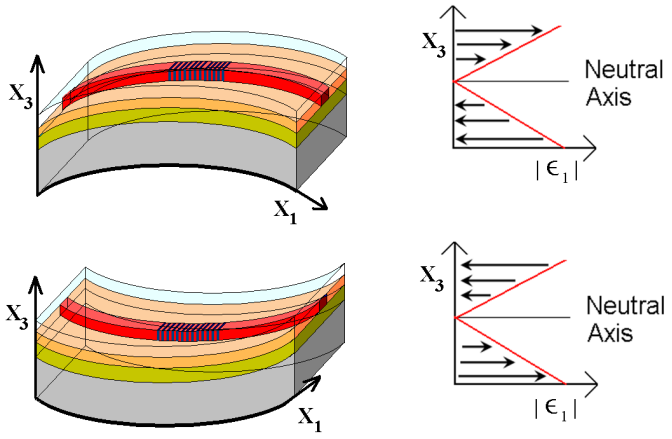


**Figure 5.9:** Schematic of planar Bragg grating under tensile and compressive strain, showing the strain $\epsilon_1$ along the devices $x_3$ cross section

results in the top edge of the beam being extended and the bottom shortened, corresponding to tensile and compressive strain respectively. It follows that between these changes there must be a neutral axis, N, within the beam that undergoes no strain, represented by length CD and illustrated in Figure 5.10 (b).

(a) (b)

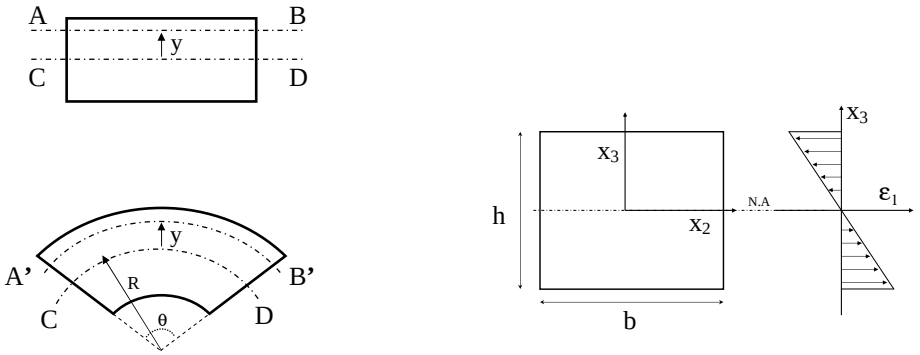


**Figure 5.10:** Schematic of a rectangular beam undergoing elastic bending depicting (a) deformation of the beam (side view) and (b) varying strains across the beam (cross sectional area)

Considering an arbitrary length AB that is a distance y from the neutral axis. For an applied moment it becomes stretched to A'B', illustrated in Figure 5.10 (a). Mathematically this strain can be expressed as

$$\begin{aligned} \epsilon_1 &= \frac{A'B' - CD}{CD} = \frac{(R+y)\theta - R\theta}{R\theta} \\ &= \frac{y}{R} \end{aligned} \tag{5.30}$$

which in terms of stress becomes

$$\sigma_1 = \frac{Ey}{R} \tag{5.31}$$

Considering total force on the cross-sectional area of the beam

$$\Sigma F_1 = \Sigma \sigma_1 dA = \Sigma \frac{Ey}{R} dA \tag{5.32}$$

This has a moment about the neutral axis of

$$\Sigma F_1 y = \frac{E}{R} \Sigma y^2 dA = \frac{E}{R} I \tag{5.33}$$

where I is the second moment of area. Rearranging and inserting Equation 5.33 into Equation 5.30 gives

$$\epsilon_1(x_1, x_3) = \frac{M(x_1)(x_3 - N)}{EI} \tag{5.34}$$

As the device is a composite material it has effective mechanical properties, which for the case of bending requires a moment of area approach [122].

### 5.5.2 Moment of Area for a Composite

Due to the different mechanical coefficients of the silica and silicon an equivalent cross sectional area technique is required to interpret the moment of area and neutral axis. The equivalent area technique reinterprets the areas of the constituent material parts such that the Young's modulus of each section can be considered equal, as illustrated in Figure 5.11 [3].

[3] The following treatment shall assume that all the silica and thermal oxide layers have identical mechanical properties.

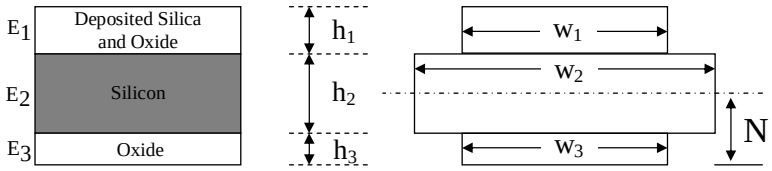


**Figure 5.11:** A schematic of the equivalent cross section for silica-on silicon composite

The neutral axis can be determined as the average neutral axis of each section weighted by their area, determined by

$$N = \frac{\sum_i w_i h_i N_i}{\sum_i w_i h_i} \tag{5.35}$$

The moment of area is a summation of the individual moment areas of the sections about the centroidal axis. Each layer is understood to have a moment area equal to that of a beam, giving a total moment of area determined by

$$I = \sum_i \left( \frac{w_i h_i^3}{12} + w_i h_i (N - N_i)^2 \right) \tag{5.36}$$

The values for the silica-on-silicon composite used for the following tests gave widths of 10 mm for $w_1$ and $w_3$ respectively and 23.14 mm for $w_2$. This gives the location of the neutral axis to be at 0.52 mm and the moment of area to be 2.05 $mm^{-4}$.

This theory can now be applied to three-point and four-point bending techniques.

### 5.5.3 Three-Point Bending

Three-point bending achieves a moment through a three-point leverage system, illustrated in Figure 5.12 (a).

The strain along the beam is illustrated in Figure 5.12 (b) and can be understood by taking the moment, M, of the system

(a) (b)

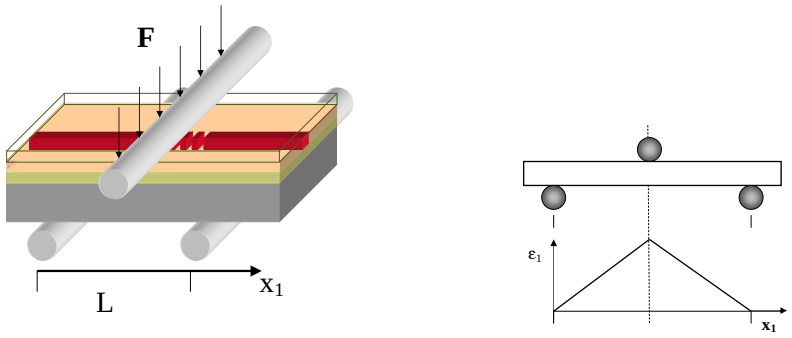


**Figure 5.12:** Schematic showing (a) planar Bragg grating under compressive strain using 3 point bending (b) the strain distribution involved

$$M(x_2) = \begin{cases} \frac{Fx_2}{2} & x_1 < L_1/2 \\ \frac{F(L_1 - x_2)}{2} & x_1 > L_1/2 \end{cases} \tag{5.37}$$

Substituting this moment into Equation 5.34 gives the theoretical strain for an applied force.

$$\epsilon_1(x_1, x_3) = \begin{cases} \frac{Fx_1(x_3 - N)}{2EI} & x_1 < L/2 \\ \frac{F(L - x_1)(x_3 - N)}{2EI} & x_1 > L/2 \end{cases} \tag{5.38}$$

For the setup used the length $L_1$ was 30.0 $\pm$ 0.1 mm. By placing the silica side up or down compressive or tensile stress was achieved at the grating respectively. A tuning range of $\pm$43 N was tested as it was found experimentally that for a load of $\pm$48 N the ultimate shear strength of the device was catastrophically exceeded.

The overall strain tuning performance of the device is depicted in Figure 5.13 (a). The maximum wavelength shift observed for TE polarisation was 2.49 nm, corresponding to 311 GHz of tuning at 1550 nm. Normalising to an equivalent device with transverse width of 1 mm the tuning is 280 pmN$^{-1}$ and 290 pmN$^{-1}$ for TM and TE polarisations respectively. The tuning of the device was linear in terms of applied load as is expected from theory. Any deviation of the tuning from linearity was within the temperature stability of the laboratory and the known 10 pm$^{o}$C$^{-1}$ thermal response of the device.

As the length of the grating is under linear varying strain (dictated by Equation

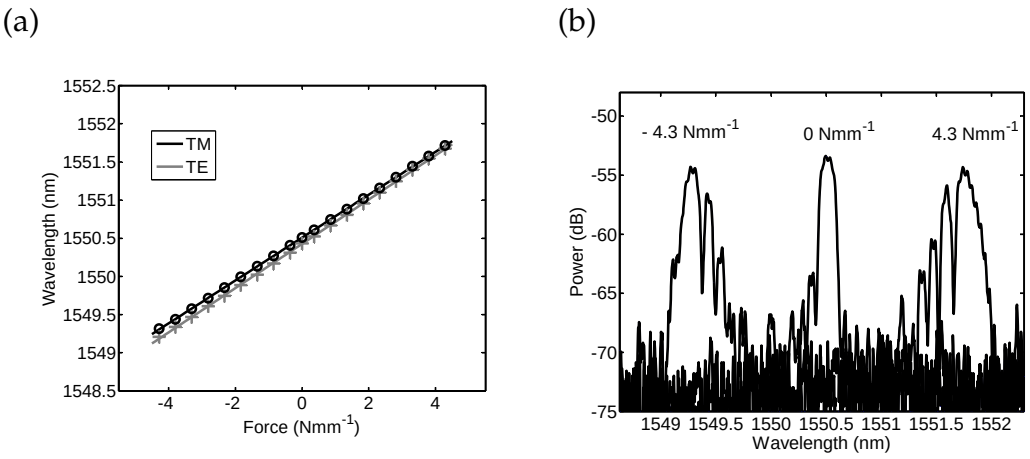


**Figure 5.13:** The tuning of a direct UV written Bragg grating undergoing three-point bending, displaying (a) the tuning curves for TE and TM polarisations and the (b)reflection spectra with and without load, for TE polarised light

5.38) there is a maximum and minimum spectral response that occurs for any given load. The maximum spectral response occurs at the location along the grating that experiences maximum strain (i.e. $x_1$ = L/2). The minimum spectral response occurs at the location along the grating that has minimum strain (i.e. the start and end of a grating). It must be noted that these maxima and minima occur for one particular load. For the maximum load that can be applied (43 N), the maximum and minimum spectral values have been calculated, listed in Table 5.1. The averaged TE and TM theoretical shifts are 2.48 $\pm$ 0.01 nm and 2.44 $\pm$ 0.01 nm respectively. The TE and TM shift deviates from the measured value by 0.01 nm and 0.03 nm respectively. The empirical and theoretical tuning of the TE polaisation lies within the accepted error of each other. However, the theoretical tuning for TM polarisation overestimates the empirical response by 0.8 % from accepted error. This discrepancy may be a result of the approximation used for the photoelastic constants, which were approximated for bulk fused quartz at 589.3 nm wavelengths, not direct UV written doped silica waveguides at 1550 nm wavelengths.

The reflection spectra for three different applied forces are shown in Figure 5.13 (b). It is clear from these that gratings with a $\pm$4.3 Nmm$^{-1}$ load are considerably less symmetric than the unstressed grating. This can be understood by considering Equation 5.38. The greater the central load the larger the linear variation in strain over the grating. Although such an effect may be desirable for dispersion compensation devices, for OADM filter symmetry is important. Forcing a constant strain over the grating using a four point bending system might remove this

| Maximum Spectral Response | | Minimum Spectral Response | |
|---|---|---|---|
| $\epsilon_1$ | 1.13x10$^{-3}$ | $\epsilon_1$ | 7.89x10$^{-4}$ |
| $\epsilon_2$ | -3.11x10$^{-4}$ | $\epsilon_2$ | -2.18x10$^{-4}$ |
| $\epsilon_3$ | -3.89x10$^{-4}$ | $\epsilon_3$ | -2.73x10$^{-4}$ |
| TE | 2.92 nm | TE | 2.04 nm |
| TM | 2.89 nm | TM | 2.01 nm |

**Table 5.1:** Theortical values for three point bending

phenomenon [129].

### 5.5.4 Four-Point Bending

Another way of inducing bending is through using a four point leverage system, as illustrated in Figure 5.14. The configuration illustrated induces compressive strain and inverting the orientation induces tensile strain.

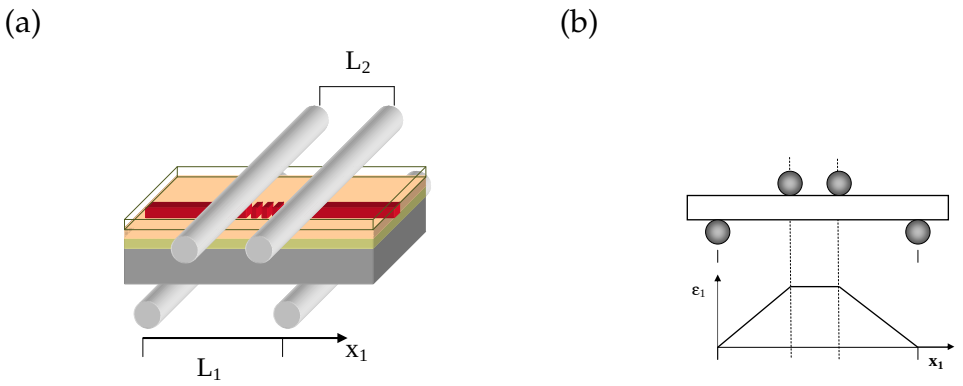


**Figure 5.14:** Schematic showing (a) planar Bragg grating under compressive strain using four-point bending and (b) its respective stress distribution along a beam undergoing four-point bending)

The moment for such a bending configuration between the smaller of the two pivots is

$$M(x_2) = \frac{F(L_1 - L_2)}{4} \tag{5.39}$$

Substituting the moment into Equation 5.34 gives

$$\epsilon_1(x_3) = \frac{F(L_1 - L_2)(x_3 - N)}{4EI} \tag{5.40}$$

Unlike for three-point bending, four-point bending can induce a constant strain over the grating length. In order to achieve this, the length of $L_1$ and $L_2$ were set at $30 \pm 0.01$ mm and $10 \pm 0.01$ mm respectively. The Bragg grating was located over the 10 mm length, as this was the location of constant strain.

The maximum magnitude of force that this four-point bending technique can withstand is 5.8 $\text{Nmm}^{-1}$, compared with 4.8 $\text{Nmm}^{-1}$ for the three-point bending configuration. This can be understood with reference to Equations 5.38 and 5.40. For four-point bending the load required is greater to achieve the same maximum stress/strain on the device which all relates back to a failing strain/stress of the silica-on-silicon.

As a result of constant strain being applied a symmetric spectral response is predicted when tuned, this can be observed by comparing Figures 5.13 (b) and 5.15 (b). The spectra for the four-point bending is considerably more symmetric than that of three-point bending, however there is still an element of spectral broadening. This is believed to be a result of the stress affecting the defects of the silica and so affecting the distribution of refractive index resulting in spectral broadening.

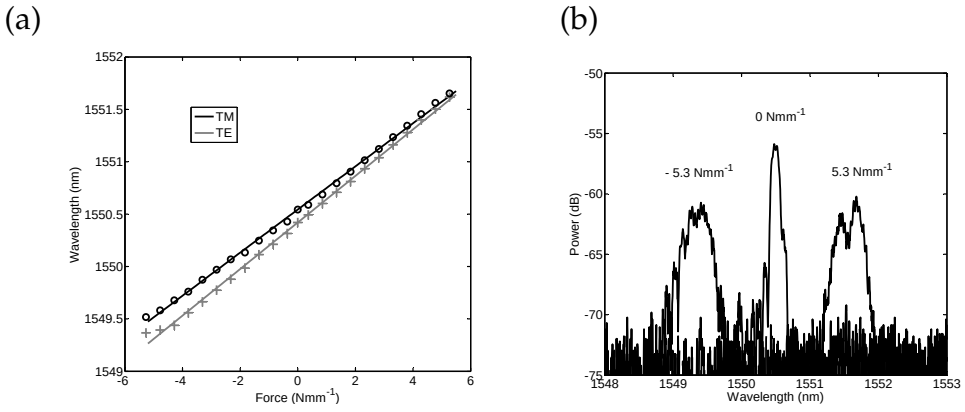


**Figure 5.15:** The tuning of a Direct UV written Bragg grating undergoing four-point bending, displaying (a) the tuning curves for TE and TM polarisations and the (b)reflection spectra of with and without load (TE polarised light)

The overall strain tuning of the device is depicted in Figure 5.15. The device has maximum TE and TM wavelength shifts of 2.31 nm and 2.14 nm respectively, which is comparable to that achieved with three-point bending. From Figure 5.15, if we normalise the tuning response for a 1 mm thick device the TE and TM mode

| | |
|---|---|
| $\epsilon_1$ | 9.26x10$^{-4}$ |
| $\epsilon_2$ | -2.55x10$^{-4}$ |
| $\epsilon_3$ | -3.20x10$^{-4}$ |
| TE | 2.39 nm |
| TM | 2.36 nm |

**Table 5.2:** Theoretical values for four point bending

tuning sensitivities are 218 pmN$^{-1}$ and 202 pmN$^{-1}$ respectively, which is lower than that for three-point bending. This is due to the moments for three-point bending inducing a larger leverage upon the sample.

It is apparent from Table 5.2 and Figure 5.15 that there is discrepancy between theoretical and empirical readings, of 0.08 nm for TE and 0.22 nm for TM polarisations. These discrepancies between theoretical and measured values are greater than those previously calculated for three-point bending. One potential reason for this discrepancy is a result of curve fitting inaccuracies, due to spectral broadening with increasing applied force. The theoretical response of the tuned Bragg grating stipulates a linear trend with applied force. The larger the applied force the greater the spectral broadening and so the greater the deviation from the theoretical linear response, which is apparent in Figure 5.15 (a). It must be noted that the largest deviation between theoretical and measured tuning occurs for TM polarisations. However, the data for TM better approximates a linear fit, as understood from R-squared values. Other potential reasons for deviation are variations of the approximations assumed, such as the photoelastic constants.

To measure the photoelastic constants for silica glass a lateral compression experiment was undertaken. So far the photoelastic approximation for germanium doped silica has been approximated to that of fused silica, which has served as a sufficient approximation. However, deviations may exist for structures experiencing greater strains.

## 5.6 Lateral Compression

A lateral compression is an effective method of obtaining the photoelastic constants of a material, as it achieves the largest difference between TE and TM polari-

sation. Lateral compression refers to a unidirectional force along the $\mathbf{x}_3$ dimension. The corresponding strains of which are

$$\epsilon_{1,2} = -\frac{\nu_{31}\sigma_3}{E_3} \tag{5.41}$$

$$\epsilon_3 = \frac{\sigma_3}{E_A} \tag{5.42}$$

where $E_3$ is the effective Young's modulus and $\nu_{31}$ is the effective Poisson ratio, having values of 74.98 GPa and 0.119 respectively and $E_A$ is the Young's modulus of silica. Inserting the respective strains into Equations 5.28 and 5.29, it is possible to solve the photoelastic constants $p_{11}$ and $p_{12}$ by rearranging the equation into the form.

$$\frac{1}{\lambda_2}\frac{d\lambda_2}{d\sigma_3} = (A - B_2 p_{11} - C_{13} p_{12}) \tag{5.43}$$

$$\frac{1}{\lambda_3}\frac{d\lambda_3}{d\sigma_3} = (A - B_3 p_{11} - C_{12} p_{12}) \tag{5.44}$$

where for convenience

$$A = -\frac{\nu_{31}}{E_3} \tag{5.45}$$

$$B_2 = -\frac{n_2^2}{2}\frac{\nu_{31}}{E_3} \tag{5.46}$$

$$B_3 = \frac{n_3^2}{2E_A} \tag{5.47}$$

$$C_{13} = -\frac{n_2^2}{2}\left(\frac{\nu_{31}}{E_3} - \frac{1}{E_A}\right) \tag{5.48}$$

$$C_{12} = -n_3^2\frac{\nu_{31}}{E_3} \tag{5.49}$$

Equations 5.44 and 5.44 are just simultaneous equations which can be solved.

In order to deliver and monitor the lateral stress/strain an Instron 5569 electromechanical test machine (with a ±50kN static load cell) was used, alongside a specially adapted jig machined from mild steel, which applied force to a 30 ± 0.5 mm x 10± 0.5 mm area on the device, illustrated in Figure 5.16. The jig also acted as a thermal reservoir, maintaining the temperature of the sample to within ±0.5 $^o$C

over the ~10 minute test period. This thermal drift was inferred through monitoring the temperature of the jig with a thermocouple during experimentation and assuming jig and sample had sufficient thermal contact. Experiments were undertaken individually for each polarisation.

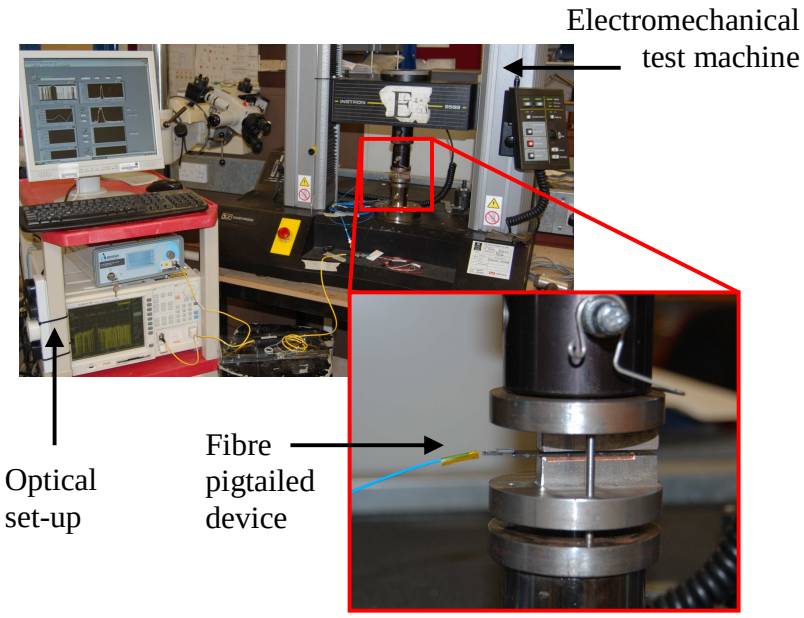


**Figure 5.16:** Lateral compression experimental set-up

The Bragg wavelength (TE) and strain response to force is shown in Figure 5.17 (a). It can be seen that for forces >1500 N the relationship is not linear as expected with an elastic composite. Only after 1500 N of applied force does the expected elastic behaviour takes place. This is believed to be a result of initial slop in the jig. As such TE and TM measurements were taken for stresses above 1500 N.

The spectral quality as a function of applied lateral force is shown in Figure 5.17 (b). As expected from Equations 5.28 and 5.29 lateral compression results in a positive shift in Bragg condition. What is also noticed from the spectra is broadening, which is thought to be a result of density distribution due to small variations in internal stress. As the fitting quality of a Gaussian to the spectral data diminishes for forces above 4000 N, this shall be considered to be the ceiling force for experimentation.

Figure 5.18 shows the relationship between Bragg wavelength and applied lateral compression for both TE and TM polarisations in the range 2500 N to 3500 N.

The spectral response for compression presented graphically in Figure 5.18 is -0.345 pmN$^{-1}$ and -0.387 pmN$^{-1}$ for TE and TM respectively. Placing these values

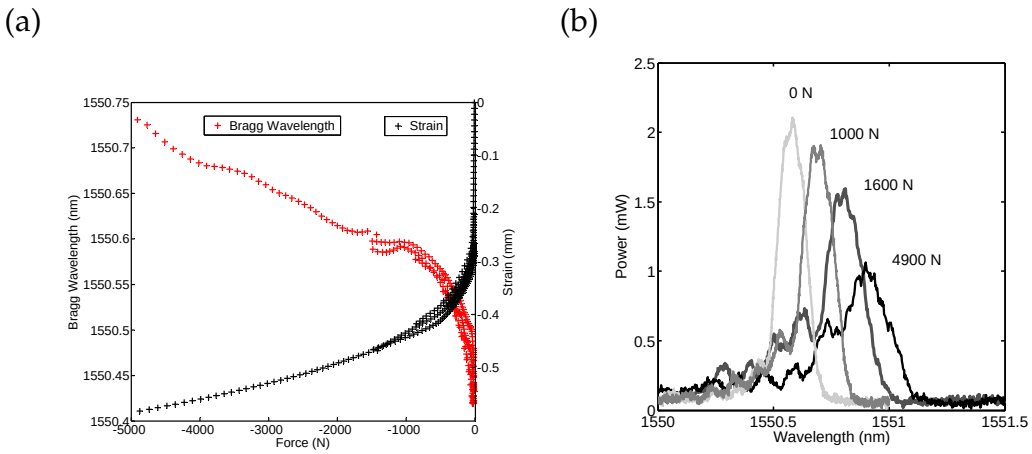


**Figure 5.17:** The response of a DUW chip under lateral applied force over a 30 $mm^2$ area depicting (a) the spectral dependence and strain dependence on applied force (b) the nature of the spectral response for four different applied forces

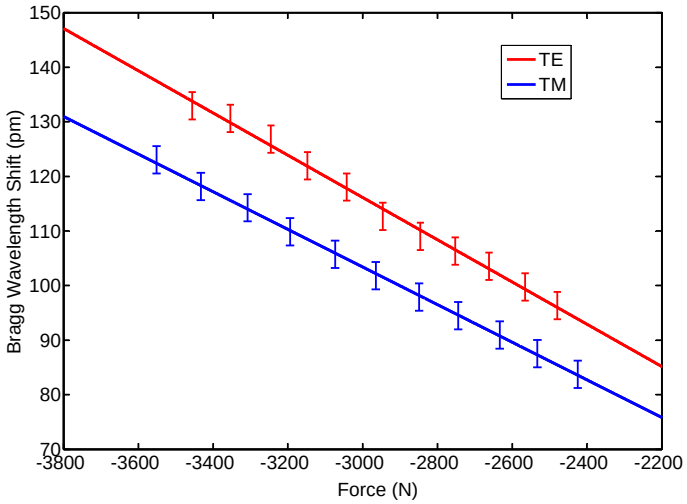


**Figure 5.18:** Lateral compression experimental set-up

into the simultaneous equations (Equations 5.44 and 5.44) gives the photoelastic constants to be 0.4761 and 0.5272 for $p_{11}$ and $p_{12}$ respectively. These values are much greater than those previously assumed for silica. It is noted that although the mechanical properties of the silicon and silica have been combined such to account for their composite form, the actual stress observed by the grating maybe different. This may arise from an inherent curvature of the device and/or inaccuracies in the assumptions made for the composited behaviour, which lead to inferred effective indices.

## 5.7 Conclusions

We have demonstrated for the first time an applied strain tuning of ∼311 GHz (corresponding to 2.49 nm of tuning at 1550 nm wavelengths) achieved by three-point and four-point bending a direct UV written silica-on-silicon integrated optical chip. This degree of tuning leads to potential application in optical networks as an OADM. Normalised to a device of a 1 mm width, the grating response to force for three-point bending was is 280 $pmN^{-1}$ and 290 $pmN^{-1}$ for TM and TE polarisations respectively. This was in comparison to 202 $pmN^{-1}$ and 218 $pmN^{-1}$ for four-point bending.

For large applied moments the grating spectra in the three-point bending case displayed an apodised response, which can be understood from the variation in strain, predicted by theory, across its length. A four-point bending system did not display the asymmetric response associated with this apodisation. However, spectral broadening was observed, which is believed to be a result of variations in stress in the sample effecting internal densities.

The photoelastic constants for DUW waveguides were measured by applying lateral stress to the device. The measured values at 1550nm were 0.4761 and 0.5272 for $p_{11}$ and $p_{12}$ respectively. These measurements deviate greatly from expected values extrapolated from known values of fused silica. It is believed that the approximation assumed for lateral compression breaks down, especially for the large applied stresses considered. Using the polarisation data from three point bending the $p_{11}$ and $p_{12}$ effective photoelastic constants can be inferred to be 0.099 and 0.292 respectively.

The dynamic range and practicality of the fabricated devices to be used as physical sensors is limited by the devices dimensions, and the silicon wafers having mechanical weakness along their crystal planes. However, altering the dimensions or replacing the silicon could be a way of bridging the gap between these devices and the physical sensor market. A hypothetical future device may consist of an FHD layer deposited onto a silica window, which may be subject to extremes in stress (e.g. viewing window in a deep-sea submarine, jet plane or space shuttle). In such a composite structure, stresses in the window could be monitored in real time using direct UV written Bragg gratings in the FHD deposited layer.

To monitor shifts in a Bragg grating (e.g. for physical sensor applications) characterisation equipment similar to that used to characterise these devices (e.g. an OSA, broadband source and data interpreting software) can be used. However, the expense of this set-up would be significantly large, making the detection method less economically viable. However, the cost per device could be reduced through multiplexing several sensors into one system such that the cost per device would be distributed between many sensors. Another way to reduce cost would be to alter the interrogation set-up. For example, a photodiode and single frequency laser source could be used to replace the OSA and a broadband source respectively. Such a system would require the laser source to be aligned spectrally on top of the Bragg grating, which is to be monitored. The reflected laser light could then be monitored in reflection, transmission or both. As the Bragg grating shifts relative to the spectrally fixed laser light source the reflected power measured at the photodiode would vary and could be interpreted.

# Chapter 6

# Membrane Transducers

## 6.1 Introduction

Membranes are a proven means to detect pressure and flow in lab-on-a-chip based devices [115]. A sufficient pressure difference across a membrane will result in its deformation, this physical effect can be monitored using optical [131], [132] or electronic [133], [134], [135] techniques, and can be used to measure pressure and/or flow.

Optical methods for monitoring pressure differentials across a membrane can be categorised into either intensity modulated [136], [137], polarization modulated [138], [139] or phase modulated [140], [141], [142] techniques. Arguably, Bragg gratings fall into this later category of phase modulation, although they are different to interferometric techniques in that the phase change is seen as a shift in the Bragg reflection wavelength rather than an intensity change, making them more immune to intensity variation of the source.

The majority of Bragg grating based membrane pressure sensors are based upon fibre Bragg gratings attached to a point on a membrane so that they stretch as the membrane deforms [143], [144] rather than being structurally part of the membrane. The following work outlines fabricated devices that consist of a direct UV written Bragg grating contained within a thin silica membrane, for pressure and flow sensing applications. Combined with temperature and chemical sensing capabilities this component will enhance future lab-on-chip realisation of direct UV written waveguide technology.

## 6.2 Theory

A pressure monitoring device can be realised by placing a Bragg grating within a thin silica membrane, illustrated in Figure 6.1 (a). Applying a sufficient pressure differential, $\Delta P$ ($=P_2$-$P_1$), across the membrane will cause it to buckle inducing strain on the grating within the membrane, illustrated in Figure 6.1 (b).

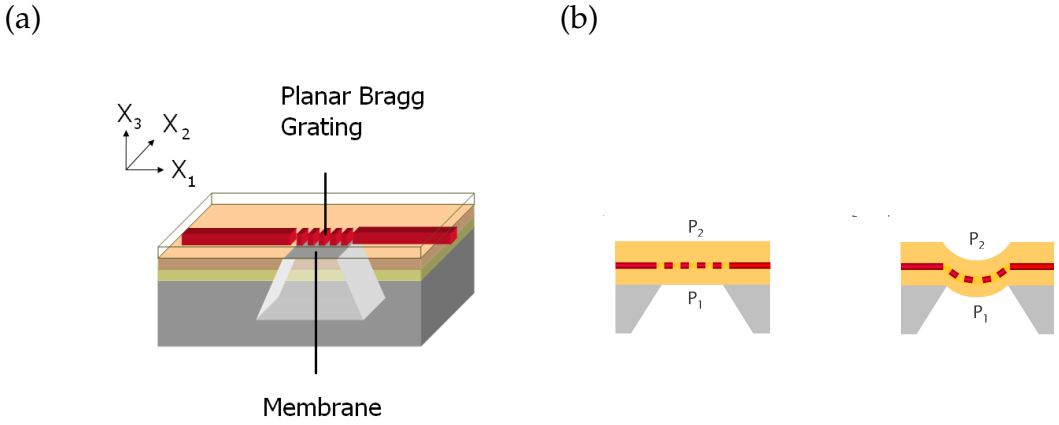


**Figure 6.1:** Conceptual schematic of (a) the membrane based planar Bragg grating pressure sensor construction (b) the gratings response to a pressure differential, visualised from the membranes cross section

Considering an arbitrary rectangular membrane of $x_1$ dimension a and $x_2$ dimension b, with the coordinate system centred on a corner of the membrane, then the first order buckling shape is defined as [145]

$$w(x_1, x_2) = \frac{w_0}{4}\left(1 - cos(\frac{2\pi x_1}{a})\right)\left(1 - cos(\frac{2\pi x_2}{b})\right) \tag{6.1}$$

where $w_0$ is the maximum buckling located at the centre of the membrane. This strain with respect to the buckling can be derived to be of the form

$$\epsilon_{1,2} = \left(1 + \left(\frac{dw}{dx_{1,2}}\right)^2\right)^{1/2} - 1 \tag{6.2}$$

From Equation 6.2 the strains $\epsilon_1$ and $\epsilon_2$ can be determined. The strain $\epsilon_3$ can be found using the Poisson ratio of silica.

It must be noted that the idealised conceptual membrane response to pressure differentials illustrated in Figure 6.1 (b) is a simplification of the system. As a result of the FHD process the silica layers are under compressive stress. For specific

membrane parameters, this results in the buckling downwards of the membrane [146], [147]. Meaning particular membrane designs will exist is in a buckled state when $P_1$=$P_2$.

The inherent (total) compressive stress, $\sigma$, the silica layers possess is contributed to by the thermal mismatch stress[1] between the silica and silicon, $\sigma_t$, and intrinsic stress, $\sigma_i$ [148]. By its nature, intrinsic stress is difficult to quantify other than by empirical measurements. Thermal mismatch stress, however, can be analytically quantified. Assuming this is an example of a thin film system, differences in contraction of the film and substrate generate the thermal mismatch stress related as [148].

$$\sigma_t = E(\alpha_{SiO2} - \alpha_{Si})\Delta T \tag{6.3}$$

where $\alpha_{Si}$ and $\alpha_{SiO2}$ are the expansion coefficients of silicon and silica, having values of 2.6x10$^{-6}$ $^{o}$C$^{-1}$ and 4.9x10$^{-7}$ $^{o}$C$^{-1}$ respectively, $\Delta$T is the difference between the consolidation temperature and room temperature which is $\sim$1200 K, resulting in a stress of $\sim$180 MPa. If the inherent stress is greater than a critical stress the membrane will buckle.

First order membrane buckling of an arbitrary rectangular membrane is understood to have a calculable critical stress $\sigma_{cr}$, defined as [145]

$$\sigma_{cr} = \frac{1}{9}\frac{\pi^2 E h^2 a^2}{1-\nu^2}\left(\frac{3}{a^4} + \frac{3}{b^4} + \frac{2}{a^2 b^2}\right)\left(1 + \frac{a^2}{b^2}\right)^{-1} \tag{6.4}$$

where E is the Young's modulus and $\nu$ the Poisson ratio of the silica. Figure 6.2 indicates the critical stresses for three membrane dimension ratios that have a set thickness of 40 $\mu$m.

Values below the thermal mismatch stress line are expected to satisfy the condition $\sigma > \sigma_{cr}$ and hence are expected to buckle, indeed this trend has been observed experimentally for membranes of the respective dimensions.

[1]Thermal mismatch stress is often incorrectly shortened to thermal stress. However, it must be noted that thermal stress is the stress that is incurred with a thermal gradient.

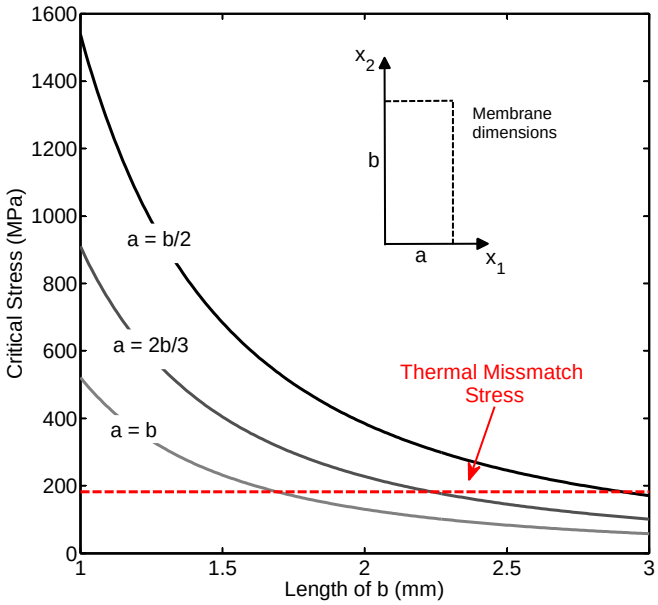


**Figure 6.2:** The critical stress required for buckling with respect to membrane dimension and the thermal stress missmatch (values are calculated for a 40$\mu$m thick membrane)

## 6.3 Fabrication

For membrane fabrication three-layer silica-on-silicon wafers were used as a thin layer of silica was desired. This choice ensures buckling of millimetre dimension membranes, as understood from Equation 6.4. All Bragg gratings were Gaussian apodised and written at a fluence of 20 kJcm$^{-2}$ and duty cycle of 0.5. The fabrication steps post DGW are illustrated in Figure 6.3

To fabricate a membrane an area of the thick thermally grown oxide was selectively removed on the underside of the device. As the remaining thermal oxide is thick it acts as an effective etch mask for the device. Several methods for removing the thermal oxide were attempted. HF etching the oxide required polyimide tape to mask the FHD layers. The oxide could also be physically removed using a diamond scribe or aluminium oxide grinding bit (used in conjunction with a dremel tool), the latter of which can be used to remove a large proportion of silicon $\sim$0.5 mm prior to etching. This significantly reduces the total time required for etching.

The exposed silicon was anisotropically etched in 50 % KOH solution for $\sim$7 hours at 90 $^{o}$C. This removes all the silicon under the grating such that the three silica

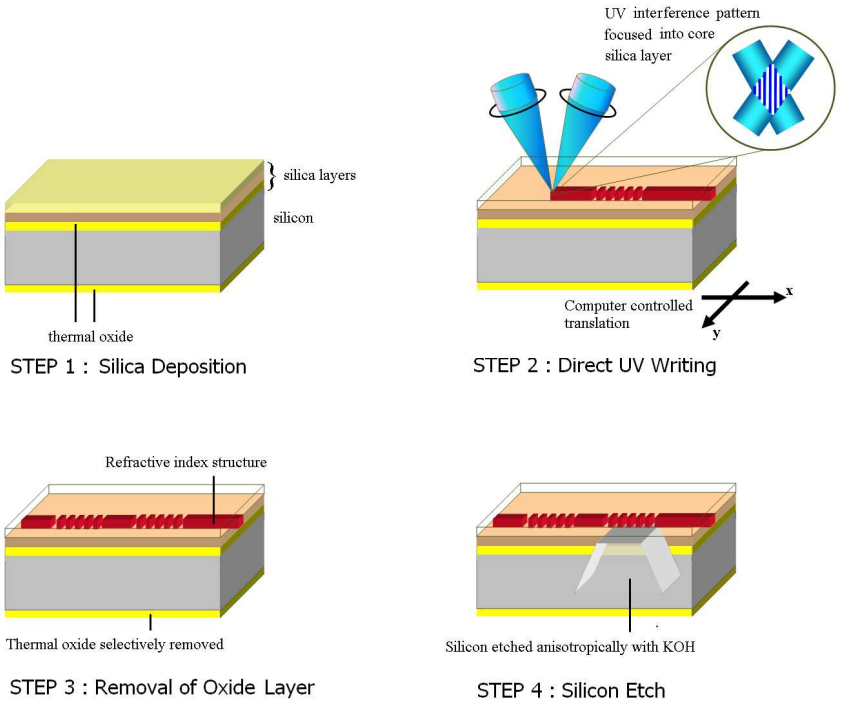


**Figure 6.3:** Illustration detailing the fabrication process for a direct UV written pressure sensor chip

layers form a thin membrane. As the side of the chips are exposed silicon, they were masked by PTFE tape. At temperatures (above 70°C) this resulted in a white residue being left on the sample, which was could later be removed by flash etching the device in KOH for a further 2 minutes.

To deliver light into the device a fibre optic polarising maintaining V-groove chip was aligned to the input channel waveguide and permanently secured using an epoxy.

## 6.4 Devices

Using the outlined fabrication procedure three types of membrane based transducer were fabricated: a pressure transducer; membrane strain map; and a flow transducer.

### 6.4.1 Pressure Transducer

The membrane based pressure transducer exploited the inherent buckling effect (discussed in theory section of this chapter) to distinguish positive and negative pressure differentials.

The fabricated membrane was 2 mm by 3 mm and had a thickness of 40 $\mu$m. The critical stress of such a membrane can be calculated to be 101 MPa, which is significantly less than the thermal mismatch stress, observed graphically in Figure 6.2. A Bragg grating resided along the membranes 2 mm width and was centralised along the 3 mm length. To deliver a pressure differential across the membrane the device was glued to an aluminium fixture that could deliver positive or negative pressure to the membrane using the inlet and outlet feeds from a vacuum pump, as illustrated in Figure 6.4.

The fabricated device was observed to have a maximum pressure sensitivity of 20 pm/kPa and by exploiting the inherent buckling of the membrane can distinguish between positive and negative pressure differentials, over a 100 kPa range, as shown in Figure 6.5. Note that when the pressure on top of the membrane, $P_2$, is greater than that on the bottom, $P_1$, the pressure differential was considered to

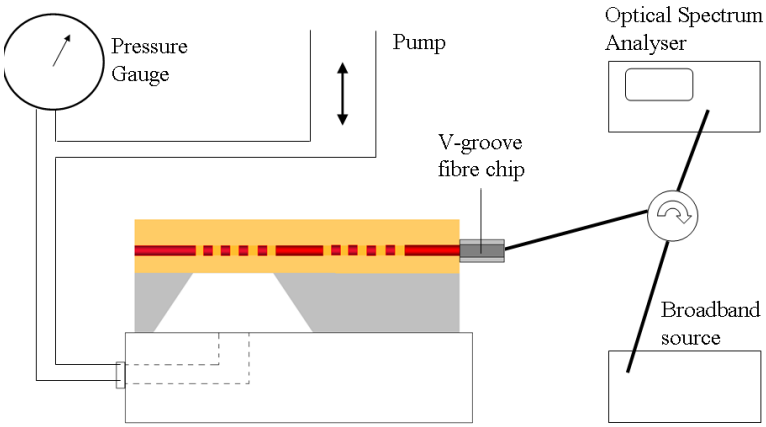


**Figure 6.4:** Schematic of the pressure delivery and optical interrogation set-up

be positive (see Figure 6.1 (b)). Assuming the minimum resolvable spectral shift is 1 pm, this membrane can resolve pressure differences of 5 Pa.

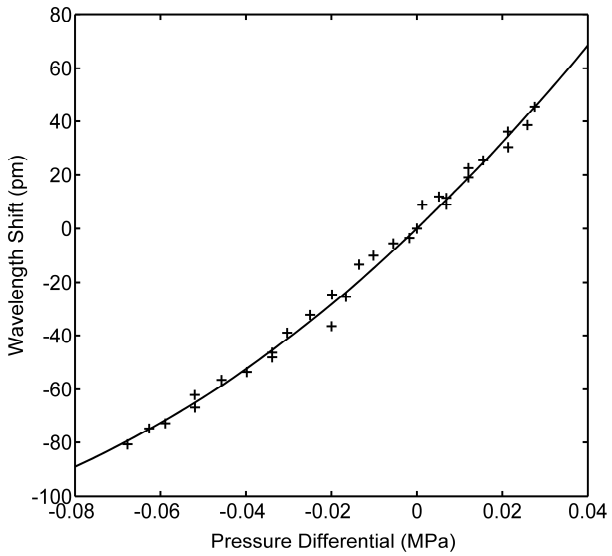


**Figure 6.5:** The spectral response of the Bragg grating for a range of pressure differentials

It is understood that the relationship between pressure and maximum membrane buckled displacement, $w_0$, is linear [147]. As the buckling displacement of the membrane is relatively small with respect to its dimensions it is expected from Equations 6.1 and 6.2 that strain will have an approximate positive quadratic nature. This will mean, from Equations 5.28 and 5.29, that the Bragg wavelength

response is quadratic, which is the form observed in Figure 6.5.

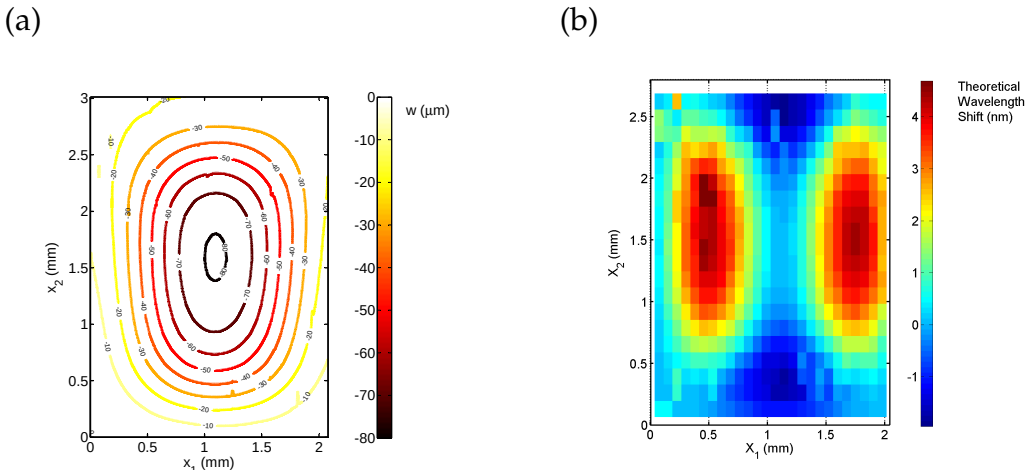


**Figure 6.6:** Properties of the fabricated membrane depicting the (a) buckling and (b) the spectral response of a horizontal Bragg grating localised at any position along the length of the membrane

Using a step profiler the 3-dimensional topography of the buckling was measured, the data of which is shown in Figure 6.6 (a). This is an example of first order buckling as it fits the characteristics of Equation 6.1. The maximum deflection $w_0$ for this membrane is 82 $\mu$m. Using the 3-dimensional information from the step profiler (Figure 6.6 (a)) the strain pre-etching and post-etching can be deduced. Using this information and Equations 5.28 and 5.29 the spectral shift was inferred for any grating waveguide along the $x_1$ direction, as represented in Figure 6.6 (b). For the calculation, that led to this graphical representation the photoelastic constants calculated in Chapter 5 were implemented. The apodised grating measured in this work spans the 2 mm width of the membrane for $x_2$ = 1.5 mm. As Figure 6.6 (b) indicates for its size the grating is in the optimum position. However, the size of the grating relative to the membrane results in variation in strain across its length, which results in a variation of pitch and refractive index over the grating, in accordance with Equations 5.28 and 5.29. The result of this can be seen in Figure 6.7 for the gratings spectral response pre and post KOH etching. It must be noted that the reflected power before etching is less than that post etching. This is believed to be a result of coupling losses as a fibre pig-tail was not maintained during the silicon etch step. Due to this strain variation, there is a spectral broadening and an asymmetric form to the response, similar to the effect observed in Chapter 5 for the three-point bending device. However, it must be noted that this effect does not limit the ability to measure grating shifts.

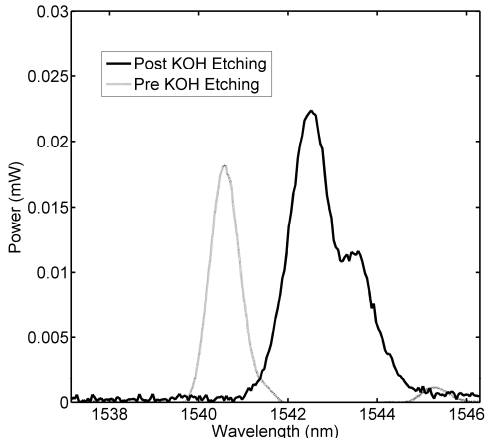


**Figure 6.7:** The spectral response of the grating located over the membrane pre and post KOH etching

The theoretical maximum spectral shift post-etch compared to pre-etch, can be obtained from Figure 6.6 (b). This maximum theoretical shift is around 4.4 nm, however our grating extends across the whole membrane and so shows a smaller peak shift of around 2.5 nm, Figure 6.7. It must be noted that the increase in power post etching observed in Figure 6.7, is a result of poor coupling into the waveguide prior to the wet etching stage. In fact it has been observed that negligible loss (bend loss, Raleigh loss) results from the removal of the silicon beneath the silica area. It must be noted that to suppress spectral side lobes the written grating has been Gaussian apodised with an optimised spatial standard deviation of 0.35 mm. The nature of the apodisation is understood to reduce the contribution of the higher index variation sites at $x_1$ equal to 0.5 mm and 1.5 mm. It is also noted that the theoretical calculations used known values for 589.3 nm wavelengths in bulk quartz, not in DUW channels in germanium doped silica at 1550 nm wavelengths, and so more deviations would be expected.

The sensitivity of the developed device to membrane deflection is dependent upon where wavelength shift is measured, since chirping is shown. Reducing the physical length of the Bragg grating could reduce this chirping effect. From Figure 6.6 (b) insights into the optimum location for grating position can be found. The strain on the membrane can be calculated from Equations 6.1 and 6.2. It can be seen from these equations that the maximum strain occurs at the maximum/minimum of the cosine derivative function, of Equations 5.28 and 5.29, meaning the optimum wavelength shift occurs at $x_2 = b/2$ and $x_1 = a/4$ , $3a/4$ as these are the locations of maximum strain. It must also be noted for future device refinement that it is not

just maximum strain that gives maximum spectral response, but rather the way they each interact described by Equations 5.28 and 5.29, which is also dependent upon the waveguide orientation on the membrane.

So far only a single grating has been placed on the membrane and its response elsewhere inferred through theory. To corroborate with theory a membrane mapping experiment was undertaken. The objective of this task was to map out the spectral shift as a function of gratings position on the membrane.

### 6.4.2 Membrane Deflection Map

A 100 apodised Bragg grating array was written on a sample in order to map deflections in the membrane, post etching. The array was arranged in a series of 10 parallel channels spaced 1 mm apart, which took over 2 hours to UV write, using a fluence of 20 kJcm-1. Each channel had 10 'array' gratings each one 1 mm in length and placed end-to-end, such that a 10 mm by 10 mm sensing area was blanketed over the membrane. In addition to the 100 gratings placed over the membrane area were temperature reference gratings, placed at a 2 mm distance from the membrane, for each channel. The 10 channels, each containing 11 gratings were characterised individually by scanning a fibre across their length, illustrated in Figure 6.8.

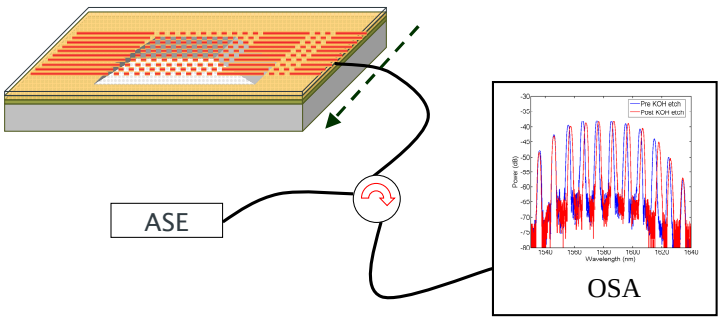


**Figure 6.8:** Schematic of membrane mapping configuration

The fabricated device used a wafer with silica thickness of ~40 $\mu$m, which was diced to 20 mm x 20 mm chips. This allowed for larger membranes to be tested. It was found experimentally that for silica thickness of ~40 $\mu$m the largest membrane that could be fabricated is 6 mm x 6 mm. To take advantage of the 100 grating array

a membrane of 10 mm x 10 mm was partially etched, such that some silicon still remained and formed part of the membrane. This partial etch allowed a 10 mm x 10 mm membrane to be fabricated. The thickness of silicon remaining on the underside of the membrane was difficult to quantify as it varied across the length, with the central area of the membrane showing an absence of silicon. This partial etching and subsequent uneven distribution of remaining silicon resulted in an asymmetric buckling nature of the membrane, illustrated in Figure 6.9, which is in contrast to the symmetry possessed in Figure 6.6 (a).

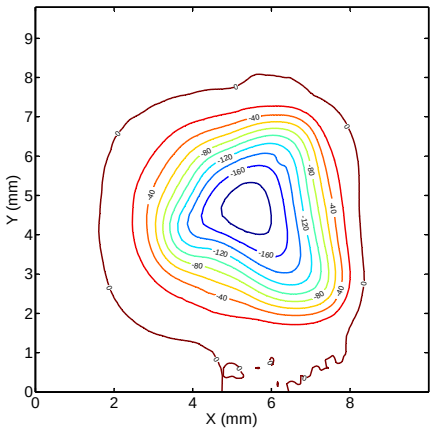


**Figure 6.9:** Membrane deflection as measured by a surface profiler

Using this deflection data the spectral shift pre-etch and post-etch can be inferred, as was done previously for the case of the pressure transducer, the only difference being is that the theoretical model (Figure 6.10 (a)) can be corroborated directly with spectral measurement (Figure 6.10 (b)).

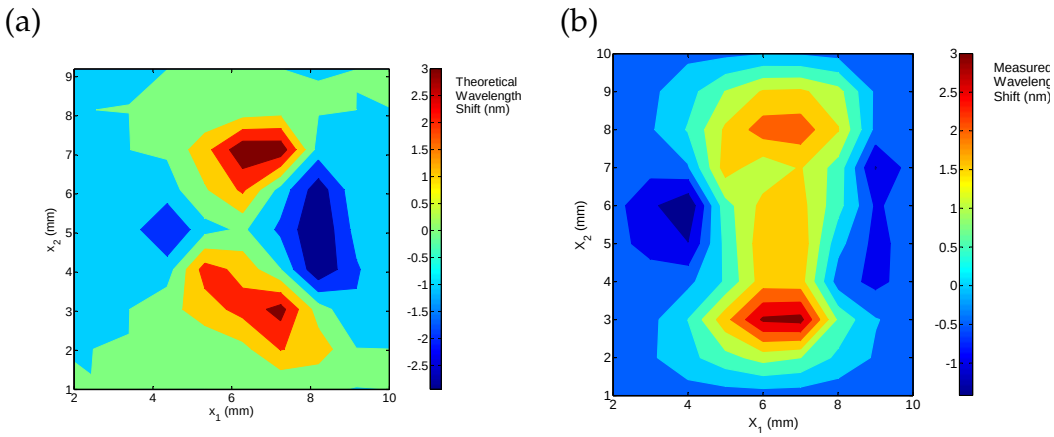


**Figure 6.10:** The spectral response according to (a) theoretically data inferred from measured deflection (b) emperimentally measured

The theoretical prediction and the measured spectral shift display similar characteristics. The photoelastic constants calculated in Chapter 5 were again used to calculate the theoretical shift. The accepted photoelastic constants for fused quartz show a similar predicted response, but with a spectral range from -1 nm to 4 nm as a result of a smaller strain-optic contribution. Deviations between theoretical and predicted data may be contributed to by the presence of the partially etched silicon, which is not considered in the model.

### 6.4.3 Flow Transducer

Mass markets in biotechnology, medical diagnostics, pharmaceutical research and homeland security drive demand for lab on a chip based technology. Flow based sensors form an integral part of these chips for their use as dosing systems and mass flow controllers. A single membrane can monitor pressure, and pressure in turn can be used to monitor flow. However, it is not sufficient to infer flow from a single pressure measurement. If flow, I, is to be quantified one requires a pressure differential, $\Delta P$, and the resistance of flow, R, between the pressure differential. This resistance is dependent upon the viscosity of the fluid and parameters of the channel. The relationship between these terms is analogous to Ohms law in electronics (potential difference $\rightarrow$ pressure difference, electric current $\rightarrow$ flow, electrical resistance $\rightarrow$ flow resistance) and can be formulated as[2]

$$\Delta P = (P_2 - P_1) = IR \tag{6.5}$$

Membrane techniques can be used to monitor a pressure differential across a channel in one of two ways, either by accessing a single membrane from both sides or by monitoring the pressures of two membranes. Both geometries have advantages and disadvantages for lab-on-a-chip applications. Single membranes can deal with larger pressures, assuming the output pressure is greater than atmospheric pressure, as the back-flow pressure would offset the input pressure. Two separate membranes have the advantage of being more sensitive (again assuming the output pressure is greater than atmospheric pressure) and have the ability to quantify the actual pressure as well as the pressure differential. The reason why

[2]It is understood that this equation holds for laminar flow conditions. For turbulent flow the resistance of the channel becomes flow rate dependent.

a two membrane system would be more sensitive than one, stems from the fact that the response to pressure differential is quadratic, as observed in Figure 6.5. If both membranes are working at higher pressure differentials they are expected to demonstrate an improved flow resolution.

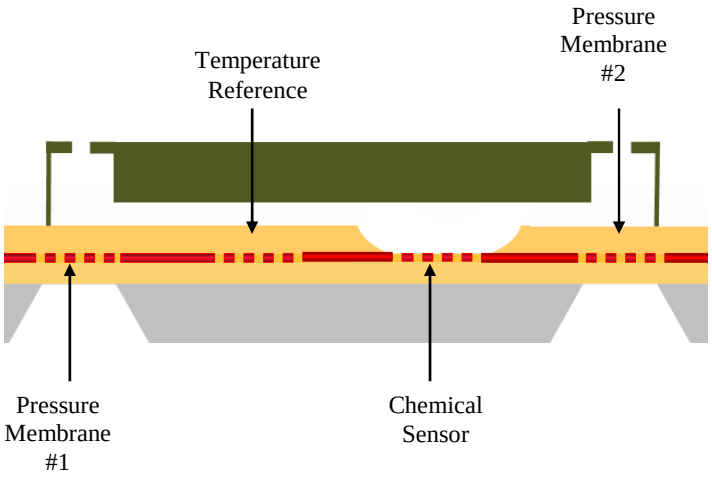


**Figure 6.11:** A conceptual schematic of a fully integrated chip with chemical, temperature, pressure and flow sensing capability

A two membrane system, illustrated in Figure 6.11, was fabricated to monitor fluid flow. To fully realise the integration capability of a direct UV written chip, the fabricated device consisted of four Bragg gratings, which collectively monitored pressure, flow, chemical and thermal fluctuations, illustrated conceptually in Figure 6.11. This device was realised upon a 10 mm by 20 mm chip. As with the pressure transducer the silica thickness was 39.8 $\mu$m and contained two membranes of dimensions 2 mm x 3 mm, illustrated in Figure 6.12. The written gratings were 2 mm long and Gaussian apodised, written with a duty cycle of 0.5 and a fluence of 20 kJcm$^{-2}$. They were located over the membranes smallest dimension and cantered upon it longest length, just as in the case of the previously outlined pressure transducer.

In the fabrication of this device the chemical sensor grating was etched using HF acid, which was sequenced prior to the KOH silicon etch, as the silica was easier to mask prior to membrane fabrication. The fully integrated pressure, flow, chemical and temperature device fabricated is pictured in Figure 6.12.

The reflection spectra of the device pre-etch and post-etch is depicted in Figure 6.13. As well as the reflection spectra indicating a shift in the membrane gratings due to the inherent buckling, a shift was also observed for the chemical grating

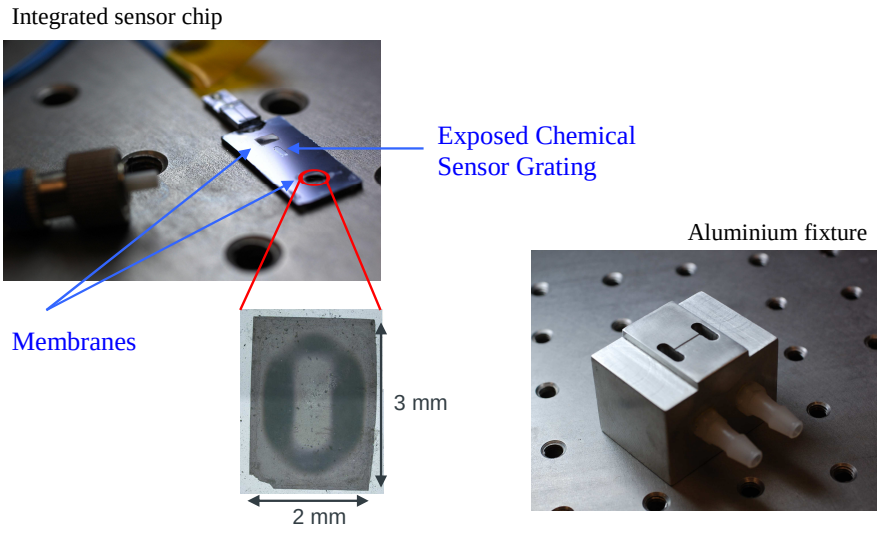


**Figure 6.12:** A photograph of the fully integrated pressure, flow, temperature and chemical chip

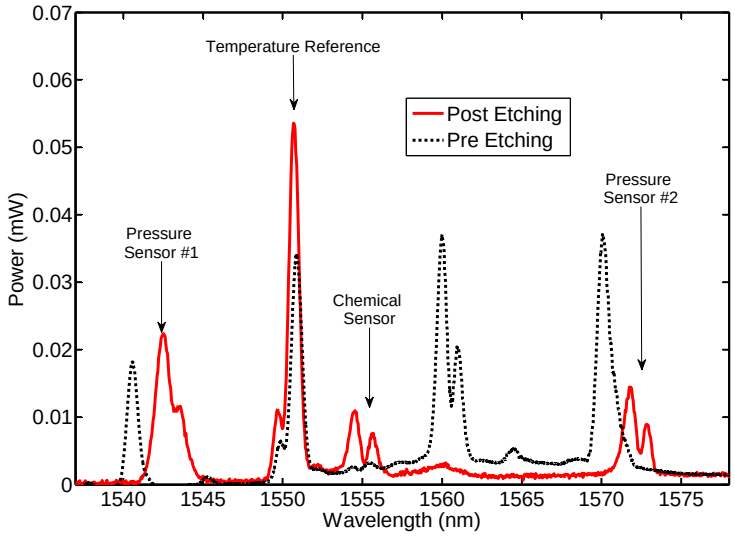


**Figure 6.13:** The spectral response of a fully integrated pressure, flow, temperature and chemical chip depicting the reflection spectra pre-etch and post-ecth

post etching. What is interesting, is that this spectral shift or $\sim$ 5 nm shift, is much greater than the expected spectral shift of $\sim$1 nm, observed experimentally in similar devices. It was found that post HF etching the expected $\sim$1 nm shift occurs. However, after the KOH etch this reduced by a further $\sim$4 nm, which effects the exposed Bragg grating but not the buried gratings (i.e. no response occurs with the temperature reference grating). This effect did not degrade the sensitivity of the exposed grating, but may be suppressed by effectively masking of the grating during the KOH etch.

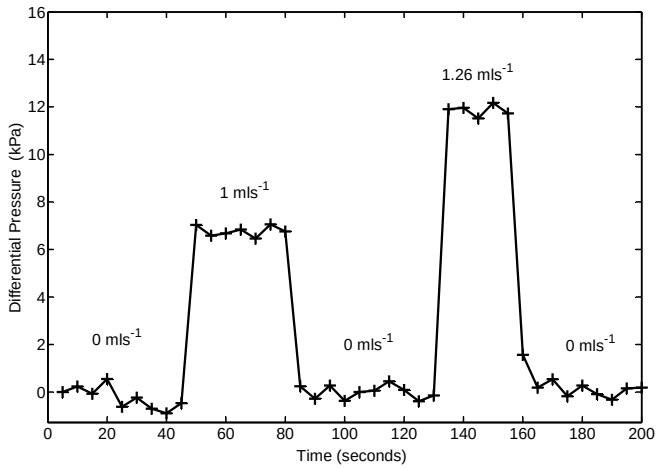


**Figure 6.14:** The pressure differential calibrated from the gratings pressure response for two different flow rates

To allow flow from one membrane to the other, via the temperature reference and chemical sensor grating an aluminium fixture as illustrated in Figure 6.12 was used. The fixture contained an 8 mm long channel of thickness 1 mm and depth 100 $\mu$m. Figure 6.14 depicts two different flow rates along the channel with respect to the calibrated differential pressure of the membranes. The flow resolution for this device is $\sim$33 $\mu$ls$^{-1}$, however, it must be noted that this resolution is dependent upon the flow resistance of the channel.

## 6.5 Conclusions

A differential pressure sensor has been realised by removing a section of the underlying silicon in our silica-on-silicon device, such that a thin silica membrane remains. Integrating the membrane component into the established grating based

sensors allows the realisation of a lab-on-a-chip based device that is capable of monitoring pressure, flow, temperature and have chemical sensitivity.

The maximum pressure resolution demonstrated so far has been 5 Pa, which has been achieved over a 100 kPa range. Fabricating a membrane such that the inherent thermal mismatch stress is greater than the critical stress required for buckling allows for the differentiation between positive and negative pressure differentials.

The spectral response of a grating upon a deformed membrane can be understood through the theoretical strain response the grating undergoes. Using this information has identified optimum locations for grating positioning and can be utilised in future device refinement.

# Chapter 7

# Thermo-Optic Effects

## 7.1 Introduction

Thermo-optic effects, which are refractive index changes caused by temperature variations in a material, have been demonstrated in commercial OADM configurations. These devices are of particular interest as there typical tuning speed is millisecond order [149].

Silica-on-silicon devices are ideal platforms for thermo-optic based OADM devices as they are physically and chemically stable. The majority of literature covering thermo-optically tuned Bragg gratings describes devices in fibre [150]. However, fibre based devices do not possess the integration advantages associated with planar technology [112]. Thermo-optic based OADM have also been demonstrated in several material platforms including silica-on-silicon, silicon-on-insulator [151], [152] and polymers [153], [112]. For large thermo-optic tuning ranges in planar devices ( 2500 GHz, corresponding to 20 nm in the C-band) polymer based substrates are best suited [112]. While polymers offer impressively large tuning ranges, there is an advantage in using silica-on-silicon technology especially as it is well established in telecom networks where it is used for AWG's, splitters and thermo-optic switches [27].

This chapter considers thermo-optic tuning of DGW devices for potential OADM applications.

## 7.2 Theory

The operational theory of the presented devices uses local heating of a Bragg grating to induce strain and thus tune the grating. Two geometrical configurations are considered, one configuration acts to polarise the input light as well as thermo-optically tuning it whilst the other does not polarise the light. The purpose of this section is to outline the theory of device operation for the two geometries examined.

### 7.2.1 Thermal Response

The thermo-optic effect is basically a special case of the strain-optic effect, where strain is a result of a temperature change. It is understood that a temperature increase results in thermal expansion, which can be expressed as strain such that

$$\epsilon_i = \alpha \Delta T \tag{7.1}$$

where $\alpha$ is the thermal expansion coefficient. Inserting Equation 7.1 into Equations 5.28 and 5.29 gives

$$\frac{\Delta\lambda}{\lambda} = \Big(1 - \frac{n^2}{2}(p_{11} + 2p_{12})\Big)\alpha\Delta T \tag{7.2}$$

which has assumed that the thermal expansion is equal along each principle axis. It is noted that the spectral shift resulting from temperature variation is different for each polarisation only as a consequence of the devices initial birefringence. Equation 7.2 is generally put more elegantly as [154].

$$\Delta\lambda_B = \lambda_B(\alpha + \zeta)\Delta T \tag{7.3}$$

where $\alpha$ is the thermal expansion coefficient and $\zeta$ is the thermo-optic coefficient. These coefficients correspond to change in grating pitch and effective index respectively. At the 1550 nm telecom wavelengths bulk heating experiments show the summation of these two coefficients to be about $10 \pm 1$ pmK$^{-1}$.

### 7.2.2 Localised Heating

While bulk temperature monitoring for thermal referencing is a proven tool, bulk temperature manipulation for tuning applications has many disadvantages including a poor response time and low energy efficiency. By locally heating a grating element, one is manipulating a smaller thermal mass thus faster response time and greater energy efficiency is achieved. Local heating also has the advantage of multiple tuning elements being placed on one chip and tuned independently.

The proposed concept, illustrated in Figure 7.1, considers a small heating filament aligned over the top of the Bragg grating element. As the thermal conductivity of silicon is one-hundred times greater than silica's, heat is effectively removed from the local area allowing fast switching.

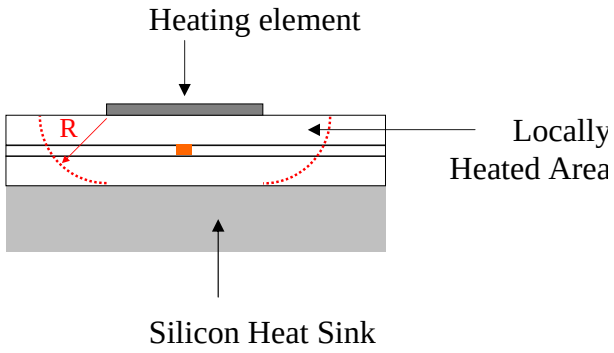


**Figure 7.1:** Schematic of localised thermal tuning concept

The silicon in turn can be placed in contact with a more effective heat sink. As a loose approximation for low dissipated powers the thermal gradient can be approximated to be within the red perimeter line, indicated in Figure 7.1.

There are two adaptations of the geometry illustrated in Figure 7.1, the basic geometry as shown and an adapted geometry were the overclad is removed, leaving the filament in direct contact with grating. Tuning range, tuning efficiency and response time is expected to be improved through removing the overclad layer. However, due to the large imaginary part of the metal heating filament, the adapted geometry is observed to act as a polariser, whilst the basic geometry does not.

### 7.2.3 Metal-Clad Polariser

A metal clad polariser is fabricated by depositing a thick metal layer onto the core of a guided mode. As previously discussed in Chapter 4, a plasmon hybrid mode is established for TM but not TE polarisations, as a result of Maxwell's equations. The TE and TM guided modes can be visualised, illustrated in Figure 7.2. These simulations consider a 350 nm thick nichrome layer of refractive index 3.542 + 6.436i [7].

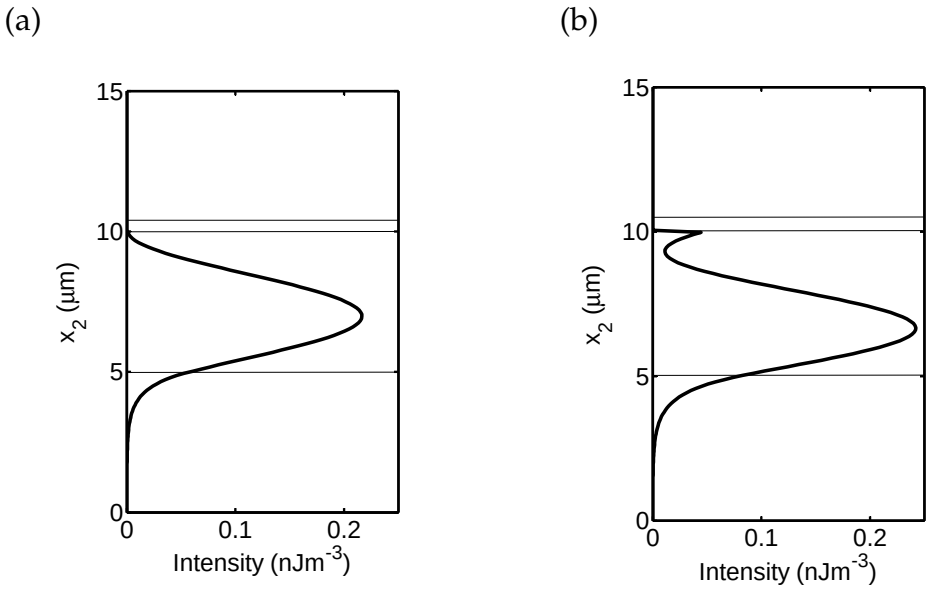


**Figure 7.2:** The supported modes for a topless sample with a thick NiCr filament overlay for (a) TE polarisation (b) TM polarisation

For such a thickness of nichrome the TE mode has an effective index of 1.4552 + 2.624x$10^{-5}$i and the TM mode has an index of 1.4539 + 8.274x$10^{-4}$i. As the imaginary effective index for the TM hybrid mode is greater than the normal supported TE mode, the TM polarisation undergoes greater absorption, thus polarising the input light. This effect is indeed observed in the reflection spectra of the fabricated device for mm lengths.

## 7.3 Fabrication

In this work local heating was realised through the use of a nichrome filament, which was deposited using a standard photolithographic technique and e-beam

sputtering system. As previously discussed in Chapter 3 photolithography is an optical means for transferring patterns onto a substrate, in this instance a heating filament was aligned over a pre-DUW grating. The fabrication process involved in this lift-off technique is depicted in Figure 7.3.

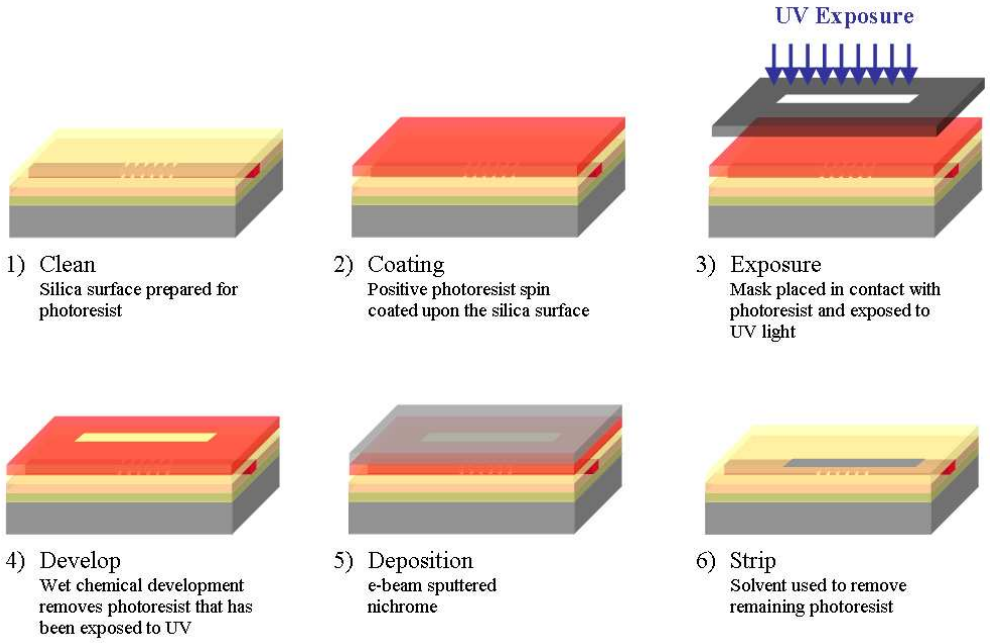


**Figure 7.3:** The photolithography technique

Firstly the pre-diced wafer was cleaned of contaminants and degreased, using solvents and distilled water. Subsequent to this cleaning a prebake step was required in order to evaporate solvent residue. Prebaking was done in a convection oven at 100$^o$C for 20 minutes. A positive photoresist was spin-coated to an even thickness of 1$\mu$m, upon the wafer.

Using a contact mask aligner the filament design depicted in Figure 7.4 was aligned over the Bragg grating. Subsequent UV exposure of the design resulted in the decomposition of a development inhibitor within the photoresist, such that on exposure to developer solution the photoresist in the exposed area dissolved.

To stabilize and harden the developed resist a post-bake stage was made. The sample was then placed into an e-beam sputterer where nichrome was deposited. Swilling the device after sputtering removed the remaining photoresist and the nichrome which lay upon it, leaving a single heating element remaining.

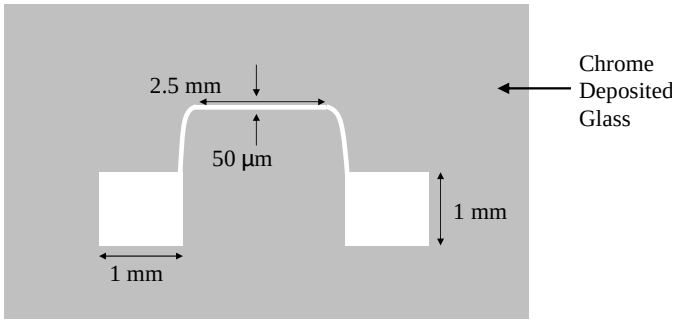


**Figure 7.4:** The specification of the heating filament

While alternative materials such as gold and chromium could have been used as a heating filament nichrome was chosen as it has a moderately large resistivity for a conductor and less readily oxidises.

The filament widths tested were 25 $\mu$m , 50 $\mu$m and 100 $\mu$m wide, with approximate thicknesses of 400 nm. As a thinner filament allows a more localised heat delivery, and the 25 $\mu$m filament was observed to burn out before a substantial tuning range could be achieved, a 50 $\mu$m filament was used in the following experiments.

The two devices fabricated were taken from two different types of wafer, one with an FHD overclad layer and one without. Both samples had a transverse width of 10 mm and length of 20 mm. A set of four Gaussian apodised Bragg gratings of 2 mm length and separated by 1 mm intervals were UV written into each device. The bandwidth of the gratings was 1 nm, corresponding to 125 GHz in the C band. It must be noted that this is too large for DWDM applications, but could be made narrower for future commercial realisation.

The final device, illustrated in Figure 7.5, was V-groove pigtailed and mounted on an aluminium block. Thermal heatsink compound was placed between the silicon wafer and the thermal reservoir (aluminium block) to improve the thermal conductivity. The device also featured a printed circuit board which was glued onto the nichrome terminals using conducting silver epoxy.

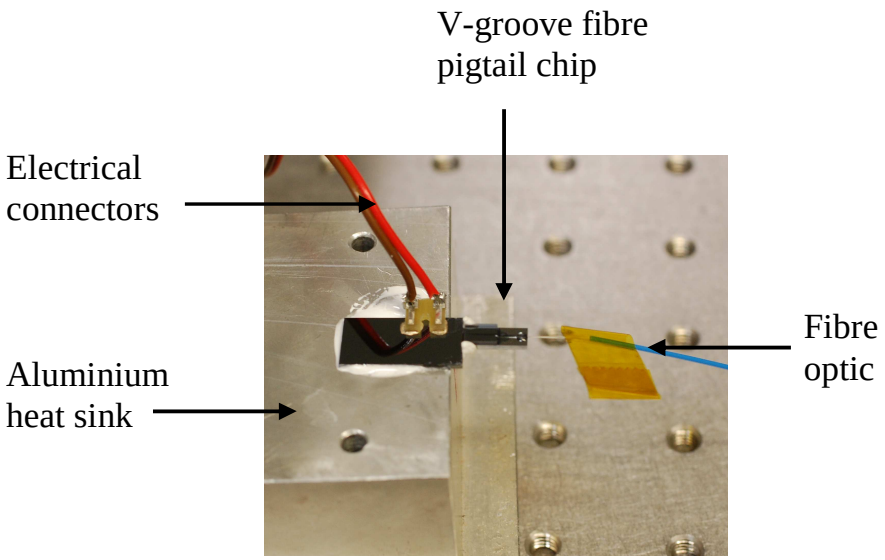


**Figure 7.5:** The thermal tuning device

## 7.4 Non-Polarising Filament

For the non-polarising geometry a 16 $\mu$m FHD overclad layer separates the nichrome filament and the grating. The total thickness of the device is 1.04 mm and has a total silica thickness 39 $\mu$m. The deposited filament has a thickness of 400 nm and a total resistance of 1.16 k$\Omega$.

Maximum tuning of the device occurred when the nichrome filament was dissipating 2.4 W of power. This resulted in a spectral shift of 1.23 nm, illustrated in Figure 7.6. This corresponds to a 154 GHz shift in the C band, which is over three times a typical 50 GHz DWDM channel. The thermal response of the grating is known to be 10 pm$^o$C$^{-1}$, meaning 154 GHz of tuning is the result of 123 $^o$C temperature change in the core. To obtain the desired 50 GHz of tuning for DWDM applications only a 40 $^o$C temperature change is required in the core.

By setting the central wavelength of a tunable laser to the full width half maximum point on the Bragg grating spectra the response time of the device was measured, as illustrated in Figure 7.7. A square wave signal with a peak of 24 V and trough of 0 V was supplied to the filament with a frequency of 1 Hz. The rise time of the supply was $\sim$0.2 $\mu$s, as measured from a digital oscilloscope. This corresponded to a maximum dissipated supplied power of 0.5 W and spectral shift of 0.26 nm. Figure 7.7 shows an exponential decay in reflected laser power from the grating as the filament is switched on. This is due to the central wavelength of the grating

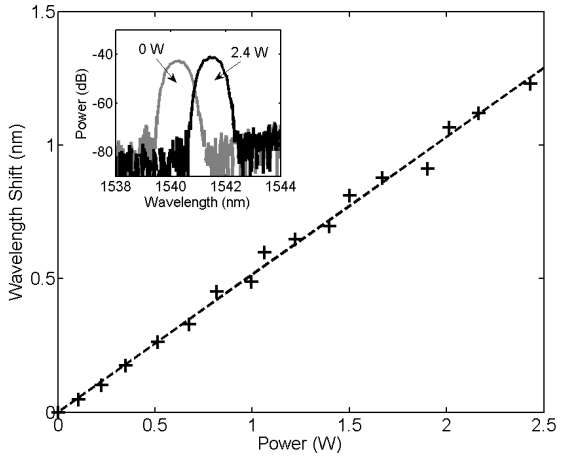


**Figure 7.6:** Thermo-optic tuning curve in relation to the power supplied to NiCr filament

response being tuned to higher wavelengths. The time response of this effect is 1.02 ms. This value is comparable for both switching the filament on and off.

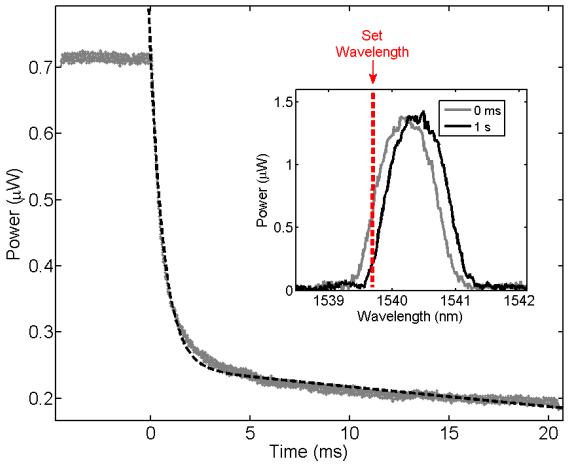


**Figure 7.7:** Response time for a set wavelength, in a thermo-optic tuned Planar Bragg Grating

Placing a cold plate, set to 10 $^{o}$C, in contact with the silicon reduced a small bulk heating/cooling effect observed after the initial local heating/cooling took place. The time constant of this effect was 1 s. The tuning efficiency at this temperature was 65 GHzW$^{-1}$, as compared to 54 GHzW$^{-1}$ without the presence of the cold plate.

Bulk heating can be controlled by placing the device on a cold plate and manipulating the cold plate's temperature. This process reduces bulk heating through

increasing heat flow between the heat sink and the filament, as a result of a larger thermal gradient. Heat flow between the filament and heat sink can also be increased by reducing the thickness of silica and/or silicon. The following section shall reduce bulk heating by altering the geometry of the silica-on-silicon device. The considered device does not reduce the thickness of the silica or silicon but is such that the overclad of the silica is removed and an underclad of equal thickness replaced. This means that filament is in direct contact with the grating and thus more efficiently heats the grating. Due to the improved efficiency a lower temperature gradient between the filament and heat sink is required to achieve the same level of tuning, thus reducing bulk heating effect at higher tuning ranges. It must be noted that the presence of the underclad acts as a control in these experiments (i.e. the effect not being a result of the silica thickness) and future devices can remove this layer.

## 7.5 Polarising Filament

For the polarising geometry the total thickness of the device was 1.04 mm and a total silica thickness of 40 $\mu$m FHD. The deposited filament had a thickness of 350 nm and a total resistance of 1.15 k$\Omega$.

Both polarising and non-polarising devices used a similar filament construction. As a dissipated power of 2.4 W resulted in the burning out of the filament, the following experiments did not exceed a power dissipation range of 1.3 W. At this power the polarising device displayed 1.06 nm of tuning, illustrated in Figure 7.8.

The tuning efficiency of this device is 102 GHzW$^{-1}$ which is a 60% increase in efficiency compared to the non-polarising device. Potentially the device can be tuned up to 1.96 nm if the maximum operating current is taken.

Tuning of a single 50 GHz channel corresponds to 0.4 nm of tuning at 1550 nm wavelengths. Tuning of over one entire channel is depicted in Figures 7.9 (a) and (b) for a non-polarising and polarising device respectively. The instantaneous tuning of both devices is of the order $\sim$1 ms. However, due to the non-polarising geometry having a lower tuning efficiency an additional 0.4 W is required to tune the grating by the same amount. As greater powers are supplied a bulk heating effect is observed, which is absent for the case of the more efficient polarising de-

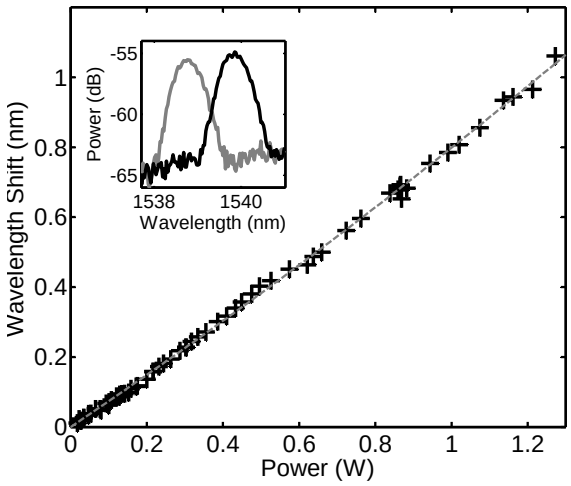


**Figure 7.8:** The tuning range of a topless device

vice.

(a) (b)

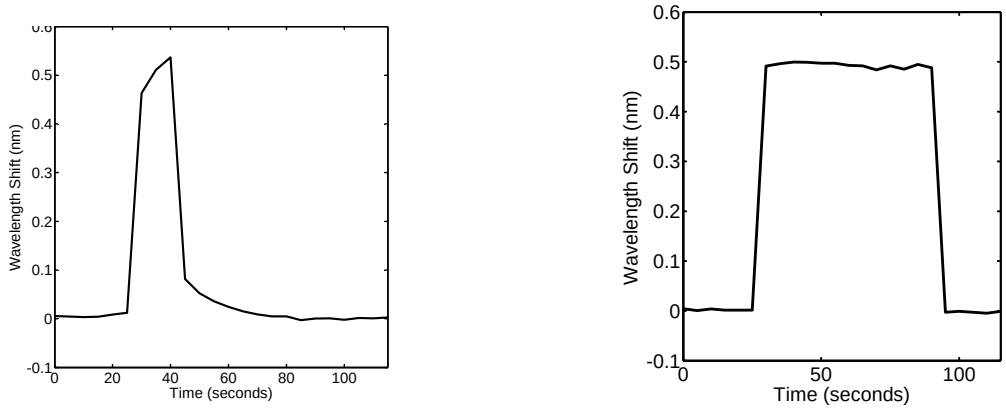


**Figure 7.9:** The response of thermal tuning chips showing (a) overclad geometry showing bulk heating and cooling (b) a device without an overclad showing negligible bulk heating and cooling for a similiar tuning range

An interesting effect that was discussed in Chapter 4 is that TE modes, with a metal overclad, are insensitive to index change. This is illustrated in Figure 7.10 where the tunable grating shows no sensitivity, but the other gratings without a metal clad do. As all of the chip, apart from the locations under the filament are sensitive to the analyte, a specific analyte can be selected to give athermal control on the chip [155]. That is to say, if the refractive index response of the analyte is of opposite magnitude to that of silica and of sufficient magnitude, the intermodal

dispersion can counter-act the fractional change in pitch of the grating. Interestingly, this effect would only affect the areas of the chip that are not covered with a filament. This could potentially allow circuit structures with thermal control to be more tightly packed.

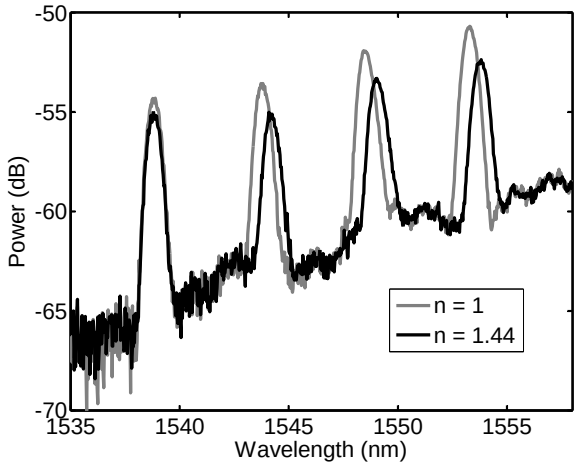


**Figure 7.10:** The spectral response of four gratings of TE polarisation in a topless sample under two different refractive index ovelays. The lowest wavelength reflection peak has a thick NiCr overlayer between the grating and the exposed index.

## 7.6 Conclusions

The fabricated devices demonstrated a tuning capability of over two DWDM channels, the degree and speed of tuning indicates potential application in dynamic optical networks, as an optical add-drop multiplexer.

So far the heating elements have been placed parallel to the grating length. However, future devices may consider placing multiple heating elements perpendicular to the grating such that their individual tuning would manipulate the grating chirp.

Future devices may also consider the use of trenches, similar to those considered in Chapter 4, to manipulate heat flow making the devices more effective and efficient. Similar concepts have been previously introduced by Kasahara et al to improve device efficiency of a thermo-optic switch [156].

# Chapter 8

# Multimode Inteference Device

## 8.1 Introduction

The Multimode Interference (MMI) component is a useful building block in photonic integrated circuits, with many practical applications [157]. These include 3 dB couplers, Mach-Zehnder interferometers (MZI), ring lasers, and optical switches. The advantages they have include superior performance, a small device footprint and an excellent tolerance to polarization and wavelength variations [158].

MMI based components predominantly operate in the index guiding regime, which has been explained in Chapter 2. It has been found that when direct UV writing MMI devices through raster scanning out diffusion [4] and proximity effects [159] become problematic. As discussed in earlier chapters, out diffusion is time dependent. The time taken to fabricate a raster scanned MMI device is entirely dependent upon the dimensions of the MMI device desired and intensity of the laser. Using typical scan speeds of 1 mm/min for a 100 $\mu m$ by 2.5 mm MMI device would require approximately 100 minutes to fabricate. OH-flooding a sample prior to UV writing or cooling a sample during UV writing can be implemented to reduce the effect of out-diffusion. However, OH-flooding has an associated extrinsic loss increase and cooling a sample has associated complications when applied to a dual beam configuration, as discussed in Chapter 3.

This chapter presents theoretical direct UV written MMI devices that potentially reduce out diffusion and proximity effects acting in the guiding MMI area as well as reducing the level of excess loss. Measurements from proof of principle devices

are presented and fabrication considerations highlighted.

The novel device operates in a leaky mode regime, reducing excess loss by optimising an interference based waveguide concept. To develop the concepts behind this novel device the accepted theory for guided mode based MMI components and interference based waveguides needs to be discussed.

## 8.2 Theory

The theory of MMI devices is extensively covered in works by Okamoto [27] and Soldano [157], which are considered good foundation stones in MMI literature and shall be summarised in this section.

Generally MMI designs are based on waveguides in the guided mode regime (also known as the TIR regime) [157]. However, interest in making gas and liquid based waveguides has directed some research towards reducing excess loss in leaky modes though interference guiding [160]. The purpose of this section is to outline the theory of MMI devices then apply these concepts to interference based waveguides.

### 8.2.1 Multimode Interference Coupler

The basic concept of an MMI device is that it is a large waveguide and so can support many modes. MMI devices are three dimensional constructions but for analysis can be reduced to a two dimensional problem, by using the effective index method [27]. To inject and remove light a number of access waveguides are placed at the beginning and end of the MMI device, illustrated in Figure 8.2.1. Such a structure is known as an n x m MMI device, n being the number of input and m the number of output channels, thus Figure 8.2.1 illustrates a 1 x 4 MMI.

The MMI section has a Length $L_{MMI}$ and a width $W_{MMI}$. As treated throughout this thesis the coordinate axes are defined such that propagation is along the $x_1$ direction. The device operation consists of an input field located at $x_1$=0, which acts to excite each of the guided slab modes by various amounts. Assuming such a slab structure supports J modes numbered j = 0,1,2,...(J-1), with propagation constants

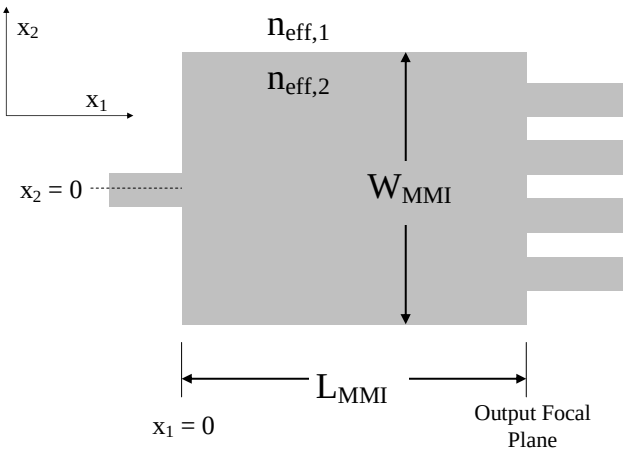


**Figure 8.1:** The two dimension representation of an MMI device

$\beta$, defined as

$$\beta_j = k_0 n_{eff}^{(j)} \tag{8.1}$$

where $n_{eff}^{(j)}$ is the effective index of the $j^{th}$ mode and $k_0$ is the free space propagation constant. Each mode propagates through the slab in the $x_1$ direction, with a different velocity. For the case of a 1 x n symmetric MMI coupler, only even modes are excited in the slab. The lateral field profiles of the slab modes thus have the form

$$\psi_j(x_2) = \begin{cases} B_m exp[q_j(x_2 + W_{MMI}/2)] & x_2 < -W_{MMI}/2 \\ A_m cos(h_j x_2) & |x_2| < W_{MMI}/2 \\ B_m exp[q_j(x_2 - W_{MMI}/2)] & x_2 > W_{MMI}/2 \end{cases} \tag{8.2}$$

where for convenience

$$h_j^2 = k_0^2 n_{eff,2}^2 - \beta_j^2 \tag{8.3}$$

$$q_j^2 = \beta_j^2 - k_0^2 n_{eff,2}^2 \tag{8.4}$$

$$h_j = \frac{(j+1)\pi}{W_{eff}} \tag{8.5}$$

here $W_{eff}$ is an effective MMI width which is greater than the fabricated width and arises due to the lateral penetration depth of each mode into the cladding, in

accordance to the Goos-Hänchen shifts at the waveguide boundaries [161]. Equivalently, this can be inferred through BPM simulation.

At specific lengths along the MMI device the input light distribution is found to be self imaged. The location of this self imaging can be calculated by firstly substituting Equations 8.4 and 8.5 into each other

$$\left(\frac{(j+1)\pi}{W_{eff}}\right)^2 = k_0^2 n_{eff,2}^2 - \beta_j^2 \tag{8.6}$$

this can be rearranged and approximated by a binomial expansion to give

$$\beta_j = \left(k_0^2 n_{eff}^2 - \left(\frac{(j+1)\pi}{W_{eff}}\right)^2\right)^{0.5} \tag{8.7}$$

$$\approx k_o n_{eff} - \frac{(j+1)^2 \pi \lambda}{4 W_{eff}^2 n_{eff}} \tag{8.8}$$

Considering the propagation function and Equation 8.8 it can be shown that self imaging will occur at periodic lengths of [27]

$$L_{MMI} = \frac{n_{eff,2} W_{eff}^2}{\lambda} \tag{8.9}$$

It is understood [27] that N equally spaced images occur at lengths given by

$$x_1 = L_{MMI}/N \tag{8.10}$$

which is true for any integer.

MMI components are currently being realised under leaky mode operation using interference based waveguides. Interference based regimes can use antiresonance reflection [41] [160] [162] or photonic bandgap mechanisms [163] [164] to quasi-guide light. It must be noted, that the formulism derived for guided mode MMI devices hold true for leaky mode MMI devices. The presented MMI device operates using an antiresonance based waveguide structure to quasi-guide light.

### 8.2.2 Antiresonance Based Waveguides

Antiresonance based waveguides reduce the leakage of energy from a waveguide structure by incorporating high and low refractive index cladding layers of correct thickness as proposed by Duguay et al [162]. The cladding layers behave as Fabry Perot reflectors which can be composed of single or multiple elements. This acts to suppress energy leakage of a certain mode. Such structures are labelled as Antiresonance Reflecting Optical Waveguide (ARROW) components.

To derive the conditions for resonance or antiresonance, it is best to consider geometrical optics. A plane wave characterised by wavevector **k** will replace each mode in this instance. The components of which are $\beta$ and u, as illustrated in Figure 8.2.2.

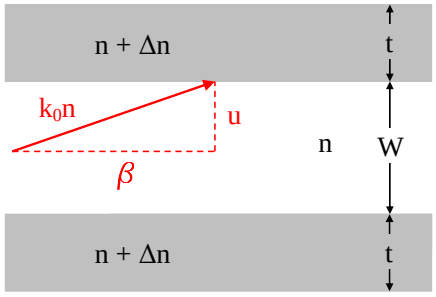


**Figure 8.2:** Waveguide based upon ARROW principle

If the thickness of the ARROW element (shaded in grey in Figure 8.2.2) is considered, a round trip within it accumulates a phase $\phi$ expressed as

$$\phi = 2tu + \phi_B \tag{8.11}$$

As illustrated in Figure 8.2.2, t is the thickness of the elements of the waveguide and u is the perpendicular component of a wavevector. $\phi_B$ is due to the boundary reflections, equal to $\pi$, for our single element case. Now, if $\phi$ is an even multiple of $\pi$ then the wave interferes constructively with itself and is in resonance with the element. Likewise for an odd multiple of $\pi$, the plane wave is in antiresonance. After mathematical derivation from Equation 8.11 the analytical solutions for constructive and destructive resonance become of the form [165]

$$t = \frac{m\lambda}{4(n+\Delta n)}\left[1 - \left(\frac{n}{(n+\Delta n)}\right)^2 + \left(\frac{\lambda}{2(n+\Delta n)W}\right)^2\right]^{-0.5} \tag{8.12}$$

where m odd corresponds to optimised low loss and m even, high loss.

An issue with the ARROW device is that its antiresonance is optimised for an arbitrary length of waveguide. Considering a 1 x n MMI structure, from the input waveguide the light diffracts out, becoming incident with a wall at varying wavevector components u, dependent upon the distant from the input. The following work develops ideas that manipulate the ARROW structure such to reduce the energy leakage for this diffracting mode.

## 8.3 Antiresonance DUW MMI Device

Previous work to fabricate MMI devices using DUW has been undertaken by Knappe et al [4] and involved raster scanning the device with the UV laser spot, illustrated in Figure 8.3.

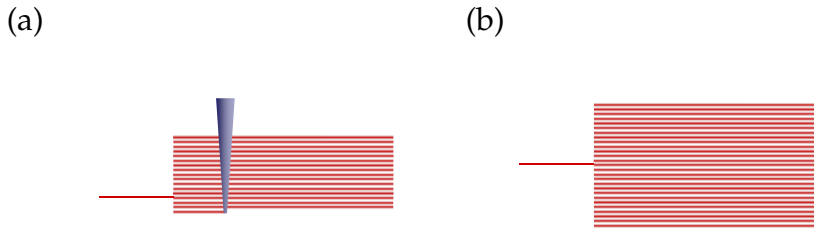


**Figure 8.3:** Schematic of a raster scanned DUW device illustrating (a) fabrication (b) complete structure used in [4]

Several problems arise as a result of this raster scanning technique, including a significant level of out-diffusion arising from its associated long writing time. As an antiresonant structure only requires side wall definition it has a much reduced writing time and hence reduced level of out diffusion. It is also believed that proximity effects when UV writing produce a non homogenous index structure [159]. Again as the antiresonant structures are outside the main body of the device and not integrally part of it, the effects of proximity writing on the basic MMI operation are reduced.

The simplest way of achieving an antiresonace structure would be to write 'single element' boundaries for the MMI, illustrated in Figure 8.4.

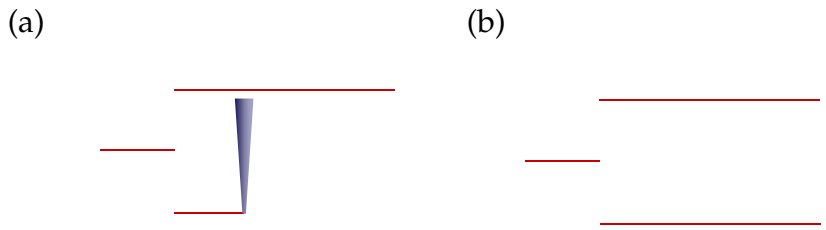


**Figure 8.4:** Schematic of a single element DUW device illustrating (a) fabrication (b) complete structure

An improvement to the single element construction would be to have multiple elements of constant period illustrated for five elements in Figure 8.5.

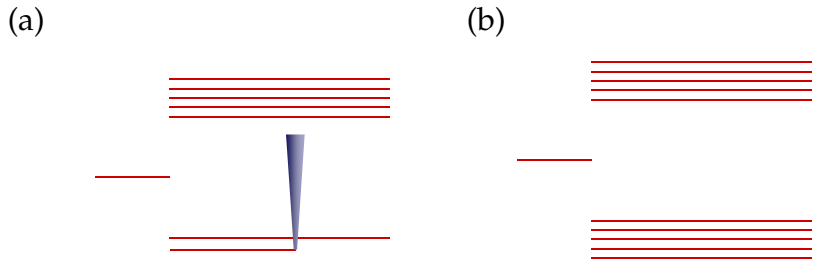


**Figure 8.5:** Schematic of a five element DUW device illustrating (a) fabrication (b) complete structure

Utilising the 2D control of the translation stages it is possible to fabricate a device with 'locally optimised' period, a concept that is difficult to realise using traditional ARROW fabrication processes. Due to the low index contrast associated with DUW, this local optimisation becomes more essential.

The following work considers the optimisation of a 1 x 4 MMI device using the BPM algorithm outlined in Appendix A. Optimum designs for single, multiple and locally optimised elements shall be addressed.

### 8.3.1 Single Element

As the real refractive index profile of the UV written channel is unknown two different constructions for the single element side walls were tested, one was a top-hat index profile and the other a Gaussian index change, as illustrated in Figure

8.6. Both simulations defined an imaginary refractive index, at the boundaries of the simulation, which did not overlap with the MMI structure, such to make the boundary conditions absorbing[1].

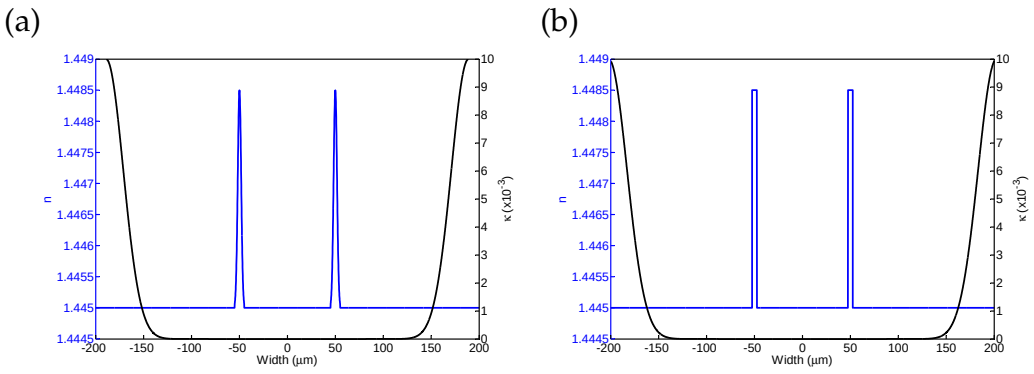


**Figure 8.6:** The two tested index profiles for single element operation depicting the real n and imaginary $\kappa$ constructions for, (a) Gaussian elements and (b) top-hat elements

Figure 8.7 depicts the BPM simulation of the index construct in Figure 8.6. Due to the top-hat walls having discrete reflection locations the intensity pattern is sharper. To compare the effectiveness of the simulation, the end face outputs of both the Gaussian and top-hat simulation were compared to a fabricated device.

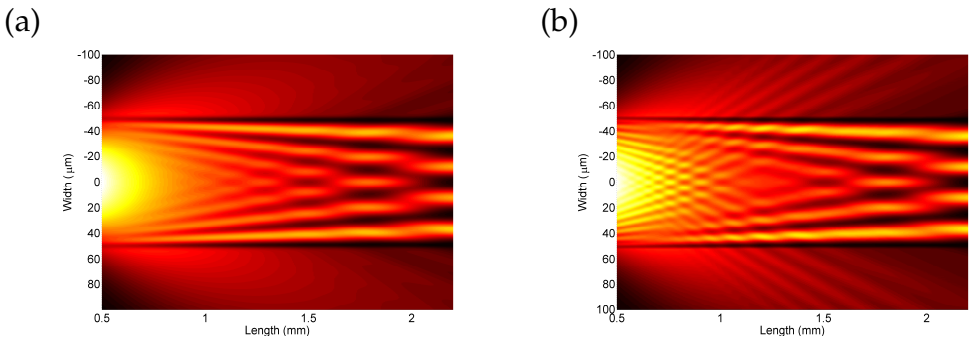


**Figure 8.7:** The field intensity of a 1 x 4 single element MMI device as simulated by BPM, considering (a) Gaussian and (b) top-hat elements

The device was fabricated into a non index matched silica-on-silicon wafer, which had a high concentration of germanium in the core allowing for single mode confinement in the lateral direction. The dual beam set-up was used to write a 100 $\mu$m by 2.2 mm single element MMI structure, with a fluence of 15 kJcm$^{-2}$. Prior to UV writing the samples were side polished and hydrogen loaded at 120 bar for

[1]Technically these should be described as absorbing walls and not absorbing boundary conditions

two weeks. The MMI device was written up to the polished edge and viewed in transmission. To aid characterisation alignment a grating was written in the input waveguide. For alignment of light out of the device a HeNe was launched into the input waveguide and observed in transmission through coupling into a SMF-28 fibre. After HeNe alignment a tuneable laser set at 1550 nm was used to launch light through the device, as illustrated in Figure 8.8.

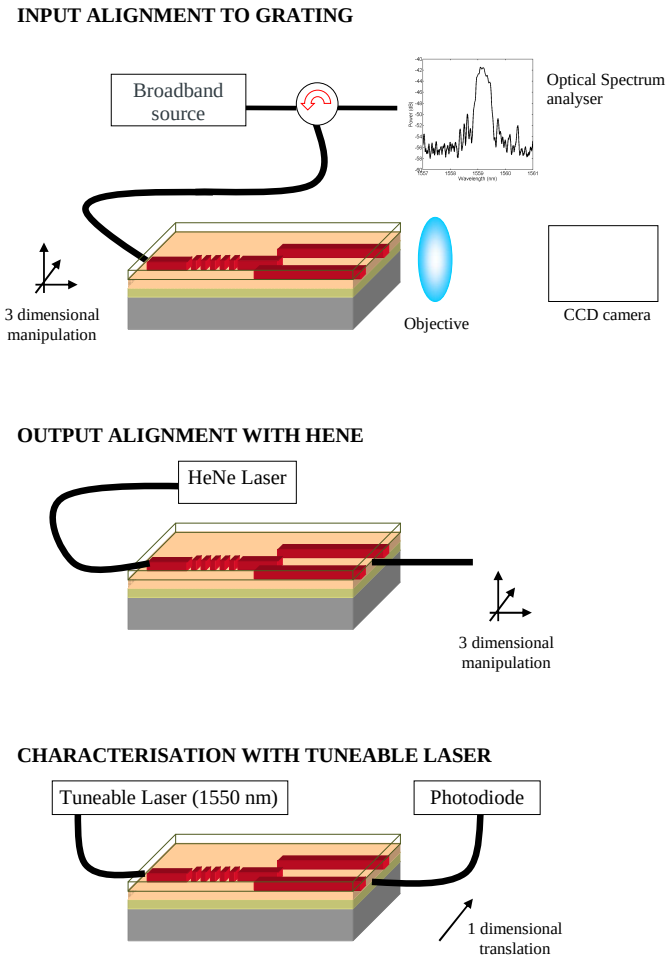


**Figure 8.8:** Characterisation and alignment set-up of the direct UV written MMI device

The power coupled into the fibre was measured at different lengths along the output face. To compare the simulated and empirical data the simulated data was convoluted with a Gaussian, which represented the scanned fibre in the empirical measurement, illustrated in Figure 8.9.

There are small deviations between the simulated and empirical data sets, illustrated in Figure 8.9. The top-hat elements appear to give an intensity profile that

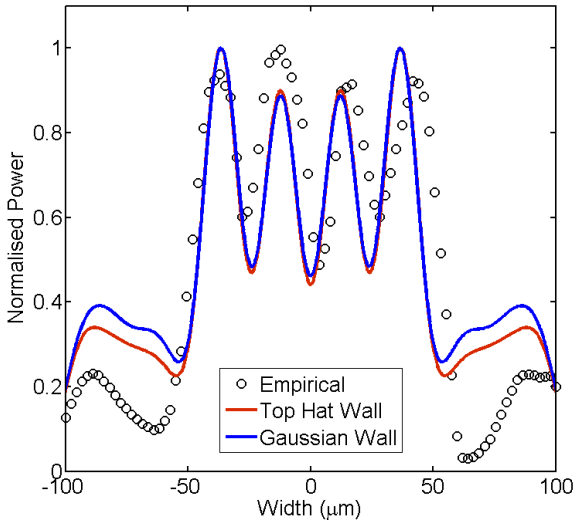


**Figure 8.9:** An endface scan of a fabricated 1x4 single element MMI device compared with BPM simulation of tophat and Gaussian side walls

is closer to that empirically measured and so justifies use of it as the index profile in the following simulations.

The single element device can minimise excess loss by manipulating the index change[2] and element width, as simulated in Figure 8.10 (a). The form of this graph can be understood from Equation 8.12, which is plotted graphically in Figure 8.10 (b). Note the maxima and minima of the simulation coincide well with the analytical values. In addition as the index contrast reduces so too does the magnitude of the Fresnel reflections, as seen in Figure 8.10 (a) shows a greater blurring between the resonant and antiresonant conditions at lower index contrasts.

The lowest excess loss indicated from Figure 8.10 (a) is 25% or 1.25 dB. However, it must be noted that these regions of low loss coincide with regions of high index contrast, which are not achievable using the DUW technique. For the purpose of this work an index increase of $<5\text{x}10^{-3}$ shall be considered. To optimise element thickness for this index ceiling fabrication practicalities have to again be considered.

The optimum element thickness can be realised by either varying the focus of a single beam set-up, or encoding multiple passes, which can be achieved by the single or dual beam set-up. Defocusing the single-beam setup to achieve optimum

[2]It must be noted that the element index is considered as the increase in $n_{eff}$ which, although is similar to, is not the same as saying the induced index change of the channel.

(a) (b)

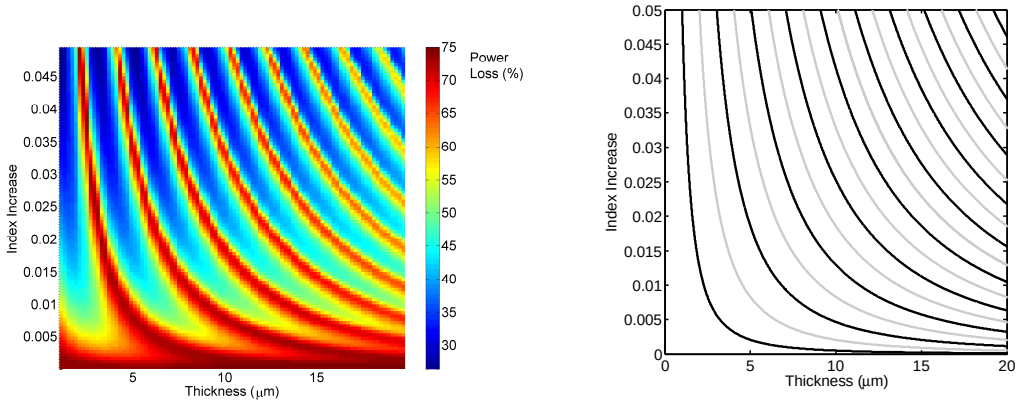


**Figure 8.10:** Optimum channel width and refractive index contrast as (a) modelled by BPM simulation (b) analytical evaluation from Equation 8.12 where the black lines indicate low loss (antiresonant) and grey lines high loss (resonant)

element thickness has an associated fabrication difficulty, more importantly single-beam operation removes the potential for incorporating Bragg gratings in device design. The use of multiple passes has additional complexities in fabrication due to proximity effects. Assuming the written channel of the cross beam setup has a fixed width of 5 $\mu$m the optimum index contrast is $\sim$0.0035, which corresponds to a theoretical loss of 4.6 dB.

Considering the two reflection faces of a single element contributing to two effective widths of the MMI the self-imaging lengths as calculated from Equation 8.9 are 9.3 mm 8.4 mm. Figure 8.11 illustrates self imaging occurring between these values.

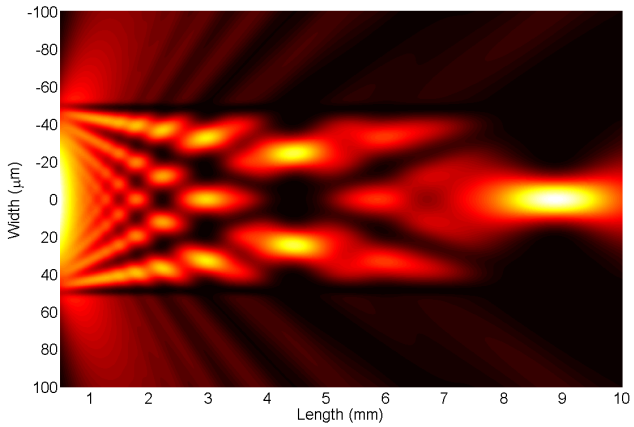


**Figure 8.11:** A BPM simulation depicting a 1 x 1 self imaging MMI single element device with index contrast 0.0035 and period 5 $\mu$m

Working with an element width of 5 $\mu$m and index contrast of 0.0035, multiple elements of constant period will be considered, in order to further reduce loss.

### 8.3.2 Constant Period

The index profile for a five element constant period device is shown in Figure 8.12 and has an imaginary index part similiar to that in the single element case.

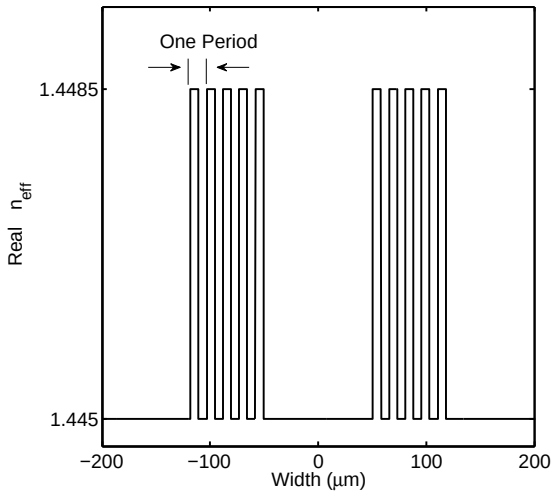


**Figure 8.12:** The real refractive index construction of a 5 element constant period MMI device

Considering the effect of multiple elements it is observed in Figure 8.13 (a) that as expected further increasing element number can further decrease the excess loss. Due to the fixed length of the device there is little advantage in increasing the period to over 5 elements.

Taking the 5 element device Figure 8.13 (b) illustrates the simulation of loss as a function of period and MMI width such to vary it between 0 and $^1/_2$ multiples of the period (defined as $\pi$). It is observed that there is negligible relation between the phase of the two walls and indeed this is true for a self imaged device.

An optimised and unoptimised five element construct is depicted in Figure 8.3.2, along with the respective losses along the length. For an unoptimised period of 14.3 $\mu$m (Figure 8.3.2 (b) and (d)) the light can be seen to spill through the elements. In contrast Figure 8.3.2 (a) and shows light filtering back in from the elements as they are under an antiresonance condition. Figure 8.3.2 (c) clearly shows

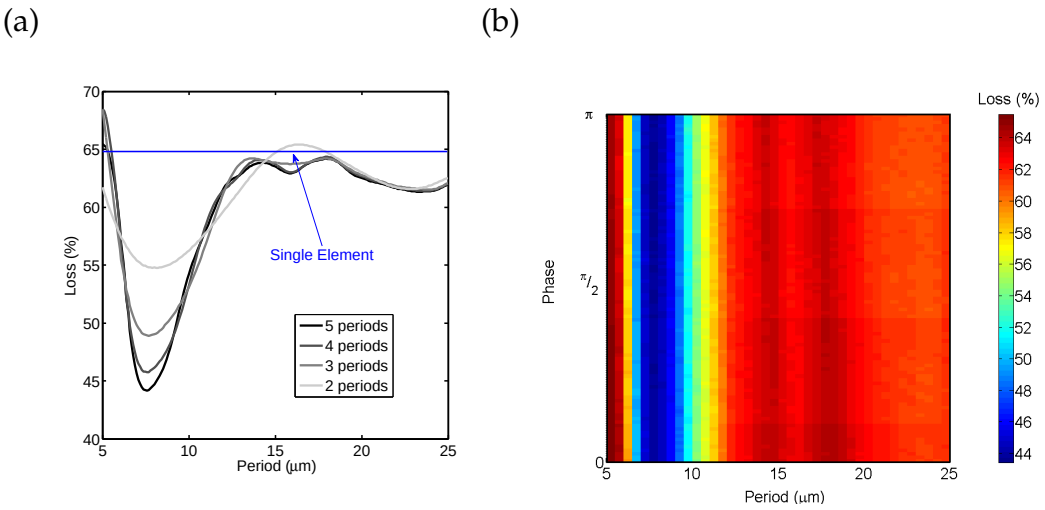


**Figure 8.13:** The MMI loss dependence for a constant period construct considering (a) different number of periods (the thin blue line representing the loss for a single element) and (b) the relationship between device loss, period and phase for a five element construct

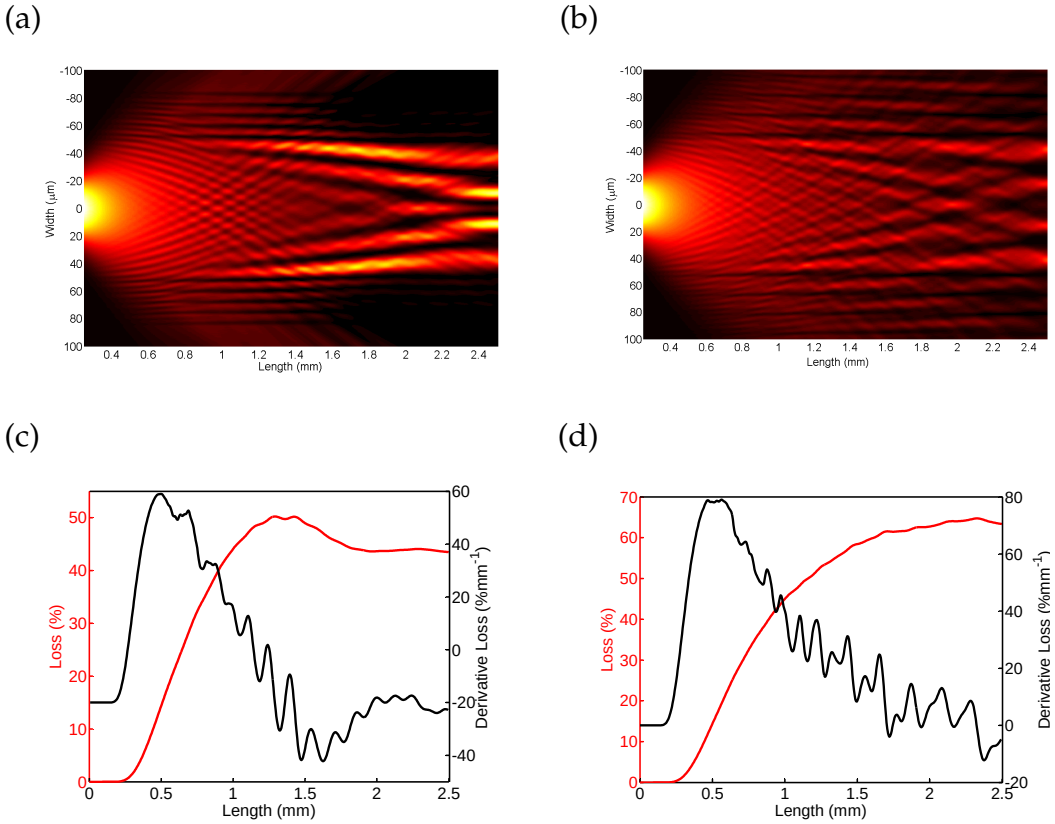


**Figure 8.14:** BPM simulations showing (a) intensity and (c) loss distribution for optimised five element period of 7.6 $\mu$m period and (b) intensity and (d) loss distribution for an unoptimised five element period of 14.3 $\mu$m period

the light filtering back into the device and a reduction in loss. It is also be observed when compared to Figure 8.7 (b) that the multiple element constructs have a larger imaging length. This is due to the multiple elements acting to give a larger effective width of the device. Which in turn makes the self-imaging length greater, as dictated by Equation 8.9.

Considering the five element construct, the optimum period results in a 2.5 dB loss, this is already a significant improvement on the single element device. To further drive down this loss the next construct will be a locally optimised period device.

### 8.3.3 Adaptive Period

The adaptive period construction was optimised by fitting a third order polynomial equation to the period as a function of the propagation length and a separate third order polynomial to the index contrast. Bounds were set for the period between 5 $\mu$m and 30 $\mu$m and for the index contrast between 0 and 5x10$^{-3}$, such that if the polynomial dictated values higher or lower than these bounds the return value would be the value of the bounds.

The seed values to optimize the polynomial were taken as the optimized constant period and refractive index values previously discussed. The Matlab function fminsearch, which uses Nedler-Mead algorithm [166] was then implemented to optimize the polynomial. Table 8.2 indicates the parameters for optimum index contrast, $\delta$, and period, $\Lambda$.

$$\begin{pmatrix} \delta \\ \Lambda \end{pmatrix} = \sum_{i=0}^{3} \begin{pmatrix} a_i \\ b_i \end{pmatrix} x_1^i \tag{8.13}$$

| coefficient \ i | 0 | 1 | 2 | 3 |
|---|---|---|---|---|
| a | 3.527e-3 | 1.372e-4 | 1.205e-4 | -2.153e-5 |
| b | 2.135e-6 | 4.840e-3 | 1.582e-4 | -3.639e-3 |

**Table 8.1:** The parameters of Equation 8.13, which give minimum excess loss for a 1 x 4 MMI

The form of the optimisation is given in Figures 8.3.3 (a) and (b).

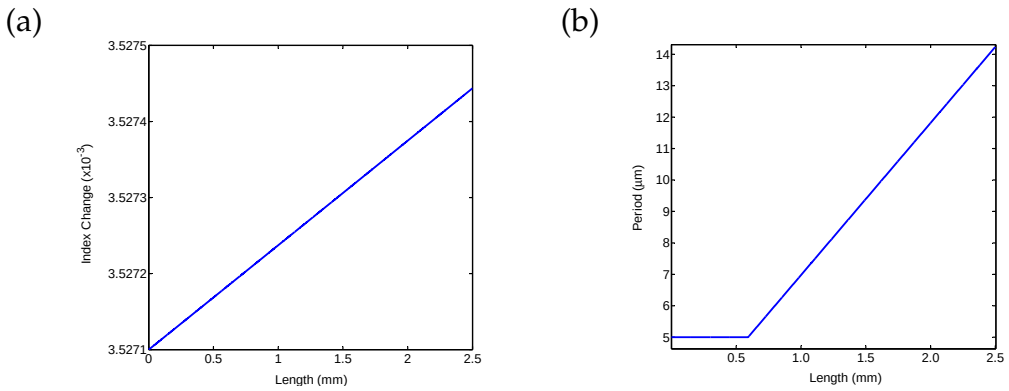


**Figure 8.15:** The form of the optimised period and index contrast with respect to propagation length along the MMI

The locally optimised period and index is of the form expected from theory. As can be visualised in Figure 8.2.2, for greater propagation lengths the wavevector component, u, is smaller and so the Bragg condition requires a larger period [125]. The picture of this device is more complicated as one obtains subsidiary bounces which also need to be considered. However, it can be appreciated that subsidiary bounces themselves have the same trend. Discrepancy between the optimised period and that suggested by the Bragg condition is believed to be a result of the capped width of the written element, which the period optimises to [125].

Figure 8.3.3 compares the simulated excess loss for a locally optimised MMI device with that of a raster scanned device. The Raster scanned simulation has an index contrast and width equal to the maximum index contrast of the local optimisation and a length of 3.9 mm. The output excess loss for the Raster scanned device is 1.65 dB compared to with 1.61 dB for the locally optimised arrangement. It can be seen that, for the same index contrast the locally optimised device has a lower associated loss! This comes in addition to other benefits such as a reduced writing time and the removal of proximity effects from the functional MMI region.

An interesting observation with the raster scanned device, illustrated in Figure 8.3.3 (d) is that loss appears to increase and decrease along the propagation length of the device, meaning some quantity of light is returning back into the raster scanned section of the MMI. This effect is believed to be the result of the Goos-Hänchen shift, allowing a fraction of the guided light to exist 'outside' the main raster scanned body of the MMI.

Excellent tolerance to wavelength variations is a key feature an MMI device pos-

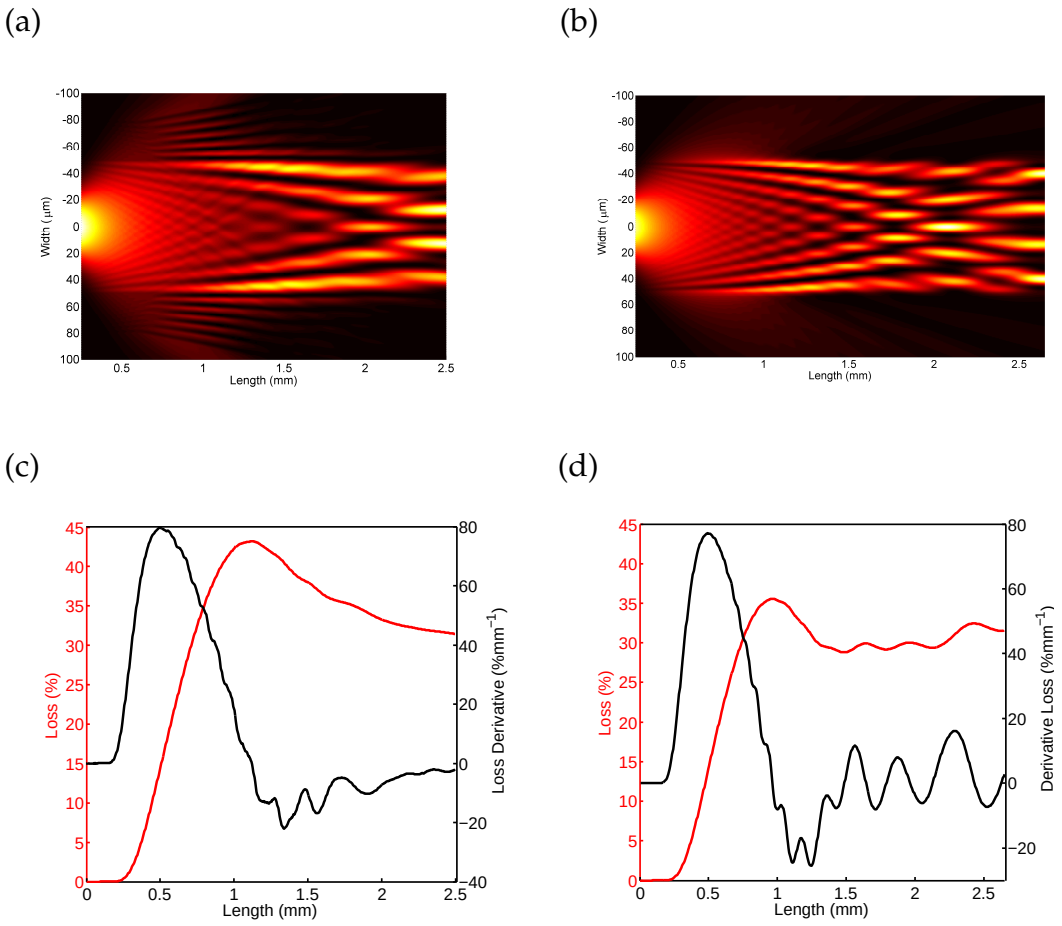


**Figure 8.16:** BPM simulations showing (a) intensity and (c) loss distribution for a locally optimised device and the (b) intensity and (d) loss distribution for a Raster scanned device

sesses. The adaptive period technique should thus show a comparable spectral loss variation and indeed this was observed through simulations, as illustrated in Figure 8.3.3. The adaptive period device is optimised to 1550 nm wavelengths and as can be seen from Figure 8.3.3 values that deviate from this optimised wavelength have an increased loss.

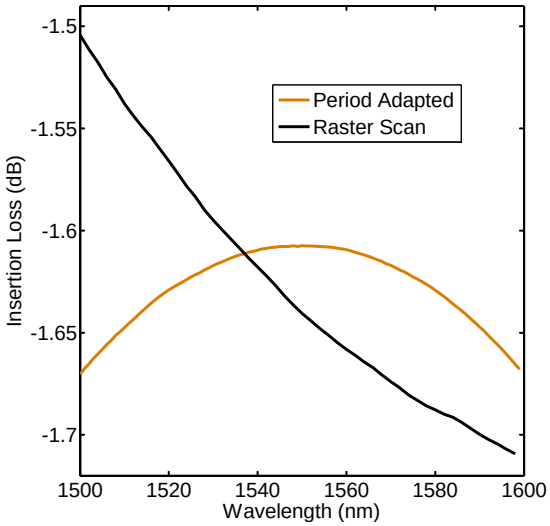


**Figure 8.17:** A simulation of excess loss with respect to variations in wavelength, for an MMI device optimised about 1550 nm wavelengths

The raster scanned device has a comparable spectral loss variation to the adaptive period, over the 200 nm spectral range simulated. However, the trend of the spectral losses is different. For the raster scanned device higher wavelengths show an increase in loss whilst lower wavelengths show a decrease in loss. This can be understood from Equation 8.9, reducing the wavelength, $\lambda$, acts to increase the required length, $L_{MMI}$, of the MMI device to achieve the same fold symmetry. As the length of the MMI device set is shorter than the length required to achieve the desired fold of symmetry one is effectively sampling the power 'upstream' thus there is less loss. This argument is conversely true for longer wavelengths.

It must be noted that due to the limitation of index contrast the optimised index has only a small influence on optimisation. Having control over the width of the written elements may further reduce the excess loss and widening the improvement it has over the raster scanned device.

## 8.4 Fabrication Considerations

Single mode confinement in the $x_3$ dimension of the device is required for optimum coupling between the single mode input and output waveguides. So far it has been assumed that there is single mode confinement in the $x_3$ dimension, however as the three silica layers in the conventional wafer design are index matched, multimode operation is observed in the $x_3$ dimension, as all three layers act to form a 40 $\mu$m guide. To achieve single mode confinement wafer fabrication requires non index matched layers, the core layer of which having a higher refractive index, as a result of higher germanium concentration. Such wafers have been fabricated, as shown in Figure 8.18, and indeed show single mode confinement in the $x_3$ dimension, as shown in Figure 8.4.

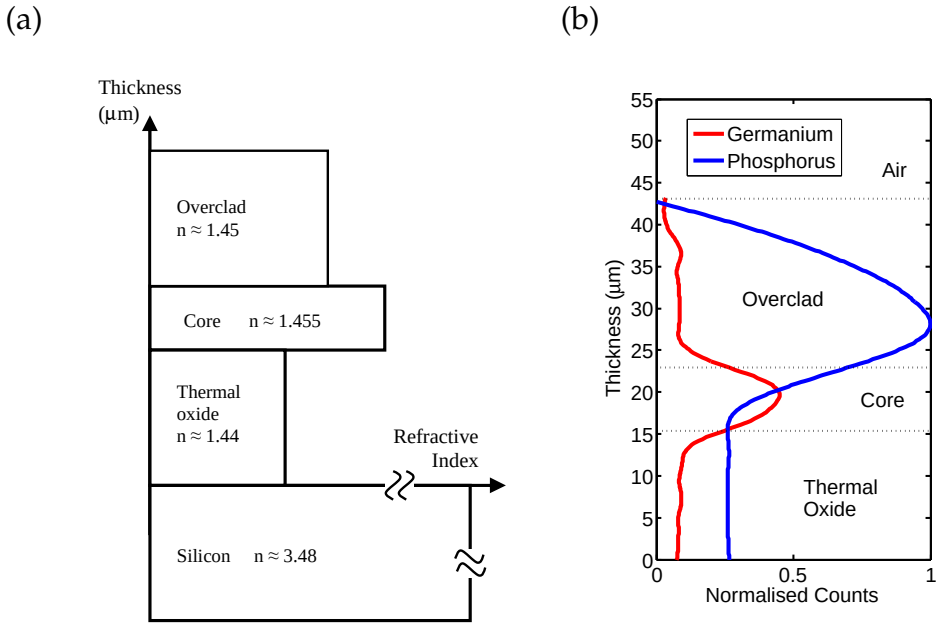


**Figure 8.18:** (a) Refractive index profile of 0 delta and non 0 delta samples (b) EDX analysis of non 0 delta silica layer composition

For proof of principle device operation single element constructions have been so far fabricated, which corroborate with simulations. Future work shall consider the more complicated multiple element designs, with constant and locally optimised period. It is understood that these designs may have to account for proximity effects that locally alter the refractive index of subsequent written areas, as investigated by Adikan [159].

(a) (b)

**Figure 8.19:** Image from a CCD camera of a 1550 nm launch into a polished output face antiresonant DUW MMI (a) index matched layers and (b) high index core layer

## 8.5 Conclusions

The concept of a locally optimised DUW antiresonant guiding MMI device has been realised. Table 8.2 compares the simulated operation of antiresonance guided structures with a raster scanned device of comparable index contrast.

| Design | Device Footprint ($mm^2$) | Writing Time (Normalised) | Excess Loss (dB) |
|---|---|---|---|
| Raster Scanned | 0.265 | 1 | 1.65 |
| Single Element | 0.231 | ~1/50 | 4.56 |
| Constant Period | 0.374 | ~1/10 | 2.52 |
| Adaptive Period | 0.588 | ~1/10 | 1.61 |

**Table 8.2:** Comparison of three interference based designs with respect to raster scanned device

In addition to the attributes detailed in Table 8.2 these devices have additional degrees of fabrication freedom in that waveguides and gratings can be written within the structures to form new device architectures.

Future work shall implement the theoretical optimum localised designs and consider such devices for sensing applications. Topless indexed matched samples may be best suited for this means as the resulting supported modes are expected to have more power in the measurand.

# Chapter 9

# Conclusions

This PhD thesis has demonstrated numerous extensions to the potential application of direct UV written structures for OADM applications, novel MMI based power splitters and chemical and physical actuators. Micromachining, etching and sputtering techniques have been implemented to enhance the performance of these devices and realise the implementation of new geometries. The following sections shall summarise the developed devices into telecommunication and sensing categories.

## 9.1 Telecommunication Devices

The actuation of direct UV written Bragg gratings have been demonstrated, as a potential means for optical add/drop multiplexing in telecommunication networks. Bragg grating actuation was achieved using thermo-optic and strain-optic means.

Through applying localized thermal and mechanical strain maximum tuning ranges of 154 GHz and 311 GHz at 1550 nm wavelengths were respectively demonstrated, which is in excess of a typical 50 GHz DWDM spacing. Although the mechanically tuned devices demonstrate a larger tuning range they also displayed spectral broadening/asymmetry for larger tuning amounts, as a consequence of the mechanical bending and the composite nature of the silica-on-silicon platform. Comparatively, the thermo-optic device did not depict this trend over its tuning range.

Removing the overclad of a locally optimised thermo-optic device, such that the heating filament was in closer proximity to the Bragg grating, gave a tuning efficiency of 102 GHzW$^{-1}$ which is a 60% increase in efficiency compared to a device with a 15 $\mu$m cladding layer. Tuning ranges may be enhanced through the use of grooves to better guide the flow of heat energy in the thermo-optic device, which may allow for a higher efficiency thus giving a higher overall tuning capability.

The mechanically tuned Bragg grating had a stress efficiency of 0.29 nm/N, modifications of the design could utilise piezo-electric actuation. The limit to tuning range for the thermal device is oxidation of the filament. The limit to tuning range for bending was applied the bending moment's position with respect to the crystal planes of the silicon. Mechanically stressing the device such that it is not in line with the planes of the silicon structure may increase the tuning range of the device.

A novel leaky mode MMI power splitter was demonstrated, which used a period adaptive Bragg mirrors to minimise excess loss. The excess loss of the optimised device was modelled to be 1.61 dB, which is an improvement upon a comparable raster scanned device (loss 1.65 dB). More importantly the UV writing time is only 1/10 th that of a raster scanned device, so can overcome issues of out-diffusion and internal device proximity effects. In addition these devices have a unique degree of freedom as waveguide gratings and structures can be written within the body of the MMI device to form new device architectures.

Sensing devices optimised the chemical as well as physical transduction of a Bragg grating to monitor environmental variations.

## 9.2 Sensing Devices

Both physical and chemical sensors have been investigated in this PhD thesis. The chemical sensors are based upon refractive index evanescent field sensing techniques. Exposure of the evanescent field has been investigated using top access and a novel side access geometry. The side access geometry is achieved using micromachined groove structures, which form an inherent platform for microfluidic manipulation.

Enhancement layers can be used to increase the sensitivity of a native sensor. The

greatest bulk sensitivity around a refractive index of water can be achieved for TE polarisation. Considering a 50 nm titania overlay the corresponding sensitivity is $1 \times 10^5$ pmRIU$^{-1}$. The surface sensitivity of a 10 nm surface change is an order of magnitude less than this value.

The monitoring of differential pressure and flow has been realised through the use of thin ($\sim$40 $\mu$m) silica membranes, in which Bragg gratings are inherently defined. It was demonstrated that an integrated device containing temperature, chemical, pressure and flow sensing Bragg gratings can be integrated upon a single chip. This gives a greater dynamic range for future lab-on-a-chip based devices.

# Chapter 10

# Future Work

## 10.1 Plasmon Enhanced Sensing

In Chapter 4 it was found that dielectric and metallic enhancement layers can improve the sensitivity of a native device. An optimised thickness of metal enhancement was computationally observed to display a lower potential sensitivity than an optimised dielectric enhancement for both bulk and surface sensitivity. It has been theoretically posed by Nemova and Kashyap [100] that a pure plasmon mode can be coupled using a Bragg gratings wavevector and a plasmon-hybrid mode. It is believed that such a pure plasmon will give a significant improvement of surface sensitivity as opposed to the plasmon-hybrid mode and more importantly enhancements made by dielectric ovelayers.

## 10.2 Low-Mass Transducers

The membrane based Bragg grating devices have proven to be an effective tool in monitoring pressure differentials. Theoretical treatment of the membranes response to buckling and pressure differentials has been understood.

Scope exists to interpret the spectral response of a Bragg gratings and other direct UV written structures inherently defined in alternative membrane constructions, such as bossed membranes for accelerometer based applications [115].

Cantilevers are another low mass structure used in physical sensing. Using the

saw machining technique, detailed in Chapter 4 it is possible to remove sections of silica through to the silicon. Combined with the KOH etching technique detailed in Chapter 6 it is possible for a very small cantilever to be fabricated, illustrated in Figure 10.1.

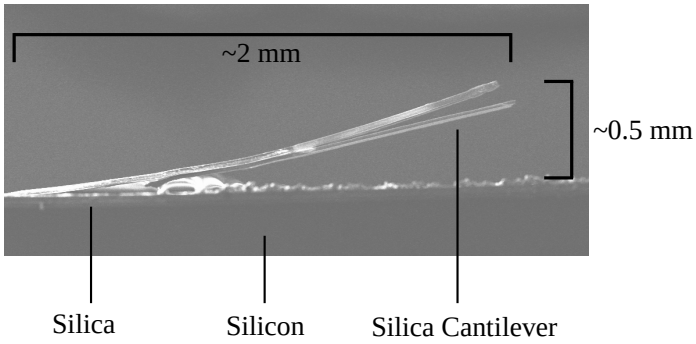


**Figure 10.1:** A prototype DGW cantilever SEM image from the side of the device

The fabricated cantilever has direct UV written Bragg gratings written along its length. The inserted image in Figure 10.2 depicts the locations of gratings A and B on the cantilever. As the different silica layers have different consolidation temperatures, there are different levels of stresses between them. This results in the cantilever curling up, away from the silicon, thus resulting in a spectral shift of grating's A and B (Figure 10.2).

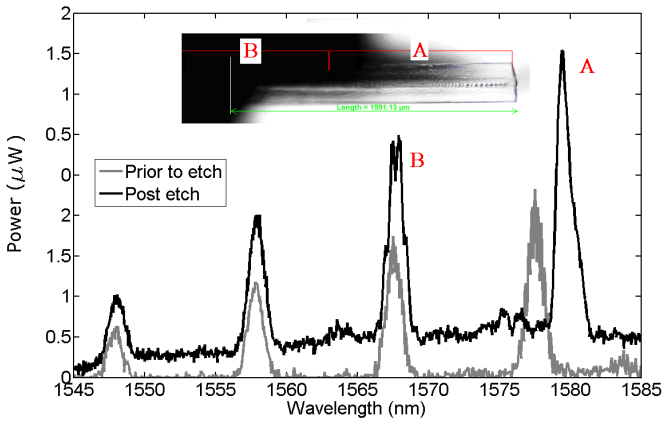


**Figure 10.2:** A prototype DGW cantilever spectral response of the stress release, a comparison of pre-etch to post-etch

Cantilever-based sensors have received increasing interest over recent years, as they offer a completely new type of miniaturised transducer with both chemical

and physical monitoring capabilities [167]. If the cantilever is mechanically resonated, quantitative and qualitative measurements can be monitored which can be enhanced to monitor a particular measurand through surface manipulation.

## 10.3 Ultra-Precision Machining

During this PhD the ultra-precision machining of grooves features have been investigated. The authour has demonstrated that surface roughness can be qreatly reduced through using rapid thermal annealing processing.

Future devices, machining micron order features into silica-on-silicon wafers, may be viable using. A proof of concept device using a 50 $\mu$m saw blade has already been demonstrated, illustrated in Figure 10.3.

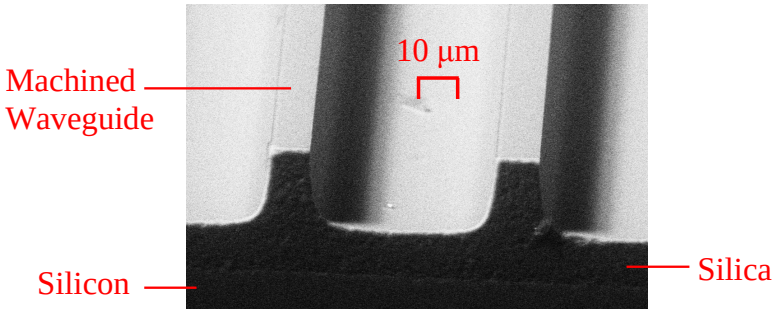


**Figure 10.3:** Waveguide fabricated using ultra-precision machining technique

The current issues with this process include surface roughness, size and being limited to straight channels. Using precision stages, similar to those applied to the DUW process and air-baring spindles, practical 2D integrated optical devices may be machined.

The novelty of this approach is that it removes expensive and time consuming cleanroom process such as the use of photoresist and etching. This approach is flexible and creates devices with a quick turn around time for rapid prototyping.

# Appendix A

# Publication List

**The journal and conference proceeding publications arisen from this work.**

**C. Holmes**, J.C. Gates, C.B.E. Gawith, P.G.R. Smith, 'Strain tuning of a composite silica-on-silicon direct ultraviolet written planar Bragg grating', Optical Engineering, 49 (4), (in press), 2009.

**C. Holmes**, D. O. Kundys, J. C. Gates, C. B. E. Gawith, P. G. R. Smith, '150 GHz of thermo-optic tuning in direct UV written silica-on-silicon planar Bragg gratings', Electronic Letters, 45 (18), pp.954-956, 2009.

**C. Holmes**, H. E. Major, J. C. Gates, C. B. E. Gawith, P. G. R. Smith, 'Period Adapted Bragg Mirror Multimode Interference Device', CLEO/QELS 2009, Baltimore, 1-7 June 2009.

**C. Holmes**, H. E. Major, J. C. Gates, C. B. E. Gawith, P. G. R. Smith, 'Flow Monitoring in Optofluidic Channels Using Planar Bragg Gratings', CLEO/QELS 2009, Baltimore, 1-7 June 2009.

**C. Holmes**, J. C. Gates, C. B. E. Gawith, P. G. R. Smith, 'Optical Differential Pressure Transducer using Planar Bragg Gratings in an Etched Membrane', CLEO 2009, Munich, 13-21 June 2009.

**C. Holmes**, M.F.R.Adikan, A.S.Webb, J.C.Gates, C.B.E.Gawith, J.K.Sahu, P.G.R.Smith, D.N.Payne, 'Evanescent field sensing in novel flat fiber', CLEO/QELS 2008, San Jose, 4-9 May 2008.

J.C.Gates, **C. Holmes**, B.D.Snow, C.B.E.Gawith, P.G.R.Smith, 'UV written evanes-

cent devices fabricated in micro-structured substrates for optofluidics', CLEO/QELS 2008, San Jose, 4-9 May 2008.

J.C.Gates, **C. Holmes**, A.Webb, M.F.R.Adikan, C.B.E.Gawith, J.K.Sahu, P.G.R.Smith, 'Direct UV written waveguides and Bragg gratings in novel substrates', Photonex 07, Coventry, 17 Oct 2007.

M.F.R.Adikan, **C. Holmes**, H.Major, C.B.E.Gawith, J.C.Gates, P.G.R.Smith, 'Direct UV written optical planar devices', Malaysian Research Group International Conference 2006 (MRG-IC2006) Manchester 19-21 Jun 2006.

J.C.Gates, **C. Holmes**, M.F.R.Adikan, C.B.E.Gawith, P.G.R.Smith, 'New geometry for planar UV written refractive index sensors', SPIE Europe Optics and Optoelectronics, Prague, 16-20 Apr 2007.

J.C.Gates, F.R.M.Adikan, **C. Holmes**, C.B.E.Gawith, P.G.R.Smith, 'Lateral groove geometry for planar UV written evanescent devices - new flexibility new devices', CLEO-Europe/IQEC Munich, 17-22 Jun 2007, CE4-4-TUE

P.G.R.Smith, C.B.E.Gawith, J.C.Gates, **C. Holmes**, B.D.Snow, F.R.M.Adikan, 'UV written planar Bragg grating sensors - geometries and applications', Photon '08 Edinburgh, 26-29 Aug 2008.

P.G.R.Smith, C.B.E.Gawith, J.C.Gates, D.M.Kundys, M.F.R.Adikan, **C. Holmes**, H.E.Major, M.Garcia-Ramirez, B.D.Snow, 'UV written waveguide devices - Bragg gratings and applications in sensors', ICAMN 2007 Langkawi, Malaysia 29 May - 1 Jun 2007 (Invited)

M.F.R.Adikan, J.C.Gates, A.S.Webb, H.E.Major, **C. Holmes**, M.A.G.Ramirez, B.D.Snow, D.O.Kundys, C.B.E.Gawith, P.G.R.Smith, 'Recent developments in direct-UV-written planar waveguides, gratings, sensors and substrates', ECIO 2007, Copenhagen, 25-27 Apr 2007.

F.R.M.Adikan, A.S.Webb, R.J.Standish, J.K.Sahu, **C. Holmes**, H.E.Major, D.Kundys, J.C.Gates, C.B.E.Gawith, P.G.R.Smith, D.N.Payne, 'Sense and fibrelity: Next generation optical biosensors', House of Commons Engineering Reception, (Poster) London 12 Dec 2006.

**The following are titles of papers that are being drafted for publication, which stem from the work directly undertaken as part of this PhD thesis:**

**C. Holmes**, J.C.Gates, P.G.R.Smith, 'Mapping the Stress Distribution in a Square Silica Membrane using Direct UV Written Planar Bragg Gratings', (2010)

**C. Holmes**, J.C.Gates, P.G.R.Smith, 'The Response of Direct UV written Planar Bragg Gratings in a Thin Silica Membrane to Differential Pressure', (2010)

# Appendix B

# FFT-BPM Algorithim

```
function ENDLOSS = MMI(Wavelength,Neff,Delta,UVthick,Period)
%The following is a function in which can be fed Wavelength, effective refractive
%index, index contrast, Thickness of UV written channel and period of MMI side walls

k0 = 2*pi/Wavelength;
% Fundamental Constants: permittiviy of free space, the spped of light
epsilon0 = 8.85E-12; c = 3e8;

% MMI Device Paramters (Width, Length and Offset. Offset marks the location of the
% launch wavguide, i.e. 0.5 is a symmetric centre launch)
Wmmi=100E-6; Lmmi = 2.2*1e-3; Offset = 0.5; spotX = 2.5E-6;

% Modelling Paramters
StepSize = 0.1E-5; TransverseSamplesX = 2^ 12 ; XWidth = 6*Wmmi;
XStep = XWidth/(TransverseSamplesX-1); x = ((1:TransverseSamplesX)-1)*XStep - XWidth/2;
sx = mod( 1/2 + (0:(TransverseSamplesX-1))/TransverseSamplesX ,1 ) - 1/2; sx = sx*(2*pi/XStep);

% Refractive index
N = [No No+Delta]; Damped = 0.01;
IndexFUN = RefractiveIndex(Damped,length(x),x,UVthick,Wmmi,Offset,N,XWidth,Period);

% Precursors for Fourier loop
psi = exp( -(x.^ 2) / (spotX^ 2));
A = exp( (i.*StepSize.*sx.^ 2) ./ (2*no*k0));
Z(1) = 0; kk=1; tennor = 0;
```

```
% Fourier loops
for ii=1:floor(MMIdevicelength/StepSize)
    if (ii>1)
        Z(ii) = Z(ii-1) + StepSize;
    end
    B = exp( (-i.* ( IndexFUN - n0 ) .*k0 ) .*StepSize);
    psi = ifft( fft(psi) .* A ) .* B ;
    tennor = tennor +1;
    if tennor == tennorCapture
        tennor=0;
        XSection(kk,:) = abs((IndexFUN(1,DisplayBoxX1:DisplayBoxX2).*c.*epsilon0./2)...
        .*psi(1,DisplayBoxX1:DisplayBoxX2)).^ 2;
        NewZ(kk) = Z(:,ii);
        [ending , rr] = size(XSection);
        Remain = 100* IntegrateMatrix(XSection(ending,:),1,rr,StepSize)/...
        IntegrateMatrix(XSection(1,:),1,rr,StepSize) ;
        ENDLOSS=100-Remain;
        Loss(kk) = ENDLOSS;
        kk = kk+1;
    end
end

% Crop and Plot
NewX = x(DisplayBoxX1:DisplayBoxX2); NewerZ = NewZ(Zdecapatate:NostepsZ); NewXSection = XSection(Zdecapatate:NostepsZ,:);
figure(1);surf(NewX*1e6, NewerZ*1e3,NewXSection,'edgecolor', 'none'); axis tight; view(90,90)

end
```

# Appendix C

# Kramers-Kronig Algorithim

restart;

The following algorithim converts extinction coefficient represented by a lorentzian curve to dispersion information

p := evalf(Pi); c := 3e8; These are the preliminary constants that need to be defined.

Variables defining the Lorentzian form of the extinction coefficient, in terms of wavelength.

wavFWHM := 75e-9;

wavcentred := 1200e-9;

extamplitude := 1.6e-9;

Converting variables to frequency domain

FWHM := c*2*p*((1/( wavcentred -(wavFWHM/2) )) - (1/( wavcentred +(wavFWHM/2) )));

centred := 2 * p * c / wavcentred;

Lorencon := (FWHM^2) * p * extamplitude/ wavcentred ;

samplesz := 350:

sampleszPlus := samplesz + 1:

last := 2 * p * c / 1000e-9: begin := 2 * p * c / 1600e-9: change := (last - begin) / samplesz:

i := 1: dn := array(1..sampleszPlus,1..3): Precursor of matrix definition

Principle integral, Note constants are absent from the Lorenzian

for varx from begin by change to last do; integ := int( (1/( ( (x - centred)^2 + (FWHM/2)^2) * (x^2 - varx^2) )), x=0,infinity, 'CauchyPrincipalValue');

From calculated principle integral, the real part of the refractive index difference can be obtained.

dnreal := Lorencon * integ * c / p;

dnalpha := (Lorencon / ( ( (varx - centred)^2 + (FWHM/2)^2 ) ));

dn[i,1] := varx;

dn[i,2] := dnreal;

dn[i,3] := dnalpha;

```
i := i + 1;
end do:


writedata('c:/maple data/X.txt',dn,float);
plot( dn[((angFreq-begin+change)/change) ,3] , angFreq = begin..last) ;
plot(dn[((angFreq-begin+change)/change) ,2] , angFreq = begin..last) ;
```

# References


[1] G. A. Thomas, B. I. Shraiman, P. F. Glodis, and M. J. Stephen. "Towards the clarity limit in optical fibre". *Nature*, 404(6775):262–264, 2000.

[2] M. Svalgaard. "Effect of $D_2$ outdiffusion on direct UV writing of optical waveguides". *Electronics Letters*, 35(21):1840–1842, 1999.

[3] G. M. Hale and M. R. Querry. "Optical Constants of Water in the 200-nm to 200-m Wavelength Region". *Applied Optics*, 12(3):555–563, 1973.

[4] F. Knappe, J. Voigt, H. Renner, and E. Brinkmeyer. "Direct UV writing of multimode-interference couplers". In *Bragg Gratings, Photosensitivity, and Poling in Glass Waveguides*, Technical Digest, page TuA4. Optical Society of America, 2003.

[5] M. Marz. *Integrated Optics: Design and Modeling*. Artech House, 1994.

[6] L. Eldada. "Advances in telecom and datacom optical components". *Optical Engineering*, 40(7):1165–1178, 2001.

[7] E. D. Palik. *Handbook of Optical Constants of Solids*. New York : Academic, 1985.

[8] S. E. Miller. "Integrated optics: an introduction". *Bell Syst. Tech. J.*, 48:205969, 1969.

[9] G. D. Emmerson. *Novel Direct UV Written Devices*. PhD thesis, Southampton University, 2003.

[10] I. J. G. Sparrow. *Development and Applications of UV Written Waveguide Structures*. PhD thesis, Southampton University, 2005.

[11] L. Eldada. "Optical communication components". *Review of Scientific Instruments*, 75(3):575–593, 2004.

[12] J. Aldred. *Iceland's energy answer comes naturally*. Guardian newspaper (online article www.guardian.co.uk), London, 2008.

[13] J. E. Midwinter and Y. L. Guo. *Optoelectronics and lightwave technology*. Wiley, 1992.

[14] T. Erdogan. "Fiber grating spectra". *Lightwave Technology, Journal of*, 15(8):1277–1294, 1997.

[15] C. Riziotis and M. N. Zervas. "Performance comparison of Bragg grating-based optical add-drop multiplexers in WDM transmission systems". *Circuits, Devices and Systems, IEE Proceedings*, 149(3):179–186, 2002.

[16] C. Nylander. "Chemical and biological sensors". *Journal of Physics E: Scientific Instruments*, (9):736, 1985.

[17] R. Lucklum, C. Behling, and P. Hauptmann. "Role of Mass Accumulation and Viscoelastic Film Properties for the Response of Acoustic-Wave-Based Chemical Sensors". *Analytical Chemistry*, 71(13):2488–2496, 1999.

[18] F. M. Battiston, J. P. Ramseyer, H. P. Lang, M. K. Baller, Ch Gerber, J. K. Gimzewski, E. Meyer, and H. J. Gntherodt. "A chemical sensor based on a microfabricated cantilever array with simultaneous resonance-frequency and bending readout". *Sensors and Actuators B: Chemical*, 77(1-2):122–131, 2001.

[19] E. Bakker and M. Telting-Diaz. "Electrochemical Sensors". *Analytical Chemistry*, 74(12):2781–2800, 2002.

[20] X. T. Zhou, J. Q. Hu, C. P. Li, D. Ma, C. S. Lee, and S. T. Lee. "Silicon nanowires as chemical sensors". *Chemical Physics Letters*, 369(1-2):220–224, 2003.

[21] A. D. Kersey, M. A. Davis, H. J. Patrick, M. LeBlanc, K. P. Koo, C. G. Askins, M. A. Putnam, and E. J. Friebele. "Fiber grating sensors". *Lightwave Technology, Journal of*, 15(8):1442–1463, 1997.

[22] P. V. Lambeck. "Integrated optical sensors for the chemical domain". *Measurement Science and Technology*, 17(8):R93–116, 2006.

[23] S. Balslev, A. M. Jorgensen, B. Bilenberg, K. B. Mogensen, D. Snakenborg, O. Geschke, KutterJ. P., and A. Kristensen. "Lab-on-a-chip with integrated optical transducers". *Lab on a Chip*, 6:213–217, 2006.

[24] R. Daw and J. Finkelstein. "Lab on a chip". *Nature*, 442(7101):367–367, 2006.

[25] K. Kincade. "Fiber sensors lay groundwork for structural health monitoring". *Laser Focus World*, 42(2):63–67, Feb. 2006 2006.

[26] X. Fan, I. White, S. Shopova, H. Zhu, J. Suter, and Y. Sun. "Sensitive optical biosensors for unlabeled targets: A review". *Analytica Chimica Acta*, 620(1-2):8–26, 2008.

[27] K. Okamoto. *Fundamentals of Opical Waveguides*. Elsevier, 2nd edition, 2006.

[28] K. Kawano and T. Kitoh. *Introduction to Optical Waveguide Analysis: Solving Maxwell's Equations and Schrodinger Equation*. John Wiley and Sons., 2001.

[29] A. Ghatak and K. Thyagarajan. *Introduction to Fibre Optics*. Cambridge University Press, 2000.

[30] S. O. Kasap. *Optoelectronics and Photonics: Principles and Practices*. Prentice Hall, New Jersey, 2001.

[31] R. P. Feynman, R. B. Leighton, and M. Sands. *Feynman Lectures of Physics*, volume 2. Boni Samuel, 2005.

[32] B. E. A. Saleh and M. C. Teich. *Fundamentals of Photonics*. John Wiley and Sons Inc., New York, 1991.

[33] H. Nishihara, H. Masamitsu, and T. Suhara. *Optical Integrated Circuits*. McGraw-Hill, 1989.

[34] J. Hu and C. R. Menyuk. "Understanding leaky modes: slab waveguide revisited". *Advances in Optics and Photonics*, 1(1):58–106, 2009.

[35] N. S. Kapany and J. J. Burke. *Optical Waveguides*. Academic Press, New York, 1972.

[36] P. Hammond and J. K. Sykulski. *Engineering Electromagnetism: Physical Process and Computation*. Oxford University Press, Oxford, 1999.

[37] M.V.K Chari and S.J Salon. *Numerical Methods in Electromagnetism*. Academic Press, New York, 2000.

[38] E. Schweig and W. B. Bridges. "Computer Analysis of Dielectric Waveguides: A Finite-Difference Method". *Microwave Theory and Techniques, IEEE Transactions on*, 32(5):531–541, 1984.

[39] M. S. Stern. "Semivectorial polarised finite difference method for optical waveguides with arbitrary index profiles". *Optoelectronics, IEE Proceedings J*, 135(1):56–63, 1988.

[40] K. Bierwirth, N. Schulz, and F. Arndt. "Finite-Difference Analysis of Rectangular Dielectric Waveguide Structures". *Microwave Theory and Techniques, IEEE Transactions on*, 34(11):1104–1114, 1986.

[41] C. Yeh, S. B. Dong, and W. Oliver. "Arbitrarily Shaped Inhomogeneous Optical Fiber or Integrated Optical-Waveguides". *Journal of Applied Physics*, 46(5):2125–2129, 1975.

[42] A. S. Sudbo. "Film mode matching: a versatile numerical method for vector mode field calculations in dielectric waveguides". *Pure and Applied Optics: Journal of the European Optical Society Part A*, (3):211, 1993.

[43] A. S. Sudbo. "Numerically Stable Formulation of the Transverse Resonance Method for Vector Mode-Field Calculations in Dielectric Wave-Guides". *IEEE Photonics Technology Letters*, 5(3):342–344, 1993.

[44] C. Kittel. *Introduction to Solid State Physics*. Wiley, 8th edition, 2004.

[45] S. W. James and R. P. Tatam. "Optical fibre long-period grating sensors: Characteristics and application". *Measurement Science and Technology*, 14(5):R49–R61, 2003.

[46] Y. J. Rao. "Recent progress in applications of in-fibre Bragg grating sensors". *Optics and Lasers in Engineering*, 31(4):297–324, 1999.

[47] A. Yariv. *Optical Electronics*. Holt-Saunders, Japan, third edition, 1985.

[48] M. Yamada and K. Sakuda. "Analysis of almost-periodic distributed feedback slab waveguides via a fundamental matrix approach". *Applied Optics*, 26(16):3474–3478, 1987.

[49] A. Othonos and K. Kalli. *Fiber Bragg Gratings: Fundamentals and Applications in Telecommunications and Sensing*. Artech House Publishers, 1999.

[50] R. A. Soref. "Silicon-based optoelectronics". *Proceedings of the IEEE*, 81(12):1687–1706, 1993.

[51] Y. P. Li and C. H. Henry. "Silica-based optical integrated circuits". *IEE Proceedings-Optoelectronics*, 143(5):263–280, 1996.

[52] A. Himeno, K. Kato, and T. Miya. "Silica-based planar lightwave circuits". *IEEE Journal of Selected Topics in Quantum Electronics*, 4(6):913–924, 1998.

[53] M. R. Poulsen, P. I. Borel, J. Fage-Pedersen, J. Hubner, M. Kristensen, J. H. Povlsen, K. Rottwitt, M. Svalgaard, and W. Svendsen. "Advances in silica-based integrated optics". *Optical Engineering*, 42(10):2821–2834, 2003.

[54] S. P. Watts. *Flame Hydrolysis Deposition of Photosensitive Silicate Layers Suitable for the Definition of Waveguiding Structures through Direct Ultraviolet Writing*. PhD thesis, Southampton University, 2002.

[55] M. Kawachi, M. Yasu, and T. Edahiro. "Fabrication of SiO2 TiO2 glass planar optical waveguides by flame hydrolysis deposition". *Electronics Letters*, 19(15):583–584, 1983.

[56] P. Tandon and H. Boek. "Experimental and theoretical studies of flame hydrolysis deposition process for making glasses for optical planar devices". *Journal of Non-Crystalline Solids*, 317(3):275–289, 2003.

[57] M. Svalgaard. *Ultraviolet light induced refractive index structures in germanosilica*. PhD thesis, Technical University of Denmark, 1997.

[58] R. F. Bunshah. "Critical issues in plasma-assisted vapor deposition processes". *Plasma Science, IEEE Transactions on*, 18(6):846–854, 1990.

[59] G. Grand, J. P. Jadot, H. Denis, S. Valette, A. Fournier, and A. M. Grouillet. "Low-loss PECVD silica channel waveguides for optical communications". *Electronics Letters*, 26(25):2135–2137, 1990.

[60] C. H. Henry, R. F. Kazarinov, H. J. Lee, K. J. Orlowsky, and L. E. Katz. "Low loss Si3N4-SiO2 optical waveguides on Si". *Applied Optics*, 26(13):2621–2624, 1987.

[61] M. V. Bazylenko, M. Gross, P. M. Allen, and P. L. Chu. "Fabrication of low-temperature PECVD channel waveguides with significantly improved loss in the 1.50-1.55 $\mu$m wavelength range". *Photonics Technology Letters, IEEE*, 7(7):774–776, 1995.

[62] K. O. Hill, Y. Fujii, D. C. Johnson, and B. S. Kawasaki. "Photosensitivity in optical fiber waveguides: Application to reflection filter fabrication". *Applied Physics Letters*, 32(10):647–649, 1978.

[63] B. S. Kawasaki, K. O. Hill, D. C. Johnson, and Y. Fujii. "Narrow-band Bragg reflectors in optical fibers". *Optics Letters*, 3(2):66–68, 1978.

[64] D. K. W. Lam and B. K. Garside. "Characterization of single-mode optical fiber filters". *Applied Optics*, 20(3):440–445, 1981.

[65] D. P. Hand and P. St J. Russell. "Photoinduced refractive-index changes in germanosilicate fibers". *Optics Letters*, 15(2):102, 1990.

[66] G. Meltz, W. W. Morey, and W. H. Glenn. "Formation of Bragg gratings in optical fibers by a transverse holographic method". *Optics Letters*, 14(15):823–825, 1989.

[67] M. Josephine Yuen. "Ultraviolet absorption studies of germanium silicate glasses". *Applied Optics*, 21(1):136–140, 1982.

[68] R. Kashyap, G. D. Maxwell, and D. L. Williams. "Photoconduction in germanium and phosphorus doped silica waveguides". *Applied Physics Letters*, 62(3):214–216, 1993.

[69] D. L. Williams, S. T. Davey, R. Kashyap, J. R. Armitage, and B. J. Ainslie. "Direct observation of UV induced bleaching of 240 nm absorption band in photosensitive germanosilicate glass fibres". *Electronics Letters*, 28(4):369–371, 1992.

[70] T. E. Tsai and D. L. Griscom. "Defect centers and photoinduced self-organization in Ge-doped silica core fiber". volume 1516, pages 14–28. SPIE, 1991.

[71] M. Douay, W. X. Xie, T. Taunay, P. Bernage, P. Niay, P. Cordier, B. Poumellec, L. Dong, J. F. Bayon, H. Poignant, and E. Delevaque. "Densification involved in the UV-based photosensitivity of silica glasses and optical fibers". *Lightwave Technology, Journal of*, 15(8):1329–1342, 1997.

[72] A. Wootton, B. Thomas, and P. Harrowell. "Radiation-induced densification in amorphous silica: A computer simulation study". *The Journal of Chemical Physics*, 115(7):3336–3341, 2001.

[73] L. Zheng, J. C. Lambropoulos, and A. W. Schmid. "UV-laser-induced densification of fused silica: a molecular dynamics study". *Journal of Non-Crystalline Solids*, 347(1-3):144–152, 2004.

[74] P. J. Lemaire, R. M. Atkins, V. Mizrahi, and W. A. Reed. "High pressure $H_2$ loading as a technique for achieving ultrahigh UV photosensitivity and thermal sensitivity in $GeO_2$ doped optical fibres". *Electronics Letters*, 29(13):1191–1193, 1993.

[75] J. Stone. "Interactions of hydrogen and deuterium with silica optical fibers: A review". *Lightwave Technology, Journal of*, 5(5):712–733, 1987.

[76] P. J. Lemaire. "Reliability of optical fibers exposed to hydrogen: prediction of long-term loss increases". *Optical Engineering*, 30(6):780–789, 1991.

[77] M. Svalgaard and M. Kristensen. "Directly UV written silica-on-silicon planar waveguides with low loss". *Electronics Letters*, 33(10):861–863, 1997.

[78] K. M. Davis, K. Miura, N. Sugimoto, and K. Hirao. "Writing waveguides in glass with a femtosecond laser". *Optics Letters*, 21(21):1729–1731, 1996.

[79] G. D. Marshall, M. Ams, and M. J. Withford. "Direct laser written waveguide-Bragg gratings in bulk fused silica". *Optics Letters*, 31(18):2690–2691, 2006.

[80] S. Nolte, M. Will, J. Burghoff, and A. Tuennermann. "Femtosecond waveguide writing: a new avenue to three-dimensional integrated optics". *Applied Physics A: Materials Science and Processing*, 77(1):109, 2003.

[81] G. D. Emmerson, S. P. Watts, C. B. E. Gawith, V. Albanis, M. Ibsen, R. B. Williams, and P. G. R. Smith. "Fabrication of directly UV-written channel waveguides with simultaneously defined integral Bragg gratings". *Electronics Letters*, 38(24):1531–1532, 2002.

[82] G. D. Emmerson, C. B. E. Gawith, S. P. Watts, R. B. Williams, P. G. R. Smith, S. G. McMeekin, J. R. Bonar, and R. I. Laming. "All-UV-written integrated planar Bragg gratings and channel waveguides through single-step direct grating writing". *Optoelectronics, IEE Proceedings -*, 151(2):119–122, 2004.

[83] C. R. Giles. "Lightwave applications of fiber Bragg gratings". *Lightwave Technology, Journal of*, 15(8):1391–1404, 1997.

[84] H. Srensen, J. Canning, and M. Kristensen. "Thermal hypersensitisation and grating evolution in Ge-doped optical fibre". *Optics Express*, 13(7):2276–2281, 2005.

[85] M. Lancry, P. Niay, and M. Douay. "Comparing the properties of various sensitization methods in H2-loaded, UV hypersensitized or OH-flooded standard germanosilicate fibers". *Optics Express*, 13(11):4037–4043, 2005.

[86] J. Canning, A. Canagasabey, and N. Groothoff. "Hypersensitisation of optical fibres with 355nm". In *Microwave and Optoelectronics Conference, 2003. IMOC 2003. Proceedings of the 2003 SBMO/IEEE MTT-S International*, volume 2, pages 973–976 vol.972, 2003.

[87] M. Fokine and W. Margulis. "Large Increase in Photosensitivity through Massive Hydroxyl Formation". In *Bragg Gratings, Photosensitivity, and Poling in Glass Waveguides*, volume 33 of *OSA Trends in Optics and Photonics Series*, page CA4. Optical Society of America, 1999.

[88] A. Canagasabey and J. Canning. "UV lamp hypersensitisation of hydrogen-loaded optical fibres". *Optics Express*, 11(13):1585–1589, 2003.

[89] C. Riziotis, A. Fu, S. Watts, R. Williams, and P.G.R. Smith. "Rapid heat treatment for photosensitivity locking in deuterium-loaded planar optical waveguides". In *Bragg Gratings, Photsensitivity and Poling in Glass Waveguides (BGPP) 01*, 2001.

[90] M Svalgaard. "Zero birefringence UV written optical waveguides". In *Bragg Gratings, Photosensitivity, and Poling in Glass Waveguides*, volume 33 of *OSA Trends in Optics and Photonics Series*, page CB3. Optical Society of America, 1999.

[91] F. Baldini, A. N. Chester, J. Homola, and S. Martellucci. *Optical Chemical Sensors*. Springer, Dordrecht, 2004.

[92] C. McDonagh, C. S. Burke, and B. D. MacCraith. "ChemInform Abstract: Optical Chemical Sensors". *ChemInform*, 39(18), 2008.

[93] P. V. Lambeck, J. van Lith, and H. J. W. M. Hoekstra. "Three novel integrated optical sensing structures for the chemical domain". *Sensors and Actuators B: Chemical*, 113(2):718–729, 2006.

[94] R. G. Heideman and P. V. Lambeck. "Remote opto-chemical sensing with extreme sensitivity: design, fabrication and performance of a pigtailed integrated optical phase-modulated Mach-Zehnder interferometer system". *Sensors and Actuators B: Chemical*, 61(1-3):100–127, 1999.

[95] H. J. Patrick, A. D. Kersey, and F. Bucholtz. "Analysis of the Response of Long Period Fiber Gratings to External Index of Refraction". *Journal of Lightwave Technology*, 16(9):1606, 1998.

[96] H. J. Patrick, G. M. Williams, A. D. Kersey, J. R. Pedrazzani, and A. M. Vengsarkar. "Hybrid fiber Bragg grating/long period fiber grating sensor for strain/temperature discrimination". *Photonics Technology Letters, IEEE*, 8(9):1223–1225, 1996.

[97] J. Homola, S. S. Yee, and G. Gauglitz. "Surface plasmon resonance sensors: review". *Sensors and Actuators B: Chemical*, 54(1-2):3–15, 1999.

[98] M. Piliarik and J. Homola. "Surface plasmon resonance (SPR) sensors: approaching their limits?". *Optics Express*, 17(19):16505–16517, 2009.

[99] W. L. Barnes. "Surface plasmon-polariton length scales: a route to sub-wavelength optics". *Journal of Optics A: Pure and Applied Optics*, (4):S87, 2006.

[100] G. Nemova and R. Kashyap. "Theoretical model of a planar integrated refractive index sensor based on surface plasmon-polariton excitation". *Optics Communications*, 275(1):76–82, 2007.

[101] J.D. Jackson. *Classical Electrodynamics Third Edition*. Hamilton Printing Co., 1998.

[102] L. Ward. *The Optical Constants of Bulk Materials and Filmes*. IOP Publishing Ltd, Bristol, second edition, 1994.

[103] F. Wooten. *Optical Properties of Solids*. Academic Press, New York, 1972.

[104] L. H. Donnell. *Beams, Plates and Shells*. McGraw-hill, New York, 1976.

[105] G.W.C Kaye and T.H. Laby. *Tables of Physical and Chemical Constants*. Harlow Longman, 16th edition, 1995.

[106] T. S. Narasimhamurty. *Photoelastic and Electrooptic Properties of Crystals*. Plenum, New York, 1981.

[107] K. Vedam. "The Elastic and Photoelastic Constants of Fused Quartz". *Physical Review*, 78(4):472–473, 1950.

[108] K. Schmitt, K. Oehse, G. Sulz, and C. Hoffmann. "Evanescent field Sensors Based on Tantalum Pentoxide Waveguides: A Review". *Sensors*, 8(2):711–738, 2008.

[109] S. Mo and W. Y. Ching. "Electronic and optical properties of three phases of titanium dioxide: Rutile, anatase, and brookite". *Physical Review B*, 51(19):13023, 1995.

[110] W. Wang and S. Chao. "Annealing effect on ion-beam-sputtered titanium dioxide film". *Optics Letters*, 23(18):1417–1419, 1998.

[111] Z. Zhao, B. K. Tay, and G. Yu. "Room-Temperature Deposition of Amorphous Titanium Dioxide Thin Film with High Refractive Index by a Filtered Cathodic Vacuum Arc Technique". *Applied Optics*, 43(6):1281–1285, 2004.

[112] L. Eldada, R. Blomquist, M. Maxfield, D. Pant, G. Boudoughian, C. Poga, and R. A. Norwood. "Thermooptic planar polymer Bragg grating OADM's with broad tuning range". *IEEE Photonics Technology Letters*, 11(4):448–450, 1999.

[113] R. M. Measures, M. M. Ohn, S. Y. Huang, J. Bigue, and N. Y. Fan. "Tunable laser demodulation of various fiber Bragg grating sensing modalities". *Smart Materials and Structures*, (2):237, 1998.

[114] Y. J. Rao. "In-fibre Bragg grating sensors". *Measurement Science and Technology*, 8(4):355–375, 1997.

[115] S. Beeby, G. Ensell, M. Kraft, and N. White. *MEMS: Mechanical Sensors*. Artech House, Massachusetts, 2004.

[116] P. V. Lambeck and H. Hoekstra. "Integrated optical sensors". In *Lasers and Electro-Optics Society, 2003. LEOS 2003. The 16th Annual Meeting of the IEEE*, volume 2, pages 967–968 vol.962, 2003.

[117] T. A. Dawood, R. A. Shenoi, and M. Sahin. "A procedure to embed fibre Bragg grating strain sensors into GFRP sandwich structures". *Composites Part A: Applied Science and Manufacturing*, 38(1):217–226, 2007.

[118] Y. Okabe, S. Yashiro, R. Tsuji, T. Mizutani, and N. Takeda. "Effect of thermal residual stress on the reflection spectrum from fiber Bragg grating sensors embedded in CFRP laminates". *Composites Part A: Applied Science and Manufacturing*, 33(7):991–999, 2002.

[119] C. Riziotis and M. N. Zervas. "Design Considerations in Optical Add/Drop Multiplexers Based on Grating-Assisted Null Couplers". *Journal of Lightwave Technology*, 19(1):92, 2001.

[120] C. Riziotis and M. N. Zervas. "Novel Full-Cycle-Coupler-Based Optical Add-Drop Multiplexer and Performance Characteristics at 40-Gb/s WDM Networks". *Journal of Lightwave Technology*, 21(8):1828, 2003.

[121] T. Chu, H. Yamada, S. Ishida, and Y. Arakawa. "Tunable optical add-drop multiplexer based on silicon photonic wire waveguides". In *Optical Fiber Communication Conference, 2006 and the 2006 National Fiber Optic Engineers Conference. OFC 2006*, pages 1409–1411, 2006.

[122] W. C. Young and R. G. Budynas. *Roarks Formulas for Stress and Strain*. McGraw-Hill, seventh edition, 2005.

[123] R. M. Jones. *Mechanics of Composite Materials*. Hemisphere Publishin Corporation, New York, 1975.

[124] N. Maluf. *An Introduction to Microelectromechanical Systems Engineering*. Arctech, Boston, first edition, 2000.

[125] J. R. Hook and H. E. Hall. *Solid State Physics*. The Manchester Physics Series. Wiley, second edition edition, 2000.

[126] J. J. Wortman and R. A. Evans. "Young's Modulus, Shear Modulus, and Poisson's Ratio in Silicon and Germanium". *Journal of Applied Physics*, 36(1):153–156, 1965.

[127] W. P. Mason. *Physical Acoustics and the Properties of Solids*. D Van Nostrand Company Inc., New Jersey, 1958.

[128] R.M. Christensen. *Mechanics of Composite Materials*. Wiley, 1979.

[129] S. Takahashi, J. Z. Hao, Y. W. A. Lee, Z. Cai, T. T. Do, and B. Y. R. Ng. "Effect of bending methods on FBG lateral force sensor". *Electronics Letters*, 41(23):1270–1271, 2005.

[130] S. Magne, S. Rougeault, M. Vilela, and P. Ferdinand. "State-of-strain evaluation with fiber Bragg grating rosettes: application to discrimination between strain and temperature effects in fiber sensors". *Applied Optics*, 36(36):9437–9447, 1997.

[131] C. Holmes, J. C. Gates, C. B. E. Gawith, and P. G. R. Smith. "Optical differential pressure transducer using planar Bragg gratings in an etched membrane". In *CLEO Europe - EQEC*, Munich, 2009.

[132] C. Holmes, J. C. Gates, C. B. E. Gawith, and P. G. R. Smith. "Flow monitoring in optofluidic channels using planar Bragg gratings". In *CLEO IQEC*, Baltimore, 2009.

[133] R. E. Oosterbroek, T. S. J. Lammerink, J. W. Berenschot, G. J. M. Krijnen, M. C. Elwenspoek, and A. van den Berg. "A micromachined pressure/flow-sensor". *Sensors and Actuators A: Physical*, 77(3):167–177, 1999.

[134] R. E. Oosterbroek, T. S. J. Lammerink, J. W. Berenschot, A. van den Berg, and M. C. Elwenspoek. "Designing, realization and characterization of a novel capacitive pressure/flow sensor". In *Solid State Sensors and Actuators, 1997. TRANSDUCERS '97 Chicago., 1997 International Conference on*, volume 1, pages 151–154 vol.151, 1997.

[135] P. Norlin, O. Ohman, B. Ekstrom, and L. Forssen. "A chemical micro analysis system for measurement of pressure, flow rate, temperature, conductivity, UV-absorption and fluorescence". In *Solid State Sensors and Actuators, 1997. TRANSDUCERS '97 Chicago., 1997 International Conference on*, volume 1, pages 507–510 vol.501, 1997.

[136] M. J. Kohl, S. I. Abdel-Khalik, S. M. Jeter, and D. L. Sadowski. "A microfluidic experimental platform with internal pressure measurements". *Sensors and Actuators A: Physical*, 118(2):212–221, 2005.

[137] J. Song and S. Lee. "Photonic microphone based on a dual-core multimode fiber head combined with a micromirror diaphragm". *Microwave and Optical Technology Letters*, 49(1):135–137, 2007.

[138] M. Ohkawa, M. Hayashi, H Nikkuni, N. Watanabe, and T. Sato. "Feasability of a silicon-based guided-wave optical microphone". In *IPNRA*, Boston, 2008.

[139] W Lukosz and P. Pilska. "Integrated optical nanomechanical light modulators and microphones". *Sensors and Materials*, 3:261–280, 2008.

[140] L. Mohanty, L. M. Koh, and S. C. Tjin. "Fiber Bragg grating microphone system". *Applied Physics Letters*, 89(16):161109, 2006.

[141] K. Hosokawa and R. Maeda. "In-line pressure monitoring for microfluidic devices using a deformable diffraction grating". In *Micro Electro Mechanical Systems, 2001. MEMS 2001. The 14th IEEE International Conference on*, pages 174–177, 2001.

[142] C. W. Wong, Y. Jeon, G. Barbastathis, and S. Kim. "Analog tunable gratings driven by thin-film piezoelectric microelectromechanical actuators". *Applied Optics*, 42(4):621–626, 2003.

[143] H. Sheng, W. F. Liu, K. Lin, S. Bor, and M. Fu. "High-sensitivity temperature-independent differential pressure sensor using fiber Bragg gratings". *Optics Express*, 16(20):16013–16018, 2008.

[144] W. Zhang, F. Li, and Y. Liu. "Fiber Bragg grating pressure sensor with ultrahigh sensitivity and reduced temperature sensitivity". *Optical Engineering*, 48(2):024402, 2009.

[145] S. P. Timoshenko. *Theory of Elastic Stability*. McGraw-Hill, New York and London, first edition, 1936.

[146] D. S. Popescu, T. S. J. Lammerink, and M. Elwenspoek. "Buckled membranes for microstructures". In *Micro Electro Mechanical Systems, 1994, MEMS '94, Proceedings, IEEE Workshop on*, pages 188–192, 1994.

[147] D. S. Popescu, D. C. Dascalu, M. Elwenspoek, and T. Lammerink. "Silicon Active Microvalves Using Buckled Membranes For Actuation". In *Solid-State Sensors and Actuators, 1995 and Eurosensors IX.. Transducers '95. The 8th International Conference on*, volume 2, pages 305–308, 1995.

[148] L. Eckertova. *Physics of Thin Films*. Plenum, second edition, 1986.

[149] K. Iga and Y. Kokubun. *Encyclopedia of Integrated Optics*. Taylor and Francis, Boca Raton, 2006.

[150] F. Bilodeau, D. C. Johnson, S. Theriault, B. Malo, J. Albert, and K. O. Hill. "An all-fiber dense wavelength-division multiplexer/demultiplexer using photoimprinted Bragg gratings". *Photonics Technology Letters, IEEE*, 7(4):388–390, 1995.

[151] T. Watanabe, T. Goh, M. Okuno, S. Sohma, T. Shibata, M. Itoh, M. Kobayashi, M. Ishii, A. Sugita, and Y. Hibino. "Silica-based PLC 1x128 thermo-optic switch". In *Optical Communication, 2001. ECOC '01. 27th European Conference on*, volume 2, pages 134–135 vol.132, 2001.

[152] S. Honda, Z. Wu, J. Matsui, K. Utaka, T. Edura, M. Tokuda, K. Tsutsui, and Y. Wada. "Largely-tunable wideband Bragg gratings fabricated on SOI rib waveguides employed by deep-RIE". *Electronics Letters*, 43(11):630–631, 2007.

[153] S. Homampour, M. P. Bulk, P. E. Jessop, and A. P. Knights. "Thermal tuning of planar Bragg gratings in silicon-on-insulator rib waveguides". *physica status solidi (c)*, 6(S1):S240–S243, 2009.

[154] A. Othonos. "Fibre Bragg gratings". *Rev. Sci. Instrum.*, 68(12):4309–4341, 1997.

[155] K. Okamoto. "Recent progress of integrated optics planar lightwave circuits". *Optical and Quantum Electronics*, 31(2):107–129, 1999.

[156] R. Kasahara, M. Yanagisawa, A. Sugita, T. Goh, M. Yasu, A. Himeno, and S. Matsui. "Low-power consumption silica-based 2x2 thermooptic switch using trenched silicon substrate". *Photonics Technology Letters, IEEE*, 11(9):1132–1134, 1999.

[157] L. B. Soldano and E. C. M. Pennings. "Optical multi-mode interference devices based on self-imaging: principles and applications". *Lightwave Technology, Journal of*, 13(4):615–627, 1995.

[158] J. Porque, P. Coudray, R. Charters, K. Kribich, P. Etienne, and Y. Moreau. "WDM based on multimode interference-coupler built in an organic-inorganic material". *Optics Communications*, 183(1-4):45–49, 2000.

[159] F. R. Mahamd Adikan, J. C. Gates, C. B. E. Gawith, and P. G. R. Smith. "Quantitative Determination of Photosensitivity Proximity Effects in Multi Exposure Direct UV Writing for High Density Integrated Optics". In *CLEO/Europe and IQEC 2007 Conference Digest*, pages CE4–3. Optical Society of America, 2007.

[160] R. Bernini, E. De Nuccio, A. Minardo, L. Zeni, and P. M. Sarro. "2D MMI devices based on integrated hollow ARROW waveguides". *Selected Topics in Quantum Electronics, IEEE Journal of*, 13(2):194–201, 2007.

[161] R. Ulrich and G. Ankele. "Self-imaging in homogeneous planar optical waveguides". *Applied Physics Letters*, 27(6):337–339, 1975.

[162] M. A. Duguay, Y. Kokubun, T. L. Koch, and Pfeiffer Loren. "Antiresonant reflecting optical waveguides in SiO2-Si multilayer structures". *Applied Physics Letters*, 49(1):13–15, 1986.

[163] H. Kim, I. Park, B. O, S. Park, E. Lee, and S. M. Lee. "Self-imaging phenomena in multi-mode photonic crystal line-defect waveguides: application to wavelength de-multiplexing". *Optics Express*, 12(23):5625–5633, 2004.

[164] H. Schmidt and A. R. Hawkins. "Optofluidic waveguides: I. Concepts and implementations". *Microfluidics and Nanofluidics*, 4(1-2):3–16, 2008.

[165] J. L. Archambault, R. J. Black, S. Lacroix, and J. Bures. "Loss calculations for antiresonant waveguides". *Journal Lightwave Technology*, 11:416423, 1993.

[166] C. Lagarias Jeffrey, A. Reeds James, H. Wright Margaret, and E. Wright Paul. "Convergence Properties of the Nelder–Mead Simplex Method in Low Dimensions". *SIAM J. on Optimization*, 9(1):112–147, 1998.

[167] N. V. Lavrik. "Cantilever transducers as a platform for chemical and biological sensors". *Review of Scientific Instruments*, 75(7):2229–2253, 2004.